CHARACTERIZATION OF THE MAGNETIC NOZZLE REGION OF HIGH POWERED ELECTRIC PROPULSION THRUSTERS USING NUMERICAL SIMULATION, RF INTERFEROMETRY AND ELECTROSTATIC PROBES

by

Christopher A. Deline

A dissertation submitted in partial fulfillment
of the requirements for the degree of
Doctor of Philosophy
(Electrical Engineering)
in The University of Michigan
2008

Doctoral Committee:

Professor Brian E. Gilchrist, Chair
Professor Alec D. Gallimore
Associate Professor Mahta Moghaddam
Franklin R. Chang-Diaz, CEO, Ad Astra Rocket Company

ACKNOWLEDGMENTS

I was fortunate to have enjoyed the support of a tremendous number of people throughout the course of this work – coworkers, co-authors, champions and cheerleaders without whom this dissertation would have been impossible. They are the giants whose shoulders have borne me.

I would first like to give a big Thank You to my dissertation chair and committee for the feedback and review that helped to produce this document. Brian, your comments and conversations were invaluable throughout the entire process, and the dedication you show for your students is wonderful. I am grateful to have been involved with your research since my freshman year in college, more than a third of my life ago. Franklin- many thanks for being a committee member, my NASA-GSRP fellowship sponsor and for being a big encouragement along the way. Your boundless optimism and personal zero-g anecdotes helped bring home why I was enamored with the idea of spaceflight since age twelve, and why I continue to be so. Alec and Mahta, thank you too for your service on this committee, and for your guidance both in the lab and in the classroom.

The fellow graduate students with whom I was delighted to serve also deserve some thanks. Tom Liu, Keith Fuhrhop, Louis Musinski, Dave Morris, Eric Choiniére, Chris

Davis, Hannah Goldberg and Allen Victor – thanks for being there when I needed expert advice, informed opinion, comic relief or an excuse to procrastinate. Whether by example or counter-example, I learned a great deal from you all!

Adrian Lopez and several other undergraduate students at the U of M provided support to me by running numerical simulations, modeling structures and providing graphics for papers and presentations. Also, Eric Choiniére proved invaluable in the running of KiPS-2D computer simulations for the triple-probe theory section of this work. His computer simulations were fast, accurate and precisely what I needed. Thanks for the months of technical support while we plowed through the hundreds of simulations required.

The team at NASA Marshall was a huge help in collecting, analyzing and deciphering experimental data, not to mention setting up and supporting the experiment. I truly could not have done this without you all. Greg Chavers, Jonathan Jones and Chris Dobson – your help with manuscript drafts, data reduction and error analysis were a godsend. Julie, Mike, Damon, Bart, Keith and Jeff, you were a terrific support crew and kept the machines humming along.

The University of Texas provided a good deal of direct and indirect support for this experiment as well. Roger Bengtson and Boris Breizman were intimately involved with the proposal and funding of this experiment, and provided a great deal of guidance along the way. Mikhail Tushentsov, Jackie Meyer and Alexey Arefiev were also a great help,

providing, respectively, MHD simulation software, Mach probe data and theoretical advice.

The Ad Astra Rocket Company was also a great contributor to the success of this effort, both by funding two semesters of my research assistantship, and by providing the motivation for the data set. Especially in the face of reduced support for electric propulsion research at NASA, you stepped up where others could not. Franklin Chang-Diaz and Jared Squire, your leadership is inspiring a new generation of engineers to do great things. Jacob Chancery, Greg McCaskill and Lenny Cassady, your technical expertise continues to be most helpful. And Andrew Ilin and Mark Carter, thank you for the conversations on numerical simulation that helped guide me through unfamiliar territory.

On a personal note, I'd like to thank my family including my parents, my sister Andrea and my wife Hollie. You always see the potential in others. Thank you for helping me to achieve mine.

Chris Deline
April 23, 2008

TABLE OF CONTENTS

LIST OF FIGURES

LIST OF TABLES

LIST OF APPENDICES

GLOSSARY

α_0 = Interferometer attenuation coefficient

α = Hybrid method proportionality constant (compares probe voltage and density)

α_{adj} = α adjusted to account for an incomplete scan

B = Magnetic field [T]

β = Plasma beta; ratio of kinetic energy to magnetic energy

β_r = Interferometer reflected wave's phase shift

C_k = Fitting coefficients for fitting data to an analytical model

C_s = Ion sound speed [m/s]

c = Speed of light in vacuum [m/s]

D_{Bohm} = Bohm diffusion coefficient [m^2/s]

D_e = Classical electron diffusion coefficient [m^2/s]

DDEX = Demonstration of Detachment Experiment conducted at NASA Marshall

E = Electric field strength [V/m]

e = Fundamental charge [C]

ε_0 = Permittivity of free space [F/m]

f = Interferometer local oscillator frequency [s^{-1}]

ϕ_0 = Interferometer initial phase prior to plasma turn-on

$\Delta\phi$ = Interferometer phase shift during plasma

ϕ_Q = Quadrature phase offset [rad]

g_0 = Gravitational constant [m^3 s^{-2} kg^{-1}]

Γ_i = Ion flux [m^{-2} s^{-1}]

γ = Ratio of specific heats C_p/C_V

h_s = Sheath thickness [m]

η_{noz} = Nozzle efficiency

$\eta_{N,jet}$ = Nozzle power efficiency

I_d = Gun discharge current [A]

I_{gas} = Gas flow rate current [A equivalent]

I_e^{sat} = Electron saturation current [A]

I_i^{sat} = Ion saturation current [A]

I_{sp} = Specific impulse [s]

i = Imaginary number (OR) index for position in a scan or a series

k = Wavenumber [m^{-1}]

k_0 = Free space wavenumber [m^{-1}]

k_p = Plasma wavenumber [m^{-1}]

k_B = Boltzmann's constant

Λ = Coulomb parameter

λ_D = Debye length [m]

$\lambda_{i,n}$ = Ion-neutral mean free path [m]

M = Ion Mach number

m = Mass [kg]

m_e = Electron mass [kg]

m_i = Ion mass [kg]

μ_0 = Magnetic permeability of free space [H/m]

N = Refractive index

N_e = Line integral electron density [m^{-2}]

n_c = Critical (cutoff) density [m^{-3}]

n_i = Ion particle density [m^{-3}]

n_{neut} = Neutral particle density [m^{-3}]

ν_{ee} = Electron-electron collision frequency [s^{-1}]

ν_{ii} = Ion-ion collision frequency [s^{-1}]

$\nu_{i,n}$ = Ion-neutral collision frequency [s^{-1}]

P = Neutral pressure in the chamber [Pa]

P_{jet} = Jet power in the exhaust [W]

q = Particle charge [C]

$R(z)$ = Plume ½ - max radius at axial position z

Res = Numerical residue from least-squares fitting

r_{ce} = Electron cyclotron radius [m]

r_{ci} = Ion cyclotron radius [m]

r_p = Probe radius [m]

ρ = Interferometer reflection coefficient

S_p = Probe surface area [m^2]

σ = One standard deviation from the center value of a Gaussian distribution. +/- 2σ includes 95% of the distribution

σ_{CEX} = Charge exchange cross-section for ion-neutral collisions [m^2]

σ_{total} = Collision cross-section including charge exchange and momentum transfer [m^2]

T = Thrust [N]

T_e = Electron temperature [eV]

T_i = Ion temperature [eV]

T_{neut} = Neutral particle temperature [K]

t = Time [s]

V_D = Interferometer 'dark' voltage [V]

V_{d2} = Triple-probe bias provided by a battery [V]

V_{d3} = Bias of triple-probe electron collector with respect to floating potential [V]

V_i = Langmuir probe voltage at step i [V]

V_p = Langmuir probe plasma potential [V]

V_f = Langmuir probe floating potential [V]

v = Velocity [m/s]

v_z = Bulk plume velocity [m/s]

v_A = Alfvén velocity [m/s]

v_{th} = Ion thermal velocity [m/s]

v_D = Radial velocity due to classical cross-magnetic field diffusion [m/s]

W_B = Magnetic energy density [J/m^3]

W_k = Kinetic energy density [J/m^3]

w = Plume $1/\sqrt{e}$ radius; one standard deviation from the center value

ω_p = Electron plasma frequency [rad^{-1}]

ω_{ci} = Ion cyclotron frequency [rad^{-1}]

ω_{ce} = Electron cyclotron frequency [rad^{-1}]

Δx = Step size between points in a scan [m]

ABSTRACT

CHARACTERIZATION OF THE MAGNETIC NOZZLE REGION OF HIGH-POWERED ELECTRIC PROPULSION THRUSTERS USING NUMERICAL SIMULATION, RF INTERFEROMETRY AND ELECTROSTATIC PROBES

by

Christopher A. Deline

Chair: Brian E. Gilchrist

Experimental results are presented from the plume of a high powered (200 kW) DC plasma gun emitting into an applied magnetic nozzle. The plasma source operated on helium and hydrogen and was attached to a large (3 m x 5 m) vacuum chamber kept at low background pressure (< 2×10^{-6} Torr). Density profiles, electron temperature and ion velocity are measured in a region where the ratio of plasma kinetic pressure to magnetic pressure was $\beta = 0.2 - 20$. Numerical simulations are employed to compare experimental results with theoretical predictions of plasma detaching from magnetic fields. Significant particle deviation from confining magnetic fields was found for conditions approximating $\beta > 1$ in accordance with magnetic detachment theory.

Unique accomplishments of this research include measurements of propulsion-appropriate plasmas exiting a magnetic nozzle and transitioning from $\beta < 1$ to $\beta > 1$. This region is of particular interest for magnetized plasma thrusters since inefficient magnetic detachment may result in a serious efficiency penalty for their use in proposed in-space propulsion systems. Nozzle efficiency estimates are provided based on simulated and measured experiment conditions. In particular, an optimized magnetic nozzle condition is found that theoretically improves nozzle efficiency by 10% over the standard magnetic dipole condition.

Plasma diagnostics are utilized, including microwave interferometers and Langmuir triple probes. Diagnostic theory is reviewed for these tools, specifically for the conditions found in this experiment. Prior theory was sometimes found inapplicable to the experimental conditions, particularly in the case of a Langmuir triple probe in a flowing plasma. To account for inadequacies in standard theory, numerical simulations were conducted to find calibration factors for the appropriate experimental conditions.

In addition, a new measurement methodology is developed utilizing electrostatic probes and microwave interferometers in tandem. Detailed density profiles were collected using this method, and a comprehensive error analysis was conducted. The error in density measurements was determined to be much lower than the error in electrostatic probe measurements, and on the order of microwave interferometer uncertainty – as low as 10%.

CHAPTER 1

INTRODUCTION

1.0 Overview

1.1 Motivation for Electric Propulsion

The National Vision for Space Exploration which was unveiled in 2003 has given a focus to the space industry in America. That focus is to look beyond our near-earth environment and to begin expanding our human presence to the Moon, Mars and beyond. As Michael Griffin, then-NASA chief stated during a 2003 congressional hearing: "Human expansion into space is a continuation of the ancient human imperative to explore, to exploit, to settle new territory when and as it becomes possible to do so." And while he conceded that conventional rocket propulsion will suffice to get us around in the near-term, "In the long run, some form of nuclear-electric propulsion is likely to offer the best combination of efficiency and packaging capability for interplanetary flight." [Griffin 2003]

The technology of electric propulsion that he was speaking of differs from conventional rocket propulsion in that electrical energy from the spacecraft bus is converted into kinetic energy in the rocket exhaust. [Martinez-Sanchez 1998] This is particularly useful for deep space missions because of the limitations of standard rocket fuel which is

seen in the following equation. The thrust developed from a rocket exhaust is equal to $T = \dot{m} v_{ex} = \dot{m} g_0 I_{sp}$, where I_{sp} is the specific impulse of the exhaust, and g_0 is the gravitational acceleration at the earth's surface. Since longer missions benefit from a reduction in propellant mass fraction, in order to maintain a high thrust level, I_{sp} must be increased proportionately. While a standard chemical rocket e.g. the space shuttle main engine produces a maximum I_{sp} of 460 s [Humble 1995], electric thrusters such as the ion thrusters used on NASA's DS1 mission produce a much higher I_{sp} = 3200 s. [Rayman 2000] Thus, less propellant mass need be used for a given mission, leaving more mass for larger payloads, or greater mission Δv. If one considers that with the use of conventional rockets and without gravity assist or aerobraking, a Mars mission is required to carry 85% of its weight as fuel, vs. e.g. 15% for a 3000 s I_{sp} electric propulsion thruster [Racca 2001], the benefits of EP can be enormous.

In particular, when ferrying humans across the solar system, trip times must be kept as short as possible to limit the deleterious effects of space travel, including heavy ion radiation bone loss and psychological difficulties [White 2001]. This is why Michael Griffin suggested high-powered nuclear-electric propulsion as a technology worth pursuing, since in-space nuclear fission reactors could theoretically provide power levels greater than the ~1x10^5 W levels of power reasonably generated by solar arrays [Wertz 1999]. This propulsion technology could reduce trip times by 50% [Karavasilis 2001] [Sankaran 2004]. High-powered electric propulsion can also be an enabling technology for deep space missions that require a large change in orbital velocity (ΔV) to visit planetary bodies of interest, such as the icy moons of Jupiter in the now-canceled JIMO

mission [Olesen 2004]. In these long duration missions, the improved lifetime of electrodeless plasma thrusters can be highly desirable. [Longmier, 2006]

1.2 Magnetic nozzle background

A trait typical of some but not all of these high powered propulsion systems is the need for an applied magnetic field in order to produce or heat the exhaust plasma. Downstream of the system's magnetic coils, the applied field diverges, forming a magnetic nozzle analogous to the de-Laval rocket nozzle. The magnetic nozzle serves to direct and expand the plasma flow, increasing its directed axial energy and minimizing plume impingement on the surrounding spacecraft structure. Some high powered EP concepts employing a magnetic nozzle include applied-field MPD thrusters [Tikhonov, 1997], fusion rockets, [Kammash, 2000],[Williams, 2004] , the Variable Specific Impulse Magnetoplasma Rocket (VASIMR) [Squire, 2003] [Arefiev, 2004] and helicon thrusters. [Charles, 2006] , [Toki, 2006]. A notional magnetic nozzle is shown in Figure 1.1 exhibiting axisymmetry and a magnetic field and plasma flux oriented principally in the z direction.

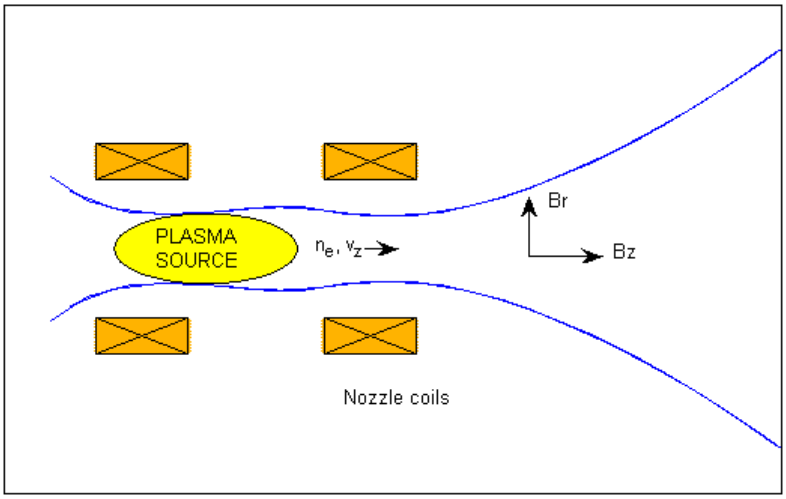

Figure 1.1: Notional magnetic nozzle showing plasma source emitting on-axis into an expanding magnetic field.

In order for the magnetic nozzle to have any effect, the plasma must be magnetized. This means conceptually that the applied magnetic field is sufficiently strong to hold ions and electrons in orbits around the axial field. A measure of this condition is plasma Beta β where

$$\beta = \left(\frac{v}{v_A}\right)^2 = \frac{\mu_0 n_i m_i v^2}{B^2} \tag{1.1}$$

β is equal to the ratio of kinetic energy in the plasma flow to magnetic energy, defined in these terms as $\beta = W_K / W_B$ when $W_K = m_i n_i v^2 / 2$ and $W_B = B^2 / 2\mu$. β is also equal to the ratio of the ion flow velocity to the Alfvén velocity v_A squared where

$$v_A = \frac{B}{\sqrt{\mu_0 n_i m_i}} \tag{1.2}$$

The Alfvén velocity is the velocity at which perturbations in the applied magnetic field (Alfvén waves) propagate.

What this all means for a magnetized plasma is that if β is less than unity, the magnetic field is strong enough to direct and confine the plasma flow. If β is greater than unity (or equivalently flow velocity $v > v_A$) the plasma flow is uninfluenced by the applied magnetic field, with some amount of magnetic flux trapped along with the plasma flow. For this final separation condition, the ratio of ion kinetic energy density outweighs the confining magnetic field energy density, and the plasma expands freely. This is analogous to the solar wind expanding away from the sun's magnetic field.

If the above theory holds true for electric propulsion thrusters as well as for the solar wind, the prospects of producing useful thrust from such a thruster are good. However it is not universally accepted that the same theory applies to both situations, and experimental evidence is wanted to strengthen this theoretical claim. If measurements could be conducted in the high β region of a magnetized plasma source, and show that the plume is detached from magnetic fields by the time $\beta > 1$, it would show strong support for the aforementioned theory. However, if the plasma plume fails to detach from the curving magnetic field or diverges excessively, the thrust of the rocket will be greatly reduced.

Several previous studies have been conducted to investigate the accelerating potential of magnetic nozzles, and their ability to produce a plume detached from applied magnetic fields. These studies provide the background for this current work.

1.2.0 Magnetic nozzle literature survey

A diverging magnetic nozzle has been investigated both numerically and experimentally in conjunction with MPD arcjets. [Walker 1971] [Chubb, 1972] [Inutake 2002] The detachment issue was not dealt with explicitly in these works, but the accelerating effect of magnetic nozzles was successfully studied. In these cases the effect of a magnetic nozzle was to reduce the electron temperature by a factor of 3-6x, and to increase the ion Mach number by a factor of ~2x. These results can be understood in two ways, which will be investigated more thoroughly in Section 2.4. The first process occurring is isentropic expansion whereby thermal energy in the form of ion and electron temperature is converted to directed kinetic energy as the plume expands. The second process is conservation of magnetic moment whereby azimuthal kinetic energy is converted to axial kinetic energy as B_z decreases. Thus ion acceleration was shown to occur for plasma flowing in a diverging magnetic nozzle, and thermal energy was experimentally demonstrated to be converted into directed axial energy by the magnetic pressure of the diverging magnetic nozzle.

An early investigation of plasma detachment from magnetic fields was produced by Gerwin et al. [Gerwin 1989]. A 2-D ideal MHD analysis of a diverging magnetic nozzle was conducted for a large range of input temperatures (1eV – 100 eV), and densities (6

orders of magnitude) of a hydrogen plasma. For plasma with high conductivity the flow tended to follow diverging magnetic field lines. Gerwin et al. did not address systems in which the plasma beta is greater than one, and thus does not replicate the conditions considered in this work. Several other limited analyses were also completed giving an estimate of cold collisionless (infinite conductivity) plasma flow detaching from diverging magnetic fields. [Sercel, 1990] [Hooper, 1993] The results of these analyses showed that a small portion (4%) of the magnetic nozzle is able to produce detached plasma flow without the need for collisional transport across field lines. However, in a real device, finite conductivity and turbulence were theorized to improve on this detachment rate. These initial ideal MHD simulations provided a bleak outlook on the prospect for magnetic detachment due to the restrictive assumptions of plasma confinement, neglecting cross-field diffusion and ignoring the loss of confinement for $\beta > 1$ conditions.

Further resistive MHD simulations accounted for these non-ideal factors and gave a much higher and more accurate estimate of detachment efficiency. [Mikellides, 2002] completed a simulation of a high power (GW class) fusion thruster with a detached flow and 70% nozzle efficiency. Both MHD simulations and Particle-in-cell simulations were completed for the VASIMR thruster geometry [Ilin 2002] . Several hallmarks of magnetic detachment were shown in this simulation after a distance of z = 2-3 meters. This includes a stabilization of axial ion energy, ion Larmor radius ρ_i becoming greater than the magnetic field curvature $\nabla B / B$ and the plasma β growing greater than unity

The transition of a plasma flow from sub-Alfvénic to super-Alfvénic (β increasing above unity) was investigated in an ideal MHD analysis by Arefiev et al. [Arefiev 2005] . In their analysis, a $\beta > 1$ flow is guaranteed to detach from the spacecraft. The detachment efficiency of the nozzle is limited by cosine losses and induced currents in the nozzle wall (if applicable), but overall efficiency was determined to be much greater than in previous ideal MHD analyses which neglected this $\beta > 1$ condition. A recommendation was made for efficiency purposes that the applied magnetic nozzle fields be made with straight diverging lines (decreasing with $1/R^2$ rather than dipole fields decreasing with $1/R^3$) to limit the formation of inefficient diamagnetic currents. This recommendation is investigated later in Chapter 5.

1.2.1 Helicon double layer

The present work does not deal directly with this phenomenon, but due to its similarity in application, a literature review is provided. The discovery of a current-free double layer in a helicon discharge is a relatively recent occurrence that has been said to have potential for electric space propulsion. [Charles, 2003 ; Cohen, 2003] In a current-free double layer a narrow potential drop (< 100 Debye lengths in width) results in an accelerated ion beam in the downstream direction, and an accelerated electron beam back towards the plasma source. The Argon ion beam in [Charles, 2003] was reported to be accelerated to > 20eV which is highly supersonic (M = 2-3). The potential drop in the double-layer was found to be highly sensitive to pressure, only occurring for pressures of $2\text{x}10^{-1}$ – $2\text{x}10^{0}$ mTorr. [Lieberman, 2006] PIC simulations show that the double layer formation is also dependent on the rate of expansion of the plasma in the diverging magnetic nozzle.

[Meige, 2005] This double-layer has been suggested as a mechanism to provide thrust for in-space propulsion [Charles, 2006]. Although thrust has not yet been measured from such a device, and its utility as a means of electric space propulsion may in practice be lower than expected ([Fruchtman, 2006]), it has been suggested via simulation that the ion beam emerging from a helicon double layer will be magnetically detached. [Gesto, 2006]. If a helicon double-layer thruster proves to be a feasible system for in-space propulsion, it could provide a potential area of applicability for the magnetic nozzle work presented in this dissertation.

1.3 Summary of contributions

Several previous simulations have investigated a high – β plasma exiting a magnetic nozzle, and previous experiments have investigated nozzle physics for low β. However, no prior experiment has been conducted that focused on high-β plasma at a distance of several meters from the plasma source. No prior experiment has combined a high powered plasma source with a large vacuum chamber and low neutral background pressure to achieve the collisionless conditions and high thrust required to achieve $\beta > 1$ detachment within the experiment scale length.

The main theme of this work is experimental investigation of high powered EP thruster plumes, specifically those utilizing a magnetic nozzle. In particular, experimental evidence of magnetic detachment is sought. Diagnostics used for this measurement will be discussed including microwave interferometers and electrostatic probes. Measurements from these diagnostics will be presented along with detailed simulation

and analysis to compare measurement with theory. The questions that will be investigated include – Is magnetic detachment occurring in this experiment? Under what conditions will the magnetized plasma plume detach from its applied magnetic fields? And at what efficiency will this detachment occur?

The unique contributions from this work include:

- Detailed measurement and description of the plasma environment for a high-powered (> 200 kW) DC thruster plume in regions of plasma β spanning from 0.2 to 20.
- Development of a novel hybrid measurement technique incorporating both RF interferometer and electrostatic probe that combines the strengths of both measurements. A detailed error analysis was conducted showing the absolute density error of this method to be comparable to the error of the microwave interferometer alone. The results from this method were compared with scanning microwave interferometry with Abel inversion, and standard Langmuir probe theory.
- Numerical simulations of a Langmuir triple probe immersed in flowing plasma. Classical diagnostic theory does not account for Langmuir triple probes in a flowing plasma, and errors associated with their use were formerly unknown except in a few conditions. A range of plasma conditions was simulated including those encountered in the experiment. The relative error of the classical Langmuir triple probe measurement for these conditions was calculated and compared with previous results.
- Development of a quasi-1D numerical simulation of the DDEX experiment comparing the experimentally determined density profiles with theoretical plasma profiles. A

simulation utilizing initial conditions and results similar to the experiment suggests that magnetic detachment plays a role in determining plume profiles.

- Theoretical estimates of nozzle efficiency based on simulation. Computer code was developed to predict the efficiency of various magnetic nozzle configurations. An optimized condition was found that is theorized to increase nozzle efficiency by ~10% over a simple magnetic dipole condition.
- Benchmarking of quasi-1D code with a second 2D MHD code. Both codes produced similar plume profiles and nozzle efficiency predictions given identical initial conditions. The second code which has heritage in the magnetized fusion community helps to increase confidence in the simpler 1D model.

1.4 Thesis outline

The dissertation is arranged as follows:

Chapter 1 provides motivation, background information and a literature review of the study of magnetic nozzles. It also states key findings of this dissertation, and poses major questions that the research intends to answer.

Chapter 2 details the theory of plasma diagnostics used in this experiment. Also, the details of a novel hybrid method of plasma density profile measurement will be provided. Prior theory on the physics occurring in the magnetic nozzle region of the experiment will also be given. Experimental results will be compared with this prior theory in later chapters.

Chapter 3 gives experimental details on the facility, the plasma source and the diagnostics. A detailed neutral pressure analysis of the vacuum chamber is given, and error terms in the microwave interferometer diagnostics is provided.

Chapter 4 presents experimental results and analysis. Plasma density profiles are provided at several locations in the experiment, along with electron temperature and flow velocity measurements. Estimates of error are given including a calibration factor for Langmuir triple probes in flowing plasma.

Chapter 5 compares experimental results with theory and simulation. A novel computer code is detailed and benchmarked against other similar codes. Nozzle efficiency estimates are given for multiple experiment conditions.

Chapter 6 concludes the research, provides a summary of key findings, and gives suggestions for future research.

CHAPTER 2

THEORETICAL BACKGROUND

2.0 Overview

This section includes diagnostic theory, an introduction to the hybrid measurement technique used in this experiment, and an overview of magnetic nozzle physics.

The diagnostics sections will provide background theory on the plasma diagnostics used in this work. An effort was made to limit the scope of this overview to only that theory which is of critical importance to understanding the measurements conducted. Langmuir probe theory is investigated in the context of using Langmuir triple-probes to provide ion density and electron temperature measurements (n_i and T_e). Interferometer theory is applied towards a quadrature homodyne RF interferometer used to detect line-integral electron density.

In the hybrid measurement section, theory is given on a novel measurement technique combining both Langmuir triple-probes and RF interferometers in what is termed a hybrid approach. [Deline, 2007] The relevant assumptions made for each diagnostic is presented, along with limitations and sample data.

The magnetic nozzle section explains physical processes that govern plasma exhaust as it exits a magnetic nozzle. Different magnetic nozzle zones are defined, with the relevant governing equations provided for each region. Prior experimental results are given for those regions that are not studied in detail with this experiment.

2.1 Langmuir probes

2.1.0 Introduction

Simple conducting in-situ probes to measure the plasma voltage-current characteristic are one of the first plasma diagnostics ever developed, and remain some of the most useful and widespread diagnostics [Langmuir, 1926]. Their size and shape and construction can vary, depending on the conditions of the plasma to be measured. With these in-situ electrostatic probes, the ion and electron fluxes are directly sampled from the plasma. A modulation of the probe voltage with respect to the plasma is accomplished thorough external circuits, which provides a current-voltage characteristic $I(V)$. It should be noted that the circuit must be closed by grounding the external circuit to the experiment chamber or the plasma generating electrode, providing an adequate return current path. The shape of a typical $I(V)$ characteristic is given in Figure 2.1. The traits typical of all probe characteristics are the plasma potential V_p, the floating potential, V_f, and ion and electron saturation currents I_i^{sat} and I_e^{sat} respectively.

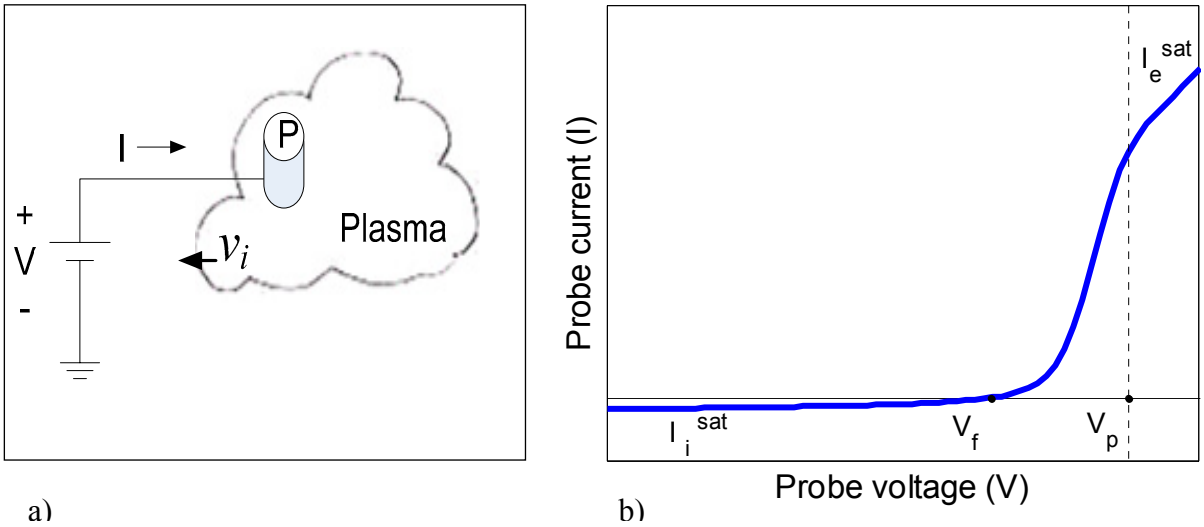

Figure 2.1: a.) Notional Langmuir probe (P) in contact with a plasma showing the definition for collected current and probe voltage. B.) General form of the Langmuir probe characteristic. V_f is the floating probe potential at I = 0. V_p = 0 is the plasma potential, I_e^{sat} and I_i^{sat} are the electron and ion saturation currents, respectively.

The plasma potential is the potential of the undisturbed plasma surrounding the probe. At this potential, no electric field is formed around the probe, and no particles are accelerated to it. However, due to the lower mass and higher velocity of the electron, more thermal collisions of negative particles take place with the probe, giving it a net positive current. As the probe bias is decreased, electrons are repelled and ions are attracted to the collector. In a Maxwellian distribution of electrons, the current characteristic decreases exponentially with probe potential until the current contributions from the ions and electrons are equal. At this point, the net current is zero, and the probe is at the floating potential. This is the voltage to which an insulated body will float when it is placed in contact with plasma. Although no current is being drawn, the surrounding plasma is perturbed by the formation of a sheath in which electrons are depleted. The thickness of this sheath is on the order of a few Debye lengths where

$$\lambda_D = \sqrt{\frac{\varepsilon_0 T_e}{n_e e^2}} \tag{2.1}$$

is the electron Debye length.

The ion saturation current I_i^{sat} is reached when the bias is sufficiently negative to repel the majority of electrons, with mainly ion current being collected. The $I(V)$ characteristic continues to collect additional ion current beyond the ion saturation current as the probe sheath expands outwards. A standard measurement of sheath thickness h_s can be approximated for planar collisionless sheaths in non-drifting plasma by [Raizer, 1991]:

$$h_s \approx \lambda_D \left(\frac{e|V|}{T_e} \right)^{3/4} \tag{2.2}$$

The electron saturation current I_e^{sat} is likewise attained when ions are excluded by the probe bias and electrons are solely collected. This occurs at a bias slightly higher than V_P the plasma potential.

2.1.1 Probe size, shape and construction concerns

The collecting area of the electrostatic probe must be chosen carefully such that the probe conforms to the theory used to deduce relevant plasma parameters. One such consideration is that the probe sheath be considered collisionless around the probe, thus $\lambda_{mfp} / \lambda_D >> 1$ where λ_{mfp} is the collisional mean free path for the relevant particle species.

For ion collection, the relevant particle collisions are ion-ion and ion-neutral, while for electron collection the relevant particle collisions are electron-electron and electron-neutral. Electron-ion collision rates are equal to or lower than any of these other collision processes. Furthermore, in all experiments considered here, $\lambda_{mfp} / \lambda_D >> 1$. Another consideration is the radius of the probe r_p with respect to plasma Debye length λ_D. In the limiting case of $r_p / \lambda_D < 1$ the probe collects particles according to orbital-motion limited (OML) theory. This is an appropriate case for small cylindrical wires in low density plasmas, e.g. space plasmas. The opposite limiting case for the work here is the thin sheath limit where $r_p / \lambda_D >> 1$ or more appropriately, $(h_s + r_p)/r_p \sim 1$ where h_s is the sheath thickness. In this limiting case, also known as space-charge limited collection, the ion saturation current is not expected to increase with bias since the probe sheath is considered a planar sheath which only expands in 1-D. The use of thin sheath theory is appropriate for our condition of large cylindrical geometries in high density laboratory plasmas. Both theories assume that the probe length is long compared with its radius to reduce the influence of current collection at the tip.

The shape of the electrostatic probe also provides an element of freedom for the probe designer with typical shapes being planar, cylindrical or spherical. In the case of this experiment, cylindrical probes were chosen for their ease of construction and close tolerance in diameter. They are oriented perpendicular to the flow of the plasma, and also perpendicular to the magnetic field lines in this experiment to minimize non-ideal collection due to cross-magnetic field transport issues. Flow effects will be explained in detail below. In addition to the shape, the composition of the probe must be considered.

The collection or emission of secondary electrons from the probe surfaces is undesired as it results in a net decrease or increase in ion saturation current respectively. The probe material was chosen to be stainless steel as this has both a moderate secondary electron emission (SEE) coefficient, and a high melting point. [Schächter, 1998] Exotic materials like Tanatalum were considered for their lower SEE coefficient, but their difficulty to work with and high cost outweighed their benefits. Another concern for the accurate measurement of electron temperature T_e is the uniformity of the collection surface. Variation in the work function of the material leads to additional error in T_e. However this is more of an issue when working with low temperature space plasmas. For the higher temperatures found in the laboratory plasmas considered here, the probe's material non-uniformity is much less of a concern.The influence of surrounding insulators was also considered, as alumina ceramics can readily give off secondary electrons. [Hopman, 2003] This was not found to be a large concern for this diagnostic since ion saturation current was the measurement of most importance, the collection of which results in the repulsion of any secondary electrons born from surrounding insulators.

Another concern for our laboratory plasma is the flow velocity. Standard probe theory assumes a non-flowing collisionless plasma, which is seen in the following equation. The ion saturation current collected to a cylindrical conductor for static, or slowly drifting plasma with $\frac{1}{2}m_i v_i^2 < eT_e$ is: [Hoegy, 1973]

$$I_i^{sat} = S_p n_i q_i \frac{h_s + r_p}{r_p} \sqrt{\frac{eT_e}{2\pi m_i}} \left(1 + \frac{m_i v_i^2}{2eT_e} + \ldots\right) \tag{2.3}$$

where: q_i = ion charge, v_i = ion drift velocity, T_e = electron temperature [eV], m_i = mean ion mass, S_p = probe surface area and $\left(h_s + r_p\right)/r_p$ is the ratio of probe radius to cylindrical sheath radius ≈ 1 for the thin sheath approximation.

For $v_i = 0$, equation (2.3) reduces to the standard Bohm formulation for thin-sheath ion saturation current collection. [Mott-Smith (1926) eq. 25]

The addition of a greater flow component $½m_i v_i^2 > eT_e$ results in additional ion saturation current collected to the probe. The combination of thermal current plus ram current collected to a cylindrical probe in the thin-sheath limit is: [Hoegy, 1973]

$$I_i^{sat} = \frac{1}{\pi} S_p n_i q_i v_i \frac{h_s + r_p}{r_p}\left(1 + \frac{eT_e}{2m_i v_i^2} + \ldots\right) \tag{2.4}$$

An assumption was made in the derivation [Hoegy, 1973 Eq. (11a)] that $½m_i v_i^2 > eT_e$ thus equation (2.4) does not reduce to the standard Bohm equation for ion saturation current at $v_i = 0$, like equation (2.3) does.

In addition to providing increased ion saturation current, the flow component requires that multiple Langmuir probes not be oriented in a line parallel to the flow vector, otherwise the first probe will shadow the other probes. This concern is considered during the experiment setup in Chapter 3.

2.1.2 Langmuir triple-probe theory

Collecting the entire $I(V)$ characteristic through a full probe bias sweep will provide all of the plasma parameters of interest: T_e, n_e, V_p and n_i. However, in a transient plasma with parameters changing faster than the duration of the sweep, a full bias sweep will not be fast enough to provide adequate temporal resolution. A triple-probe configuration like that in Figure 2.2 allows the measurement of n_i and T_e to high temporal resolution. For a more detailed description of this device, the reader is directed to Chen and Sekiguchi (1965) or Bufton (1996).

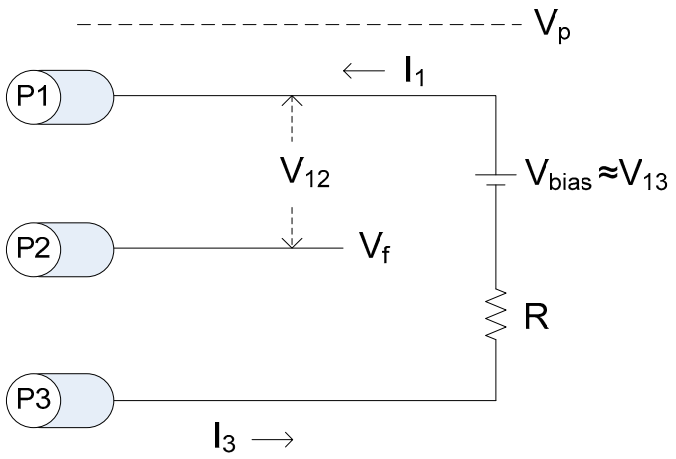

Figure 2.2: Circuit schematic for Langmuir triple-probe. Resistor R is the sensing resistor for measuring ion saturation current. V_{12} is the floating probe measurement ≈ 1 V, and V_{bias} is the supplied voltage bias, which is nearly equal to V_{13} due to the small voltage drop across resistor R. V_p is the plasma potential, and V_f is the floating potential.

The following assumptions are made for current flowing to these probes: 1) The electron energy distribution is Maxwellian, 2) the collisional mean free path for electrons is large with respect to both the ion sheath thickness h_s and probe radius r_p, and 3) the thickness

of the ion sheath is smaller than the probe separation so that interaction between the three probes is negligible. The validity of these assumptions is considered in Section 3.2.1.

Under these conditions, the currents to probes 1, 2 and 3 are as follows:

$$-I_1 = -I_e^{sat} \exp(V_1 / T_e) + I_i^{sat}(V_1) \tag{2.5}$$

$$I_2 = -I_e^{sat} \exp(V_2 / T_e) + I_i^{sat}(V_2) \tag{2.6}$$

$$I_3 = -I_e^{sat} \exp(V_3 / T_e) + I_i^{sat}(V_3) \tag{2.7}$$

where V_1, I_1 are the bias and collected current for the positively biased probe, V_2, I_2 are the bias and collected current for the floating probe, and V_3, I_3 are the bias and collected current for the negatively biased probe. Since the floating probe is at the floating potential, $I_2 = 0$. Additionally, I_i^{sat} is the ion "saturation" current given by Eq. (2.4), and I_e^{sat} is the electron saturation current: [Hoegy, 1973]

$$I_e^{sat} = S_p n_e q \left(eT_e / 2\pi m_e \right)^{1/2} \tag{2.8}$$

In the original triple-probe theory, the assumption is made that the variation in ion current $I_i^{sat}(V)$ with the change in probe potential is negligible compared with that of the electron current, i.e. $I_i^{sat}(V_1) = I_i^{sat}(V_2) = I_i^{sat}(V_3)$ [Chen, 1965]. This is not rigorously correct, and this assumption can yield significant errors in the measurement of T_e, which will be considered in Section 4.1.3. However, by following the original ideal theory we can pursue a useful mathematical simplification:

$$\frac{I_1 + I_2}{I_1 + I_3} = \frac{1 - \exp(-\phi_{12})}{1 - \exp(-\phi_{13})} \tag{2.9}$$

Where $\phi_{13} = V_{13} / T_e = (V_1 - V_3)/ T_e$ and $\phi_{12} = V_{12} / T_e = (V_1 - V_2)/ T_e$. Furthermore we can also state that $I_2 = 0$, and $I_1 = I_3$. Therefore:

$$\frac{1}{2} = \frac{1 - \exp(-\phi_{12})}{1 - \exp(-\phi_{13})} \tag{2.10}$$

Since V_{13} is a known voltage, and is typically set to be much larger than T_e/e, the RHS denominator of Eq. (2.10) reduces to 1 and the electron temperature in eV can be written as

$$T_e[\text{eV}] = V_{12} / \ln 2 \tag{2.11}$$

As was previously stated, the preceding derivation for T_e contains assumptions which tend to over-estimate T_e, as will be discussed in 4.1.3.

2.2 Diagnostics theory – microwave interferometry

2.2.0 Interferometer overview

A microwave interferometer is an instrument for detecting the refractive index of a medium by passing a high frequency wave through it, and comparing the wave's phase shift with a reference that does not pass through the medium. A simple schematic (Figure 2.3) shows the major components, including the oscillator, mixer, and transmit and receive antennas. In this interferometer, a mixer determines the relative phase difference between a *reference* leg, which is connected directly from the power divider to one terminal of the mixer, and a *scene* leg, which is transmitted between two horn antennas through the plasma medium. The phase of the reference beam remains constant while the phase of the scene beam changes based on the plasma's refractive index. The mixer output is equal to the phase difference between the legs, plus a DC offset. A *quadrature* mixer includes a second phase output that is offset from the first by 90 degrees in phase. Heterodyne interferometers are not considered here.

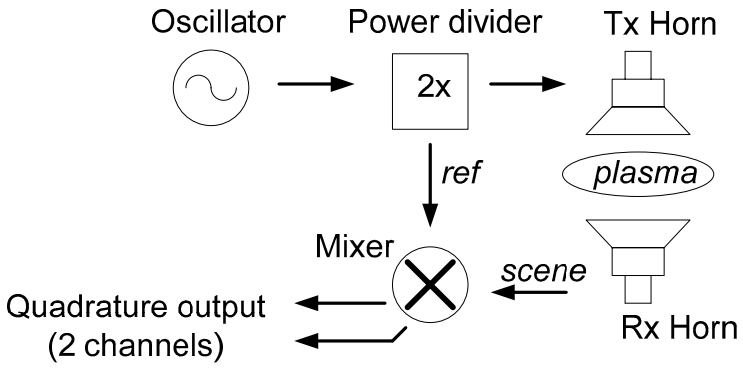

Figure 2.3: A basic microwave interferometer schematic. The mixer has two inputs, the *scene* leg which includes the link between the Tx and Rx horn antennas, and a *reference* leg, which is typically contained entirely within waveguide. The two quadrature output channels are 90^{o} out of phase.

The use of microwave interferometers for active probing of plasmas has several advantages over in-situ diagnostics like the Langmuir probe. First, the interferometer is a non-intrusive diagnostic which does not perturb the ambient plasma. This reduces the uncertainty arising from probe-plasma interactions, and allows measurements in high temperature plasmas that would otherwise destroy physical probes. Secondly, the measurement error for a properly calibrated interferometer is generally much lower than the error in a Langmuir probe measurement due to probe theory's dependence on multiple plasma parameters. [Overzet, 1993] Some limitations of a microwave interferometer include a limited ability to obtain spatial density. Because it provides a line-integrated density measurement, a spatial distribution must often be assumed to determine local plasma density. One option to obtain a limited spatial distribution is a spatial scanning of the plasma plume with the microwave interferometer, using Abel inversion to determine local plasma density. [Hutchinson, 2002] [Gilchrist,1997] This can be a time consuming process, particularly if an accurate alignment is taken for the interferometer instrument at each radial location. The inversion also requires radial symmetry in the plasma column. Another limitation of microwave interferometry is the inability to measure electron temperature and plasma potential, which the Langmuir probe is able to collect. A derivation of the governing equations for microwave interferometry requires a look at electromagnetic waves propagating through a plasma.

2.2.1 Electromagnetic wave propagation in plasmas

Electromagnetic (EM) waves propagating through a plasma have been studied by many researchers for a variety of reasons. In this chapter we will limit our investigation to the ordinary (o) EM wave propagating through a plasma column. The o-wave is a high frequency ($\omega > \omega_p$) wave propagating in absence of an applied magnetic field $\mathbf{B}_0$, or with the electric field $\mathbf{E} \parallel \mathbf{B}_0$. Suggested resources for a more in-depth formulation of this and other propagating waves include [Stix, 1992] [Heald, 1978] and [Hutchinson, 2002]

The plasma frequency, ω_p can be derived from first principles as follows. Consider a plane slab of plasma in which the electrons have been displaced by a small distance $-\Delta x$. Assume that the ions are stationary. Also assume that no magnetic field is present, or that a static field $\mathbf{B}_0 = B_x$ is present. The Lorentz force for electrons in $\hat{x}$ is

$$m_e \dot{v}_x = -e\overline{E}_x \tag{2.12}$$

where m_e and e are the electron mass and charge. If an electromagnetic wave were launched in the $\hat{x}$ direction of form

$$\mathbf{E} = \overline{E} e^{(k\mathbf{r} - i\omega t)} \tag{2.13}$$

then Eq. (2.12) can be written as

$$m_e \dot{v}_x = -m_e i\omega v_x = -eE_x \tag{2.14}$$

Solving for v_x :

$$v_x = \frac{-ie}{\omega m_e} E_x \tag{2.15}$$

An equation for current density can now be written using Ohm's law:

$$j_x = -en_e v_x = \sigma_x \cdot E_x \tag{2.16}$$

where

$$\sigma_x = \frac{ie^2 n_e}{\omega m_e} = \frac{i\varepsilon_0}{\omega}\omega_p^2 \tag{2.17}$$

and

$$\omega_p^2 = n_e q_e^2 / \varepsilon_0 m_e \tag{2.18}$$

is the plasma frequency squared. Using the relation for dielectric constant of a medium, ε_x:

$$\varepsilon_x = \left(1 + \frac{i}{\omega\varepsilon_0}\sigma_x\right) = \left(1 - \frac{\omega_p^2}{\omega^2}\right) \tag{2.19}$$

The dispersion relation for an ordinary wave can now be written using the familiar equation from optics :

$$\frac{c^2 k_p^{\ 2}}{\omega^2} = \varepsilon_x = \left(1 - \frac{\omega_p^2}{\omega^2}\right) \tag{2.20}$$

The plasma conductivity and dielectric constant are generally written in tensor form to account for plasma anisotropy, thus, the above formulation is only valid for the ordinary wave, for which interactions with the applied magnetic field can be ignored. This is the case when $E_x \parallel \mathbf{B}_0$ or for propagation frequencies $\omega >> \omega_{ce}$. (Here, ω_{ce} is the electron cyclotron frequency):

$$\omega_{ce} = \frac{eB}{m_e} \tag{2.21}$$

The overall phase ϕ of a plane wave traveling from distance $-L$ to L is

$$\phi = \int_{-L}^{L} k \, \mathrm{d}\ell \tag{2.22}$$

Where k is the wavenumber, thus the relative phase shift for a wave traveling through a region of plasma is found by integrating Eq. (2.20):

$$\Delta\phi = \phi_p - \phi_0 = k_0 \int_{-L}^{L} \left(\sqrt{1 - \omega_p^2 / \omega^2} - 1 \right) \mathrm{d}\ell \tag{2.23}$$

Assuming sufficiently high scene beam frequency (such that $\omega_p^2 / \omega^2 < 0.1$) Eq. (2.23) can be expanded by Taylor series to

$$\Delta\phi = k_0 \int_{-L}^{L} \left(-\frac{1}{2} \frac{\omega_p^2}{\omega^2} \right) \mathrm{d}\ell \tag{2.24}$$

$$\Delta\phi = \frac{-e^2}{2c\varepsilon_0 m_e \omega}\int_{-L}^{L} n_e \, \mathrm{d}\ell \tag{2.25}$$

where ω is the interferometer frequency, $2L$ is the plasma column diameter, and n_e is the electron density. The above formulation assumes that collisional dissipation is negligible, ($\nu_c / \omega << 1$) and that attenuation from refraction and reflection is limited. It is further assumed that the spatial distribution of density varies slowly, such that $|\nabla k| / k^2 << 1$. This is termed the geometric optics approximation that allows the EM wave to be considered a plane wave even in the presence of a density gradient. [Jeffreys, 1946] It is also assumed that the plasma extent is much larger than the scene beamwidth, although techniques exist to deal with this exigency. [Kraft, 2006]

The superposition of the two electric fields at the microwave detector is then equal to:

$$E = E_r e^{-i\omega t} + E_s^{\,i(\phi_0 + \Delta\phi - \omega t)} \tag{2.26}$$

Where E_r is the reference electric field, E_s is the scene electric field, ϕ_0 is the initial phase difference between the scene beam and the reference beam, and $\Delta\phi$ is the phase shift due to the plasma. Reflections and attenuation are considered separately in the next section.

2.2.2 Attenuation and reflection of waves

An EM wave traveling through plasma will undergo a certain amount of attenuation and reflection due to interaction with the plasma, or the experiment chamber. With a non-quadrature interferometer, beam attenuation can be mistaken for a phase shift and attributed to electron density. However a quadrature mixer utilizes two reference channels- one 90 degrees out of phase with the other. This results in two output voltages, and decouples amplitude and phase of the received signal, allowing beam attenuation to be considered separately. Thus, attenuation due to plasma interactions need not be considered an error term since its effects are removed from the phase measurement of the interferometer. The sources of beam attenuation are electron-ion collisions, and refraction of the plasma beam. Heald et al. [Heald, 1978] states that the attenuation coefficient α_0 due to collisions is

$$\alpha_0 \approx \frac{\nu_e \omega_p^{\,2}}{2c\omega^2}\left(1-\frac{\omega_p^{\,2}}{\omega^2}\right)^{-1/2} \quad [\mathrm{m}^{-1}] \tag{2.27}$$

Electron-ion collisions are deemed to be small in all experiments **(** $\nu_e < 0.3$ GHz; $\alpha_0 < 0.05$ m^{-1}**)** thus the majority of attenuation will be due to beam refraction. Refraction effects can be substantial, especially if the transmitting antenna is on the order of the size of the plasma column. [Ohler, 1996] [Davis, 2006] These authors pursued a ray-tracing analysis to determine the spatial evolution of discrete portions of the wave. The ray trajectory is solved by a differential form of Snell's law, whereby the plasma acts as a diverging lens. Only those rays that are intercepted by the receiver antenna are counted

towards the total power, therefore the wave is attenuated when compared with the non-plasma case. An illustration of this process is shown in Figure 2.4.

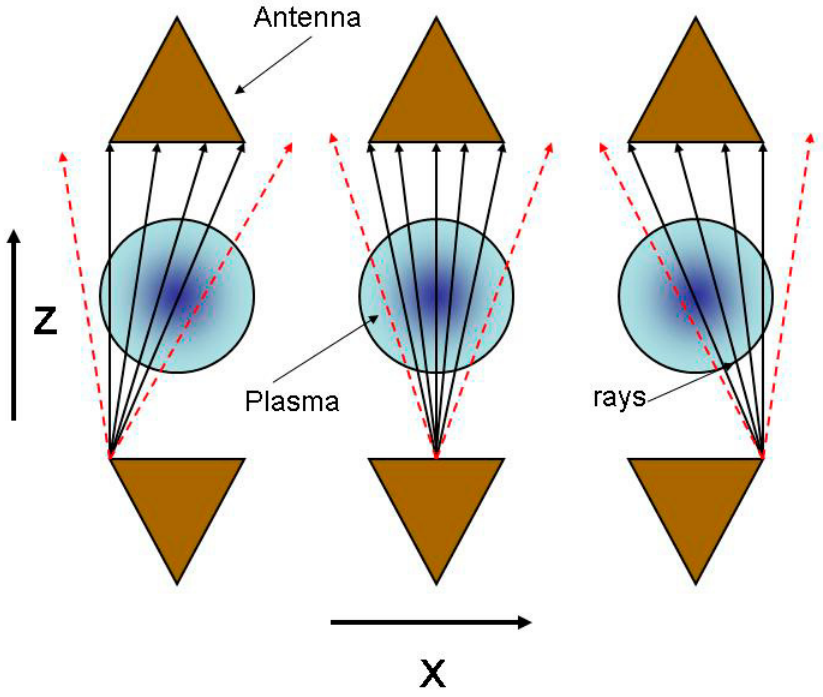

Figure 2.4: Example of the ray tracing process for three different points along the antenna aperture. The dashed rays represent example rays that would not be received by the antenna. [Davis, 2006]

An analysis of refraction and attenuation for the present experiment setup is given in Section 3.2.4.4.

Reflections of the EM wave are also possible both from gradients in the plasma refractive index, and from the vacuum chamber walls. Due to the geometric optics condition $|\nabla k|/k^2 << 1$, reflections from plasma gradients are ignored. However, multiple reflections from walls could result in indirect radiation reaching the receive antenna.

This case is assumed here to be a double reflection, with the wave exiting the transmit horn, reflecting from chamber walls twice (thereby traversing the plasma column a total of three times), and arriving at the receiving antenna with arbitrary phase and amplitude. The amplitude and phase of the reflected wave are determined via calibration of the instrument, which is discussed in Section 2.2.3. Equation (2.28) shows a modification of Eq. (2.26) for the reflected portion of the wave at the detector. An attenuation coefficient α_0, reflection coefficient (amplitude) ρ, and reflection coefficient (phase) β_r are included to match the assumption of a triple-reflection.

$$E_{rfl} = (1-\alpha_0)^3 \rho E_s^{\,i(3\Delta\phi+\phi_0+\beta_r-\omega t)} \tag{2.28}$$

With a proper calibration, the reflections arising from surrounding objects can be accounted for in the final interferometer measurement, and can be calibrated out of the resulting density measurement. Higher order reflections (>3) are not specifically included in (2.28), but their contribution to error is small, as will be discussed in Section 3.2.4.

2.2.3 Diagnostics theory - interferometer calibration

We will now consider a quadrature interferometer model using Eqs. (2.26) and (2.28). Two separate RF paths are combined at the mixer – a reference path of amplitude E_r and a scene (plasma) path containing both the direct radiation E_s, and the reflected radiation E_{rfl}. (Figure 2.5)

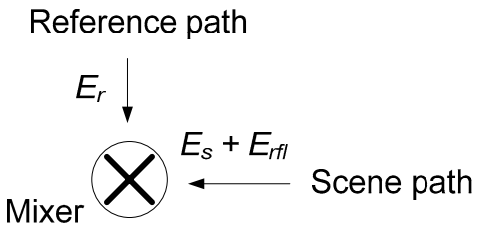

Figure 2.5: Electric field superposition for the mixer in Figure 2.3. Scene path includes direct (E_s) and reflected (E_{rfl}) waves while reference path includes E_r.

A microwave detector (mixer) compares the phase of the two RF paths. The electric field at the microwave detector is a superposition of the fields given in Eqs. (2.26) and (2.28):

$$E = E_r e^{-i\omega t} + (1-\alpha_0) E_s^{\,i(\Delta\phi+\phi_0-\omega t)} \left[1 + (1-\alpha_0)^2 \rho e^{i(2\Delta\phi+\beta_r)} \right] \tag{2.29}$$

where again, E and ω are the field amplitude and frequency, respectively; the subscripts r and s denote the reference and scene fields, respectively; α_0 and ρ are the attenuation and reflection magnitude coefficients, respectively; $\Delta\phi$ is the phase shift of the scene beam relative to its initial phase without plasma perturbation; ϕ_0 is the initial phase difference between the reference beam and the non-reflected scene beam; and β_r is the added phase shift of the reflected component of the scene beam. The attenuation coefficient α_0 is included to account for cases in which there is modulation of the scene beam amplitude when the plasma is present (e.g., refractive bending); by definition $\alpha_0 = 0$ when the plasma is absent.

Furthermore the voltage output from the interferometer quadrature detector can be modeled as: [Dobson, 2004]

$$\tilde{V} = E_r^2 + 2(1-\alpha_0)^4 \rho E_s^2 \cos\left(2\Delta\phi + \beta_r\right) + \left((1-\alpha_0)E_s\right)^2 \left[1 + \left((1-\alpha_0)^2 \rho^2\right)\right] + 2(1-\alpha_0)E_r E_s \left[\cos(\Delta\phi + \phi_0) + (1-\alpha_0)^2 \rho \cos\left(3\Delta\phi + \phi_0 + \beta_r\right)\right] + V_D \tag{2.30}$$

where V_D is the diode "dark" voltage. Eq. (2.30) can be used to model both the in-phase, and quadrature channel, although the individual coefficients will be unique for each channel.

A simplified version of Eq. (2.30) is developed as follows. Assuming the special condition $\rho = 0$ (no reflections), Eq. (2.30) reduces to

$$\tilde{V} = C_1 \cos\left(\Delta\phi + \phi_0\right) + C_4 \tag{2.31}$$

for the in-phase channel and

$$\tilde{V}' = C_1' \cos(\Delta\phi + \phi_0 - \pi/2 + \phi_Q) + C_4' \tag{2.32}$$

for the quadrature channel, where primed values are for the quadrature channel, $C_1 = 2(1-\alpha_0)E_r E_s$, $C_4 = E_r^2 + ((1-\alpha_0)E_s)^2 + V_D$ and ϕ_Q is the quadrature phase offset: $\phi_Q = \phi_0' - \phi_0 + \pi/2$. In the special case that the *I* and *Q* channels of the mixer are exactly 90° offset, then $\phi_Q = 0$. Eq. (2.31) and Eq. (2.32) allow one to solve directly for $\Delta\phi$ by

$$\Delta\phi = \tan^{-1}\left[\frac{C_1\left(\tilde{V}' - C_4'\right)}{C_1'\left(\tilde{V} - C_4\right)\cos(\phi_Q)} - \tan\left(\phi_Q\right)\right] \tag{2.33}$$

If each of the coefficients of the above equation were known then the phase shift ϕ would be a function of the two detector voltages. A physical calibration of the interferometer is necessary to obtain these values.

In order to find the necessary calibration coefficients in Eq. (2.33) an in-line phase shifter can be used to change the effective measurement pathlength through more than one wavelength λ. By artificially changing $\Delta\phi$ in Eq. (2.31) and (2.32), $\tilde{V}$ and $\tilde{V}'$ can be changed through a full 2π revolution, allowing calibration data to be fit to the interferometer model. This procedure will provide C_1, C_4, and ϕ_Q, or the detectors' amplitude, DC offset and quadrature offset respectively, which are the major calibration coefficients in the special case $\rho = 0$ (zero reflections). In order to determine the effect of reflections however, a phase shifter is not enough; the horn antennas must be physically moved through at least $x = 1$ λ and the entire equation of Eq. (2.30) used. Instead of a plasma perturbation or phase shifter changing $\Delta\phi$, the substitution $\phi = kx$ is made, where x is the antenna motor position during the calibration. This process is necessary because simply shifting ϕ is not enough to determine the effect of ρ and β_r in Eq. (2.30). By physically moving the horn antennas, the reflection components $\rho(x)$ and $\beta_r(x)$ change non-linearly, and can be isolated from the linear change of $\phi = kx$. If reflections are to be accounted for, the simplified equation for phase given in Eq. (2.33) cannot be used.

Using this process, there are seven coefficients that must be fit in Eq. (2.30): E_r, E_s, ρ, β_r, ϕ_0, V_D and k. Assuming $\rho = 0$ and substituting $\phi = kx$ requires only four coefficients to be fit to the simplified Eq. (2.31): C_1, C_4, k and ϕ_0. The results of interferometer calibration in this experiment are addressed in Chapter 3.

2.2.4 Diagnostics theory - Abel inversion

Abel inversion requires taking multiple line-integrated density measurements along separate chords of the plasma column. This technique enables one to estimate a radial distribution of density $n(r)$ with an instrument that only gives line integral density values $N(r)$. For the technique to work, one has to make the assumption that the plasma column is cylindrically symmetric, i.e. it is independent of θ in the coordinate system (r, θ, z). But given this constraint, the Abel inversion allows a series of chord integrals to be transformed into a radial distribution. This formulation is known as the "symmetric" Abel inversion [Whittaker 1902]. Further information on the topic are supplied by [Gottardi, 1979], [Hutchinson, 2002], and [Ha, 2004]:

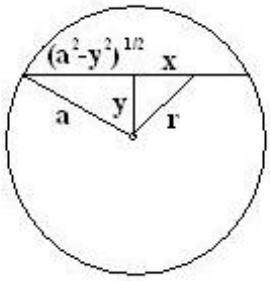

Figure 2.6: Coordinates for Abel inversion of a vertical scanning interferometer

Beginning with equation (2.25) then transforming to cylindrical coordinates, one finds an equation for the line integrated phase shift $\Delta\phi$:

$$\Delta\phi = \frac{k_0 e^2}{2\omega^2 \varepsilon_0 m_e} 2\int_y^a \frac{n(r) r\, dr}{(r^2 - y^2)^{1/2}} \tag{2.34}$$

The inverse Abel transform is then written as:

$$n(r) = \frac{-2\omega^2 \varepsilon_0 m_e}{\pi k_0 e^2} \int_r^a \frac{d}{dy} \left(\Delta\phi(y)\right)\left(y^2 - r^2\right)^{-1/2} dy \tag{2.35}$$

The above formulation can be used as-is to determine the radial density distribution. Numerically speaking, the radial distribution can be found by summing the derivatives of the measured phase shift over the plasma column edge to the radial point of interest. The derivative is approximated by taking the difference between the function at two points and dividing by the distance between the two measurements. The step size can be greatly reduced by fitting an analytic function to the discrete measurements of $\Delta\phi$. The analytic function allows $n(r)$ to be calculated with higher resolution, and reduces the noise contribution from the derivative $\frac{d}{dy}(\Delta\phi)$. In the case of the experiment considered here, the radial distribution does fit to an analytic Gaussian distribution, as will be discussed in Chapter 4. We can also substitute for the detected interferometer line integral N_e into Eq. (2.35):

$$\Delta\phi = \frac{k_0 e^2}{2\omega^2 \varepsilon_0 m_e} N_e \tag{2.36}$$

Resulting in:

$$n(r) = \frac{-1}{\pi}\int_r^a \left[\frac{d}{dy} N_e(y)\right]\left(y^2 - r^2\right)^{-1/2} dy \tag{2.37}$$

Again, as will be discussed in Chapter 4, the line integral density $N_e(y)$ can be fit to a Gaussian distribution with 3 fitting coefficients, C_1, C_2, and C_3:

$$N_e(y) = \left[C_2 \exp\left(\frac{-(y - C_3)^2}{C_1^2}\right)\right] \tag{2.38}$$

If we substitute Eq. (2.38) into Eq. (2.37) and numerically solve the integral, we have:

$$n_e(r) = \frac{2C_2}{\pi C_1^2} \frac{C_1\sqrt{\pi}}{2e^{r^2/C_1^2}} Erf\left[\frac{\sqrt{a^2 - r^2}}{C_1}\right] = \frac{C_2}{C_1\sqrt{\pi}} \exp\left[\frac{-r^2}{C_1^2}\right] Erf\left[\frac{\sqrt{a^2 - r^2}}{C_1}\right] \tag{2.39}$$

For small C_1, the error function approaches 1 thus giving a Gaussian radial density. Alternative methods utilize a Fourier transform allowing generic functions to be analyzed, [Smith, 1988] but these methods are more sensitive to measurement noise and provide no advantages in the present situation.

Details for the uncertainty analysis for the above Abel inversion are described in Appendix B.

2.3 Diagnostics theory – Hybrid measurement

A novel method for producing accurate radial density profiles was developed for this experiment, with an overview given here. [Deline, 2007] First a Langmuir probe was scanned across the plasma column collecting ion saturation current along a microwave interferometer chord. Shot to shot variation from the plasma source was factored out by normalizing each probe data point to the interferometer measurement for that shot. Since the interferometer is kept stationary, it provides a record of temporal changes in the plasma source. Probe measurements at various radial positions provide the shape of the plasma column. The individual probe measurements are integrated across the scan width, and compared with the RF interferometer signal. The interferometer chord density measurement, which already is a line integral density, is matched to the line integrated probe density measurement by introducing a scalar constant. Accurately calibrated point density at each of the scan positions results from this process. This method takes advantage of the benefits of both instruments: accurate density measurements from an RF interferometer, and high spatial resolution measurements from an electrostatic probe. The radial density profile of the plasma is thus accurately measured over several plasma shots and probe measurements.

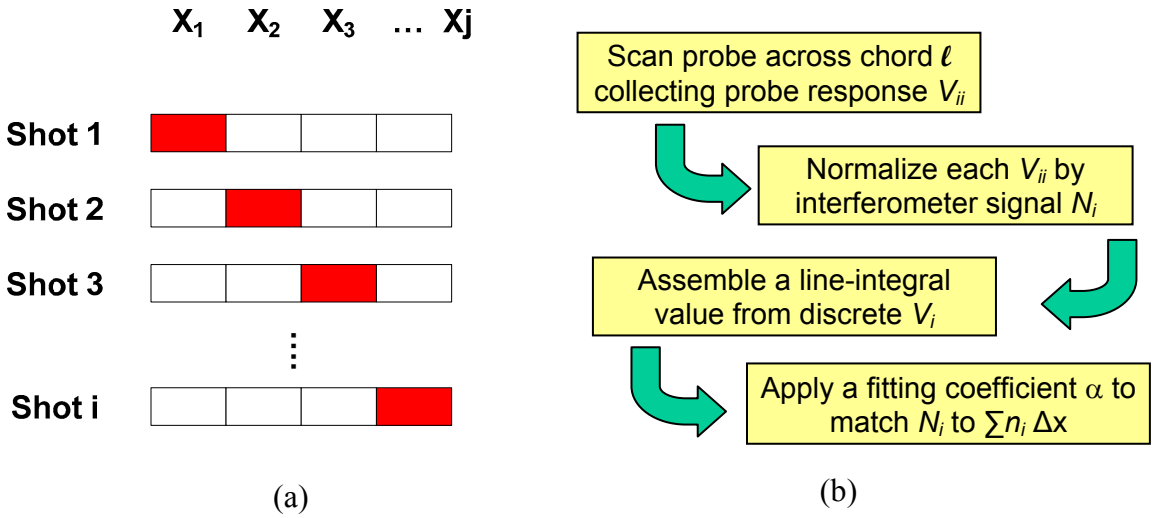

Figure 2.7: Hybrid method description. (a) illustrates a transverse probe scan over multiple plasma shots *i* with a probe measurement [solid red] taken at a different position x_j for each plasma shot. (b) shows the steps of the hybrid method, including normalization of the probe response, summing over the scan length and comparing the sum with microwave interferometer measurements.

A detailed analysis of the hybrid method is as follows: A transverse scan across the plasma plume at axial location z consists of a number i=1, M of plasma shots each taken with the Langmuir probe at a particular radial position x_j, j=1, M. (Figure 2.7) In the analysis here, a single time point t in the discharge is considered, resulting in a single data point for each shot with the two diagnostics: V_i from the Langmuir triple-probe and N_i from the RF interferometer. Note that N_i is a line integral density measurement, and V_i is a voltage reading across the probe's current sensing resistor R as in Figure 2.2. As this is in essence an ion saturation current measurement, V_i is related to a point density n_i through a proportionality factor. We define this factor α as :

$$n_i = \alpha V_i \tag{2.40}$$

where α is constant over a transverse scan. One could equivalently say that $n_j = \alpha V_j$ since α is constant. Please note the distinction between this proportionality factor α, and the attenuation coefficient α_0 discussed earlier as there is no relation between these two similar-looking variables.

In a transverse scan, then, $n_{i,j}$ represents the density at a given position during a given shot, noting that only one density per shot is actually measured by the probe: $n_i \equiv n_{i,i}$. The other M-1 positions are sampled during different shots. Thus, in order to accurately combine probe measurements from different radial positions, shot-to-shot variation must be accounted for. In this technique, it is assumed that all shots are identical except for a global scale factor given by N_i. That is, for any given position j, the ratio of n's for a pair of shots i and i' is

$$\frac{n_{ij}}{n_{i'j}} = \frac{N_i}{N_{i'}} \tag{2.41}$$

For $i' = j$,

$$n_{ij} = \frac{N_i}{N_j} \tag{2.42}$$

where $n_{ij} = n_j$ is a measured value. The line integral density N_i for a given shot is approximately equal to the sum:

$$N_i = \sum_{j=1}^{M} n_{ij} \Delta x_j \tag{2.43}$$

where the Δx_j are contiguous segments centered on the x_j. Using Eqs. (2.41) and (2.42) in Eq. (2.43) we have

$$N_i = \sum_{j=1}^{M} n_{jj} \frac{N_i}{N_j} \Delta x_j = N_i \alpha \sum_{j=1}^{M} \frac{V_j}{N_j} \Delta x_j \tag{2.44}$$

so that

$$\alpha = \left[\sum_{j=1}^{M} \frac{V_j}{N_j} \Delta x_j \right]^{-1} \tag{2.45}$$

The calibrated density profile is then given by Eqs. (2.40) and (2.45):

$$n_i = V_i \alpha = V_i \left[\sum_{j=1}^{M} \frac{V_j}{N_j} \Delta x_j \right]^{-1} \tag{2.46}$$

In this manner, the RF interferometer line integral density measurement is compared to the sum of electrostatic probe density measurements along the scan length $M \Delta x$.

A number of modifications can be included with this initial method if the situation warrants it. Two modifications in particular that were investigated include the situations of a radial scan that does not include the entire chord width of the interferometer, and a radial scan that does not occur at the exact same axial location as the interferometer measurement chord. Ideally the scan length from x_1 to x_M will cover the entire interferometer scene beam length ℓ, from ℓ_1 to ℓ_2. If this is not the case, a term N_i'

must be substituted for N_i that adds the discrete scans of Eq. (2.43) with that part of the interferometer chord that lies outside of the probe scan width:

$$N_i^{'} = \sum_{j=1}^{M} n_{ij} \Delta x_j + \int_{\ell_1}^{x_1} n_i(x)\, dx + \int_{x_M}^{\ell_2} n_i(x)\, dx \tag{2.47}$$

where $n_i(x)$ is the full density profile, either inferred from the partial scan, or determined explicitly from a prior scan covering all ℓ. N_i' varies with i but, by assumption, the ratio $N_i^{'}/N_i$ is constant, and the adjusted calibration constant becomes:

$$\alpha_{adj} = \alpha \frac{N_i}{N_i^{'}} \tag{2.48}$$

A further adjustment of the line integral density can be made in the event that the Langmuir probe measurement location is not along the microwave interferometer beam. Note that in general, an axial offset is not necessary because the scanning Langmuir probes can be made sufficiently small to not interfere with the interferometer measurement. However, for several probe scans in this work, the probe was positioned slightly behind the interferometer due to an error in positioning, thus this modification must be investigated. The basic adjustment is done to account for any column divergence between the two measurements. In the case of this work, as will be discussed in Chapter 4, the plasma plume had a radial profile that fit very well to a Gaussian distribution, and the velocity could be assumed to be constant over small axial distances. With these

assumptions, along with flux conservation, the change in line integral density between axial positions z_1 and z_2 can be expressed as:

$$\frac{N_{z1}}{N_{z2}} = \frac{R_{z2}}{R_{z1}} = \sqrt{\frac{n_{\max,z1}}{n_{\max,z2}}} \tag{2.49}$$

where R_{z1} and R_{z2} are the radii of the Gaussian plasma column at axial locations z_1 and z_2 respectively, and $n_{\max,z1}$ and $n_{\max,z2}$ are the centerline plasma densities at z_1 and z_2. The radius of the Gaussian plasma column is known at the two measurement locations due to either a scan of the microwave interferometer, or a scan of the Langmuir probe. Thus the change in peak density and line integral density can be estimated from Eq. (2.48). As applied to the hybrid measurement approach, the line density N_i' from Eq. (2.46) is further adjusted by a factor of $\gamma \equiv R_{z1} / R_{z2}$ such that

$$\alpha_{adj} \to \gamma \alpha_{adj} = \frac{R_{z1}}{R_{z2}} \frac{N_i}{N_i'} \alpha \tag{2.50}$$

The final formulation for electron density n_i at each measurement point x_j for $i=j$ is thus:

$$n_i = V_i \frac{R_{z1}}{R_{z2}} \frac{N_i}{N_i'} \left[\sum_{j=1}^{M} \frac{V_j}{N_j} \Delta x_j \right]^{-1} \tag{2.51}$$

Using this methodology, full radial density profiles can be produced vs. time by combining and scaling multiple Langmuir probe measurements taken at a number of radial positions. In addition, non-ideal scans including those which do not cover the entire interferometer beam width, or which include an axial offset from the interferometer beam can be accommodated, although the error associated with these measurements is increased. A full error analysis of this method can be found in Appendix A.

2.4 Magnetic Nozzle Theory

2.4.0 Introduction

There are several regions of interest at the outlet of a converging-diverging magnetic nozzle. (Figure 2.8) The diverging portion of the magnetic nozzle begins just downstream of the nozzle inlet or throat, which is the region of peak magnetic field. The near-nozzle region begins at the nozzle inlet and continues for a short distance, until the ratio of centerline magnetic field B to inlet magnetic field B_0 reaches approximately $B_0/B = 10$ (about 30 cm from the nozzle peak field). This is a region of momentum transfer and adiabatic expansion. It also contains the highest plasma density and temperature that is found in the magnetic nozzle. This is a region not studied in detail in the present experiment due to space and equipment limitations, but is important nonetheless. It will briefly be discussed with important findings from prior experiments presented.

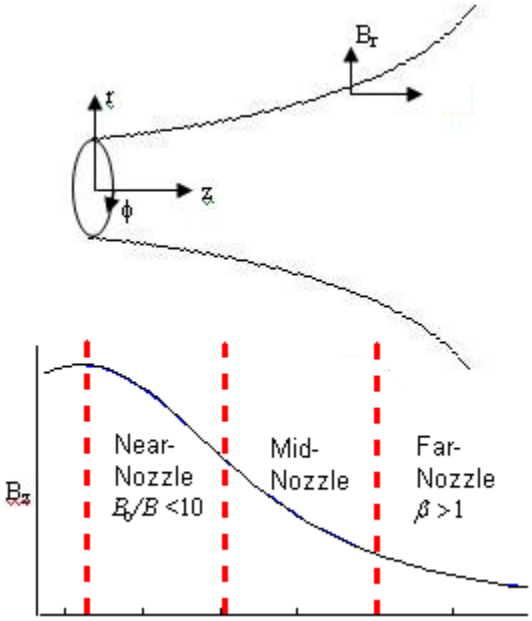

Figure 2.8: Schematic of magnetic nozzle showing nozzle coordinate system and nozzle regions.

The far-nozzle region occurs as the plume's kinetic Beta approaches unity, where

$$\beta = \frac{v^2}{v_A{}^2} = \frac{v^2}{B^2 / \mu_0 n_i m_i} \tag{2.52}$$

β is the ratio of kinetic energy to magnetic energy in the plasma flow, defined in these terms as $\beta = W_K / W_B$ when $W_K = m_i n_i v_z{}^2 / 2$ and $W_B = B^2 / 2\mu_0$. It is equivalently defined as the square of the ratio of bulk flow velocity to Alfvén velocity where:

$$v_A = B / \sqrt{\mu_0 n_i m_i} \tag{2.53}$$

is the Alfvén velocity. It is the far-nozzle region (approximately 0.9 m from the nozzle peak field in the present experiment) that is of interest for detachment experiments because it is here that the magnetic nozzle ceases to influence the trajectories of the plume, as the plasma continues on a ballistic trajectory. In this region, meaningful nozzle efficiency numbers can be measured, defined here as the portion of plume momentum that is axially directed. Nozzle efficiency will be discussed more fully in Section 2.4.6.

In between these two somewhat arbitrarily defined nozzle regions lies the mid-nozzle region. This region is characterized by nearly constant temperature, plasma expansion along magnetic field lines, and diffusion across magnetic field lines as will be discussed in the following sections.

2.4.1 Conditions for magnetized plasma

For a magnetic nozzle to have any effect on the plasma plume, the plume must be magnetized. The classical definition of this condition is $r_i < R(z)$, where r_i is the plasma ion cyclotron radius

$$r_i = \frac{v_\perp}{\omega_{ci}} = \sqrt{\frac{Tm_i}{eB^2}} \tag{2.54}$$

and $R(z)$ is the half-maximum radius of the plasma. This is a loose definition based on single particle theory, assuming that individual ion orbits must be contained within the plume diameter. When this condition is broken, the magnetic field may be too weak to confine plasma particles. Fortunately in this experiment, standard conditions resulted in $r_i < R(z)$ at least up to the far-nozzle region, as will be shown in Section 4.1.7.

The experiment must also remain collisionless in the nozzle region for momentum to be transferred and for efficiency to be maximized. Ion-neutral collisions dramatically slow the plasma flow and enhance cross-magnetic field transport. [Lieberman, 1994] These are both undesired effects in a nozzle experiment. As will be shown in the next chapter, the ion-neutral mean free path in this experiment was at least 2.2 m, which is longer than the experiment scale length. What few ion-neutral collision effects were detected in the experiment are discussed in Section 4.3.

2.4.2 Near Magnetic Nozzle Region

A converging-diverging magnetic nozzle directs a plasma flow much as its thermodynamic counterpart the Laval nozzle does. At the Laval nozzle inlet, the nozzle area is minimized, and the gas flow velocity reaches Mach 1, accelerating as the nozzle area increases [Anderson, 1990]. Similarly, for the magnetic nozzle the nozzle inlet corresponds to a point of maximum magnetic field, minimum plasma column radius, and the onset of supersonic flow. The plasma flow velocity v then increases past $M = 1$. The plasma Mach number M is defined as

$$M = v/C_s \tag{2.55}$$

where C_s is the ion sound speed:

$$C_s = \left(\frac{\gamma_e e T_e + \gamma_i e T_i}{m_i} \right)^{1/2} \tag{2.56}$$

and $\gamma = C_p / C_v \approx 1$ is the ratio of specific heats for electrons or ions.

Plasma expansion and acceleration in the near-nozzle region is governed by several physical effects. The DDEX experiment did not make any measurements in the near-nozzle region, so some previous results will be summarized here. [Inutake, 2002] and [Ando, 2006] present results of a magnetoplasmadynamic thruster (MPD thruster) emitting into a highly configurable magnetic nozzle. Triple probes, fast scanning Langmuir probes, laser induced fluorescence (LIF) and Mach probes provide electron & ion temperature measurements, density measurements and flow velocity measurements in the near-nozzle region.

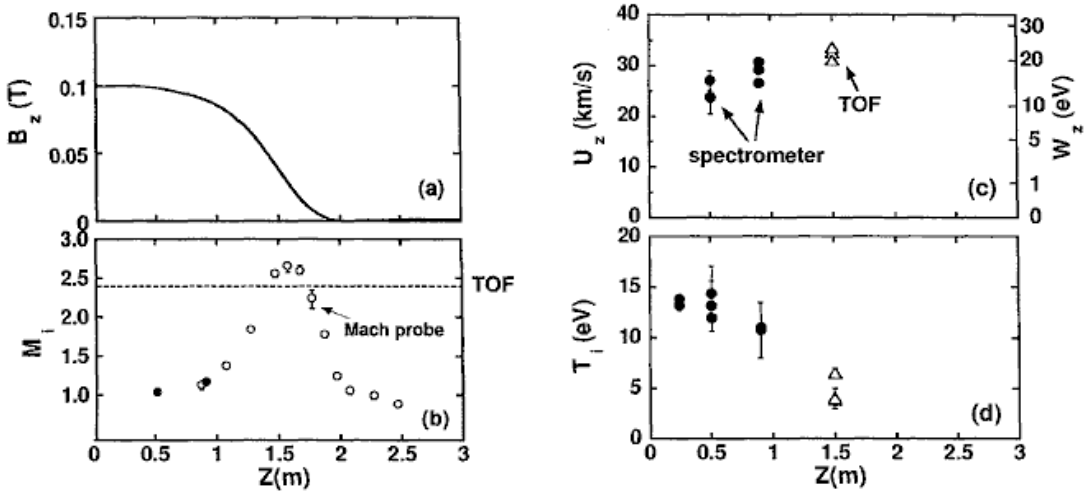

Figure 2.9: Near-nozzle measurements for a helium MPD thruster [Inutake, 2002]. Axial profiles of: (a) magnetic field, (b) M_i (c) Axial velocity (d) Ion temperature

In the near-nozzle region defined as $B_0/B < 10$, Figure 2.9 shows a number of experimental trends from the [Inutake, 2002] experiment. The ion Mach number increases from $M = 1$ up beyond $M = 2.5$ until ion-neutral collisions significantly reduce

the flow velocity. The ion temperature (along with electron temperature, not shown) decreases from a peak value of 14 eV to less than 4 eV within the $B_0/B < 10$ near-nozzle zone. Also, plasma density decreases as the plume expands. The theory used to explain the acceleration and cooling of the plume in the near-nozzle region in [Inutake, 2002] is one-dimensional isentropic flow, which assumes that no dissipative processes, and no energy-producing processes are acting on the plasma plume. Given these assumptions, the governing equations for Mach number and temperature are [Anderson, 1990]:

$$\frac{R^2}{R_0^{\,2}} = \frac{1}{M}\left[\frac{2}{\gamma+1}\left(1+\frac{\gamma-1}{2}M^2\right)\right]^{\frac{\gamma+1}{2(\gamma-1)}} \tag{2.57}$$

$$\frac{T_0}{T_i} = \left(1-\frac{\gamma-1}{2}M^2\right)^{-1} \tag{2.58}$$

Where $(R/R_0)^2$ is a ratio of the plume area roughly equal to the ratio B_0/B, and all initial variables with subscript 0 are taken at the nozzle throat where B is maximum. A ratio of specific heats γ between 1 and 1.2 best matched experiment results presented in Figure 2.9.

It was found that the preceding isentropic model is valid when frequent ion-ion collisions cause the plume to behave as a fluid, e.g. the ion collision frequency is on the order of or larger than the ion cyclotron frequency: $\omega_{ci}/\nu_{ii} < 1$. [Ando, 2006] For more infrequent collisions, $\omega_{ci}/\nu_{ii} > 1$ and the ions behave as single particles. In this single particle

regime, the ion's magnetic moment is conserved, leading to the standard 1st adiabatic invariance law of [Chen, 1984]:

$$\mu \equiv \tfrac{1}{2} m v_{\perp}^2 / B = \text{const} \tag{2.59}$$

After accounting for conservation of energy ($v_z^2 + v_{\perp}^2$ = const) the axial velocity at location z_1 is:

$$v_{z1}^2 = v_{z0}^2 + v_{\perp 0}^2 \left(1 - B_1 / B_0\right) \tag{2.60}$$

where variables with subscript 0 are taken at the nozzle throat, coincident with peak applied magnetic field. This model is more applicable in the mid-nozzle region of the present experiment, where single particle motion dominates collective motion.

It should be noted that both models are in effect taking energy from the plasma's perpendicular motion and converting it to directed axial motion. This energy transfer is occurring in the isentropic model by a decreasing temperature and increasing ion Mach number. In the single particle model, the perpendicular velocity $v_{\perp}$ decreases with B while $v_{\parallel}$ increases with B due to magnetic moment conservation.

2.4.3 Mid-Magnetic Nozzle Region

The mid-magnetic nozzle region is characterized by a lower ion and electron temperature after isentropic expansion has cooled the plasma exhaust and converted much of the perpendicular energy to parallel. Some acceleration of the flow is still possible based on Eq. (2.60), as it is assumed in this region that $\omega_{ci} / \nu_{ii} > 1$ with ions following single

particle trajectories. For the most part, ion guiding centers are frozen onto magnetic field lines. However, cross-magnetic field transport occurs, depending on the magnetic field strength. In this analysis, cross-field diffusion is driven by electron motion, with ions following along to maintain quasineutrality. [Hooper, 1993]

For sufficiently low magnetic fields and in absence of neutral collisions, electrons follow classical diffusion, characterized by a diffusion rate proportional to B^{-2}. According to [Okuda, 1973] the radial diffusion coefficient in 2D cylindrical coordinates is:

$$D_e \ [\text{mks units}] = \tfrac{100}{8}\left(\tfrac{1}{2}\pi\right)^{1/2} \frac{\omega_p{}^3}{\omega_{ce}{}^2} n_e{}^{-1} \left[1 + \left(\frac{2m_i}{m_i + m_e}\right)^{1/2}\right] \tag{2.61}$$

The above expression is only valid if electrons diffuse a distance greater than a Debye length in the execution of one gyro-orbit. In practical terms this limit condition for classical diffusion is: [Dawson, 1971]

$$B \le \left(\frac{n_e m_e}{\varepsilon_0}\right)^{1/2} \left(\frac{\varepsilon_0 T_e}{e^2}\right)^{1/3} \tag{2.62}$$

Eq. (2.62) places an upper limit on magnetic field B, therefore a high enough magnetic field can lead to the invalidation of the condition for classical diffusion. For a high enough applied magnetic field, the influence of individual particle collisions becomes less important than large-scale convective motion. The onset of low-frequency

convective plasma waves leads to a diffusion rate proportional to B^{-1} which is termed Bohm diffusion:

$$D_{Bohm}[\text{mks}] \approx \frac{1}{16}\frac{T_e}{B} \tag{2.63}$$

The condition for the onset of Bohm diffusion is similar to Eq. (2.62) and for example requires a magnetic field approximately three times higher assuming T_e = 1 eV: [Dawson, 1971]

$$B \geq \left(\frac{n_e m_e}{\varepsilon_0}\right)^{1/2}\left(\frac{\varepsilon_0 T_e}{e^2}\right)^{1/4} \tag{2.64}$$

In between these two magnetic field conditions below the Bohm lower limit and above the classical upper limit lies a middle ground that follows neither classical diffusion nor Bohm diffusion. Numerical simulations have successfully modeled this regime. [Okuda, 1973] However, modeling this middle diffusion case is not a concern for the analysis of this experiment because under all operating conditions, the applied magnetic field was low enough to result in classical diffusion based on Eq. (2.62). This will be shown in Section 4.1.8.

2.4.4 Far-nozzle region and super-Alfvénic detachment

Several analyses predict that at sufficient distances downstream of the magnetic nozzle throat, the plasma flow continues in the axial direction, detached from the influence of applied magnetic fields. [Arefiev, 2005] [Ilin, 2002] [Gesto, 2006] [Brenning, 2005] [Cassibry, 2006] In an applied magnetic nozzle, the plasma kinetic energy density

$W_k = \frac{1}{2} m_i n_i v_z^2$ decreases downstream due to flux conservation. However, magnetic energy density $W_B = B^2 / 2\mu_0$ decreases more quickly and thus $\beta = W_k / W_B$, the ratio of the plasma's kinetic energy density to magnetic field energy density, will necessarily increase downstream even if the plasma velocity remains the same. According to theory, when β becomes greater than unity, the magnetized plasma becomes unmagnetized, or at least weakly self-magnetized with the external magnetic field no longer influencing the flowing plasma. This is a situation analogous to the solar wind flowing outward from the sun's magnetic field. [Parker, 1958] Thus, just as the solar wind is able to propagate far downstream of the sun, a high-β magnetically detached electric rocket plume should continue propagating far downstream of the magnetic nozzle outlet.

This has great implications for the usefulness of magnetized plasma sources for electric propulsion, because it enables the transfer of momentum from the plasma plume despite the spacecraft's closed magnetic fields. With this allowance for momentum exchange across closed magnetic fields, the spacecraft still produces thrust even as the magnetic flux lines close on themselves.

The experiment described later in this work was designed to investigate this transition from $\beta < 1$ to $\beta > 1$. The experimental results section will provide measurements that are consistent with the above theory.

2.4.5 Polarization drift

Polarization drift is considered here because it can be an aid to cross-field transport under certain conditions. A number of detailed experiments and theoretical models have been conducted for cross-magnetic field transport experiments. These results show that for specific magnetic configurations, plasma cross-field transport can exist for $\beta < 1$ conditions. Schmidt [Schmidt 1960] initially considered the dynamics of a low – β collisionless plasma beam moving perpendicular to a magnetic field B. He shows that as the plasma moves across field lines, a self-induced electric field E arises such that $E + v \times B = 0$ where v is the plasma flow velocity. The consequence of this field is that a zero-order $E \times B$ plasma drift arises which opposes the curvature of the magnetic field, transporting the plasma across the field lines.

There are several conditions suggested by both experiment and theory for the onset of this $E \times B$ diffusion. The first condition is that the plasma exhaust must have sufficient kinetic energy to set up the polarization charge separation.

$$1 + \left(\omega_{pi} / \omega_{ci}\right)^2 >> \sqrt{\frac{m_i}{m_e}} \tag{2.65}$$

where ω_{pi} and ω_{ci} are the ion plasma frequency and gyrofrequency, respectively. [Wessel 1981] [Ishizuka 1982] [Wessel 1990].

The second condition places an upper limit on the radius of the plasma plume compared to the ion gyroradius r / r_i such that the diffusion process is dominated by $E \times B$ diffusion rather than magnetic expulsion:

$$\frac{r}{r_i} < \frac{1}{K\sqrt{\beta\,\beta_{\text{th}}}} \tag{2.66}$$

Where $\beta_{th} = W_{th} / W_B$ and W_{th} is the ion thermal energy density $n_i m_i v_{i\text{th}}^2 / 2$ and K is an experimentally determined constant ≈ 2.3. [Hurtig 2004] [Brenning 2005] . The plasma flow must have a strong perpendicular component in order to be affected in this way, which is not the case for a small divergence angle magnetic nozzle. However, given an extreme magnetic curvature, e.g. a reversed magnetic field condition, polarization drift may become more pronounced.

2.4.6 Magnetic nozzle efficiency

A performance measurement useful to the rocket systems engineer includes the thrust T or momentum flux exiting a given plane in the rocket plume, where

$$T(z) = v_z \dot{m} = \int m_i n_i v_z^2 \, dS \;\; [N] \tag{2.67}$$

This value will change throughout the magnetic nozzle as accelerating and decelerating forces influence the plasma flow. Upon detachment from applied magnetic fields, the plume trajectory and the thrust approach an asymptotic value, assuming that ion-neutral

collisions are minimal. The rocket thrust, measured at a point after detachment is attained can provide a measure of nozzle efficiency:

$$\eta_{noz} = T_{z=\infty} / T_{z=0} = \int_{z=\infty} mnv_z^2 \, dS \Big/ \int_{z=0} mnv_z^2 \, dS \tag{2.68}$$

Where $z = 0$ is the nozzle throat where axial magnetic field is at a maximum, and $z = \infty$ is in the detachment zone, i.e. $\beta > 1$ for the whole plume profile. This nozzle efficiency provides a performance metric for the rocket nozzle designer who may be interested in maximizing nozzle performance while minimizing system mass and power requirements. The above equation can also be stated as a cosine loss term, which for small values of trajectory angle θ and averaged over the plume is approximately equal to [Arefiev, 2005]:

$$\eta_{noz} \approx 1 - \frac{\theta^2}{4} \tag{2.69}$$

A second way of describing the same nozzle metric is by looking at the nozzle's power efficiency, as opposed to its thrust or momentum efficiency. A measurement of jet power P_{jet} integrates measured ion density and axial velocity over the entire 2D nozzle plane:

$$P_{jet}[W] = \frac{m_i}{2} \int_0^{R_p} \int_0^{2\pi} n(r,\theta) v_z^3 \, r \, d\theta \, dr \tag{2.70}$$

Likewise the jet nozzle efficiency $\eta_{N,jet}$ can be stated as

$$\eta_{N,jet} = \frac{P_{jet,z=\infty}}{P_{jet,z=0}} \tag{2.71}$$

Measurements of n_e and v_z across the entire plume will allow one to determine the above values by experiment.

CHAPTER 3

EXPERIMENT CONFIGURATION

3.0 Overview

Laboratory conditions suitable for magnetic detachment research must meet several conditions. First, the experiment must employ a plasma source capable of producing a sufficiently dense and energetic flow to reach the $\beta > 1$ condition. Second, the vacuum chamber used must be large enough to allow for the long pathlengths required to achieve $\beta > 1$. Third, the vacuum chamber must be kept at a neutral background pressure sufficiently low to keep ion-neutral charge-exchange mean free path less than the path length for achieving $\beta > 1$.

An experiment setup meeting the above criteria, named the Demostration of Detachment Experiment (DDEX) was set up at the NASA Marshall Space Flight Center in Huntsville, AL. This NASA project was initiated in 2005 as a response to a Broad Agency Announcement award, and was co-led by Dr. Boris Breizman and Dr. Roger Bengtson both from the University of Texas, Austin. The multiple-institution team that investigated this project hailed from Alabama (UA- Huntsville, Marshall Space Flight Center, Auburn University), Texas (UT-Austin, Ad Astra Rocket Company) and Michigan (UM- Ann Arbor) and comprised 4 faculty members, four graduate students

and numerous NASA civil servants. Though the project was only funded for one year, the collaborators produced eight conference presentations, and one journal article during the course of the experiment. [Chavers, 2006] [Deline, June 2006] [Deline, July 2006] [Schuettpelz, 2006] [Cassabry, 2006] [Deline, July 2007] [Deline, September 2007] [Breizman, 2007] [Deline, 2007]

The project's goal was to investigate the dynamics of plasma expansion within, and detachment from an applied magnetic nozzle. The applied magnetic field would have to be strong enough to initially confine the plasma, and the plasma source would have to be powerful enough to impart the plasma flow with enough kinetic energy to eventually break free from the applied magnetic fields within the limits of the vacuum chamber's physical size and collision-inducing neutral background pressure. In order to achieve this goal, a large (2.75 m x 5 m) vacuum chamber was outfitted with a 200–300 kW pulsed DC plasma source emitting into a 0.07 T peak field magnetic nozzle.

3.1 DDEX Experiment – Facilities

3.1.0 Vacuum chamber configuration

The vacuum chamber used in this experiment is a 2.75 meter diameter by 5 meter long cylindrical stainless steel tank with numerous electrical feedthroughs and diffusion pumps providing 80,000 to 100,000 liters per second pumping speed on hydrogen (see Figure 3.1 and [Chavers, 2005]). The two diffusion pumps allow the use of lighter gases (helium and hydrogen) and keep the pre-pulse chamber background pressure below

$2x10^{-6}$ Torr resulting in an estimated charge exchange mean free path in excess of the experiment size. Pressure analysis is investigated in more detail in Section 3.1.3.

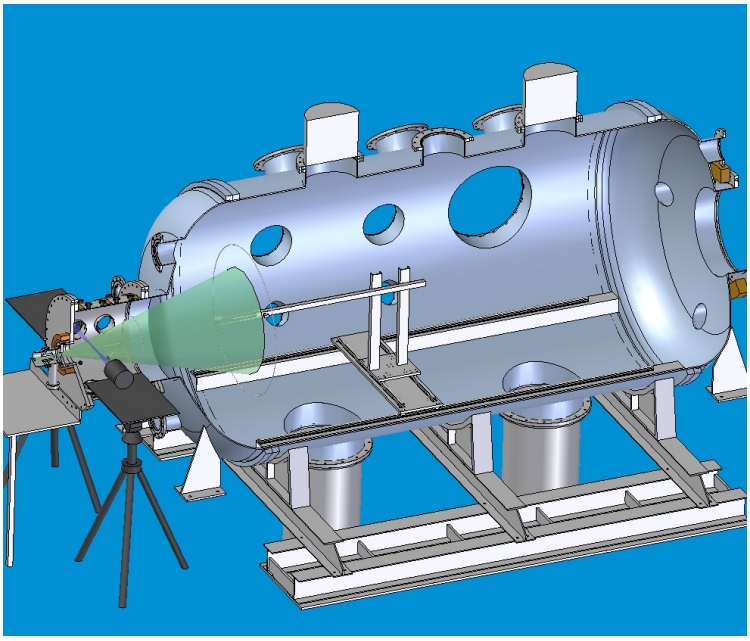

Figure 3.1: Detachment Demonstration Experiment (DDEX) 30 m^3 main chamber. Two diffusion pumps on the bottom provide 100,000 l/s pumping for light gasses. Experiment is located at NASA Marshall Space Flight Center, Huntsville, AL.

The vacuum tank has a smaller (1-m-diameter by 0.75-m-long) cylindrical extension called the "spool piece" attached to its front end, as seen in Figure 3.2. The spool piece provides a mounting location for the plasma source, a series of three external coils wrapped around its circumference, and a small bore, high field "choke magnet". The center of this choke magnet defines the origin of the chamber coordinate axis, with the axial position z = 0 m denoting both the center of the choke magnet and the position of peak magnetic field. The DC plasma source is mounted directly to the spool piece, at axial location z = -0.3 m. Access to the chamber is provided by a removable endcap on the downstream end of the chamber, opposite the plasma source.

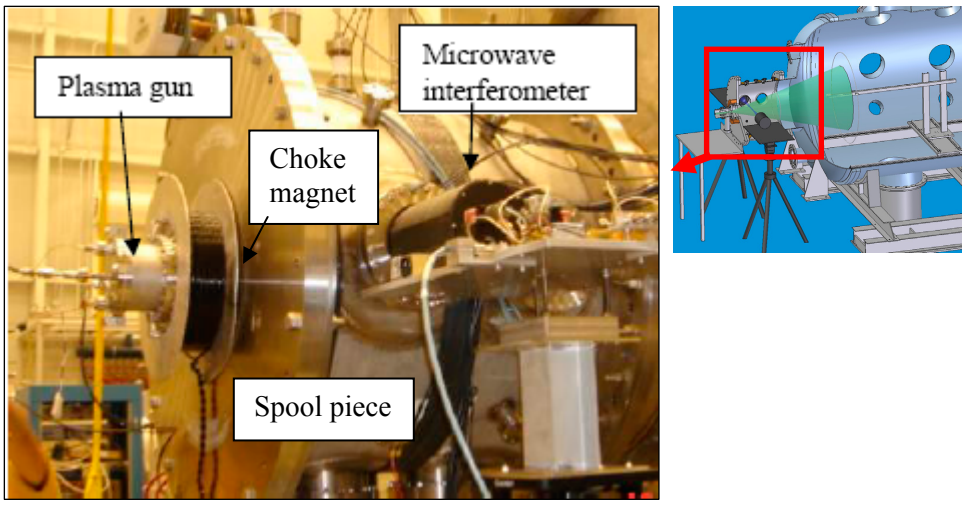

Figure 3.2: Detachment Demonstration Experiment (DDEX) magnetic nozzle section. Shown are the "spool piece", plasma gun, RF interferometer and choke magnet coil. Main tank is to the right of the photo. $Z = 0$ axial location is at the center of the choke magnet. Inset shows orientation relative to Figure 3.1.

3.1.1 Vacuum magnetic fields

The DC magnetic field inside the experiment is defined by five sets of magnet coils. The plasma source contains a 300-turn magnet with an inner diameter of 5.1 cm. The choke magnet is a 166-turn magnet with inner diameter of 25.4 cm, located at $z = 0$ m. These two small-bore coils define the majority of the applied magnetic field in the experiment. Additional current carrying coils are wound around the 91 cm diameter spool piece at $z = 0.2$ m, $z = 0.5$ m and $z = 0.8$ m, in the following number of turns: 30, 21 and 14. These external current carrying coils are made of AWG 8 wire, and are used to tailor the magnetic nozzle shape in the mid-nozzle region.

The resulting vacuum magnetic field depends on the currents flowing through the magnet coils. A standard condition (listed as Dataset #3 in Table 4.1) uses 5 A in the gun coil,

100 A in the choke coil, and 10 A, 3 A, and 3 A in the final three nozzle magnets respectively. The peak magnetic field intensity under these conditions is 0.068 T on-axis, falling off with $1/z^2$ in the nozzle section until the applied field intensity becomes ~0.001 T at a location 0.8 m from the choke magnet. (Figure 3.4) At a point 1.85 m from the choke magnet, superposition of the earth's field ($5x10^{-5}$ T, 60^o inclination) with the applied field results in constant flux lines bending downwards into the chamber walls as shown in Figure 3.3. On-axis measurements with a 3D magnetometer confirm this theoretical field map.

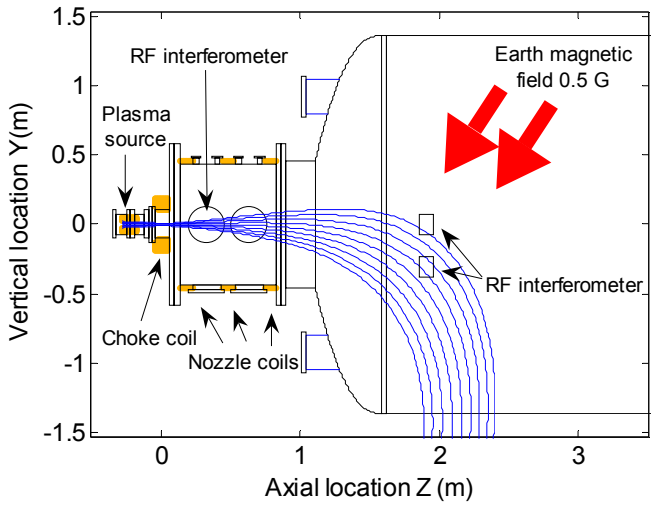

Figure 3.3 Standard magnetic field profile in the DDEX experiment. Trajectories are lines of constant magnetic flux mapped back to the plasma gun source. Magnetic field map was confirmed by magnetometer measurements.

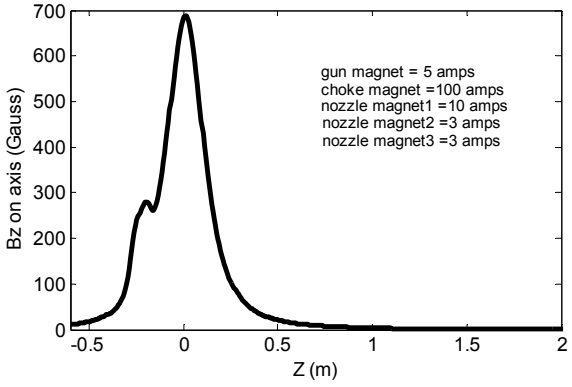

Figure 3.4: Magnetic field intensity (theoretical) on-axis for standard magnetic nozzle conditions, listed as Dataset #3 in Table 4.1.

3.1.2 Plasma source

For the DDEX experiment, one plasma source is used – a pulsed DC plasma washer gun operating at 200 - 300 kW. A schematic diagram of the gun is shown in Figure 3.5. The washer gun consists of a 2 cm tall stack of molybdenum washers of inner diameter 0.5 cm and outer diameter 2 cm. A molybdenum anode and cathode at either end of the washer stack provide the discharge arc. Isolation between the washers is provided by 1 mm thick boron nitride ceramic washers with inner diameter 1 cm. Hydrogen and helium were used as a feedgas, although other gases are possible. Typical discharge pulse lengths are a few milliseconds, with manufacturer reported plasma densities at $n_e \approx 1\text{x}10^{20}$ m^{-3} and electron temperature $T_e \approx 10$ eV at the source aperture. [Fiksel, 1996] A charged capacitor bank provides typical discharge voltages and currents of 270 V and 700 A respectively, as shown in Figure 3.6. In the nozzle experiment, measured temperatures in the nozzle section were never greater than T_e = 1.5 eV suggesting the plasma underwent significant cooling as it exited the plasma source. Given this 1.5 eV

temperature upper bound, and a magnetic nozzle two meters in length, the transit time is 0.1 ms for hydrogen. A typical pulse length is an order of magnitude longer than the transit time, thus allowing the plasma to reach steady state during this experiment.

The gas delivery system for the pulsed DC plasma source consists of a small gas reservoir that is filled by a high pressure gas tank once per day. The reservoir is kept at 5-10 psi and feeds the plasma gun through a Parker high speed solenoid valve. The response time of the Parker solenoid valve is < 5 msec for a 2.5 msec pulse. **Error! Reference source not found.** shows an example of the timing of the gas valve and discharge current. A trigger pulse of < 1 msec duration is provided by the data acquisition computer to synchronize data acquisition, gas valve opening and capacitor discharge.

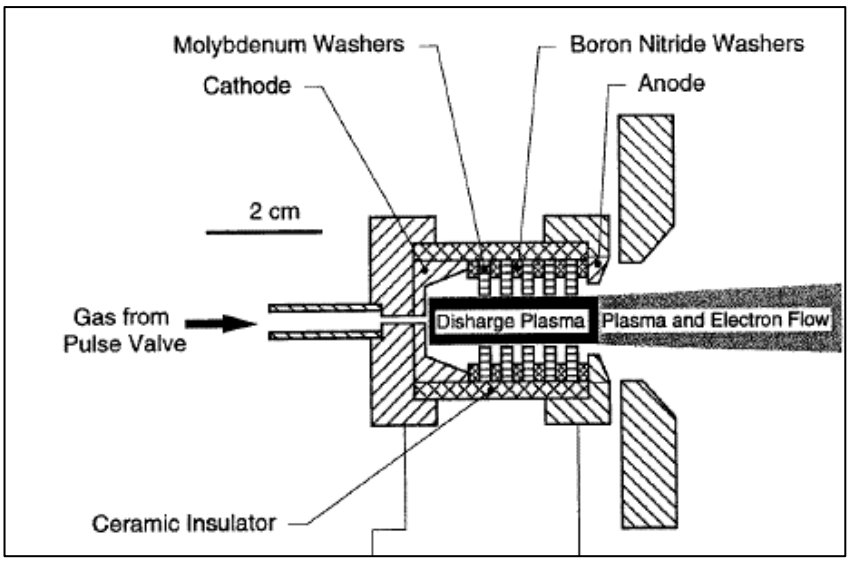

Figure 3.5 High powered plasma gun used in this experiment [Fiksel 1996]

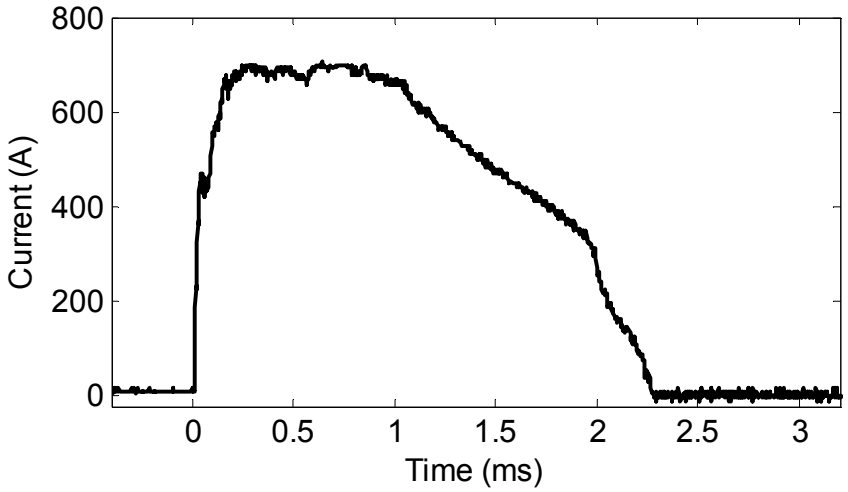

Figure 3.6(a): Plasma source discharge current measured for hydrogen shots. Discharge voltage for this typical shot was 270 V.

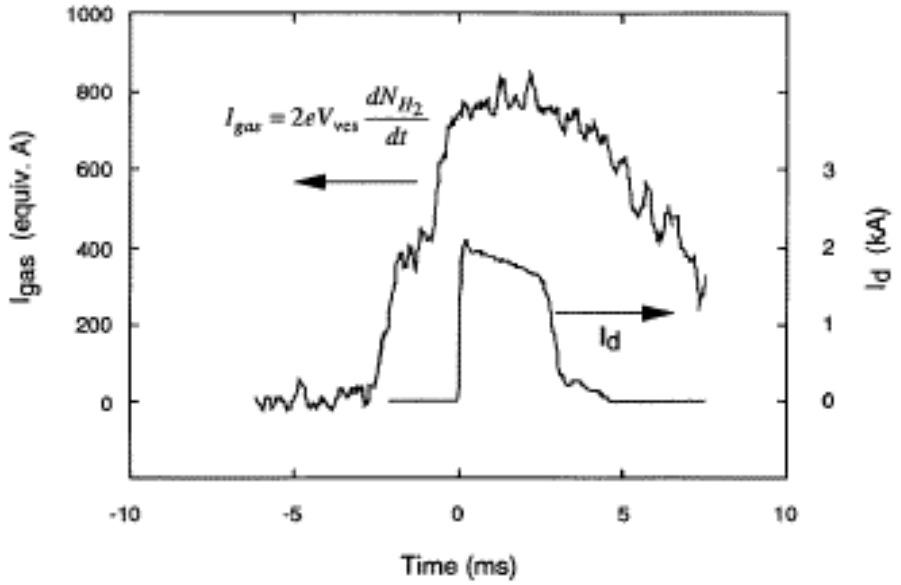

Figure 3.6(b): Example neutral gas rate I_{gas} (left) and discharge current I_d (right) [Fiksel, 1996]. Neutral gas flow is the non-ionized neutral flux leaving the source, and is reported as equivalent Amps, assuming two electrons per diatomic hydrogen molecule. Neutral gas rate is lower than discharge current due to the plasma gun's high ionization fraction.

3.1.3 DDEX Neutral pressure analysis

3.1.3.1 Pressure data

Pressure data is recorded at two locations in the DDEX experiment. An MKS Baratron 627B is located inside the spool piece to detect the pressure rise during a pulse. This capacitance manometer has a moderate time response of 20 msec and a pressure detection threshold of $2x10^{-5}$ Torr. Since this pressure sensitivity is not good enough to detect the lower baseline pressure inside the expansion chamber, a second pressure gauge is used in the main vacuum tank. The Granville-Phillips Stabil-Ion gauge is an ionizing vacuum gauge with an ultra-high vacuum sensitivity of $1x10^{-10}$ Torr. This pressure sensor is much more sensitive to lower pressure, and gives more accurate pressure readings prior to a plasma shot. However, it has a slow time response (0.5 s) compared with the Baratron. Because this ionizing pressure gauge is located downstream of the expected detachment zone, it is mainly used to provide base pressure measurements in this experiment.

Pressure data for helium and hydrogen shots are very similar, so the pressure of only one species (helium) will be presented. As shown in Figure 3.7, the pre-pulse background pressure in the DDEX experiment is measured by the ion gauge to be $1.7x10^{-6}$ Torr. The Baratron has a sensitivity of $2x10^{-5}$ Torr and thus cannot measure this low of a baseline pressure. After the shot, both the Baratron and ion gauge measure a peak pressure of $1\text{-}2x10^{-4}$ Torr with the Baratron showing the higher pressure of the two. The greater measured pressure inside the spool piece may be due to its smaller volume and greater distance from the diffusion pumps. It may also be due to differences in sensitivity

between the ion gauge and Baratron, or that that the ion gauge's slower time response misses the peak of the transient pressure rise. Superposition of a Langmuir probe trace shows the timing of the plasma shot relative to the neutral pressure rise. The timing of the Baratron measurement is crucial, as this provides the best high-speed measurement of pressure. According to the manufacturer, [MKS, 2007] the device has a 20 msec response time due to noise filtering electronics. Taking this delay into account by shifting the pressure response back by 20 msec, the background pressure measured by the Baratron during a plasma shot is $4x10^{-5}$ Torr. Because the filtering electronics results in substantial uncertainty in the timing of the pressure rise, the pressure during a plasma shot could be as high as $2x10^{-4}$ Torr, if the peak pressure value is used.

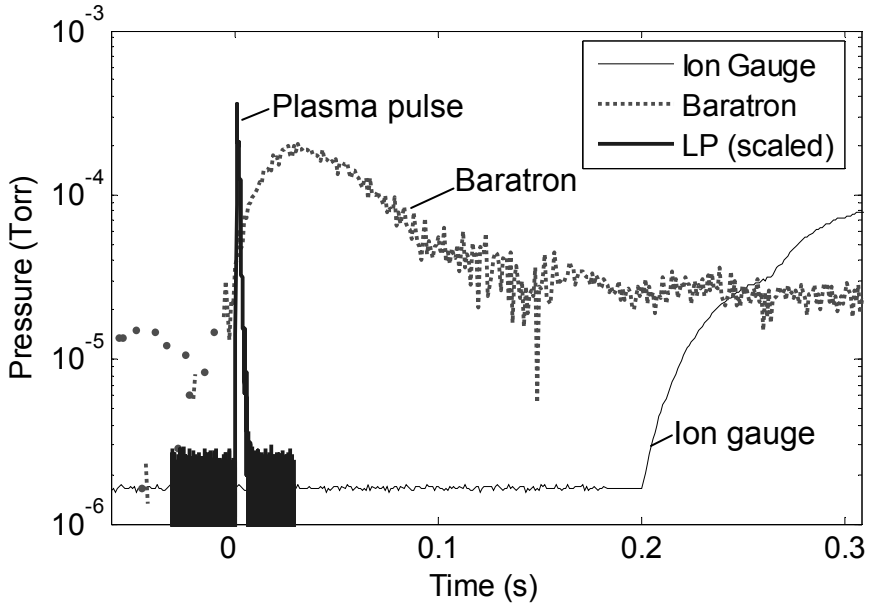

Figure 3.7: Pressure data for helium pulse. Ion gauge gives high sensitivity background pressure in the main chamber. Langmuir probe response (scaled) shows timing of the pulse. Baratron provides fast time response pressure in the spool piece. (20 msec delay accounted for). Pressure = $4x10^{-5}$ Torr during the pulse, up to as high as $2x10^{-4}$ Torr due to timing uncertainty.

The time required to return the vacuum chamber to its original low baseline pressure depends on which pressure sensor you consider. An extended pressure measurement is given in Figure 3.8. According to the Baratron sensor, the chamber pressure returns to below its measurement threshold ($2x10^{-5}$ Torr) within 2 seconds of a pulse. The ion gauge requires more time to reach this pressure reading; neutral pressure is measured at $2x10^{-5}$ Torr after 5 seconds, and a full 20 seconds are required to return to its low pre-pulse pressure level of $2x10^{-6}$ Torr. Whether it actually takes this long for the vacuum chamber to return to this low baseline pressure is unknown – trapped gas or slow response time of the ion gauge may be affecting the readings. Therefore, 20 seconds should be considered a conservative guess as to how long must be waited after a pulse for the vacuum chamber to return to favorable vacuum conditions. This timing was considered while operating the DDEX experiment, as pulses were taken at an interval of at least 60 seconds. This allowed time for the vacuum chamber to return to a baseline pressure, and also allowed time for the plasma source capacitors to recharge, and for the x-z translation stage to be moved.

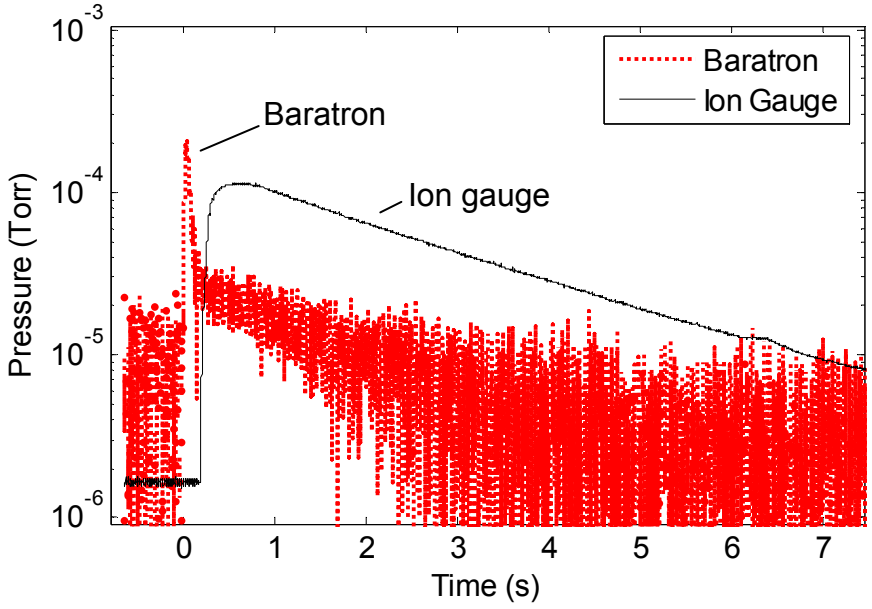

Figure 3.8: Extended pressure data for helium pulse. Ion gauge shows a long time constant to return to baseline pressure, which may be an artifact of the gauge. Baratron shows a much faster time response.

3.1.3.2 Ion gauge sensitivity to different gases

Ion gauge sensitivity is dependent on the species of gas present in the system. This is not the case with the Baratron capacitance manometer that detects the static pressure of the neutral gas against a flexible diaphragm. However, with an ion gauge reading, the measurement may have to be adjusted by a calibration constant to reflect the relative sensitivity of the ion gauge to different species.

A list of calibration coefficients is presented by [Bartmess 1983]. Helium has a relative sensitivity of 0.20, while hydrogen has a relative sensitivity of 0.44, meaning that pressure measurements from an ion gauge should be divided by these values to obtain the true pressure reading. Therefore, the ion gauge pressure readings in Figure 3.7 and Figure 3.8 may need to be increased by nearly a factor of 5 for the helium measurements

and a factor of 2 for the hydrogen measurements. This is a potential problem because by including this calibration factor the ion gauge pressure reading ends up being greater than the Baratron pressure measurements, even though it is farther from the gas source and closer to the diffusion pumps. One response to this possible problem is that it is possible that the aforementioned calibration should only be used for low pressures below $1x10^{-5}$ Torr as stated in the user's manual. [Granville-Phillips 1999] Accounting for this possible source of uncertainty, it should be noted that the peak pressure recorded by the ion gauge may be as high as $5x10^{-4}$ Torr for helium and $2x10^{-4}$ Torr for hydrogen.

The pre-pulse baseline pressure may also have a different value due to the ion gauge's species-dependent sensitivity. However, this is a difficult problem to address because whereas the post-pulse pressure rise is certainly due to the propellant gas (helium or hydrogen), the baseline pressure is more likely to be due to leaks in vacuum fittings or outgassing from hydrocarbons present inside the vacuum chamber. Therefore the exact gas species is unknown. Assuming that the likeliest source of neutral background pressure is air leaking into the vacuum chamber (Air ~ 78% N_2, 21% O_2, 1% Ar), the calibration coefficient is 0.98 ~ 1. No modification is therefore required, and the pre-pulse baseline pressure stands at $1.7 x10^{-6}$ Torr as measured by the ion gauge.

3.1.3.3 Plasma velocity vs. neutral gas velocity

A neutral gas travels at a most probable speed v_m equal to: [Tipler, 2000]

$$kT = \tfrac{1}{2}\, m v_m^2. \tag{3.1}$$

Based on this estimate, the diatomic hydrogen neutral gas released by the puff valve travels at a speed of approximately 1.6 km/s. Likewise, neutral helium gas travels at approximately 1 km/s as it is released into the DDEX experiment. The corresponding trip time for neutral gas to travel the 2 m length of the DDEX experiment is approximately 1.25 msec for hydrogen and 2 msec for helium. The equivalent trip time for ionized hydrogen or helium is an order of magnitude faster, as will be shown in Section 4.1.4. The plasma pulse duration is only 3 msec, and occurs very near the time of gas valve opening, as shown in Figure 3.6(b). This suggests that a large fraction of the downstream plume can be measured prior to the neutral gas pressure arriving at the same measurement location. Therefore, even under the worst possible pressure conditions, there exists a window of time in the first 1-2 msec of the pulse where there is not likely to be interference from neutral gas. This condition is considered in the measurements section, and density profiles are reported within the first 2 msec of the plasma pulse.

3.1.3.4 Randolph Criterion

The influence of neutral particles is an important consideration for this experiment since we are attempting to prove the transfer of momentum in a plasma plume in a simulated space environment. The Randolph criterion [Randolph, 1993] has been suggested as an

upper pressure limit for facility effects on the EP plume to be negligible, based on ion-neutral collision effects. This level has been set at 1.3×10^{-5} Torr for Hall thrusters operating on xenon. Compared with the pre-pulse pressure in the chamber of 1.7×10^{-6} Torr, the DDEX facility meets the Randolph criterion by nearly an order of magnitude prior to a shot. However, immediately following a shot, the chamber pressure rises to 2×10^{-4} Torr which is beyond the Randolph criterion. The timing of this pressure rise is crucial, because if the pressure rise occurs during a plasma shot, collisional dissipation could result.

As stated above, the Baratron pressure gauge has a 20 msec delay due to noise filtering electronics. If this delay is accounted for, the neutral pressure was measured to be 4×10^{-5} Torr during the 3 msec plasma pulse. This pressure exceeds the Randolph criterion as stated above. However, as will be shown, the Randolph criterion should be adjusted according to the gas species. Based on this adjusted pressure limit, the background pressure in this experiment meets the criteria for negligible neutral gas interaction.

3.1.3.5 Collisional mean free path

The neutral background pressure plays an important role in determining the collisional mean free path of the plasma. An additional component to this calculation is the collision cross-section. Data for the collision cross-section for Hydrogen, Argon and Helium can be consulted and used along with neutral particle density to estimate the mean free path

for collisions in the experiment. The following table lists approximate collision cross-sections for a variety of conditions:

Gas species	σ_{CEX}	σ_{total}	Ref.
He^+-He, 6eV	1.2 x10^{-19} m^2 1.6 x10^{-19} m^2	3.5 x10^{-19} m^2 ……	[McDanel 1993] [Gilbody 1957]
H_2^+-H_2, 2eV	7 x10^{-20} m^2	……	[Gilbody 1957]
Ar^+-Ar, 20eV	2.2 x10^{-19} m^2	6 x10^{-19} m^2	[McDanel 1993]
Ar^+-Ar, 500 eV	2.0 x10^{-19} m^2	4 x10^{-19} m^2	[McDanel 1993]
Xe^+-Xe, 200 eV	4x10^{-19} m^2 5.5x10^{-19} m^2	…….. ……..	[Randolph 1993] [Miller 2002]

Table 3.1: Collisional cross-sections for Helium, Hydrogen Argon and Xenon. σ_{CEX} is the charge exchange cross-section. σ_{total} is the total cross section including momentum exchange.

where σ_{CEX} is the ion-neutral charge exchange cross section and σ_{total} is the total collision cross section, including charge exchange and elastic scattering. Discrepancy between sources, where it exists, can be considered experimental uncertainty. The charge exchange mean free path is determined by

$$\lambda_{i,n} = \frac{1}{\sigma_{CEX}} \frac{1}{n_{neut}} \tag{3.2}$$

where σ_{total} could alternatively be substituted into the above equation to obtain the total collisional mean free path, and n_{neut} is determined by the ideal gas law to be:

$$n_{neut} = \frac{P}{k_B T_{neut}} \tag{3.3}$$

where P is the neutral gas pressure in Pascal, k_B is Boltzmann's constant, and T_{neut} is the neutral background temperature in Kelvin, taken to be equal to 293 K, approximately equal to the chamber temperature. Of course, the chamber temperature value is a bit of an approximation - the experiment took place in Alabama in the summertime and could have been warmer, up to 298 K. This is a relatively small contributor to uncertainty though, so the standard 293 K is taken for this analysis.

Given the above cross sections, Figure 3.9 gives the appropriate mean-free-paths. With a pre-pulse neutral background pressure of 1.7×10^{-6} Torr, the charge exchange mean free path for helium is around 110 m, and 250 m for hydrogen, both of which are much greater than the scale length of the experiment. Post-pulse the pressure spikes at 2×10^{-4} Torr, which leads to a 0.9 meter charge exchange mean free path for helium and 2.2 m for hydrogen. This is less than or on the order of the experiment scale length, ~ 2 m. Therefore, significant slowing of the plasma flow could occur if the plasma pulse occurs during this peak measured pressure of 2×10^{-4} Torr.

As stated in 3.1.3.1, by accounting for a pressure measurement delay of 20 msec, the Baratron measured a pressure of 4×10^{-5} Torr during the pulse. Due to timing uncertainty the pressure during the pulse could have been as high as 2×10^{-4} Torr. At 4×10^{-5} Torr, the charge exchange mean free path is 4.7 m for helium and 11 m for hydrogen, which is greater than the experiment path length. The total mean free path including charge and momentum exchange is 2.2 m for helium and even greater for hydrogen. All of these

mean free paths are larger than the experiment length of 2 m. However, none of the mean free paths are so large that charge exchange collisions can be neglected altogether; therefore further experimental evidence of ion-neutral charge exchange collisions will be investigated in Section 4.3. The impact of ion-neutral momentum exchange collisions on plume trajectories is considered in Section 5.1.5.3.

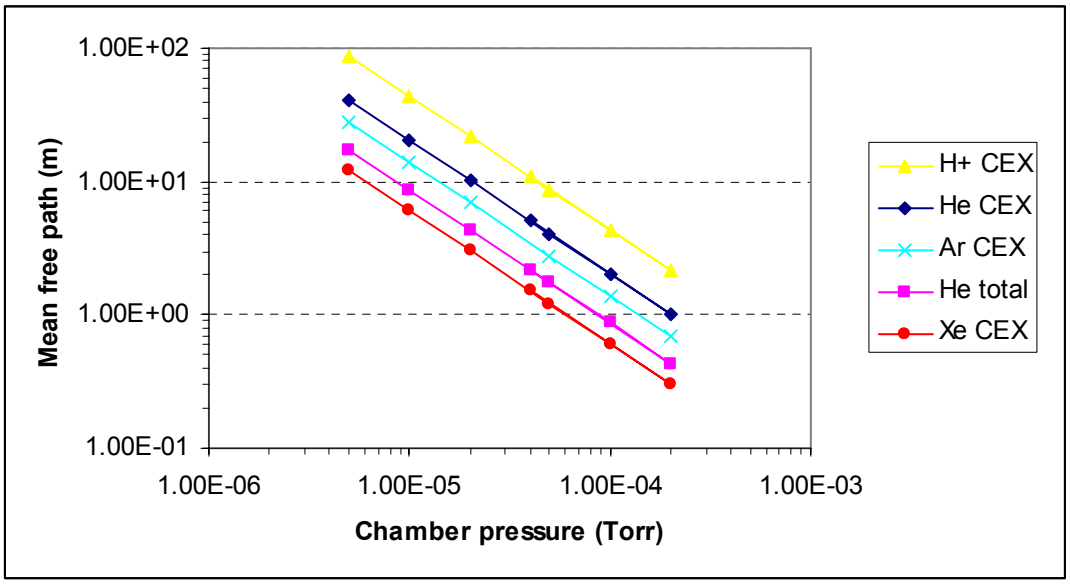

Figure 3.9: Collisional mean free path for four gas types. Xenon is included for comparison sake – no testing was performed with Xenon. CEX denotes the mean free path for charge exchange collisions. Total denotes the mean free path for both charge exchange and elastic scattering.

3.1.3.6 Species dependent Randolph criterion

It is interesting to note that for a given pressure, the charge exchange mean free path $\lambda_{i,n}$ for xenon is a factor of three less than $\lambda_{i,n}$ for helium, and a factor of seven shorter than $\lambda_{i,n}$ for hydrogen. This has importance with regards to the Randolph criterion, since the criterion was formulated specifically for the collisional effects of a thruster operating on

xenon. It is assumed that the Randolph criterion would be different for a different operating gas. A species independent limit can be found if the ion-neutral charge exchange mean free path is used instead of the neutral pressure. The Randolph limit for xenon is 1.3×10^{-5} Torr, which can equivalently be stated as a charge exchange mean free path of $\lambda_{i,n} = 4.7$ m. To match this $\lambda_{i,n}$ in H^+ and He^+, the neutral pressure limit is instead 9.2×10^{-5} Torr and 4.3×10^{-5} Torr, respectively. These pressure values can be considered species-dependent Randoph criteria for the neutral background pressure for thrusters operating on hydrogen and helium. These re-stated Randolph criteria are an improvement for this experiment, because now the 4×10^{-5} Torr pressure measured during a shot will meet the species-dependent Randolph criteria. This is reflective of the relatively long charge exchange mean free paths in the experiment.

3.2 DDEX Diagnostics

The DDEX experiment was instrumented with a variety of plasma diagnostics. Some of these will be discussed in this work, including Langmuir triple-probes, microwave interferometers, Mach probes and time-of-flight photomultiplier tubes. Other diagnostics such as flux loops and b-dot probes did not provide information useful for this work. They will not be considered further here. The experiment was focused on making measurements of magnetic detachment and the transition from $\beta < 1$ to $\beta > 1$. Diagnostics were therefore concentrated in the mid-nozzle to far-nozzle region of this experiment. Figure 3.10 shows an isometric view of the experiment, and Figure 3.11 provides a top view with the spatial layout of all diagnostics.

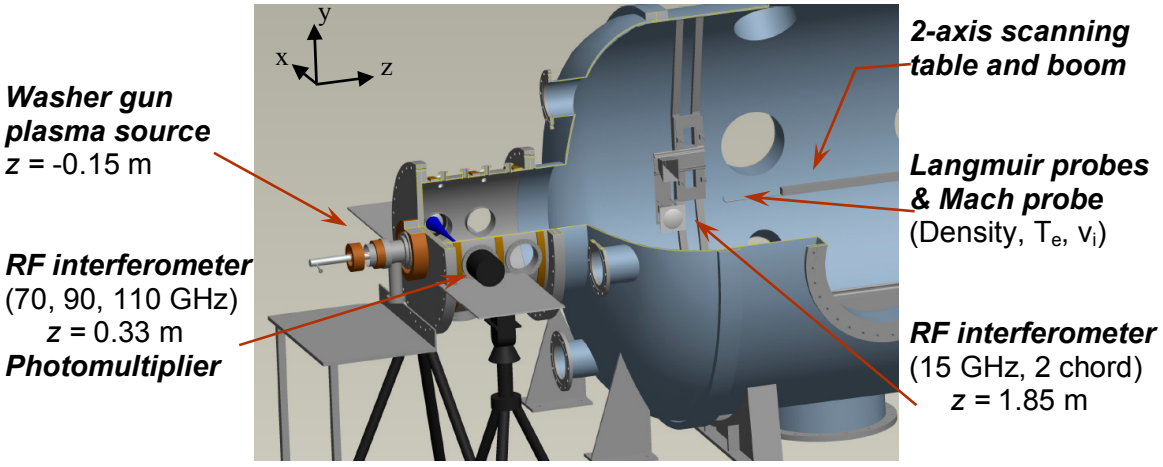

Figure 3.10: Diagnostic setup of the MSFC magnetic nozzle experiment. Axial location of diagnostic instruments are noted. Vertical triple-probe array not shown. Coordinates as follows: X-axis is transverse to the plasma flow in the horizontal direction. Z-axis is parallel to plasma flow down the chamber. Y-axis is along a vertical cross-section of the chamber.

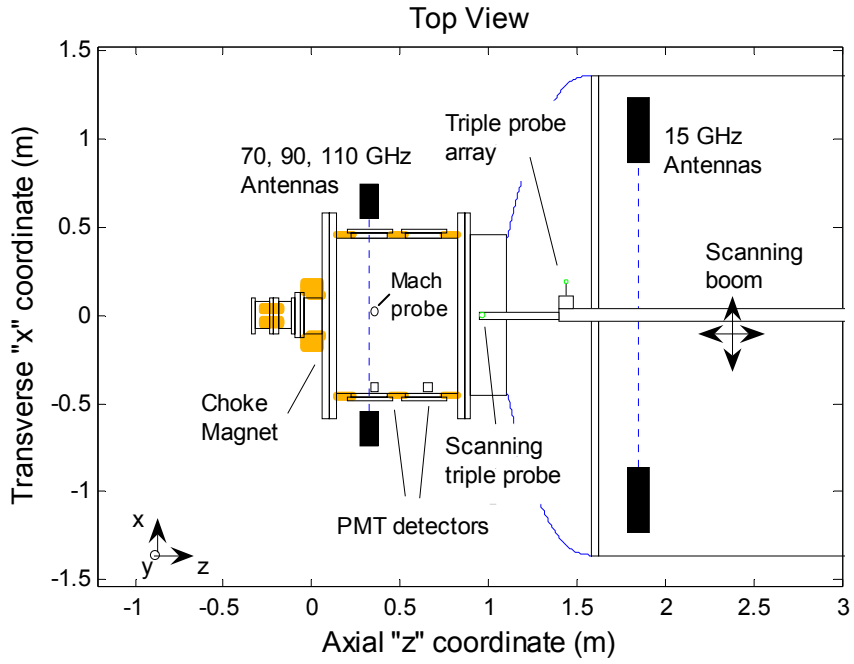

Figure 3.11: Detailed overhead view showing positions of all diagnostics. The scanning triple probe at the end of the boom can reach from z = 0 m – 2.0 m and from x = -0.5 m – 0.5 m, and is shown at the center of its extent. The Mach probe is affixed to the bottom of the chamber and slightly below centerline.

The relevant measurements to be made in the mid-nozzle to far-nozzle region of the DDEX experiment are density (n_e,n_i), temperature (T_e) and velocity (v_i) . In order to make these measurements, the following equipment was employed:

- A 2-D translation stage with diagnostics boom to allow measurements throughout the chamber with millimeter positioning accuracy.
- A small scanning triple-probe attached to the diagnostics boom to measure n_i and T_e throughout the experiment. Typical measurements were taken in a radial scan along the scene beam of a microwave interferometer
- A vertical array of six Langmuir triple-probes attached to the diagnostics boom, to provide T_e and n_i profiles for each shot.
- A microwave interferometer operating simultaneously at 70 GHz, 90 GHz and 110 GHz to provide line-integral n_e measurements close to the plasma source.
- A second, multi-channel interferometer operating at 15 GHz to provide line-integral n_e measurements in the far-nozzle region.
- Photomultiplier tubes to record natural plasma fluctuations at multiple locations, giving an estimate of v_i by time-of-flight.
- A Mach probe to measure v_i.

The following sections give further details on the above-mentioned diagnostics used in the DDEX experiment.

3.2.0 Data acquisition system

Unless explicitly stated otherwise, diagnostic signals are optically isolated by Terahertz Technologies Inc. analog to optical converters, part number LTX 510 that are powered by an isolated rack of 12 V 7.0 Amp-hour lead acid batteries. The signal is routed via optical fiber to a Terahertz Technologies TIA500 optical to analog converter. The measurement rack consists of a National Instruments BNC 2090 breakout box and a PXI 1042 chassis running four PXI 6254 analog-to-digital converter cards and a PXI 8336 timer card. This provides 128 analog channels operating at 16 bits and 1Megasample / second. A second high-speed rack consists of five PXI 5112 oscilloscope cards operating at 100 MHz, and an Acquiris DC270 providing 20 channels at 1Gigasample / second. This second rack provides high-speed digitization for high frequency measurements such as plasma gun current, B-dot probes and photomultiplier tubes. The data is digitized and stored on a network computer to be backed up and retrieved at a later date.

3.2.1 Langmuir triple- probes – plasma assumptions

In Section 2.1.1, it was assumed that the following plasma conditions were true in the area around the triple probes: 1) The electron energy distribution is Maxwellian, 2) the collisional mean free path for electrons is large with respect to both the ion sheath thickness h_s and probe radius r_p, and 3) the thickness of the ion sheath is smaller than the probe separation so that interaction between the three probes is negligible. For the DDEX experiment, these conditions are valid for the following reasons. 1) The electron collision period inside the plasma source [mks units] is [Huba, 2006]

$$\nu_{ee} = 2.91 \text{x} 10^{-12}\, n_e \ln \Lambda T_e^{-3/2} \quad \left[\sec^{-1}\right] \tag{3.4}$$

For $n_e \approx 1\text{x}10^{20}$ m^{-3} and $T_e \approx 10$ eV inside the plasma gun, this yields ν_{ee}=1x10^{-8} seconds. Given Eq. (3.1), the transit time of a 10 eV hydrogen plasma exiting the 2 cm plasma source is 4x10^{-7} seconds, meaning the electrons have several characteristic times to thermalize before exiting the plasma source. 2) Using measured data from Chapter 4 for the furthest upstream location of the probe, and using Eq. (3.4) the ν_{ee} collisional period is 2x10^{-8} seconds resulting in a mean free path of

$$\lambda_{ee} = \sqrt{\frac{eT_e}{m_e}} \Big/ \nu_{ee} \tag{3.5}$$

or λ_{ee} = 2.6 cm which is much greater than the largest probe radius used (r_p= 0.12 cm). Collisions other than electron-electron happen with even lower frequency and are also not a factor. 3) At its maximum extent, the sheath size is (from Eq. (2.2) using T_e = 1.5 eV and n_e = 1x10^{17} m^{-3}): h_s = 0.4 mm which is much smaller than the smallest inter-probe spacing of 2 mm, and also much smaller than the electron mean free path λ_{ee}. The assumptions used in Chapter 2 are therefore valid for all measurements made in the DDEX experiment.

3.2.2 Small boom-mounted Langmuir triple-probe

An X-Z translation stage inside the chamber allows remote radial scans of the plasma exhaust. A Langmuir triple-probe (Figure 3.12) is positioned on the end of a 1.3 m boom

attached to this motion stage, and oriented perpendicular to the plasma flow. The Langmuir triple-probe is composed of three stainless steel cylindrical collectors (probe tips) of radius 0.45 mm and height 5 mm. The separation of each of the three stainless steel conducting probe tips is at least 2 mm. The probes are arrayed such that each conductor is not shadowing another during the experiment. A short piece of alumina ceramic maintains the position of the collecting tips, and houses the wiring that connects to the stainless probe tips. Coaxial cables run from the probe tips down the boom out to a BNC patch panel at the vacuum chamber wall. A photograph of the small scanning triple-probe is shown in Figure 3.13.

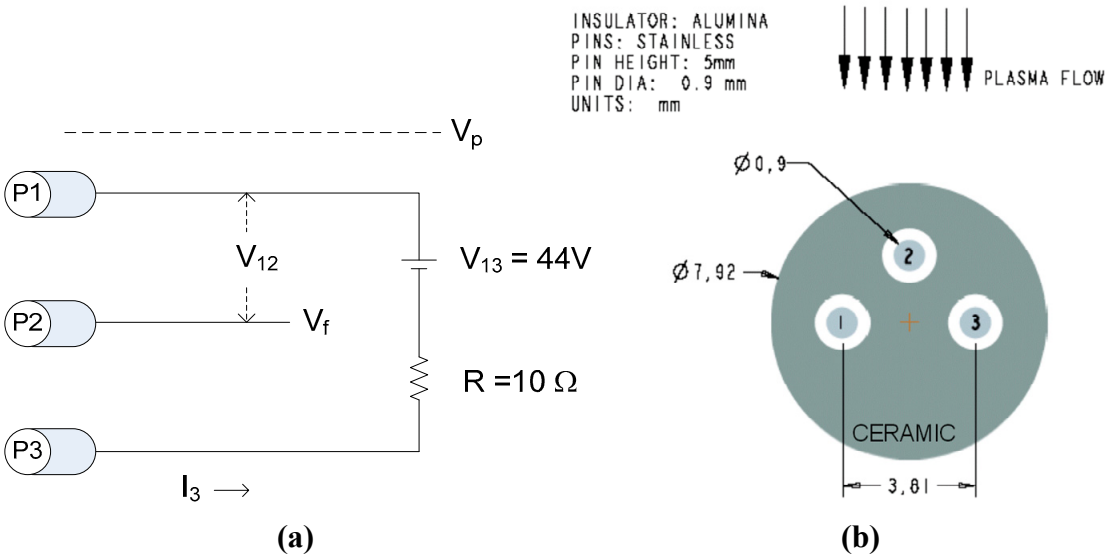

Figure 3.12: Electrical schematic (a) and top view of the scanning Langmuir triple probe (b). Probe conductor diameter and height are 0.9 mm and 5 mm respectively.

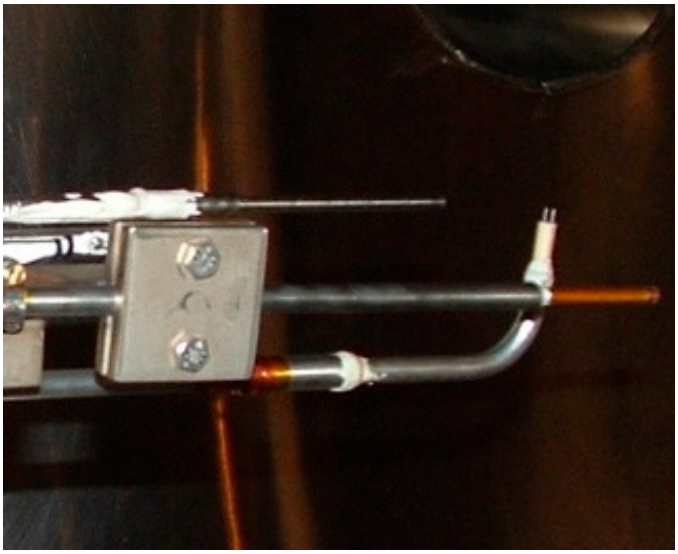

Figure 3.13: Photograph of scanning Langmuir triple probe (vertical orientation) at the end of the diagnostics boom. Two other probes are visible here (B-dot probes) but are far enough away to not affect LP measurement.

The middle pin (pin two) is left floating to provide electron temperature measurements. The floating signal is optically isolated with input impedance of 1 MΩ, resulting in a current draw several orders of magnitude below the ion saturation current. Pins one and three are biased to 44 V relative to one another by a series of 9 V batteries, with ion current measured by a 10 Ω shunt resistor. Providing a large DC bias ensures that pin 3 is well into ion saturation, collecting only ion current.

The approximate centerline plasma density at the two limiting axial locations is 3×10^{18} m^{-3} at $z = 0.43$ m and 1×10^{17} m^{-3} at $z = 1.85$ m. The electron temperature is less than 1.5 eV throughout the measured portion of the experiment. The Langmuir triple-probe tip radius r_p is therefore many Debye lengths at the upstream location ($r_p = 86\ \lambda_D$), but only tens of Debye lengths ($r_p = 16\ \lambda_D$) at the downstream location. The Langmuir

probe is assumed to be operating in the thin sheath regime, which requires $r_p >> \lambda_D$. Errors may be introduced in the Langmuir probe measurements due to large Debye lengths with respect to the probe radius r_p and therefore large sheath size. This is particularly the case for downstream measurements where the thin-sheath assumption is only partially valid, i.e. where plasma Debye length is greater than 10% of the probe radius. While the absolute density results will not be affected much (as this is determined by the hybrid probe - interferometer method) this thin-sheath violation will introduce an error term in the calculated plasma column diameter for downstream measurements. A full accounting of plume width error is provided in Appendix B. Errors in the measurement of T_e will be discussed in Section 4.1.3. It is also assumed that the radius of the triple-probe is small with regards to the radial density gradient. Given the probe radius (4.5×10^{-4} m) and the upstream plasma column radius of 8.5×10^{-2} m, this is a fair assumption. To reduce end effects, the probe must be long compared with its radius. In the case of the small scanning triple probe, the probe tip accounts for only 4 % of the total probe surface area.

3.2.3 Vertical triple-probe array

A 6-element Langmuir triple-probe array is also mounted on the boom to determine the plume's radial distribution for each shot. This array consists of six triple-probes arrayed vertically at 0.126 m intervals. Relative to the chamber centerline, the y coordinates of the six triple probes are $y = \pm 0.064$ m, ± 0.191 m and ± 0.317 m. The probe tip radius for these conductors is a larger 0.12 cm with 0.6 cm of the conductor length exposed. The conductor material is made from stainless steel welding rod that is sheathed in an alumina

ceramic tube 6.6 cm long. Unlike the small boom-mounted triple probe whose probe axis is vertical, these triple-probes are mounted horizontally, with all 18 conductors of the 6 triple-probes lying in the same vertical plane, as shown in Figure 3.14 and Figure 3.15. End effects will be more evident for this probe than the scanning triple-probe since the tip surface area comprises 9% of the total surface area. Since absolute density measurements are determined by comparison with a microwave interferometer, this end-effect error does not contribute to density measurement error.

The vertical probe array is mounted 0.34 m behind the small boom-mounted triple probe, making its measured plasma density correspondingly smaller. The larger radius allows the probe to fit within the thin-sheath criteria at the downstream position, with the ratio of probe radius to Debye length of $r_p = 43\ \lambda_D$ at $z = 1.85$ m. This is nearly a factor of 3 improvement over the small boom-mounted triple-probe which leads to an improvement in accuracy of plasma density measurements at this downstream location.

The electrical connections and data acquisition setup for the vertical Langmuir triple-probe array are identical to those described above for the small boom-mounted triple probe. A 44 V bias is provided with 9 V batteries, and ion current is detected across a 10 Ω sensing resistor. The potential of the electron-collecting probe is measured with respect to the floating pin, which is used to measure electron temperature.

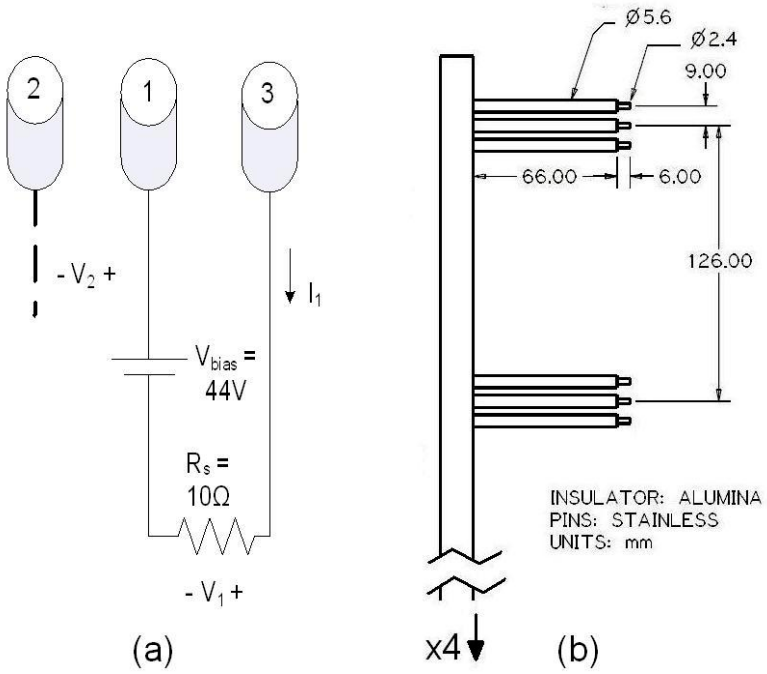

Figure 3.14: Electrical configuration (a) and dimensions (b) of triple probe vertical array consisting of 6 sets of probes. Plasma is flowing out of the page in view (b).

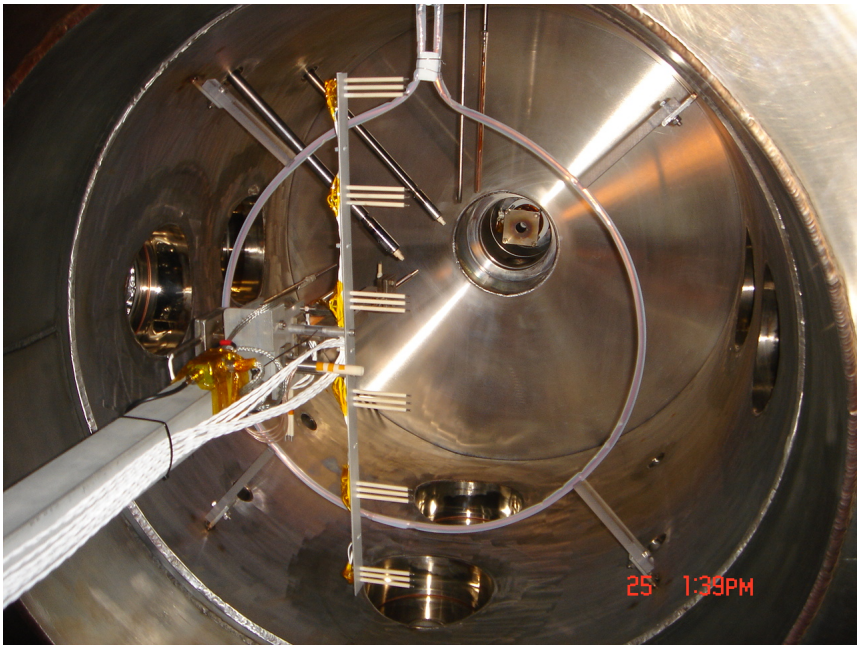

Figure 3.15: Langmuir triple-probe vertical array. Simultaneous T_e and n_e data is recorded on each of the six triple-probes.

3.2.4 Microwave interferometers - overview

Additional chamber diagnostics include microwave interferometers, positioned at two axial locations to provide spatial and temporal density measurements. The upstream interferometer is a polychromatic quadrature interferometer that operates simultaneously at 70 GHz, 90 GHz and 110 GHz. The downstream interferometer is positioned about 1.5 meters from the first interferometer, and operates at a lower 15 GHz. These particular frequencies were chosen to provide a plasma density measurement range consistent with the expected plasma density at each measurement location.

3.2.5 Polychromatic microwave interferometer

This instrument was developed and operated by the Marshall Space Flight Center, and used in prior experiments. [Dobson, 2004] The interferometer is positioned near the nozzle entrance, 0.33 m downstream from the choke magnet. The spatial resolution for this interferometer is 0.015 m, with a minimum sensitivity of 10^{16} m^{-3} over the 1 m path length. [Chavers, 2006] The transmit and receive antennas can also be moved to different vertical positions, providing a vertical density profile.

The interferometer is composed of a receiver and transmitter, connected by flexible coaxial cables for the reference leg, and horn antennas for the plasma measurement leg. Local oscillators within the transmitter section are frequency multiplied and directed to a transmitting horn antenna equipped with Gaussian optics. The optics focal length is ~0.6 m, and provides a measurement spot size of 0.02 m at 70 GHz. For each of the three frequencies, the reference and scene components are split into two signals before

combination at the receiver, one of which is shifted in phase to produce a quadrature measurement. Figure 3.16 shows a schematic drawing.

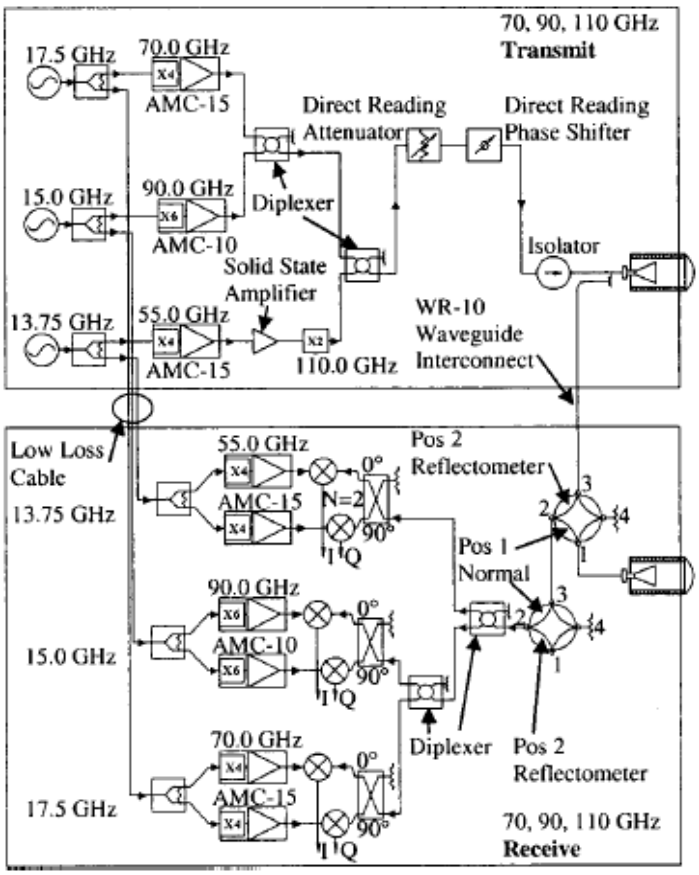

Figure 3.16: Schematic of the polychromatic interferometer showing both the transmit and receiving sections. [Dobson, 2004]

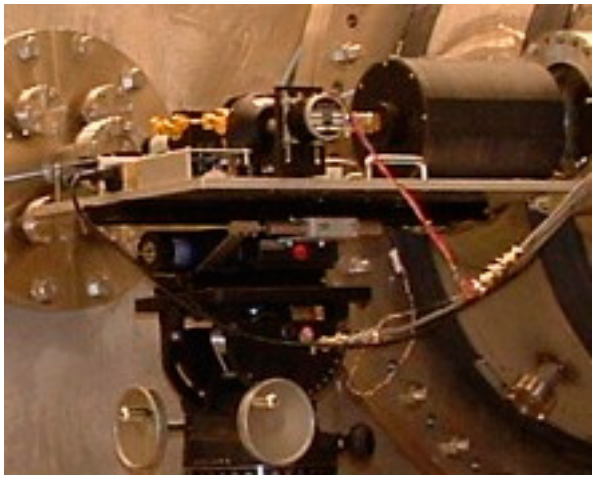

Figure 3.17: Polychromatic interferometer operating at multiple frequencies. (70 GHz, 90 GHz and 110 GHz) The interferometer can be moved vertically by a manual elevation stage. The large black cylinder on the right contains the Gaussian optics lens antenna.

3.2.5.1 Refraction and calibration of polychromatic interferometer

Calibration of the polychromatic interferometer was performed daily by the staff at MSFC. The microwave detectors were found to be quite stable from day to day, and reflections were found to be minimal due to the interferometer antenna's narrow beamwidth.

Manufacturer's data shows that the polychromatic interferometer beamwidth at 70 GHz is 1.5 cm with a focal distance of 0.6 m. Compared with the plasma's full-width half-maximum of 18cm presented in Chapter 4, the interferometer beamwidth is approximately 10x smaller. As discussed in Section 2.2.2, a ray tracing program can be implemented which predicts attenuation due to plasma refraction. Given the upstream plume measurements discussed in Section 4.1.1.1 this yields a predicted beam attenuation of -1.7 dB at 70 GHz.

3.2.6 15 GHz interferometer

A second interferometer instrument is located 1.5 m downstream of the first interferometer in the far-nozzle region, and was based on a previous University of Michigan design. [Gilchrist, 1997] This 15 GHz instrument is actually two independent systems consisting of separate horn antennas, oscillators and mixers, with one positioned 0.3 m below the other and sampling two different parts of the plume at the same axial position. The Ka- band local oscillators operate at approximately 15 GHz and are each split into two separate paths by 3-port power dividers. The scene beams are routed via coaxial cable and SMA connectors to +25 dBi standard gain pyramidal horn antennas and received on the other side of the plasma column by identical receiver antennas. A separate coaxial cable is routed from the receiver horn to one input of a quadrature diode mixer. The second input of the diode mixer is fed directly by the 15 GHz local oscillator. A schematic of this quadrature interferometer is given in Figure 3.18.

All of the active components of the system are mounted onto a copper backplane and located inside the vacuum chamber. The backplane was rigidly attached to an aluminum structure providing a thermal path to the chamber. Power was applied continuously to the system over the multiple month testing period, with no degradation or thermal variation detected. The horn antennas were attached to vertical support beams inside the chamber, with the transmit side separated from the receive side by 1.7 m. The axial position of this installation is z = 1.85 m. The vertical positions of the two channels are y = 0 m and y = -0.305 m.

Interferometer calibration is achieved by a motor stage on the transmitting antenna, shown in Figure 3.19. This servo-driven linear ball screw uses a feedback potentiometer to determine when it has moved through about 1" (2.54 cm), corresponding to one and a half wavelengths at 15 GHz. This allows pre- and post-shot calibration of the interferometers to account for changes in the DC offset and amplitude of the signal. Stability of the interferometer calibration over time suggests that only one interferometer calibration is necessary for each set of radial scans in the DDEX experiment.

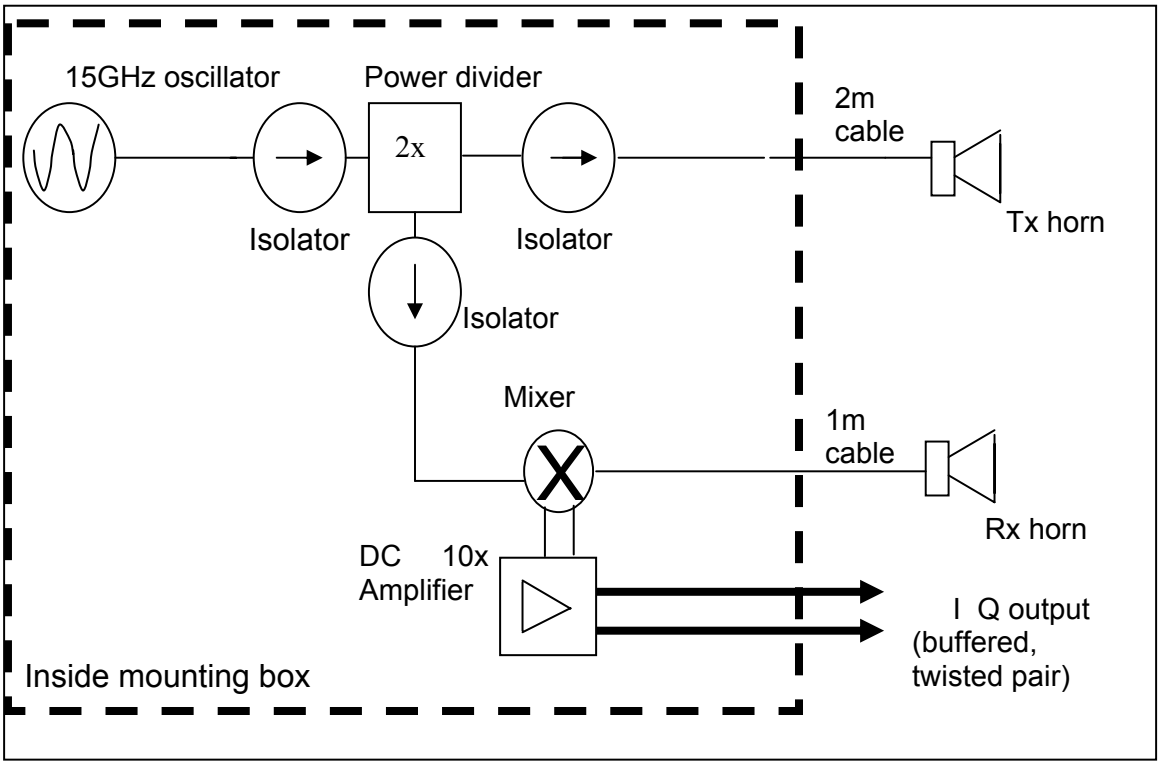

Figure 3.18: 15 GHz RF interferometer schematic. Two independent systems were used in the DDEX experiment, one on the chamber centerline and one 0.3 m below. The *I* and *Q* output denote the two phase-quadrature outputs from each interferometer system.

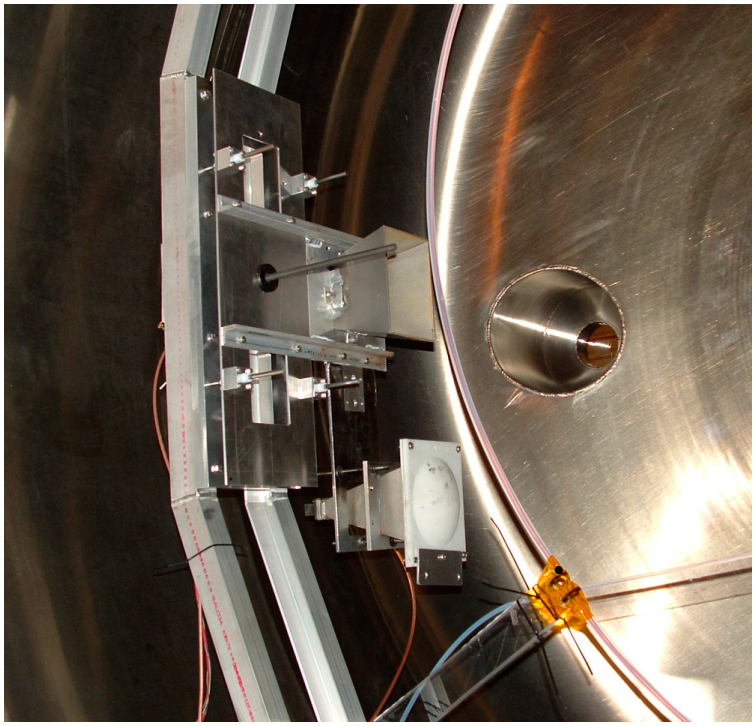

Figure 3.19: Close-up of the linear motor mechanism used to calibrate the 15 GHz interferometer. (note: the metal plate on the front of the bottom lens was removed prior to data collection)

3.2.6.1 15 GHz Interferometer density ranges and sensitivity

An RF interferometer is useful in detecting plasma up to a certain maximum density before the RF wave starts being cut off. This value is given by $\omega > 3\omega_p$. Given this assumption, the maximum plasma frequency detectable is $\omega = 2\pi$* 5GHz. Using Eq. (2.17) for plasma frequency, the maximum peak density detectable by the 15 GHz interferometer is $3x10^{17}$ m^{-3}. This is an adequate range for density measurement where the interferometer is going to be operated.

The absolute minimum sensitivity of the interferometer is driven by the mean error in phase measurement. According to Dobson et al. (2004) a phase error of 0.17 radian is

typical for a measurement that is fitted to a calibration curve employing four parameters per channel. In the context of the exhaust interferometer, a 0.17 radian minimum sensitivity corresponds to a minimum line integral density sensitivity of $3x10^{15}$ m^{-2}.

In a practical system there are other limitations to the sensitivity including the noise floor of the output channel, and the resolution of the digitizer. In the case of the current version of the 15 GHz interferometer, the mixer output is amplified 8x. This produces a signal output of 25 mV_{ppk}. The approximate noise floor of the system is 50x lower at 0.5 mV_{ppk}. This corresponds to a phase shift of $\sin^{-1}(1/50) = 2x10^{-2}$ radian. This measurement is lower than the previous estimate of 0.17 radian, so the measurement resolution should not be a limiting factor.

In summary**,** the maximum and minimum plasma density that can be measured by the 15GHz exhaust interferometer is: $n_{max} = 3x10^{17}$ m^{-3} and $N_{min} = 3x10^{15}$ m^{-2}.

3.2.6.2 Horn antenna radiation pattern and cross-channel interference test

The radiation pattern of the interferometer's +24 dBi standard gain horn was tested in the University of Michigan Radiation Lab anechoic chamber. Two horn antennas were held at 2 m separation from each other and one was rotated in the H-plane (long aperture dimension). A 15 GHz +13 dBm signal was fed to the transmit antenna, and the response detected at the receive antenna with a spectrum analyzer. As shown in Figure 3.20, a 3 dB beamwidth of 11º was detected at a horn-horn separation of 2 m. The maximum signal level detected by the receiver antenna was -68 dBm.

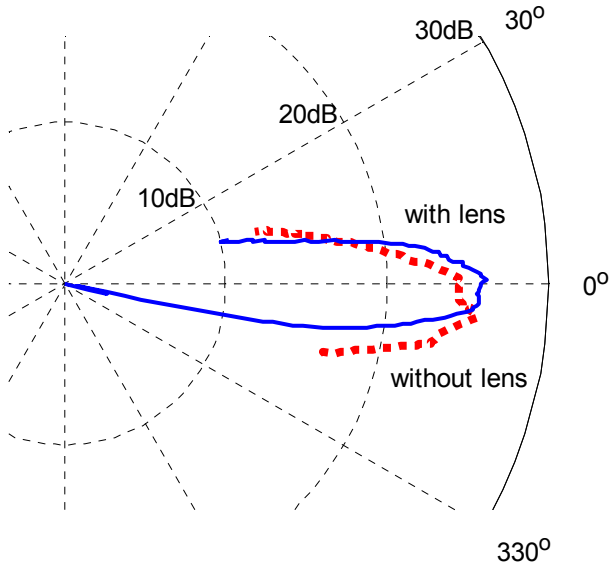

Figure 3.20: H-plane (vertical) radiation pattern of the 15 GHz horn antenna measured at 2m. +24dBi horn with 11° beamwidth, with and without correction optics.

Next, it was desired to test the cross-channel interference between the two independent interferometer channels. In order to simulate the relative isolation between adjacent channels, the transmit horn was offset by 12" (0.305 m) and kept at the same angle, so the horns were misaligned. This was intended to simulate the two channels which are separated vertically by 0.305 m. A schematic drawing of this setup can be seen in Figure 3.21. A measurement of radiation pattern resulted in a drop of 11 dB at 0º between the aligned case and the misaligned case. A peak maximum occurred at -7.5º (approximately the angle at which the receive horn is pointed at the transmit horn). From this test, it appears that the channel-channel isolation for a 0.305 m horn separation at 2 m distance is 11 dB. This corresponds to a maximum phase error of 8×10^{-2} radians, which is greater than the system noise floor, but less than the minimum phase sensitivity determined in 3.2.6.1. The use of RF absorbent foam did not appear to improve this isolation. Alternating the receive and transmit horns of the two channels so that the transmit horn of

channel 1 was opposite the transmit horn of channel 2 would further increase the channel isolation, but this was not deemed necessary for the experiment since the phase error is low compared with the minimum interferometer sensitivity.

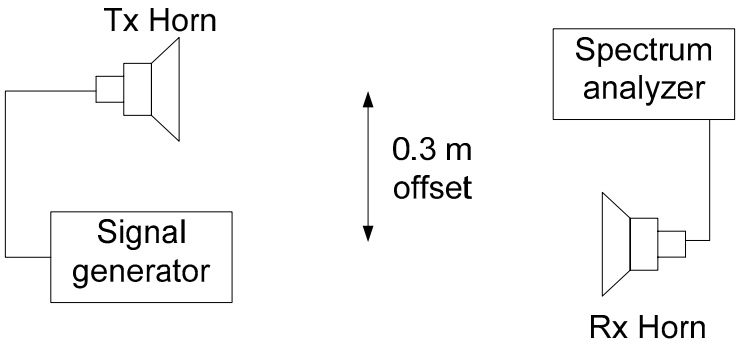

Figure 3.21: Schematic of antenna offset test inside the University of Michigan anechoic chamber. A 12" (0.3 m) offset resulted in an 11 dB attenuation, which simulates the channel-channel isolation for the two independent chords.

3.2.6.3 15 GHz Interferometer far-field calculation

The radiation pattern of an antenna can be greatly simplified in the far-field by the Fraunhofer approximation. [Balanis, 1997] This far-field approximation can be used with amplitude errors of 2% at a distance $R > 2a^2/\lambda$, where a is the longest dimension. For the 24 dBi antennas used, the aperture height is a = 15.5 cm, so the desired separation is R = 2.3 m. The separation that was used in the experiment is 1.7 m – much less than this distance. The electric field amplitude error associated with operating at R =1.7 is 5% if far-field approximations are assumed. This may increase the error in the interferometer phase measurement because of a non-uniform phase front arriving at the receive antenna.

The use of parabolic optics would remove these errors because the lenses create a uniform phase front beyond the antenna's focal length. [Oliver, 1993] In the case of the second (lower) interferometer channel, a pair of parabolic lenses was available and installed. The upper interferometer channel was left without corrective optics. Looking at relative tests of the horns with and without parabolic lenses, the beamwidth was narrowed by 1^{o} and the main lobe was made much more uniform with the use of the parabolic optics. They were omitted from the upper interferometer channel for cost and availability reasons.

The impact of neglecting parabolic optics and the far-field spacing can be estimated by computer simulation. A 2D method-of-moments simulation similar to [Davis, 2006] was employed. The aperture of the transmitting and receiving horn antennas were divided into discrete elements, 0.5 mm in length. An electric field was assigned to each finite element of the transmitting aperture according to the antenna distribution function [Balanis, 1997]

$$E(x_n) = E_0 \cos\left(\frac{\pi}{a} x_n\right) e^{-j\delta\phi(x_n)} \tag{3.6}$$

Where a is the antenna height, x_n is the x position of the transmitting element n, and $\delta\phi(x_n)$ is the phase variation across the horn aperture. This phase distribution is also given by [Balanis, 1997] to be:

$$\delta\phi(x_n) = k_0 \left(L_a - \sqrt{L_a^{\,2} - x_n^2}\right) \tag{3.7}$$

Where L_a is the antenna length and k_0 is the free-space wave number. The total electric field at each receiving element position x_m can be calculated by summing the field contributions from each transmitting position x_n.

$$E(x_m) = E_0 \sum_{n=1}^{N_{\max}} \cos\left(\frac{\pi x_n}{a}\right)\cos\left(\frac{\pi x_m}{a}\right)\frac{e^{j[k_p r_n + \delta\phi(x_n)]}}{4\pi r_n} \tag{3.8}$$

Where r_n is the separation between element x_n and x_m, and the scalar Green's function was used in (3.8). [Kong, 2000] In the absence of plasma, the free-space wave number k_0 substitutes for the plasma wave number k_p. If plasma is present, the wave number k_p is taken from Eq. 2.19. It should be noted that k_p is spatially varying due to the plasma density distribution.

If the antenna characteristics of the 15 GHz interferometer are considered, the aperture height a is 15.5 cm, and the horn length is L_a = 33.5 cm. The separation between the receive and transmit horn is 1.7 m. The plume at z = 1.85 is shown in Section 4.1.1.4 to have a peak centerline density of $n_e = 1\text{x}10^{17}\,\text{m}^{-3}$ and to follow a Gaussian profile with full-width half-max of 90 cm. Given these inputs, the phase error owing to lack of parabolic optics and antenna positioning is $8\text{x}10^{-3}$ radians. This is lower than the noise floor of $2\text{x}10^{-2}$ radians, and is not expected to contribute to measurement error.

3.2.6.4 Beam refraction and interferometer calibration

Refractions due to plasma can increase the phase errors and magnitude errors of the received signal. As previously stated, magnitude errors are not explicit error terms in this

experiment because the quadrature mixer decouples the amplitude and phase of the received signal. Phase errors can be introduced by the increased pathlength of bending rays, and by changing the distribution of the received rays on the receiving antenna aperture. These phase errors are considered error terms, as they can affect density measurements.

The ray tracing technique described in 2.2.2 is used to track the propagation of rays, and can give an estimate of the signal attenuation due to the plasma acting as a diverging lens. The 15 GHz interferometer has a horn antenna of vertical dimension a = 15.5 cm. As stated in Section 3.2.6.3, the plume at the position of the 15 GHz interferometer has a peak centerline density of $n_e = 1\text{x}10^{17}\ \text{m}^{-3}$ and follows a Gaussian profile with full-width half-maximum of 90 cm. A ray tracing simulation with these inputs was based on the Matlab code given in [Ohler, 1996] and [Davis, 2006], and the results are shown in Figure 3.22. By comparing the total E field intercepted at the receive antenna with and without plasma, the attenuation factor from refraction was found to be a modest α_0 = -0.4 dB.

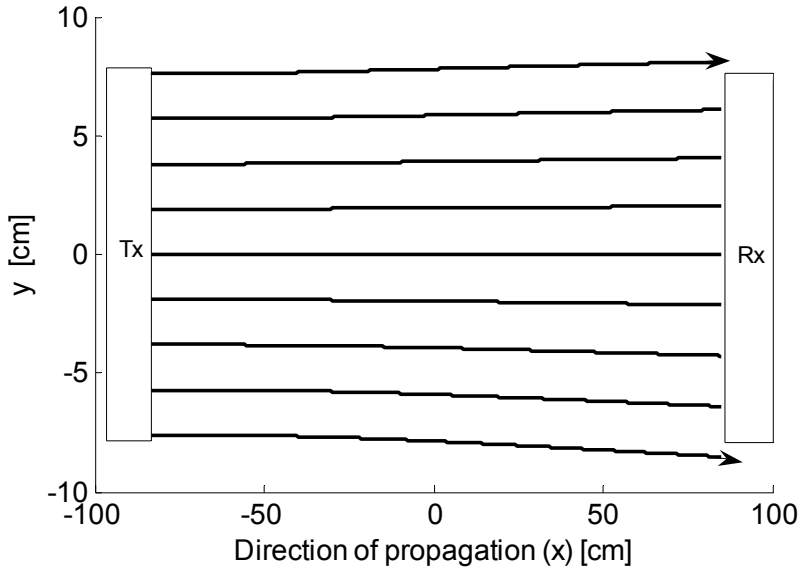

Figure 3.22: Ray tracing simulation for 15.5 cm horn antenna operating at 15 GHz and transmitting into a Gaussian plasma distribution of peak density $1x10^{17}$ m^{-3} and full-width half-maximum 90 cm. The transmitting antenna is on the left and the receiving antenna is on the right. Total beam attenuation is -0.4 dB.

The phase errors arising from refraction could be determined directly by combining the above ray tracing technique with the method-of-moments simulation of Section 3.2.6.3. This would compute the total electric field arriving at the receive antenna, accounting for refractive wave-bending. However, as this is a much more computationally intense process than the previous two simulations, and the additional error is expected to be on the order of the phase error arising from lack of parabolic optics ($8x10^{-3}$ radians), this analysis was omitted. This omission is further justified by prior analyses [Vest, 1975] [Tallents, 1984] in which the phase error from mildly refracting, axisymmetric plasma columns was found to be small.

Calibration of the 15 GHz interferometer occurred daily while testing was underway. As described in Section 2.2.3, this process detects drift in the quadrature mixers and reflections from the surrounding chamber. In practice, the separation of the horn antennas is changed by a distance x, and the voltage response of the two channels of the quadrature mixer $\tilde{V}(x)$ and $\tilde{V}'(x)$ are fit to Eq. (2.30) and (2.31) with the substitution $\Delta\phi = kx$. If reflections are to be included, Eq. (2.29) is used instead. A least-squares fitting method using the Matlab toolkit **cftool** fits the analytical models to the experimental data. Fit error is expressed as a percentage of the signal's amplitude. Figure 3.23 shows a plot of the calibration data, along with the analytical models that best fit the data.

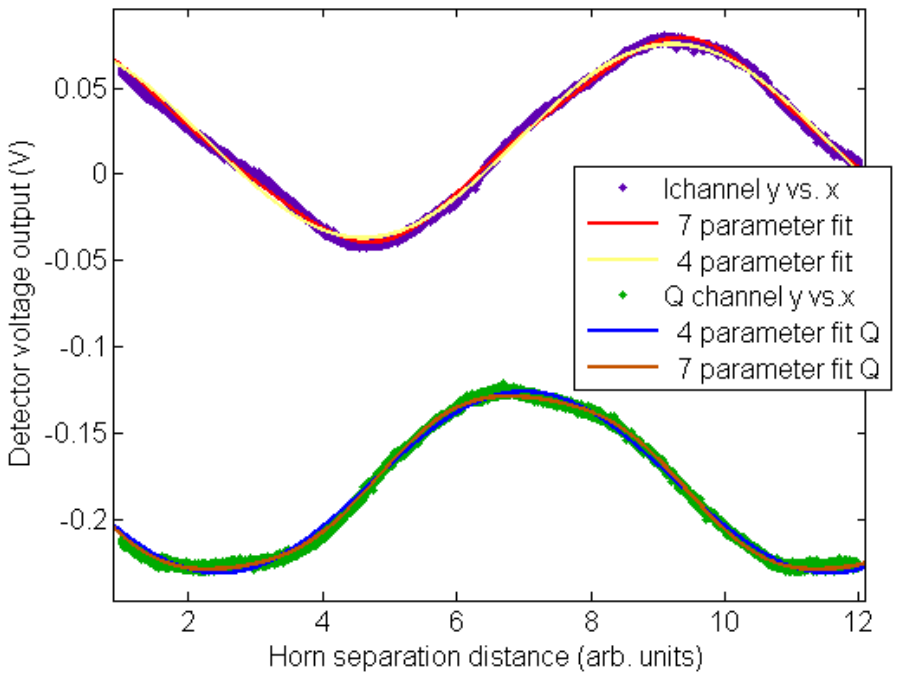

Figure 3.23: Calibration data for the upper 15 GHz interferometer. I is the primary channel and Q is the quadrature channel, offset in phase by 90°. The fitted data shows the standard 4-parameter fit, with an RMS fit error of 5.6%. The more accurate seven-parameter fit includes reflections and has an RMS fit error of 3.9%.

The root-mean-square fit error for the four interferometer channels is given in Table 3.1. The four-element fit of Eq. (2.30) neglects reflections, and resulted in an RMS fit error of 5.6% for the upper interferometer. The seven-element fit of Eq. (2.29) accounts for reflections, and improves this fit error to ~3.9%.

	15 GHz upper channel, I	15 GHz upper channel, Q	15 GHz lower channel, I	15 GHz lower channel, Q
4-element RMS error	5.6%	5.6%	2.45%	1.68%
Reflection coefficient ρ	0.06	0.064	0.022	0.006
7-element RMS error	3.9%	3.3%	1.4%	1.56%

Table 3.1: Sample calibration curve fitting for the 15 GHz interferometer, upper and lower channels, and primary and quadrature detectors. RMS error is the fit error between the calibration data and the particular model.

The fitting error for the full seven-element calibration is only a modest improvement over the simpler four-element calibration, affording a reduction of 1.7% in fit error The downside of the seven-element calibration is that Eq. (2.29) can not be expressed as a function of $\tilde{V}(x)$ and $\tilde{V}'(x)$. To solve for $\Delta\phi$, and thus N_e, Eq. (2.29) must be solved numerically at each time point, which is computationally intensive. Therefore, the simpler four-element calibration is used in this work, allowing the numerically less intensive Eq. (2.32) to be used.

3.2.6.5 2π ambiguity resolved with Langmuir probe data

On occasion, the plasma shot will yield interferometer data containing ambiguous phase shifts which could either be real phase shifts due to density changes, or spurious data due to missed fringes. This may occur during a large jump in density at the beginning of a shot, coupled with an insufficient sampling rate to detect the rising edge. This may also be the case when large amplitude RF noise is picked up on the signal line. In these cases, Langmuir probe data taken during the same shot may provide some estimate of the proper temporal shape of the plasma plume, since probe measurements are not susceptible to the same 2π ambiguity. During any given shot, the Langmuir triple-probe provides a local measurement of ion flux $\Gamma_i = n_i v_i$ which, assuming constant velocity, can provide a temporal density profile to compare with the microwave interferometer measurement.

The raw Langmuir probe voltage is scaled to match the microwave interferometer phase ϕ_{MWI} by a multiplicative constant $\kappa = \frac{\phi_{MWI}}{V_{LP}}$. The constant κ is different at different points in time, so the software utilized for this data analysis averages κ over the last 25% of the plasma shot. This timing was chosen because the microwave interferometer data was well-behaved on the trailing edge of the shot, free from 2π fringe shifts and interfering RF noise. The following plot shows the close agreement between scaled Langmuir probe data and interferometer data during the trailing edge of the plasma shot.

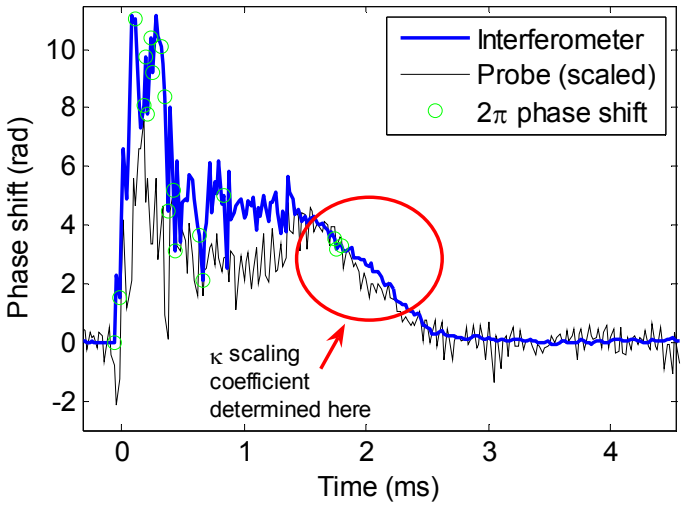

Figure 3.24: Plot of Langmuir probe data scaled to the 15 GHz interferometer. The portion of probe data where the scaling factor is calculated is highlighted.

During the bulk of the plasma shot, the microwave interferometer measurement becomes noisy, and sometimes shows a different shape than the Langmuir probe data. This may be due in part to the local nature of the probe data, while the microwave interferometer returns an averaged line-integral density measurement over the entire chord.

Once the probe data is adjusted by the κ scaling coefficient, the microwave interferometer phase is constrained by software to follow within a window around the probe data. Interferometer data $5/3\pi$ radian greater than the probe data is shifted downwards by -2π. Interferometer data $-\pi$ radian below the probe data is shifted upwards by $+2\pi$. The following plot shows the result of such an adjustment:

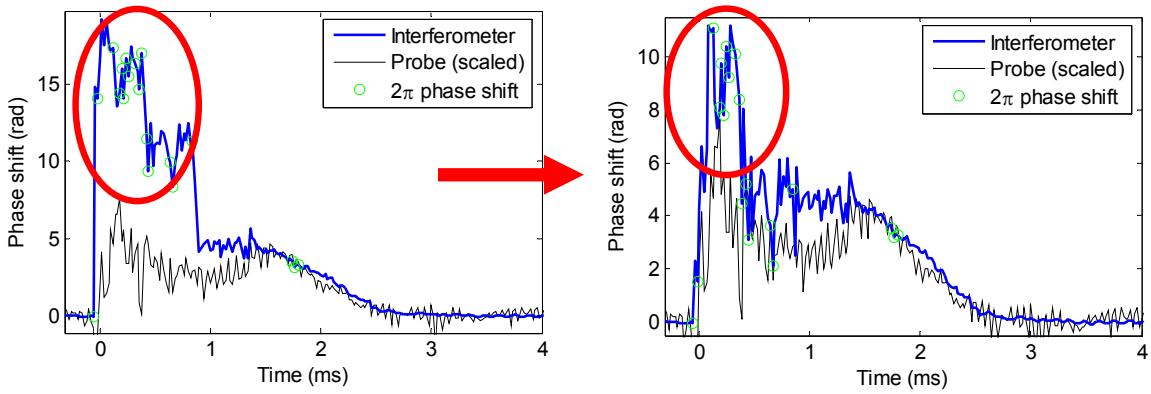

Figure 3.25: 2π ambiguity in microwave interferometer measurement resolved by comparison with probe data. The microwave interferometer density is shifted down by 2π at two locations to coincide with the scaled Langmuir triple-probe measurement.

By the above method, noisy and otherwise ambiguous interferometer data can be quickly and accurately resolved to a state which is appropriate for conversion to a density measurement.

3.2.7 Time of flight velocity detection

Ion velocity was roughly calculated using several different methods. For time of flight velocimetry, two spatially distributed sensors sample the same plasma at high time resolution. Natural fluctuations in the plasma are picked up by both sensors, with a time delay between the positions. An example of this time shifted data can be seen in Figure 3.26. The time lag along with the known sensor separation distance determines the velocity at which the plasma fluctuations and, presumably, the ions are traveling. Langmuir probes with an axial separation of 0.47 m and photomultiplier tubes with a separation of 0.3 m provide the density fluctuation measurements. A data acquisition system running at 1 GigaSample / sec provides adequate temporal resolution to detect the

plasma fluctuations. While the Langmuir probes detect ion current directly related to the plasma density, the photomultiplier tubes are measuring photoemission from the plasma, which is averaged over the 1D line of sight of the detector. It is assumed that fluctuations in this line integral photoemission and density fluctuations in the plasma move at the same speed as the bulk plasma. In other words, these fluctuations are assumed to not be waves or disturbances moving at speeds other than the axial ion velocity. This is the same approach considered by [Spores, 1993] for time of flight measurements on an arcjet thruster.

The first photomultiplier tube is positioned at z = 0.33 m, in-line with the polychromatic interferometer. The second photomultiplier tube is positioned at z = 0.63 m, therefore time of flight measurements provide average velocities between these two positions. The Langmuir probes are movable and can provide an axial scan of velocity, since they are located on the translation stage. It should be noted here that a small (0.06 m) radial offset exists between the upstream Langmuir probe and the downstream probe that was not considered in the time of flight analysis. Relative to the other sources of error, this offset does not affect measurements.

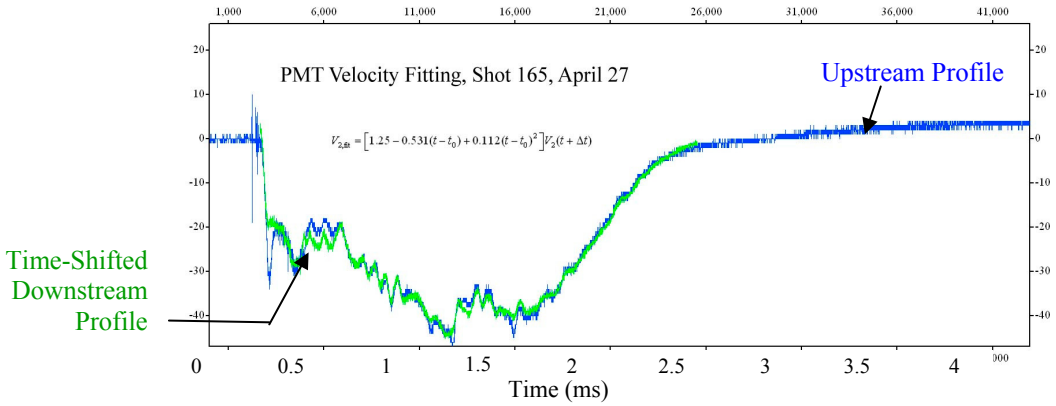

Figure 3.26: Time of flight raw data showing time shifted downstream profile. This measurement used photomultiplier tubes to detect an approximate ion flow velocity. An appropriate 23 μs time shift in the downstream data yields the approximate ion velocity = 13 km/s for Helium. [Dobson, 2007]

3.2.8 Mach probe velocity detection

Ion flow velocity was also estimated with a two-conductor Mach probe. Based in part on the design by [MacLatchy, 1992] this probe has one upstream facing pin and one downstream facing pin as shown in Figure 3.27.

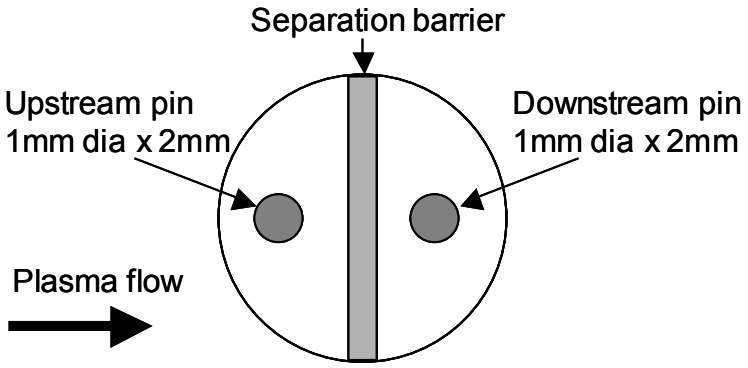

Figure 3.27: Example diagram of a Mach probe with 1 mm diameter stainless steel collectors.

The Mach probe is constructed of stainless steel, and has collecting pins of 1 mm diameter and 2 mm length. Each collecting pin is biased negatively to collect ion saturation current. An insulating separation barrier prevents axial directed flow from reaching the downstream facing pin. The Mach probe is affixed in the chamber at z = 0.33 m to detect v_i at the same axial location as the polychromatic interferometer.

The ion Mach number measurement is derived from the ratio of upstream to downstream current according to: [Hutchinson, 2002]

$$R = \frac{I_{upstream}}{I_{downstream}} \approx \exp\left(\frac{M}{0.45}\right) \tag{3.9}$$

Here the ion Mach number is defined as:

$$M = v_i \left(\frac{\gamma_e e T_e + \gamma_i e T_i}{m_i}\right)^{-1/2} \tag{3.10}$$

T_i was never measured directly in this experiment, but is assumed to be equal to T_e , as was also assumed for the hybrid measurement technique. The ratio of specific heats is also assumed to be $\gamma = 1$. These two assumptions contribute to uncertainty in the final Mach probe measurement.

Further details on the construction and analysis of the Mach probe diagnostic are given in [Meyer, 2007].

CHAPTER 4

EXPERIMENTAL RESULTS AND ANALYSIS

4.0 Overview

As discussed in Chapter 3, the DDEX experiment provided an opportunity to research a high-powered plasma source coupled with a magnetic nozzle emitting into a large, high vacuum chamber. Experimental results are presented here involving investigations of plasma flow under several different magnetic nozzle conditions. The goal of these measurements was to characterize the plume under magnetized conditions ($\beta < 1$) and unmagnetized conditions ($\beta > 1$) comparing results with detachment theory. Magnetized plasma can be found near the plasma source where applied magnetic field energy density outweighs the plume's kinetic energy density. Unmagnetized plasma can be found further downstream as the diverging magnetic nozzle's field strength drops off. To create a more dramatic decrease in magnetic nozzle strength, a reversed coil configuration was also investigated, with results from this cusp field compared with those from a standard magnetic nozzle.

The previously discussed diagnostics were applied in the plume of the DDEX experiment to measure several plasma parameters. The plasma density profile was mapped to high accuracy at a number of axial locations. Likewise the electron temperature and the ion

flow velocity were measured at multiple locations to help support numerical simulations and models of the plume's detachment from magnetic field lines. Plasma density and velocity measurements provide the plasma's beta β and therefore allows an estimate of the location of the $\beta > 1$ transition. Plume trajectories and profile widths allow comparisons with the magnetic field profile to determine the degree of detachment from magnetic fields, both while $\beta < 1$ and $\beta > 1$.

An overhead view of the experiment's magnet coil configuration is shown in Figure 4.1. Experiment conditions are given in Table 4.1 for each of the major configurations. The section of this chapter is listed in which each condition is initially discussed, along with the date on which the data were measured, the magnitude of the magnet nozzle currents, the discharge voltage of the plasma gun, and the propellant gas species. Data presented later in this chapter references Table 4.1's listed experiment configurations.

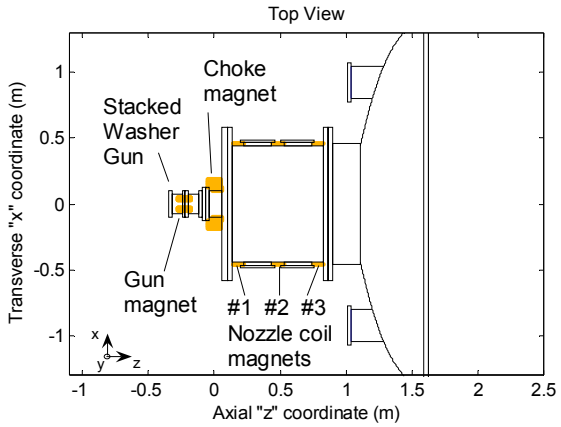

Figure 4.1: Magnet coil positions for the DDEX experiment.

	Dataset #1	Dataset #2	Dataset #3	Dataset #4
Section discussed	4.0.1	4.1.1.1	4.1.1.3	4.1.1.5
Propellant species	H	H	H	He
Experiment dates	5/31/06	8/16/06	5/30/06-6/1/06	4/27/06-5/4/06
I_gun	17A – 90A	22 A	5 A	5 A
I_choke	0 A	90 A	100 A	90 A
I_noz#1	0 A	5 A	10 A	10 A
I_noz#2	0 A	3 A	3 A	3 A
I_noz#3	0 A	3 A	3 A	3 A
Gun voltage	270 V	270 V	270 V	270 V

Table 4.1: Conditions for the experiments considered in Chapter 4. Each dataset is referenced by number later in the text.

4.0.1 Plasma source dependence on magnetic field strength

An initial minor experiment investigated the operation of the plasma gun by varying current in the plasma gun's magnet. The experiment conditions are listed as Dataset #1 in Table 4.1. This experiment was an attempt to verify that the plasma was magnetized at its source, and that the plume shape responded to different magnetic field conditions. The width of the plasma plume was measured with a scanning Langmuir probe at $z = 0.43$ m, still in the low-β (magnetized) region of the plume. The plasma gun operated on hydrogen in this experiment, with a gun magnet current between $I_{gun} = 17$ A and 90 A. The other magnet coils (choke magnet, nozzle coil magnets) were not operated at the same time. Due to the small diameter of the gun magnet, a peak magnetic field of 2700 G was produced for $I_{gun} = 90$ A as shown in Figure 4.2. The resulting plume diameter, defined as the full-width at half-maximum, is shown in Figure 4.3. An inverse

relationship exists between applied magnetic field *B* and plume diameter, with a narrower plume at higher *B*-field. Since the discharge current (not shown) remained constant, and centerline density (not shown) increased with decreasing diameter in accordance with particle flux conservation, it is not likely that this plume narrowing was due to reduced plasma flux. If the plasma plume were not magnetized, its diameter would not have changed in response to an increased *B*- field. This qualitatively indicates that the plasma is responding to the higher field by becoming more highly confined, and is therefore magnetized at the plasma source.

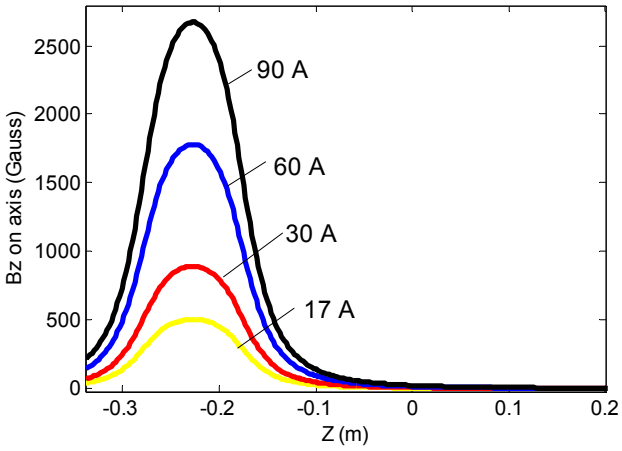

Figure 4.2: Magnetic field profile on-axis for the four gun current configurations. Magnetic nozzle is off during this particular experiment.

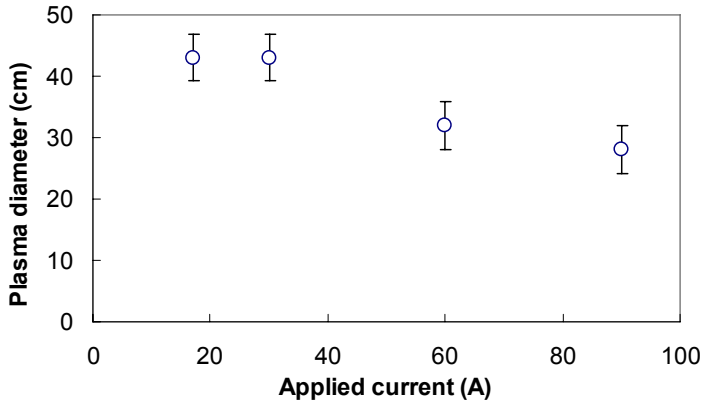

Figure 4.3: Effect of increased gun magnetic field on the full-width half-maximum plume diameter at z = 0.43 m. Higher magnet coil current reduces the plume diameter suggesting that the plume is magnetized at the source. Other nozzle coils are off during this test, and plasma source voltage and feed rate are kept constant.

Due to time constraints, the high gun magnet currents in this test were not repeated in subsequent tests; the magnetic nozzle field in subsequent tests was primarily supplied by a high current in the small-bore choke magnet, instead of in the gun magnet. Therefore a direct comparison cannot be drawn between the experiment conditions in Section 4.0.1 and those found in Section 4.1. This experiment was not necessarily intended to prove that the plume conditions in Datasets #2, #3 and #4 were also magnetized at the plasma source. It was merely included to show that conditions exist in this experiment setup wherein plume diameter is influenced by a changing magnetic field. It is possible that in the other data sets, the plume was also magnetized at the source, but this remains to be shown by other experimental methods and theory. A direct proof by varying the choke magnetic field (not the gun magnetic field) and ensuring that the plume diameter responds to the magnetic field increase was not accomplished in the DDEX experiments. However, further experiments were conducted by adjusting the nozzle coil current. These results are discussed in Section 4.2.

4.1 Experimental results – diverging magnetic nozzle field

The magnetic field configuration was kept approximately constant in these experiments to follow a "standard" nozzle coil current configuration. The coil currents are given in Table 4.1 under the headings Dataset #2 thru Dataset #4. These three data sets were collected on different days, and each has a slightly different magnet coil current setting. This situation is not ideal because we desire a comparison between the results for each data set. However, as is shown in Figure 4.4, the B - field is nearly the same for each configuration beyond the choke magnet at z = 0 m. The major difference in magnetic field profile arises from the higher gun magnetic field in Dataset #2, which is not assumed to result in a significantly different plume diameter from the other two data sets. This assumption is dealt with in more detail in Section 4.1.1.1.

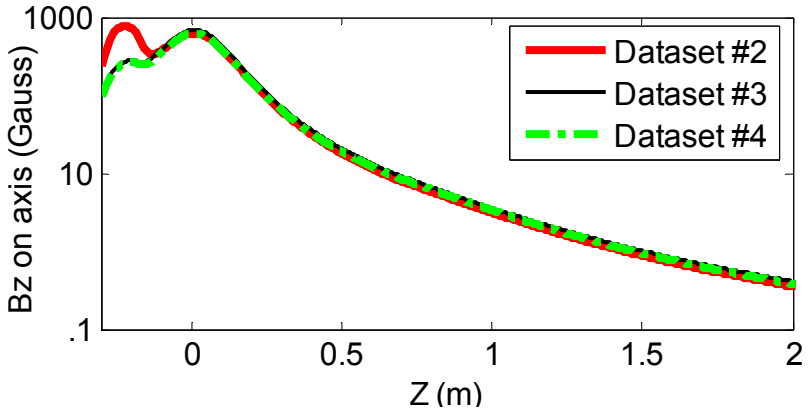

Figure 4.4: Comparison of the axial magnetic field for three of the data sets in Table 4.1.

Unlike the test conditions in Dataset #1 (Table 4.1) which has no current in the choke magnet, the choke magnet current in Datasets #2 thru #4 is quite high, with I_{choke} = 90 A-

100 A. This results in a high-field region underneath the choke magnet, and a peak magnetic field between 620 G (Datasets #2 and #4), and 680 G (Dataset #3). The nozzle coil currents resulted in straight diverging magnetic field lines until around z = 0.8 m at the farthest extent of nozzle coil #3. This nozzle configuration was the desired magnetic field configuration for the majority of plume profile measurements conducted in Section 4.1. The magnetic field strength on-axis and magnetic field contours for Dataset #3 are also displayed in Figures 3.3 and 3.4.

4.1.1 Density profiles

Density profiles were measured by a number of methods, at several axial positions. For hydrogen experiments, the scanning polychromatic interferometer produced a vertical density profile by Abel inversion at z = 0.33 m. This interferometer profile is the farthest upstream measurement that was collected in the DDEX experiment. Horizontal scans of Langmuir triple probes provided density profiles at z = 0.43 m, z = 0.90 m, z = 1.57 m and z = 1.85 m. Using the hybrid probe-interferometer theory developed in Section 2.3, accurate density profiles were produced from these scans.

Helium experiments also involved radial density measurements. Although Abel inversion was not attempted with the polychromatic interferometer using helium, horizontal triple-probe scans using the hybrid method produced accurate radial density profiles at z = 0.43 m, z = 0.90 m and z = 1.83 m.

Each of these profile scans suggested that density follows a Gaussian radial distribution that can be modeled by:

$$n(r,z) = n_{\max}(z)\, e^{\frac{-r^2}{2w^2}} = n_{\max}(z)\, 2^{\frac{-r^2}{R(z)^2}} \tag{4.1}$$

Here, two different methods of reporting the profile width are shown. $R(z)$ is the half-maximum radius, with plasma density at $r = R$ equal to half the maximum density. This convention is easy to apply experimentally and is therefore the method of choice for reporting experimental profile widths. A second convention is more often associated with statistical mathematics and uses the normal distribution. In this case the $1/\sqrt{e}$ radius = w corresponds to one standard deviation from the center of the normal distribution at a value equal to 61% of the peak.

Any error bars that are presented with experimental measurements in this work follow this statistical mathematics convention. The 2σ uncertainty terms that accompany experimental data represent a two-standard-deviation unit of error. Statistically speaking, 95% of repeated measurements will fall within this 2σ interval.

4.1.1.1 Abel inversion density profile

Line integral density was measured at z = 0.33 m by scanning the upstream polychromatic interferometer from y = -0.09 m to y = 0.09 m in 0.013 m increments. The experiment conditions for this test are listed in Table 4.1 as Dataset #2. As discussed in Section 2.2.4, the interferometer chord density $N_e(y)$ displayed a Gaussian profile in y which was fit to the following analytic function by the method of least squares:

$$N_e(y) = \left[C_2 \exp\left(\frac{-(y - C_3)^2}{C_1^2} \right) \right] \tag{4.2}$$

The C_3 vertical offset term is neglected from this analysis, as it can easily be re-introduced after the inversion process, but breaks the necessary condition of axisymmetry for the Abel integral. There was an apparent 2 cm shift vertical of centerline for the plume profile, which could be the result of a slight misalignment in magnetic field coils, or other asymmetry in the experiment setup. Figure 4.5 shows the interferometer chord density at multiple time steps, along with the appropriate Gaussian least-squares fit.

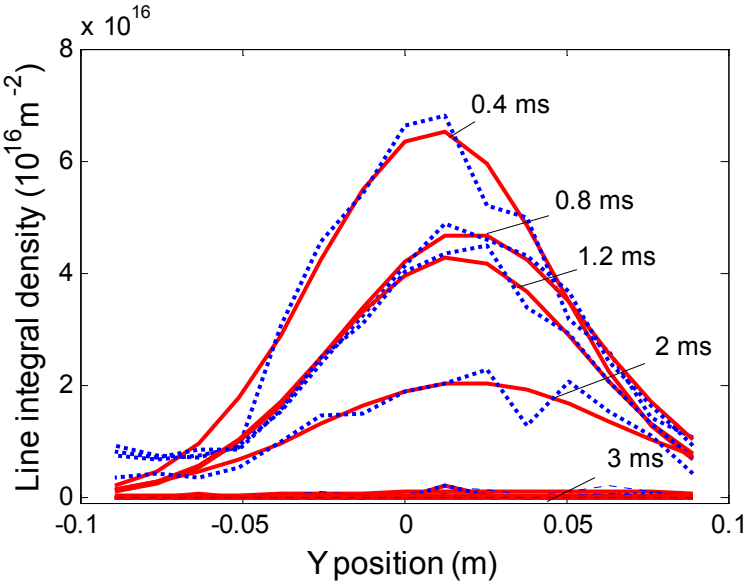

Figure 4.5: $N_e(y)$ interferometer line integral density with Gaussian best fit vs. interferometer Y location. Multiple plots show data at different time intervals during the shot, averaged over 0.2 msec. Note the approximate 2 cm offset in the plus-Y direction. Possible probe shadowing is present at y = 0.04 m.

The coefficients determined for the least squares fit of $N_e(y)$ to Eq. (4.2) are used in the equation for radial electron density $n_e(r)$ given in Eq. (2.39) and re-stated below:

$$n_e(r) = \frac{2C_2}{\pi C_1^2} \frac{C_1\sqrt{\pi}}{2e^{r^2/C_1^2}} Erf\left[\frac{\sqrt{a^2-r^2}}{C_1}\right] = \frac{C_2}{C_1\sqrt{\pi}} \exp\left[\frac{-r^2}{C_1^2}\right] Erf\left[\frac{\sqrt{a^2-r^2}}{C_1}\right] \qquad (4.3)$$

The resulting Gaussian radial profile is shown in Figure 4.6 and has a column half-maximum radius of 4.5 - 5 cm and a centerline density average of 1 x 10^{19} m^{-3}. Abel inversion requires axial symmetry, and thus the 2 cm vertical offset apparent in Figure 4.5 was manually removed from this plot. Error analysis was performed for the above measurement, and is detailed in Appendix B. 2σ uncertainty for the density amplitude is 16%. Likewise, 2σ uncertainty for the plume width is 13%.

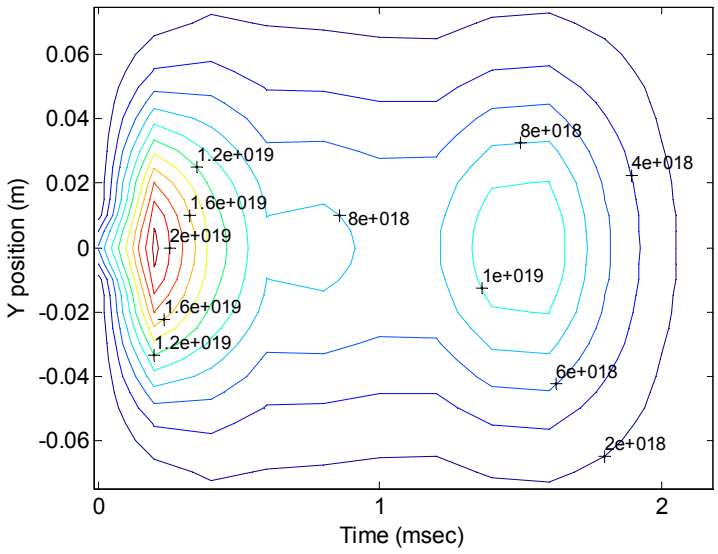

Figure 4.6: Vertical interferometer scan showing electron density in m^{-3} at z = 0.33 m. Abel inversion of 48 separate measurements produced a Gaussian distribution with half-maximum radius of 4.5 - 5 cm and centerline density average of 1x10^{19} m^{-3}. The initial transient response in the first 0.2 msec shows a density peak followed by a more stable discharge. A 2 cm vertical shift is not shown.

The time dependent profile width is plotted below in Figure 4.7. The profile closely follows a Gaussian distribution, the radius of which is given in Figure 4.7. After a 0.4 second startup, the plume reached a profile radius between 4.5 cm and 5 cm with a width uncertainty of 13%. Towards the end of the shot after approximately 2 msec, the peak centerline density decreases. The plume also expands, possibly due to collisional dissipation.

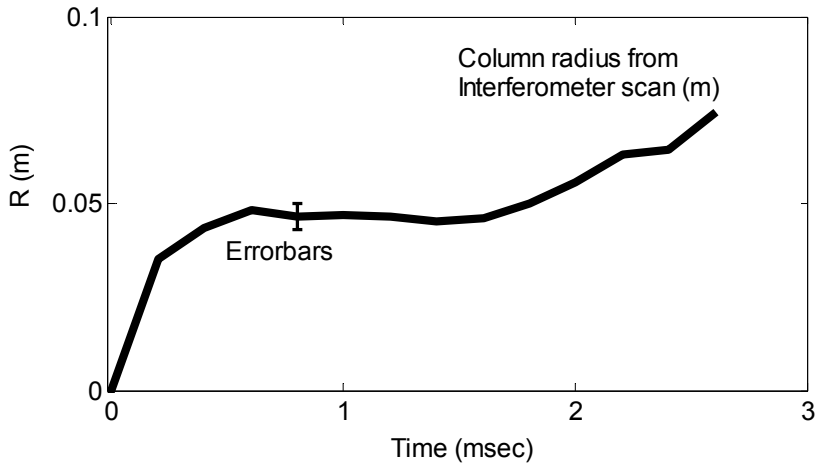

Figure 4.7: Half-maximum radius *R* is determined by fitting a Gaussian radial profile to the distribution *n*(*r*). Radius = 4.5 – 5 cm, from 0.4 – 1.6 msec. Error analysis suggests a 13% uncertainty in profile width.

This measurement suggests that during a shot, there is some time variation in the centerline density. During the shot, for the first 1.5 msec, the plume width remains constant within measurement uncertainty even though the centerline density changes by as much as a factor of 2. Also, the error bars on plume diameter are only 13% as opposed to the absolute density measurement error of 16%. Therefore the plume width is known to a higher accuracy than the absolute density. The Gaussian fit error is also low,

meaning that the plume can be described as a Gaussian distribution at this z = 0.33 m location.

In Figure 4.4, it is shown that the source magnetic field for Dataset #2 differs from that of Dataset #3. This difference primarily occurs between the axial positions of z = -0.3 m and z = 0 m, and thus does not represent a difference in the nozzle field, only in the plasma source. When comparing data between these three data sets, the magnetic field difference is assumed to have a negligible effect within the aforementioned 13-16% density measurement error bars. An argument can be made for this assumption by examining Figure 4.3 and noting that no significant plume diameter change occurred between an applied gun magnet current of 17 A and 30 A. It is possible that this plateau represents a lower plume diameter limit, in which case a further reduction of gun magnet current to 5 A would also yield no plume diameter change. In the absence of further experimental evidence, it is taken as an assumption that the plume conditions can be compared between Dataset #2 and Dataset #3 within measurement uncertainty.

4.1.1.2 Measurement of downstream plasma width using two interferometers

A method similar to Abel inversion was used downstream for determining density profiles. Rather than using multiple measurements from the same interferometer during subsequent shots, the downstream interferometer setup utilized two simultaneous independent chords. One chord was located on centerline, and the other was located 0.305 m below it. While two data points do not give a large statistical sample, this setup does give an estimate of plume size that can be compared with other methods.

As shown in Figure 4.10 and described by Eq. (4.1) the plasma density profile in DDEX is approximately Gaussian, with a varying width and peak density. A line integral of a Gaussian distribution is itself a Gaussian distribution with identical width. Thus, given two line integral density measurements: N_1 on the centerline and N_2 0.305 m below the centerline, the detected line integral density is:

$$N_2 = N_1 \, 2^{-\left(\frac{0.305}{R}\right)^2} \tag{4.4}$$

Solving for R yields

$$R = 0.305 \left(\frac{\ln 2}{\ln\left(N_1/N_2\right)} \right)^{1/2} \quad [\text{m}] \tag{4.5}$$

This method allows a measurement of the ½-maximum plume radius independent of the hybrid measurement technique. Experimental data using this technique will be presented in the following section (Figure 4.13) in addition to plume width measured with the hybrid method.

4.1.1.3 Hybrid density profile at z = 0.43 m

The hybrid density measurement method (Section 2.3) was applied to a plasma described in Dataset #3 of Table 4.1. Langmuir probe scans were conducted 0.1 m downstream of the polychromatic interferometer from x = -0.18 m to x = 0.10 m in 23 steps. The 0.28 m scan intercepted 91% of the line integral plasma density resulting in a peak density

measurement of $3x10^{18}$ m^{-3}. Figure 4.8 shows the resulting density map produced by the hybrid probe-interferometer technique. As was discussed in support of Eq. (2.48), a scan that only intercepts a portion of the line integral plasma density must include an adjustment term that is applied to the α proportionality constant. Error bar contours on the density measurement were determined by taking the $2\sigma_n$ confidence interval**,** shown in Figure 4.9, which gives a peak density uncertainty of $4x10^{17}$ m^{-3}. Details on the error analysis procedure are given in Appendix A. The relative error values $2\sigma_{n_i} / n_i$ are lowest along the centerline of the plasma column, at 9% -15% depending on the time in the shot. Relative uncertainty increases towards the plume edges and at the end of the plasma shot.

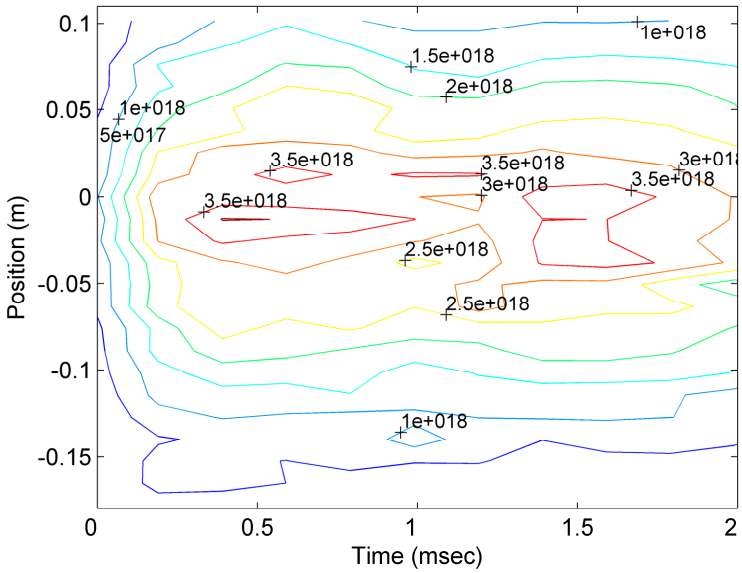

Figure 4.8: Horizontal (probe) scan showing plasma density at z = 0.43 m from 23 separate shots. Centerline density: $3x10^{18}$ m^{-3} with *R* half-maximum radius of 0.085 m.

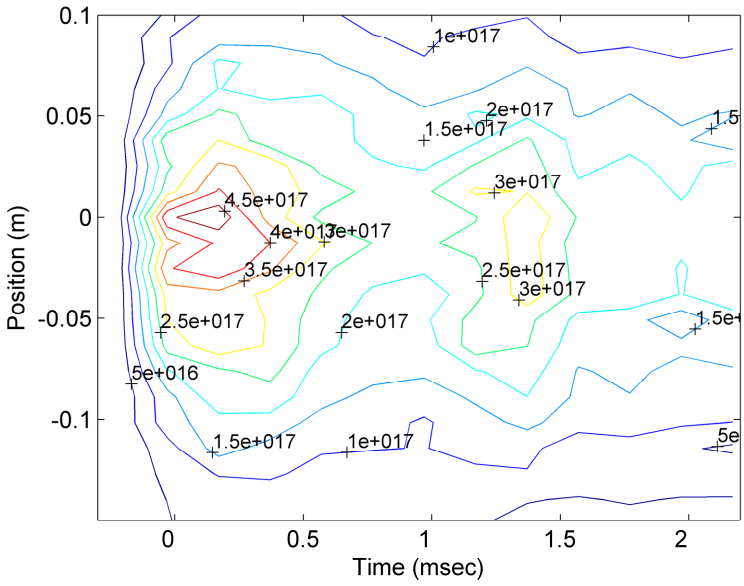

Figure 4.9: Magnitude of error for data plotted in Figure 4.8. Peak density error: 4×10^{17} m^{-3}. This includes the offset error σ_γ due to the 0.10 m probe-interferometer separation.

The plasma profile at time *t* can readily be fit to a Gaussian radial distribution in Eq. (4.1). A least-squares fit determines the Gaussian parameters by minimizing the density residue *Res*:

$$Res = \sum_{i=1}^{M} \left[n_i(t) - \tilde{n}\left(x_i; R(t); n_{\max}(t)\right) \right]^2 \tag{4.6}$$

with $R(t)$ equal to the plasma ½-maximum radius and $n_{\max}(t)$ equal to the centerline plasma density at time *t*. The upstream scan could be fit to a Gaussian distribution with an average RMS fit error of 2%, and a 0.085 m column radius at half-max. Uncertainty in the density measurements was used in a Monte Carlo analysis to determine error bars for the column width measurement, which is detailed in Appendix B. Error values of $2\sigma_w(t)$ = 8-10% are typical for the upstream scan. The radial profile data and associated

Gaussian fit for one point in time is shown in Figure 4.10. The overall profile width and goodness of fit to a Gaussian distribution for the entire shot is shown in Figure 4.11.

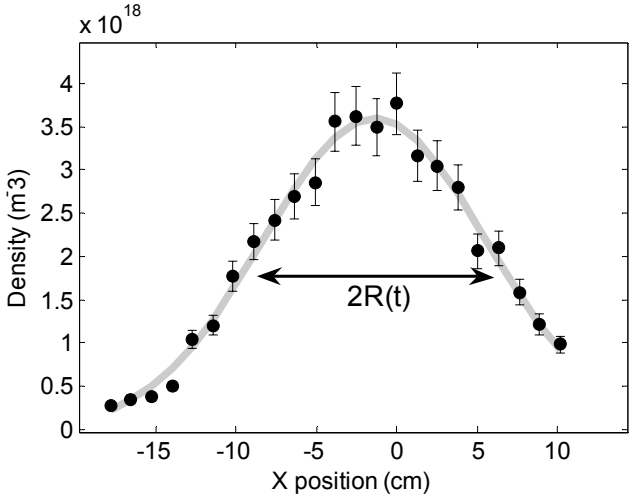

Figure 4.10: Z = 0.43 m density profile at *t* = 1.5 ms. $2\sigma_n$ error bars shown along with Gaussian least-squares fit and 2*R*(*t*) column diameter.

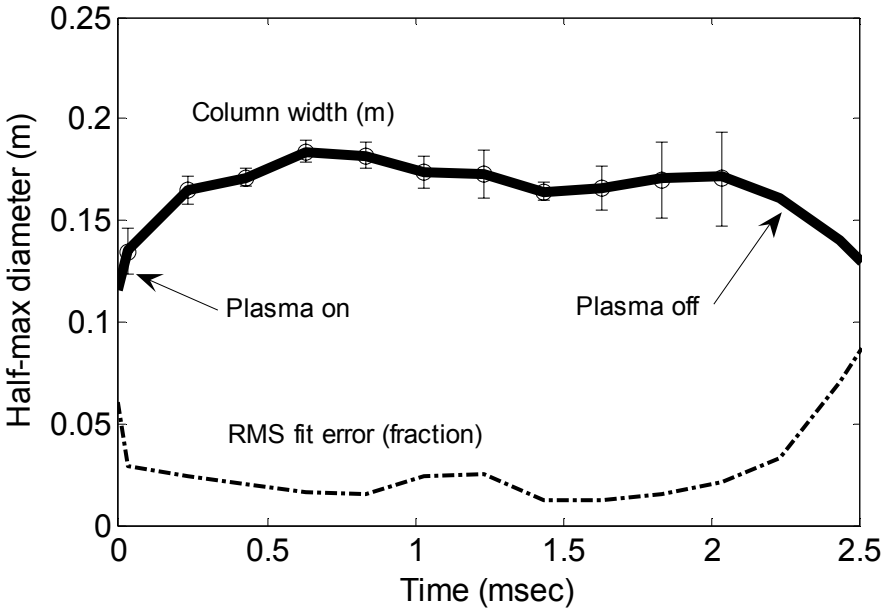

Figure 4.11: *Z* = 0.43 m column diameter 2*R* measurement vs. time. The plume averaged 0.17 m half-maximum diameter (solid) with a Gaussian fit residue of 2% (dashed). $2\sigma_w$ error bars were determined from Monte Carlo analysis.

In determining the upstream hybrid density profile, an offset correction to the line integral density was required. Two different plasma profiles were sampled, one by the Langmuir probe at z_2 = 0.43 m, where the hybrid measurement was made, and the other by the polychromatic interferometer at z_1 = 0.33 m. Ordinarily the plasma would be sampled at the same axial position by both instruments, as was accomplished at the downstream location. Here, the interferometer reading had to be adjusted to account for plasma expansion between the two instruments. For this purpose, an assumption of plasma flux conservation and constant velocity was made. The assumption of flux conservation and constant velocity is good within 20% as will be shown in Section 5.3. The contribution to the total error from these assumptions is considered below.

With this assumption, the line integral density ratio N_{z1}/N_{z2} is related to the column width and centerline density ratios as:

$$\frac{N_{z1}}{N_{z2}} = \frac{R_{z2}}{R_{z1}} = \sqrt{\frac{n_{\max,z1}}{n_{\max,z2}}} \tag{4.7}$$

where R_{z1} and R_{z2} are the widths of the Gaussian plasma column at axial locations z_1 and z_2 respectively, and $n_{\max,z1}$ and $n_{\max,z2}$ are the centerline plasma densities at z_1 and z_2. For the data presented here, R_{z1} is taken from the vertical interferometer scan described above.

For the uncertainty analysis, an additional independent error term may be included to account for this offset correction: $\sigma_{N_j}^2 \rightarrow \sigma_{N_j}^2 + \sigma_\gamma^2$. The offset error σ_γ is on the order of the overall measurement uncertainty (σ_n) and is included in Figure 4.9 and Figure 4.10.

The radial profile measurements conducted at z = 0.43 m confirm what was shown by the Abel inversion measurement at z = 0.33 m. The radial profile fits to a Gaussian distribution to within 2% for the first 2 msec of the shot. During this time, plume diameter remains relatively constant with width error at any given time at 8-10%. The plume width uncertainty is lower than absolute density uncertainty, which is $2\sigma_n / n$ = 10-15% for this scan.

4.1.1.4 Hybrid density profile at z = 1.85 m

Scans were also conducted at z = 1.85 m along the measurement chord of the centerline microwave interferometer from x = -0.46 m to x = 0.46 m in 13 steps. The plume conditions are still equal to those provided in Table 4.1 as Dataset #3. The 92 cm scan intercepted 79% of the line integral plasma density at that axial location with a peak centerline plasma density of 10^{17} m^{-3}. (Figure 4.12) Following the error analysis given in Appendix A, the $2\sigma_n$ density error bars for the downstream measurements equal ~20% along the centerline. The radial density profile fits to a Gaussian distribution with an RMS fit error of 4.8%, and a half-maximum column radius of 0.45 m.

As discussed in Section 4.1.1.2 the vertical density profile was monitored by a second interferometer chord, offset from the axial centerline by y = -0.3 m. The two separate

vertical measurements allowed an independent estimate of the plasma column diameter as described in Eq. (4.5). The $R(z)$ values from the two independent methods agree on average by 5%, as shown in Figure 4.13. Error bars on the downstream width measurement are larger than the upstream error bars on account of the greater uncertainty in the Gaussian fit and the absolute density. It should also be noted that in Figure 4.13, the probe scan shows an increasing plume diameter after 2 msec, while the two-interferometer comparison shows a decreasing plume diameter after 2 msec. This discrepancy can be explained by a decrease in measurement accuracy at lower plasma densities. At the downstream scan location, the probe-radius-to-Debye-length ratio r_p / λ_D is lower (<10) at the plume edge, and at the tail end of a shot. This exposes the probe measurement to non-ideal plasma conditions and yields an elevated density measurement due to orbit motion limited (OML) current collection as opposed to thin sheath current collection. This apparent enhancement is more pronounced at the plume edges where the density is low, therefore giving the appearance of a wider plume. The interferometer measurement method does not suffer from this non-ideal effect. Therefore, only the first 1-2 msec of plume measurements are considered for analysis where the two measurement methods agree, and any apparent disagreements after $t = 2$ msec are discounted.

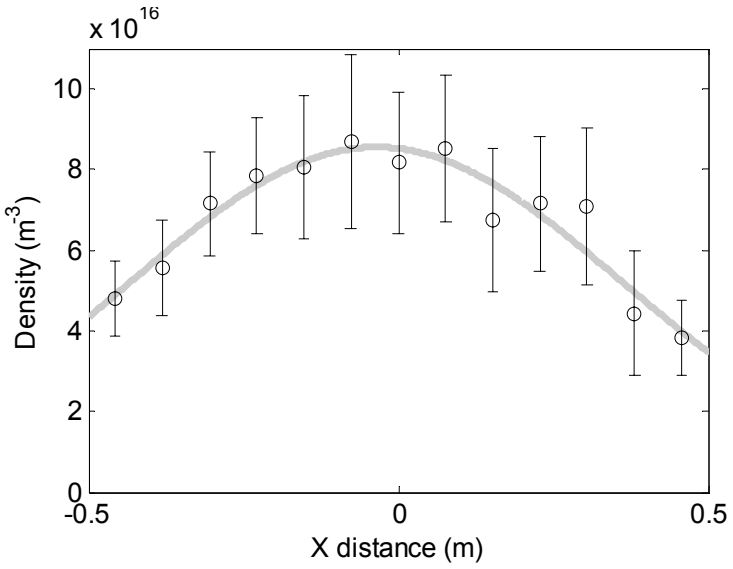

Figure 4.12: Density profile at z = 1.85 m, averaged over t = 0.5 – 1.5 msec. Average centerline density: 8.5 x10^{16} m^{-3}. Peak centerline density: 1x10^{17} m^{-3}. Error bars include $2\sigma_n$ density error and standard deviation error over 50 datapoints.

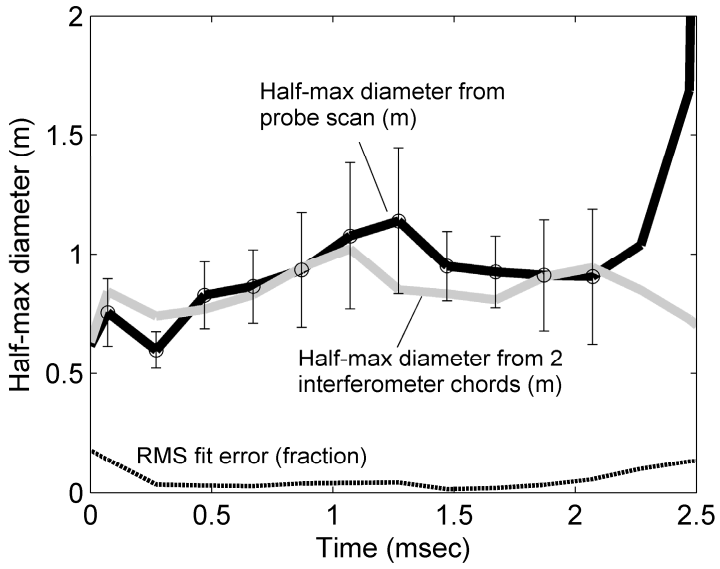

Figure 4.13: 2R plasma diameter at z = 1.85 m averaged 0.91 m. Two methods of plume width are compared: scan profile (black) and two-chord interferometer (grey). The profile shape was fit to a Gaussian with an average fit residue of 4.8%. $2\sigma_w$ plume width error bars were determined from Monte Carlo analysis.

4.1.1.5 Other hybrid density profiles

In addition to the above radial scans, a number of other profile measurements were conducted in a similar manner. Tables 4.1 and 4.2 summarize the results of the hybrid method scans for Dataset #3 and Dataset #4.

	z = 0.43 H	z = 0.90 H	z = 1.57 H	z = 1.85 H
Density (m^{-3})	$3x10^{18}$	$6.4x10^{17}$	$1.2x10^{17}$	$1x10^{17}$
R(z) radius (m)	0.085	0.188	0.41	0.45

Table 4.2: Scanning Langmuir probe results for hydrogen conditions given as Dataset #3 in Table 4.1. Density reported is the mean centerline electron density for hybrid probe-interferometer measurements. The profile width is reported as the plasma half-maximum radius.

	z = 0.43 He	z = 0.90 He	z = 1.85 He
Density (m^{-3})	$3.5x10^{18}$	$8x10^{17}$	$1x10^{17}$
R(z) radius (m)	0.095	0.19	0.50

Table 4.3: Scanning Langmuir probe results for helium conditions given as Dataset #4 in Table 4.1. Density reported is the mean centerline density for hybrid Langmuir probe-interferometer measurements. The profile width is reported as the plasma half-maximum radius.

The Table 4.2 radial profiles at z = 0.90 m and z = 1.57 m occurred farther away from the microwave interferometer than what was previously considered. The error for this density measurement is therefore greater due to the offset error σ_γ. The estimated density error for these two scan locations is 15-20% on the centerline. This falls in between the density error for the z = 0.43 m scan, and the z = 1.85 scan. The uncertainty in plume width measurement at z = 0.90 m and z = 1.57 m is also estimated at 15-20%,

which is midway between the plume width uncertainty at the farthest upstream and downstream measurements. The plume width and density measurements in Table 4.2 and Table 4.3 are to be used later in Section 5.1 as experimental verification of various magnetic detachment simulations, and summarize the plume trajectories for both helium and hydrogen operation.

Uncertainty for the helium data given in Table 4.3 is approximately equal to the uncertainty for hydrogen at the same axial position. This suggests that the relative 2-sigma error bars for z = 0.43 m measurements are a minimum of 10-15%, and 20% uncertainty at z = 1.85 m.

4.1.2 Triple probe electron temperature

Electron temperature was measured by a small scanning triple-probe for both helium and hydrogen shots (Dataset #3 and #4 in Table 4.1) throughout the course of the experiment. A vertical array of triple-probes also provided spatial temperature measurements on every shot. Temperature maps showed very little change in T_e as the probe position was changed. Triple-probe measurements close to the upstream polychromatic interferometer were the same as measurements taken farther back in the chamber, just as triple-probe measurements on the centerline of the chamber were identical to those taken at the plume edge. Plasma flow velocity may have had an effect on the T_e measurements, which is investigated by computer simulation in Section 4.1.3. These simulations suggest that a correction term based on probe diameter, probe bias and ion Mach number needs to be included in the standard triple-probe analysis. These computer simulations of biased

cylinders in a flowing plasma will be shown to suggest a temperature reduction of 14% for hydrogen triple-probe measurements, and a 8% reduction for helium measurements.

4.1.2.1 Scanning probe T_e measurement based on standard theory

The standard triple probe equation in Eq. (2.11) discussed in Section 2.1.2 was used to measure the electron temperature based on the triple-probe voltage $V_{12} = V_1 - V_2$. The helium conditions in Dataset #4 showed a constant electron temperature of 1.4 eV +/- 15% while hydrogen conditions in Dataset #3 showed a slightly lower electron temperature of 1.2 eV +/- 20%. These measurements are not adjusted for flowing plasma or sheath expansion effects, which are discussed later in Section 4.1.3. The error bars, however, are large enough to encompass uncertainty from these non-ideal effects.

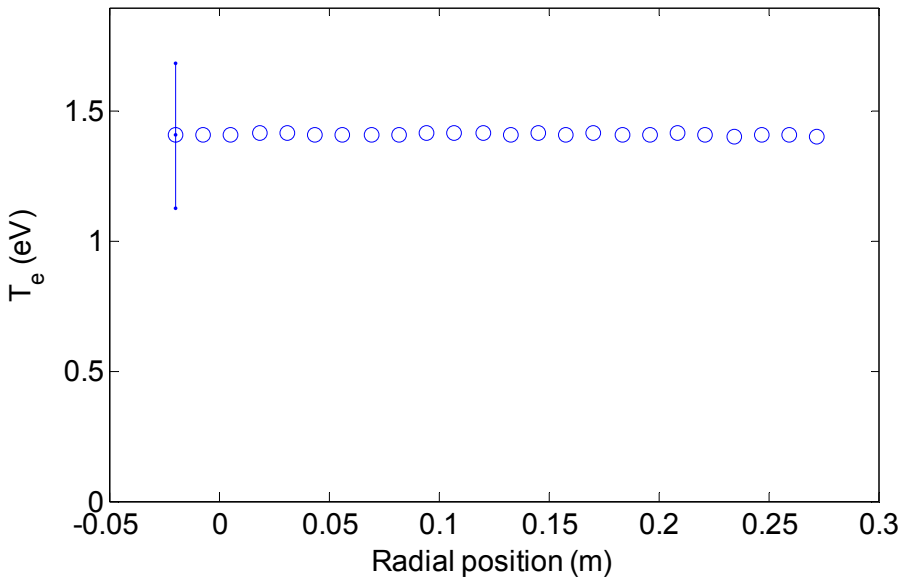

Figure 4.14: Helium radial T_e profile taken at z = 0.43 m. $T_e \sim 1.4$ eV. Error bars encompass a 8% reduction in temperature due to flowing plasma effects as discussed in Section 4.1.3.

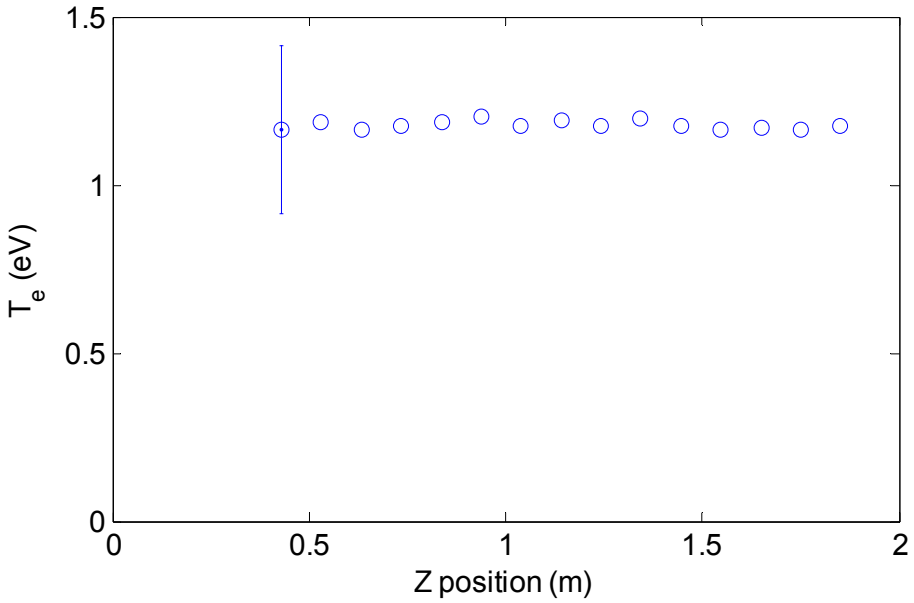

Figure 4.15: Hydrogen axial profile T_e ~ 1.2 eV. Error bars include a 14% reduction in temperature due to flowing plasma simulations as discussed in Section 4.1.3.

Error analysis was not performed in a typical statistical manner for this data because the shot-to-shot variation (random error) was much smaller than the estimated fixed error. In this case, the presence of flowing plasma and possible non-uniformity in the triple-probe collecting areas would lead to bias errors that are not apparent in shot to shot noise. An overall error of 20% for hydrogen measurements was determined from the RMS combination of ~15% uncertainty from flowing plasma simulations, and the 10% uncertainty normally associated with triple-probe measurements. [Ogram, 1979] Helium T_e measurements likewise have an overall uncertainty of 15% from the RMS combination of 8% uncertainty from flowing plasma simulations, and 10% uncertainty normally associated with triple-probe measurements.

4.1.2.2 Triple probe array T_e measurement

The vertical triple probe array was also used to measure electron temperature. The theory and methodology for this measurement is the same as for the radial scans produced with the small boom-mounted triple probe. However, the vertical array of six independent devices helps to eliminate errors due to potential fabrication mistakes in one particular instrument. In one particular helium shot, the electron temperature was simultaneously measured with the small scanning triple probe and the 6-element triple probe array. One probe array element at y = -0.19 m was not functioning due to a loose connection. The other 6 measurements are shown in Figure 4.16. As was shown in Figure 4.14, the electron temperature measurement for helium was 1.4 eV +/- 15%. One probe located at y = 0.19 m consistently under-reported electron temperature. This may be due to manufacturing error leading to a relatively larger collecting area for the positively biased pin, compared with the ion-collecting pin. Since different probes made measurements at different radial positions, the measurements shown in Figure 4.16 can be considered an indication that electron temperature is approximately constant with radial profile. This compares favorably with Figure 4.14 and Figure 4.15 to show T_e to be relatively constant with both radial and axial position.

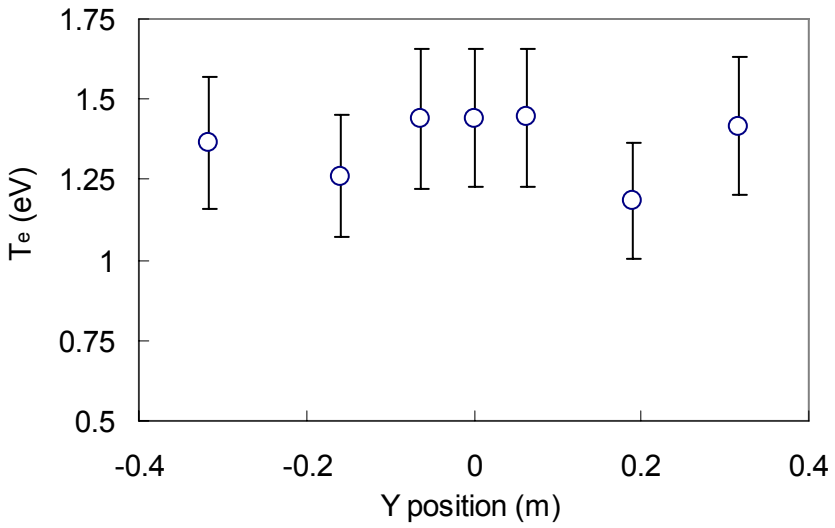

Figure 4.16: Helium T_e measurements taken with the vertical triple probe array at z = 0.90 m. The datapoint at y = 0 is the small triple probe used in Figure 4.14 and Figure 4.15. The probe element at y = 0.19 m consistently under-reported temperature.

In summary, the electron temperature was found to be uniform throughout the areas of the experiment that were measured, with standard triple probe analysis yielding T_e values of 1.2 eV +/- 20% for hydrogen, and 1.4 eV +/- 15% for helium. The experiment conditions for these two measurements correspond respectively to Dataset #3 and Dataset #4 in Table 4.1.

4.1.3 Non-ideal effects on T_e measurement

It has previously been found that an ion flow component can introduce significant errors in a triple probe's measurement of T_e. [Tilley, 1994] [Woo, 2006] This error was described in the original triple-probe method as an asymmetry in ion collection between the three biased probes due to growth of the ion sheath at large negative bias. [Chen,

1965] Since this experiment involves measuring electron temperature in flowing plasma, it is worthwhile to investigate the error introduced by the ion flow term and other non-ideal effects.

Analytical and experimental investigations have previously addressed this issue for collisional flowing plasma [Ogram, 1979], collisionless flowing plasma in the OML limit [Chang, 1977], and a directed ion beam on top of a non-flowing collisionless plasma. [Choi, 2006] For this experiment we consider the conditions of flowing collisionless plasma with electron Debye length λ_D smaller than the probe radius r_p. This condition is characterized by an asymmetric sheath structure surrounding the negative conductor, typically requiring computer simulation to accurately predict ion current collection.

Recent investigations into the collection of ion current to negatively biased cylindrical conductors have shown that rather than following a monotonic increase with increasing flow velocity, as was previously suggested [Laframboise, 1966] [Hoegy, 1973], the ion current follows a more complex non-monotonic relationship. [Xu, 1992] [McMahon, 2005] [Choinière, 2007] Using an iterative Vlasov and Poisson solver, detailed sheath structures around conducting cylinders have been simulated, and accurate ion current can be estimated. These recent advances in the simulation of ion current collected to a conducting cylinder in a moving plasma can be applied towards the configuration of a Langmuir triple probe to provide calibration factors for a range of ion flow conditions (M = 0-10) probe sizes (r_p / λ_D = 10-100) and voltage bias (ϕ = -5 – -20) where M is the ion

Mach number, $M = v / \sqrt{e(T_e + T_i)/m_i}$, r_p is the probe radius, λ_D is the Debye length and ϕ is the dimensionless probe bias V/T_e where T_e is in electron volts.

4.1.3.1 Triple probe simulation method

The numerical simulation tool KiPS-2D (Kinetic Plasma Solver 2d) has been developed to investigate charged structures placed in a flowing plasma. [Choinière, 2007] By iteratively solving the steady-state Poisson and Vlasov equations in the region surrounding probe geometries of interest, this computer code is able to simulate current collected to cylindrical conductors in a plasma environment. The adaptive mesh of KiPS-2D and its ability to run in parallel on many tens of LINUX workstations allows the accurate simulation of sheath structure and potential in a vast region surrounding any 2-D conductive object, and allows for non-dimensional potentials in excess of $\phi = V/T_e = 5000$. The KiPS solver and model has been validated against previous existing models in the low-voltage regimes where they overlap, and by high-voltage experiments involving conductive cylinders in flowing plasma. [Choinière, 2005] The unique high voltage range of this software was not required in the present simulation since probe biases were only investigated to $\phi_{13} = V_{13}/T_e = 40$. Only the lower voltage range of the KiPS code was utilized, which has been compared successfully with prior simulations and theory.

4.1.3.2 Modified triple probe T_e measurement theory

A modification can be made to Eq. (2.10) to account for deviation from ideal probe behavior. By introducing calibration factors h_1, h_2, and h_3 the new relationship between the three probe potentials is: [Chen, 1965] [Ogram, 1979]

$$\frac{1}{1+h_1\left(\phi_{13},\phi_{12}\right)}=\frac{1-\exp\left(-\phi_{12}\right)+h_2\left(\phi_{12}\right)}{1-\exp\left(-\phi_{13}\right)+h_3\left(\phi_{13},\phi_{12}\right)} \tag{4.8}$$

Where ϕ_{12} and ϕ_{13} are probe biases normalized by electron temperature in eV: $\phi_{13} = (V_1 - V_3)/T_e$, $\phi_{12} = (V_1 - V_2)/T_e$, and h_1, h_2, and h_3 are correction factors due to the difference between ideal probe current and actual probe current. In the ideal triple probe case, h_1, h_2, and h_3 become unity, zero, and zero respectively, and the triple probe equation reduces to Eq. (2.11). However, if the h correction factors are considered, Eq. (2.11) is not exact and Eq. (4.8) must be solved for T_e with the inclusion of nonzero correction factors. This yields an electron temperature adjustment of δ_T, where:

$$\phi_{12}=\ln 2\left(1+\delta_T\right) \tag{4.9}$$

It is the goal of simulations to determine the nonlinear temperature correction factor δ_T over the parameter space of interest.

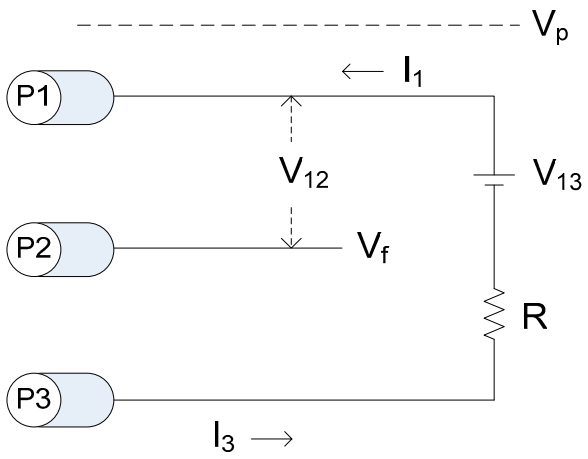

Figure 4.17 (same as Figure 2.2): Circuit schematic for Langmuir triple-probe. V_{12} is the floating probe measurement ≈ 1 V, and V_{13} is the supplied voltage bias, assuming a negligible voltage drop across R. V_p is the plasma potential, and V_f is the floating potential.

4.1.3.3 Flowing plasma simulations

Collection of ion current and electron current to the conductor is simulated for several bias conditions, Mach numbers and probe diameters. The magnetic field is assumed to be zero for all simulations. This is a valid assumption for the moderate B – field encountered here confirmed by a probe radius r_p smaller than the electron cyclotron radius r_{ce}. Figure 4.18 displays a typical trace of collected currents. Electron current collected to the probe follows an analytical profile with thermal electron current defined as [Hoegy, 1973]

$$I_e = \underbrace{S_p n_e q \left(eT_e / 2\pi m_e\right)^{1/2}}_{I_{the}} \exp\left(\phi\right) \tag{4.10}$$

where I_{the} is the thermal electron current collected at the plasma potential, and ϕ is the nondimensional probe bias with respect to the plasma potential < 0. Ion current I_i is simulated based on the KiPS-2D code [Choiniere, 2008] and summed with the electron current to determine the floating potential V_f where $I_e\left(\phi_f\right)+I_i\left(\phi_f\right)=0$.

The number of simulations and thus computation time is kept to a minimum by simulating fewer probe bias conditions and interpolating between the data points. The resolution is artificially increased by applying an exponential interpolation to I_e and a polynomial interpolation to I_i. Comparison with a case in which the data points are all simulated rather than interpolated shows an interpolation error of less than 1%.

The probe biases ϕ_{12} and ϕ_{13} are determined by iteratively solving for current collected at probes 1 and 3 until $I_{e+i}\left(\phi_f+\phi_{12}\right)+I_{e+i}\left(\phi_f+\phi_{12}-\phi_{13}\right)=0$ since the two probes are connected in series. Due to the much higher electron mobility, the positively biased Probe 1 is at a potential only slightly above the floating potential while the negatively biased Probe 3 is well below the floating potential of Probe 2. One sample I-V simulation used to determine triple-probe response is shown in Figure 4.18.

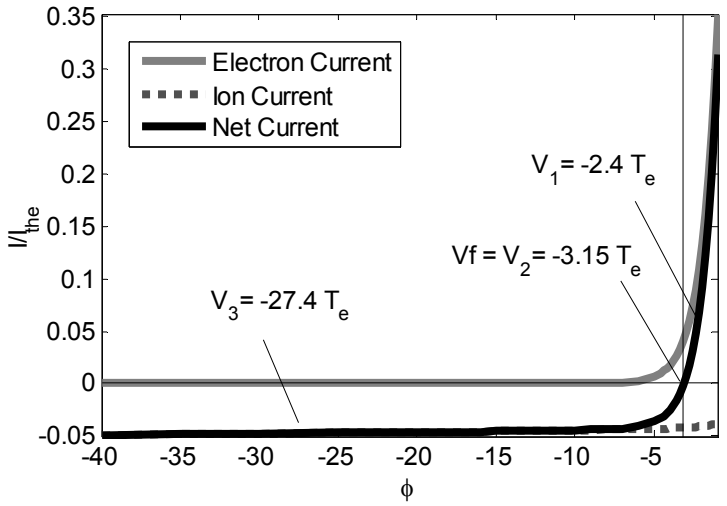

Figure 4.18: KiPS-2D simulation result showing ion and electron current collected vs. non-dimensional probe bias $\phi = V/T_e$. This representative simulation is for $r_p / \lambda_D = 105$, $M = 1.08$. Triple probe potentials V_1, V_2, and V_3 are shown on this curve for the condition $V_{13} = 25\ T_e$. V_{12} provides the T_e measurement.

The current collecting potential at probes 1 and 3 is thus determined by the probe bias ϕ_{13} and current conservation between the two probes. This fixes the voltage at probe 1 for a given ϕ_{13} and allows comparison with the floating potential $V_f = V_2$ to determine the unknown bias ϕ_{12}. It is this unknown bias that, via Eq. (4.9), determines the electron temperature correction factor δ_T.

4.1.3.4 Non-ideal results and discussion

Simulations were conducted for M = 0-3.5, r_p = 1-90λ_D and probe bias $\phi_{13} = V_{13} / T_e$ = 4-20. The triple probe response ϕ_{12} was found to vary widely from the ideal value of **ln** 2 based on the parameter varied. The probe bias ϕ_{13} contributes significantly to this variation, with ϕ_{12} increasing monotonically as probe bias ϕ_{13} increases. The response can be attributed to an expansion of the ion collecting sheath, resulting in increased

effective ion collection area vs. electron collection area. It should be noted here that this effect is pronounced for cylindrical probes and would be significantly less pronounced for flat-plate probes. This is shown by the temperature correction being greater for probes of small radius than for larger probes (Figure 4.19). Larger probes more closely approximate flat-plate collectors with a radius that is large compared with the sheath thickness. Plasma flow effects manifest themselves at small probe radius ($r_p < 30\ \lambda_D$) as well.

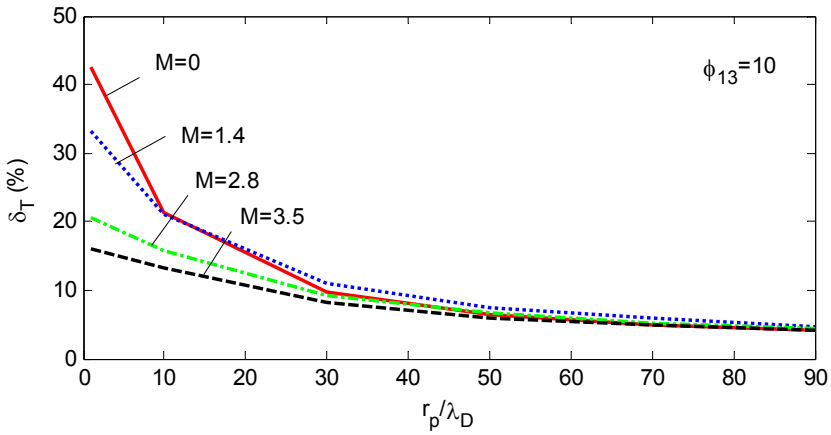

Figure 4.19: Temperature correction δ_t as a function of probe radius r_p/λ_d. Probe bias held constant at $\phi_{13} = V_{13} / T_e = 10$.

Given a large enough probe radius ($r_p > 90\ \lambda_D$) the temperature correction δ_T is less than 10% for any bias and Mach number up to $\phi_{13} = V_{13} / T_e = 20$ and $M = 3.5$.

The triple probe potential ϕ_{13} is plotted against ϕ_{12} / ϕ_{13}, the ratio of voltage response to applied voltage, in Figure 4.20. Three previously reported theoretical and experimental results are listed as well: ideal triple-probe results from (Chen, 1965), OML collisionless

results from (Kamitsuma, 1977), and flowing collisionless MPD thruster measurements from (Tilley, 1994). The simulation results can be fit to an expression of the form:

$$\phi_{13} = k_1 \left(\phi_{12} / \phi_{13} \right)^{-k_2} \tag{4.11}$$

where k_1 and k_2 are determined by the best fit, given r_p / λ_D and M constant. The goodness of fit is dependent on the simulation parameters and bias range, with most simulations fitting to ±1% for ϕ_{13} > 6. For the modest voltages considered here, the temperature calibration due to sheath expansion follows Eq. (4.11), so long as electron current is excluded ($\phi_{13} >> |\phi_f|$). The value of ϕ_{12} in these simulations is related to δ_T by Eq. (4.9).

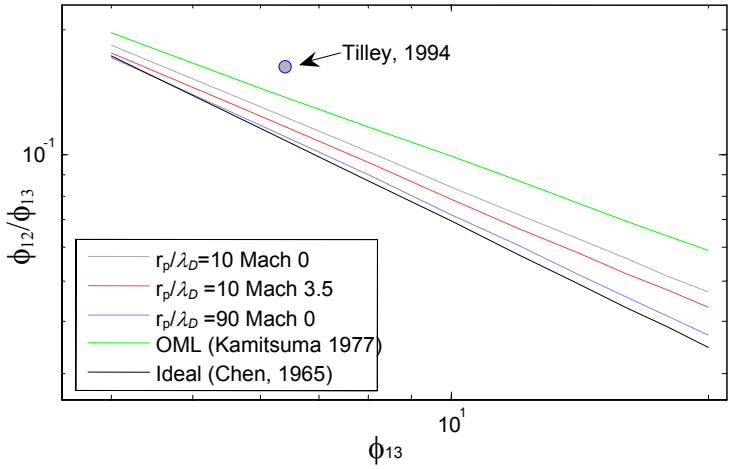

Figure 4.20: Electron temperature calibration for select conditions. Plot shows $\phi_{13} = \left(V_1 - V_3 \right) / T_e$, the nondimensional probe potential against ϕ_{12}/ϕ_{13}, the ratio of voltage response to probe voltage. (---): Orbit Motion Limited results from (Kamitsuma, 1977) for the conditions r_p / λ_D =0, M = 0 in a collisionless plasma. (---): Ideal triple probe results of Chen & Sekiguchi. (o): Experimental results of Tilley, 1994 for a high Mach number MPD thruster plume.

Non-flowing results are summarized in Figure 4.21 over a range of probe radii, r_p = 1-90 λ_D. The best-fit coefficients for Eq. (4.11) vary monotonically with probe radius r_p, with k_1 increasing from the orbital-motion limit value of 0.45 (Kamitsuma, 1977) to the ideal thin-sheath value of **ln** 2 (Chen, 1965), and with k_2 decreasing from 1.34 (OML) to 1 (thin-sheath). The goodness of the fit to Eq. (4.11) is ±1%, given ϕ_{13} > 6. The coefficients determined here by simulation precisely match values previously reported for non-flowing OML analysis of small probes (r_p < 1 λ_D) and approach ideal thin-sheath coefficients for the large probe condition (r_p > 100 λ_D).

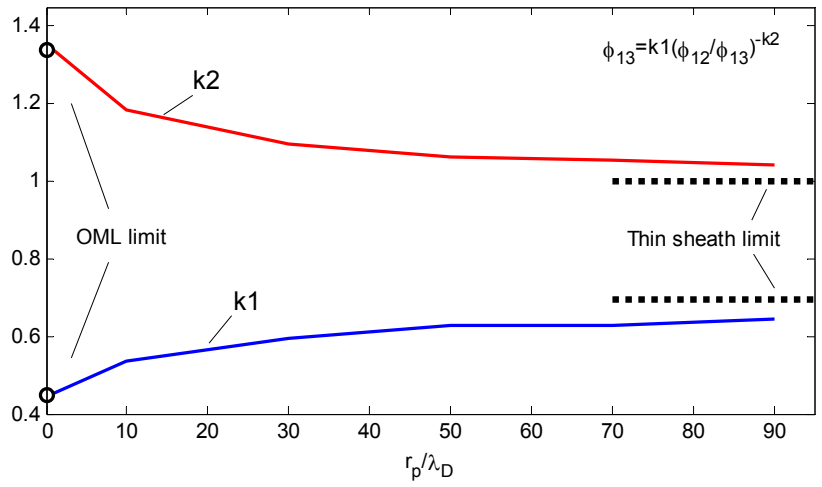

Figure 4.21: Simulated results of ϕ_{12}/ϕ_{13} for M =0, best fit coefficients to the equation: $\phi_{13} = k_1 \left(V_{12}/V_{13}\right)^{-k_2}$. OML limit results (circles) are from Kamitsuma, 1977. Thin sheath limit (dashed line) is from Chen & Sekiguchi, 1965. T_i / T_e = 1.

A finite plasma flow velocity U was introduced into the simulations to determine the effect on δ_T. As was also the case with non-flowing simulations, results are fit to Eq.

(4.11) within ±1% for $\phi_{13} > 6$. However, the dependence on M is non-monotonic, with δ_T increasing with M for $M < \sim 2$ and decreasing again for $M >> 1$. Similar behavior is seen in [McMahon, 2005] and [Choiniere, 2007] for ion current collected to conducting cylinders in flowing plasma. The behavior was previously reported for conditions of moderate probe size and plasma flow: $0.2 \lesssim r_0 \lesssim 50$; $M \lesssim 2$. Under these conditions, which are intermediate between orbital-motion-limited and sheath-area-limited current collection, the ion flow was found to introduce strong asymmetries in the sheath potential contributing to a ram-side compression of the sheath and a wake-side expansion of the sheath. McMahon *et al*. [2005] found that the effect of this sheath potential asymmetry on ion current is reduced as M increases, as the incidence angle of collected ions is reduced, and as the collected currents' dependence on electric field is thereby diminished. The effect this has on the temperature correction is to generally reduce δ_Γ for large $M > 2$. (Figure 4.22) For large M, current collection is dominated by ram current, which has the effect of reducing the disparity in electron current vs. ion current owing to ion sheath expansion. This can be seen in a reduced δ_Γ for high M. For $M \lesssim 2$, the effect of increasing Mach number appears to depend on r_p, since δ_Γ decreases with M for small r_p / λ_D, and slightly increases with M for larger r_p / λ_D.

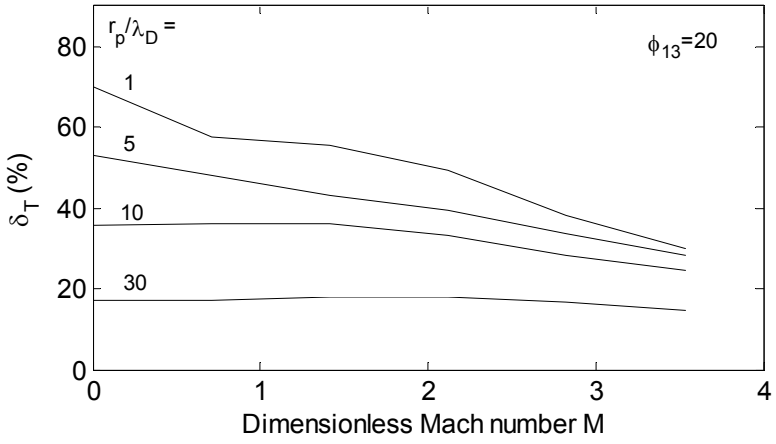

Figure 4.22: Temperature correction δ_Γ as a function of dimensionless Mach number $M = v/\sqrt{e(T_e + T_i)/m_i}$. δ_Γ decreases with M for $r_p \leq 5\ \lambda_D$, but the behavior is non-monotonic for $M \geq 10$.

k_1:	$r_p=1\lambda_D$	$r_p=10\lambda_D$	$r_p=30\lambda_D$	$r_p=50\lambda_D$	$r_p=90\lambda_D$
Mach 0	0.452	0.535	0.594	0.626	0.643
Mach 0.7	0.498	0.530	0.593	0.619	0.631
Mach 1.4	0.474	0.518	0.599	0.610	0.638
Mach 2.1	0.445	0.517	0.591	0.611	0.648
Mach 2.8	0.494	0.528	0.588	0.625	0.653
Mach 3.5	0.505	0.534	0.597	0.630	0.653

k_2:	$r_p=1\lambda_D$	$r_p=10\lambda_D$	$r_p=30\lambda_D$	$r_p=50\lambda_D$	$r_p=90\lambda_D$
Mach 0	1.34	1.18	1.10	1.06	1.04
Mach 0.7	1.27	1.19	1.10	1.07	1.05
Mach 1.4	1.28	1.20	1.10	1.08	1.05
Mach 2.1	1.28	1.19	1.10	1.08	1.04
Mach 2.8	1.21	1.17	1.10	1.06	1.04
Mach 3.5	1.18	1.15	1.09	1.06	1.04

Table 4.4: Fitting coefficients to $\phi_{13} = k_1\left(\phi_{12}/\phi_{13}\right)^{-k_2}$ for experiment conditions investigated. Goodness of fit is +/- 1% for $6 < \phi_{13} < 20$. Asymptotic values for large M and r_p / λ_D are $k_1 = \ln 2 = 0.693$ and $k_2 = 1$.

The fitting coefficients to Eq. (4.11) for several M and r_p can be seen in Table 4.4. A general trend can be seen at large M and r_p / λ_D for the k_1 and k_2 fitting coefficients to approach the thin-sheath limits of **ln2** and **1** respectively. For intermediate values of M, the trend is for the fitting coefficients to remain constant (within numerical uncertainty) or to diverge slightly, depending on the r_p / λ_D. Smaller r_p / λ_D appear to be more responsive to change in plasma flow velocity M due to the increased susceptibility to sheath asymmetry, as was found in McMahon, 2005. Uncertainty in these coefficients is estimated at 1% due to fit error. The percentage of error in a triple-probe temperature measurement δ_T can therefore be calculated for various values of ion Mach number M and probe radius r_p by using Table 4.4's values in Eq. (4.11) and Eq. (4.9).

4.1.3.5 Other uncertainties

The triple-probe schematic in Figure 2.2 includes a current sensing resistor R that was neglected in this analysis. The voltage drop over this resistor will affect the ion collecting probe bias ϕ_3, and can be modeled as a small uncertainty in the applied bias ϕ_{13}. As can be seen by the slope of Figure 4.18, a small increase in bias ϕ_{13} yields less than one percent of that increase in ϕ_{12}. We are therefore justified in neglecting resistor R in the analysis for small values of R.

In practical measurements, the temperature ratio T_i / T_e is often unknown. For the preceding simulations, only one case was studied: T_i / T_e = 1. According to the non-flowing analysis of [Kamitsuma, 1977], a reduction in T_i / T_e leads to enhanced deviation from the thin sheath ideal, similar to a decrease in M. However, the effect is limited, with

an assumption of T_i = 0 leading to only a 7% increase in δ_T for ϕ_{13} = 20. With the flowing plasma simulations of [McMahon, 2005], the ratio T_i / T_e was shown to have a greater effect, with a 15% change in the minimum ion current collected between the cases T_i / T_e = 1 and T_i / T_e = 0.5.

4.1.3.6 Experiment-specific simulations

Additional specific simulations targeted conditions relevant to the experiment's triple probe measurements: hydrogen plasma, $n_e = 3\text{x}10^{18}$ m^{-3}, T_e = 1 eV and v_i = 15 km/s. The cylindrical probe radius is r_p = 0.045 cm and the probe bias is V_{13} = -44V yielding a probe radius-to-Debye length ratio of r_p = 105 λ_D, an ion Mach number of M = 1.08, and a nondimensional probe bias of $\phi_{13} = V_{13} / T_e = 44$. These simulation parameters approximately correspond with experimental data taken with the scanning triple-probe on centerline at z = 0.43 m.

The simulations' values for δ_T in the flowing and non-flowing case provide a useful comparison with standard triple-probe theory. Including the ion Mach number M = 1.08 resulted in a correction coefficient of δ_T = 14%, suggesting that measured electron temperatures are artificially high in the presence of a flowing plasma. The non-flowing plasma simulation (M = 0) results in δ_T = 8%, suggesting a small correction factor is necessary even for a stationary plasma. Therefore, based on this analysis, the measured hydrogen electron temperature of 1.2 eV is too high by approximately 14% due to the influence of ion flow and sheath expansion. Accounting for these non-ideal effects, along with the 10% standard uncertainty for triple-probe measurements, [Ogram, 1979]

yields T_e error bars of 20%. Similar simulations of 1 eV helium plasma suggest correction factors of δ_T = 8% for v_i = 17 km/s flowing conditions. Combined with the standard triple-probe uncertainty of 10%, the result is helium electron temperature measurement of T_e = 1.4 eV +/- 15 %.

4.1.4 Ion velocity measurements

Measuring the axial component of ion velocity is important for several reasons. V_z is a term in the measurement of β, which determines the point of detachment for the exhaust plume. The axial velocity also contributes to the measurement of axial momentum, thrust and nozzle efficiency. Accurately knowing the ion velocity distribution is a key to understanding the performance of a thruster or magnetic nozzle. Highly accurate velocity measurements were not achieved in the DDEX experiment. However, time of flight velocimetry, Mach probes and Langmuir probes all gave corroborating estimates of the ion flow velocity with varying degrees of uncertainty as described below.

4.1.4.1 Time of flight velocimetry

Two separate time-of-flight campaigns were conducted. The first employed helium as a feed gas, and used both Langmuir probes and photomultiplier tubes (PMT) connected to a high-speed digitizer for time-of-flight measurements. The second campaign employed hydrogen as a feed gas, but only used photomultiplier tubes.

An axial scan was performed whereby the Langmuir probe time of flight probes were moved to different positions in the chamber while maintaining the same probe separation.

The time-of-flight measurement process is discussed in Section 3.2.7 The resulting velocity values for helium are shown in Figure 4.23. Langmuir probe time-of-flight measurement suggests an ion flow velocity of 14 km/s at the axial position z = 0.43 m increasing to v_i = 17 km/s at z = 1.85 m. The uncertainty in these measurements is 40%, obscuring any real axial trend in velocity. Further measurements and theory provided in Section 4.1.6 and Section 5.3 will suggest that the flow accelerates slightly (<30%) from z = 0.33 m to z = 1.85 m. This is not inconsistent with the Langmuir probe time-of-flight measurements given here in Figure 4.23 A second time of flight measurement was made using stationary photomultiplier tubes, showing an average v_i = 14 km/s. The mean flow velocity was measured between the two detectors, positioned at z = 0.329 m and z = 0.633 m. 2σ error bars were based on 9 separate shots and equal +/- 40% for the photomultiplier tube data.

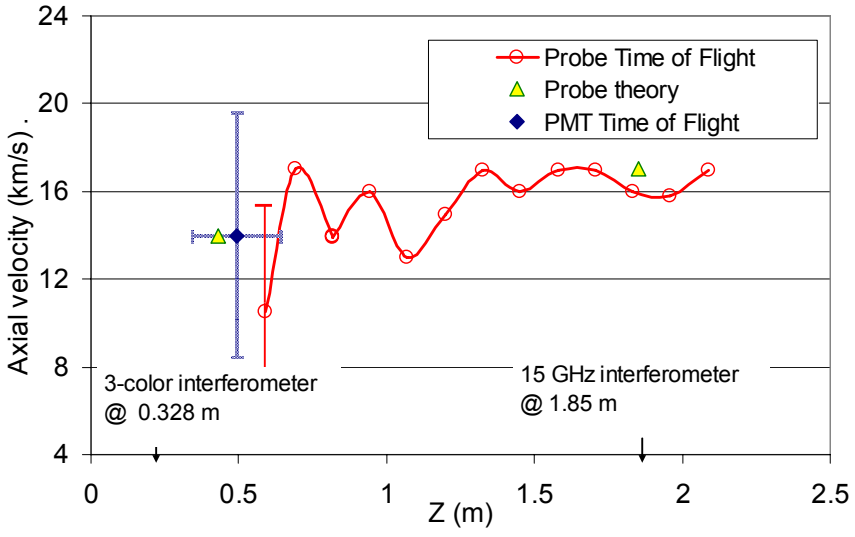

Figure 4.23: Helium ion velocity time-of-flight measurement, using photomultiplier tubes and separated Langmuir probes. 2σ error bars for probe time-of-flight is 40%. [Dobson, 2007] Probe theory velocity is discussed in Section 4.1.5.

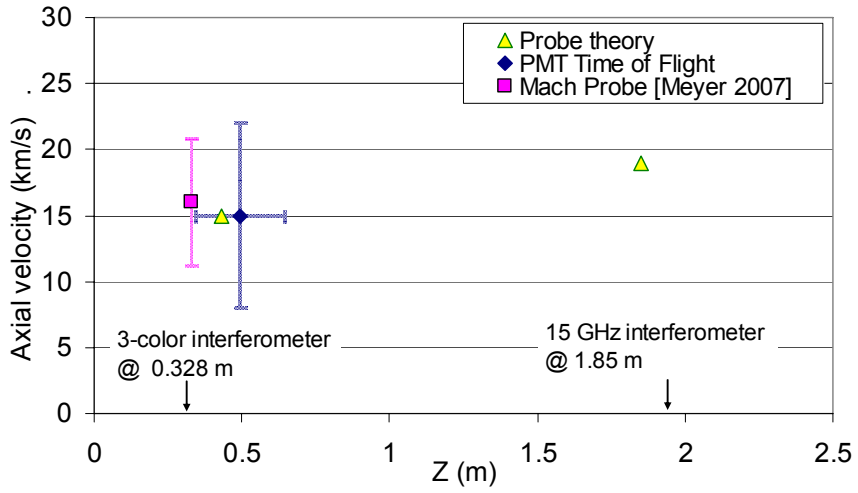

Figure 4.24: Hydrogen ion flow velocity based on photomultiplier time of flight and Mach probe measurement. No axial scan of velocity was performed. Probe theory velocity is discussed in Section 4.1.5. Mach probe data is discussed in Section 4.1.4.2.

The time of flight measurements conducted with hydrogen as shown in Figure 4.24 did not include an axial scan, and thus were only conducted with the stationary PMTs. The PMT time of flight measurements returned an average flow velocity of 15 km/s over seven measurements. The error bars for these measurements were considerably higher ~50% owing both to the higher flow velocity, and the greater standard deviation in measured velocities.

In summary, time of flight velocity measurements show that axial flow velocity for helium and hydrogen shots were between 10 km/s and 20 km/s with a possibility of a slight velocity increase with axial position. Error bars for this technique were large, but the results will be shown to be consistent with several independent velocity diagnostics.

4.1.4.2 Mach probe measurements

A Mach probe was also inserted into the plume to detect flow velocity at z = 0.33 m. Details on the data collection and analysis are given in [Meyer, 2007]. The results from this work are included in Figure 4.24 for comparison with other ion velocity measurements. Data suggests that the hydrogen plume was traveling with ion Mach number between M = 1 and M = 1.3. Given an electron temperature of 1.2 eV (and assuming $T_i = T_e$), this yields an ion flow velocity of 14 km/s – 19 km/s. The signal-to-noise ratio for this diagnostic was low, particularly for the downstream facing current collector. The error bars on the Mach probe measurement are estimated to be 30% due to the signal-to-noise ratio, and uncertainty in T_e, T_i, and γ. Helium measurements were not made with the Mach probe.

The measurement of v_z taken with the Mach probe falls within error bars of the time-of-flight velocity measurement described above.

4.1.4.3 Probe theory velocity measurement

According to Eq. (2.4), the first-order ion current collected to cylindrical probes is linear with n_i and v_i. Therefore, knowing the current response from a Langmuir probe and the plasma density at that location allows one to predict v_i. Likewise, predicting plasma density from probe theory requires an estimate of v_i. In Section 4.1.5 an independent estimate of plasma density is determined from probe theory, requiring estimates of v_i under those conditions. Based on velocity measurements from the Mach probe and time

of flight, the velocity values used for this Langmuir probe analysis are v_i = 14 km/s and 17 km/s for helium at z = 0.43 m and 1.85 m respectively, and v_i = 15 km/s and 19 km/s for hydrogen at z = 0.43 m and 1.85 m, respectively. The values are listed in Figure 4.23 and Figure 4.24 for comparison sake. These values for v_i are within the error bars of the other velocity measurements, and their use in Section 4.1.5 yields consistent density results, as will be discussed in the following section.

4.1.5 Langmuir Probe density profile

Probe theory can provide an independent plasma density measurement that can be compared with the hybrid method. Re-stating Eq. (2.4) we obtain ion saturation current I_i^{sat} in a flowing thermal plasma: [Hoegy, 1973]

$$I_i^{sat} = \frac{1}{\pi} S_p n_i q_i v_i \frac{h_s + r_p}{r_p}\left(1 + \frac{eT_e}{2m_i v_i^2} + \ldots\right) \tag{4.12}$$

As was discussed in Section 4.1.4, Mach probe and time-of-flight measurements give an estimate of the ion flow velocity. For hydrogen, the velocity was taken to be v_i = 15 km/s +/- 5 km/s at the upstream interferometer location increasing to v_i = 19 km/s +/- 6 km/s at the downstream interferometer location. As discussed in Section 4.1.2 the hydrogen electron temperature was determined by Langmuir triple-probe to be T_e = 1.2 eV +/- 0.2 eV throughout the exhaust region of the experiment. The probe sheath thickness h_s is determined by the matrix sheath equation in Eq. (2.2) to be ~ $8\lambda_D$ greater than the probe radius. Figure 4.25 gives a comparison of Eq. (4.12) (probe theory alone) with the hybrid

analysis using both upstream and downstream RF interferometers. At both measurement locations, probe theory alone provided densities 50% lower than the hybrid analysis, with an even greater discrepancy at lower density values. The discrepancy is possibly due to an over-estimate of ion collection area or over-estimate of ion flow velocity, but this result is consistent with previously under-reported density values when comparing electrostatic probes with interferometer measurement. [Kinderdijk, 1972], [Overzet, 1993]

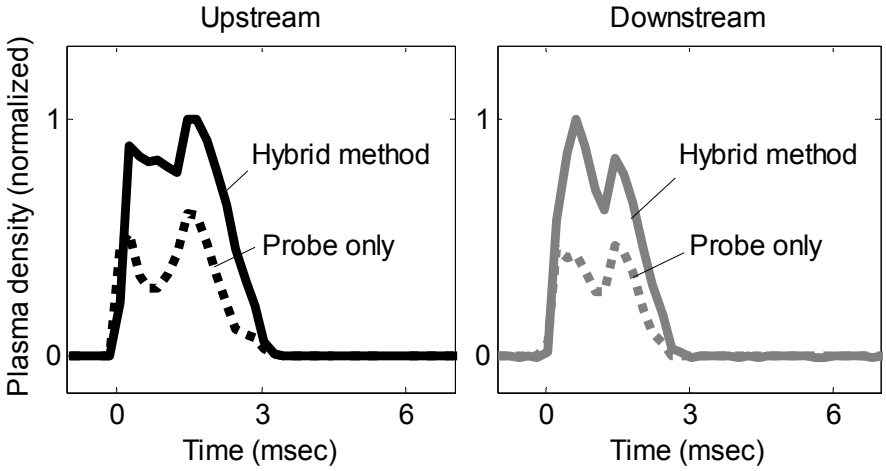

Figure 4.25: Comparison of hybrid density measurements with Langmuir probe density measurements. The curves marked "Probe only" are from Eq. (4.12), relative to the hybrid density measurement. Comparison shows that probe theory alone under-predicts plasma density by 50%.

The same procedure was repeated for helium shots, using the flow velocity suggested by time of flight analysis: v_z = 14 km/s +/- 5 km/s and 17 km/s +/- 5 km/s at the positions z = 0.43 m and z = 1.85 m respectively. Also, as was discussed in Section 4.1.2, an electron temperature of T_e = 1.4 eV was used. The probe sheath thickness h_s is found by the matrix sheath assumption to be ~ $4.5\lambda_D$ greater than the probe radius. Figure 4.26

compares the density predicted by probe theory with the hybrid theory results. As in the hydrogen case, probe theory alone under-predicts helium density- by 40% upstream and 60% downstream.

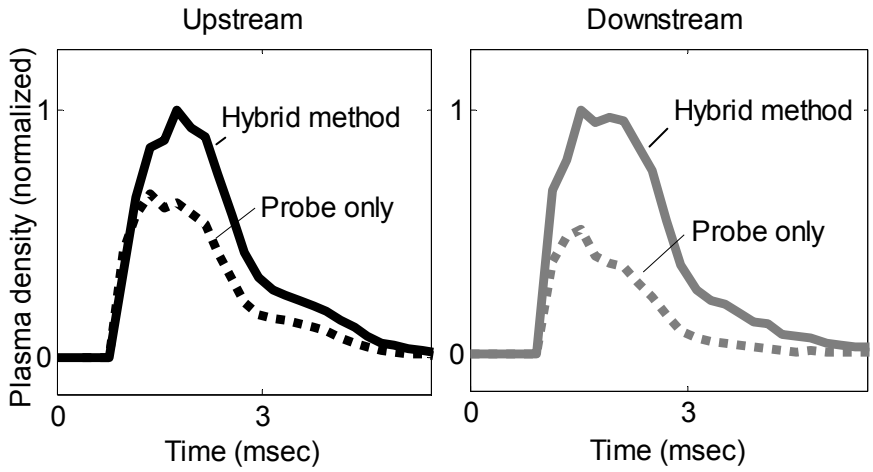

Figure 4.26: Helium probe theory at the upstream and downstream interferometer. Comparison with hybrid method suggests that probe theory alone under-predicts plasma density by 40%-60%.

The above comparisons highlight the difficulties in achieving accurate density measurements from probe theory alone, particularly when electron temperature and flow velocity measurements have significant uncertainty. Interferometer-compensated hybrid analysis is expected to have much reduced uncertainty because it is insensitive to such factors as ion flow velocity, electron temperature, probe surface area, and current sensing electronics gain.

Although density measurements were not in exact agreement between the probe theory and the hybrid probe-interferometer method, the results show that the probe density

measurement is consistently ~50% lower than the hybrid density measurement over four different plasma conditions. This consistency suggests that a bias error may be present in the measurement, e.g. a wrong assumed probe diameter, resistor value etc. that equally affects all measurements. Again, the velocity values needed to obtain these consistent results were v_z = 15 km/s and v_z = 19 km/s at z = 0.43 m and z = 1.85 m, respectively for hydrogen. The velocity values used to obtain consistent probe density results for helium were v_z = 14 km/s and v_z = 17 km/s at z = 0.43 m and z = 1.85 m, respectively. These probe theory velocity values are within the error levels of the other velocity measurements in Figure 4.23 and Figure 4.24, and are listed as "Probe theory" in these two figures. These data points are not an independent measurement of velocity, which explains why they do not have associated error bars. The data points merely document the flow velocity values used in this section to find density values from probe theory.

4.1.6 Flux conservation measurements

Mass conservation requires that ion flux is conserved over two surfaces A_1 and A_2 perpendicular to the axis: $\int_{A_1} n_i q v_z \, dA = \int_{A_2} n_i q v_z \, dA$. Simultaneous interferometer measurements give a line integral of the electron density arriving at the two interferometer axial locations: z = 0.33 m and z = 1.85 m. While the interferometers don't directly give area integral density, the aforementioned probe scans have provided profile shape and width information required to extract 2D area integrated density. Integrating Eq. (4.1) in 1D yields:

$$N(z) = \int_{-\infty}^{\infty} n_{\max}(z)\, 2^{\frac{-r^2}{R(z)^2}} dx = n_{\max} \sqrt{\pi \left(\ln 2\right)^{-1} R(z)^2} \tag{4.13}$$

while integrating Eq. (4.1) in 2D over a surface perpendicular to the axis yields:

$$\begin{aligned}\int n_i \, dA &= \int_0^{2\pi} \int_0^{\infty} n_{\max} \, r \, 2^{\frac{-r^2}{R(z)^2}} dr \, d\phi \\ &= n_{\max} \pi \left(\ln 2\right)^{-1} R(z)^2 = N(z) \sqrt{\pi \left(\ln 2\right)^{-1} R(z)^2}\end{aligned} \tag{4.14}$$

Thus area integral density is determined by $N(z)$ line integral density and $R(z)$ profile width, assuming axisymmetry and quasineutrality ($n_i = n_e$). By comparing $\int n_i \, dA$ at two axial locations, one of two measurements can be made: 1.) the acceleration of flow $\dot{v}_z$ assuming flux conservation, or 2.) the degree of flux conserved in the experiment assuming constant velocity v_z. A comparison of the total integrated density as measured by the two interferometers in this experiment located at z = 0.33 m and z = 1.85 m is shown in Figure 4.27.

The density integral $= \int n_i \, dA$ at the downstream interferometer was found to be 10%-30% lower than at the upstream interferometer for hydrogen shots. The density decrease was particularly apparent at the beginning of a shot. A possible explanation for this downstream plasma density decrease could be the influence of collisions between ions and neutral gas, or plume impingement upon diagnostic probes and other structures in the plume leading to a loss of plasma flux. An alternative explanation is that the flow velocity increased by 10-30% between the two positions. This acceleration would lead to a decrease in density due to flux conservation. In all likelihood, a combination of the two factors is occurring since loss of plasma flux is a definite possibility, but some indication of velocity increase was previously shown in Section 4.1.4. Since the flow velocity v_i

was not measured within 30% at the two interferometer positions, no definite distinction can be made between the two explanations for the drop in density.

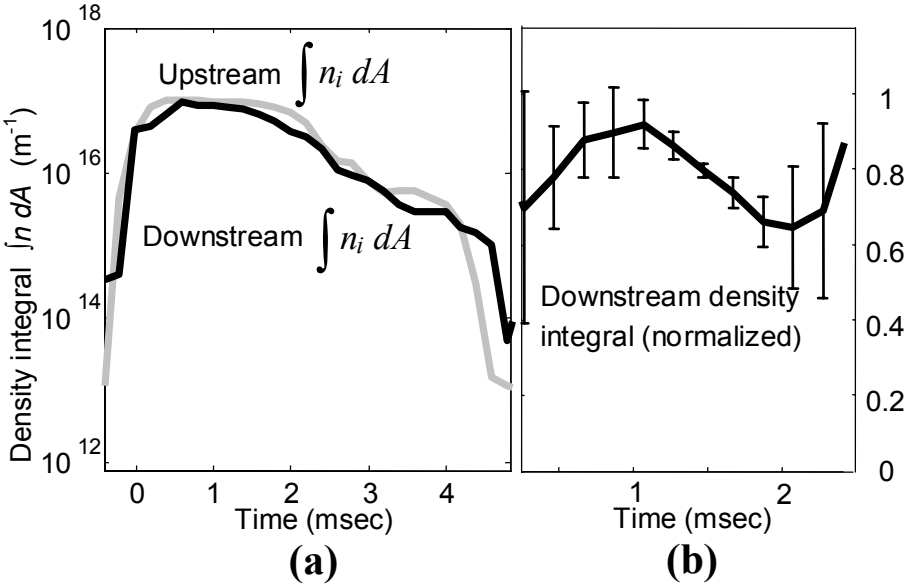

Figure 4.27: a): $\int n_i\, dA$ at two interferometer locations: z = 0.33 m and z = 1.85 m. Density integral determined from interferometer measurement and profile width. b): $\int n_i\, dA$ at z = 1.85 m, normalized to upstream measurement. 70%-90% total density conserved for most of the shot.

The same process is repeated for helium data with both upstream and downstream interferometer measurements. The z = 1.85 m profile radius R(1.85 m) was measured to be 0.50 m, and the upstream profile radius R(0.33 m) was taken to be 0.055 m. The upstream radius had to be extrapolated from measurements at z = 0.43 m because unlike the hydrogen experiments, helium experiments did not provide an interferometer scan and Abel inversion at z = 0.33 m. As will be shown in Section 0, the simulated plume radius for helium is 1 cm larger than the hydrogen plume at z = 0.33 m. This is consistent with measured plume radii at z = 0.43 m. Figure 4.28 shows a comparison of total integrated density for helium at both the upstream and downstream location.

The resulting comparison of upstream vs. downstream density integral for helium again provides an estimate of flux conservation, or flow acceleration. Like the hydrogen results, there is a slight decrease in overall density at the downstream location with 80% - 95% of the total density recorded. Assuming flux is conserved, this is consistent with a flow acceleration of 5% - 20%. Assuming constant velocity, the same data suggests that 5%-20% of the total ion flux is lost. Considering the error bars of both interferometer density measurements, and considering the assumed column radius at the upstream location, it is inconclusive which one of these conditions is occurring. However, a slight increase in flow velocity would be consistent with time-of-flight measurements and the flux probe measurements in Figure 4.23.

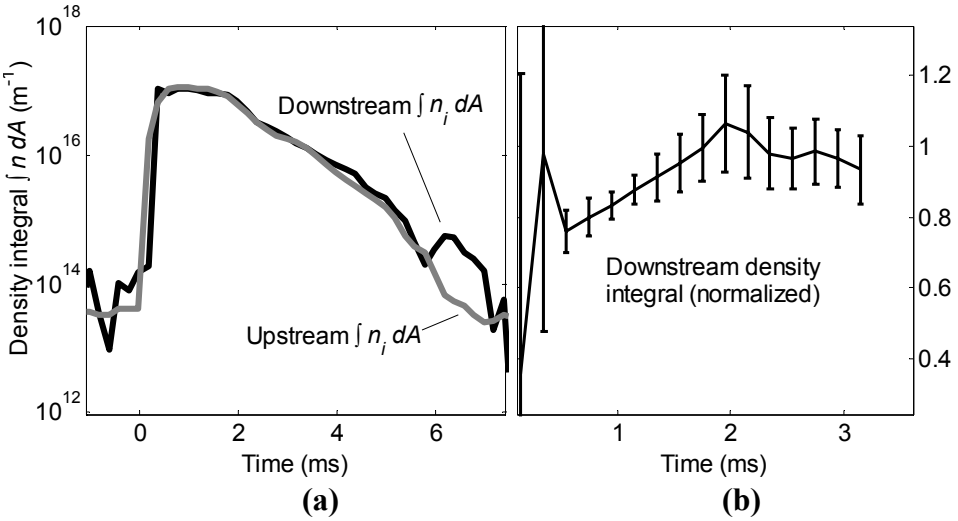

Figure 4.28: Helium interferometer measurements showing 2D integral of density at z = 0.33 m and z = 1.85 m. Plot (b) shows a ratio of downstream to upstream density integral, suggesting that 80%-95% of total density is conserved, consistent with a slight acceleration in axial velocity.

4.1.7 Ion gyroradius

It has been suggested that a plasma plume's radius must be greater than the local ion gyroradius for that plasma to be confined and directed by a magnetic nozzle. [Hooper, 1993] This alternate condition for magnetized plasma is expressed by the following relationship:

$$r_{ci} \equiv \frac{v_{\perp,i}}{\omega_{c,i}} = \frac{m_i}{qB}\sqrt{\frac{T_i}{m_i}} < r_p \tag{4.15}$$

Investigating this value is important to show that any measured detachment from magnetic fields was not caused by a breaking of this alternate magnetized plasma condition, instead of $\beta > 1$ detachment. Although we do not have values for T_i or r_p at all points in the experiment, we can make a worst-case estimate that ensures the condition in Eq. (4.15) is met for all regions of interest. Using $T_i = T_e$ is a high estimate for T_i and gives an upper bound to what ion temperature can achieve. Since no better estimate of T_i is available, this value will be used. Also, defining r_p by the half-maximum radius $R(z)$ of the plasma is a conservative measure of the plume width since only half of the Gaussian distribution would be accounted for. The more appropriate value would be $r_p = 2w$, which accounts for 95% of the distribution. (in accordance with Eq. 4.1) Given these two caveats, Figure 4.29 gives a comparison of r_p and r_{ci} for a 1.5 eV hydrogen plasma (which is itself an upper estimate of electron temperature). The plume radius was determined by the method described in Section 0, resulting in $r_p = r_{ci}$ at z = 1.0 m. Therefore, the above-mentioned condition of $r_p > r_{ci}$ holds until at least z = 1.0 m, and probably further due to the conservative estimates of T_i.

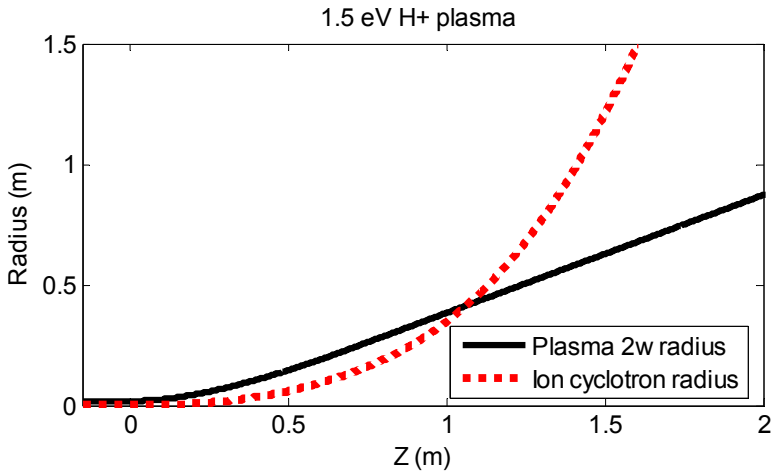

Figure 4.29: Comparison of ion gyroradius and plasma radius for hydrogen plasma. r_p and r_{ci} cross at z = 1.0 m. $T_i = T_e$ = 1.5 eV.

4.1.8 Experimental measurement of Beta

Like the measurement of ion gyroradius, an estimate of plasma Beta requires several assumptions since not all parameters were measured everywhere in the experiment. Looking at Eq. (2.52), and re-stated in (4.16) the crucial measurements to determine β are n_i and v_i given that B is known.

$$\beta = W_k / W_B = m_i n_i \mu_0 v_i^2 / B^2 \tag{4.16}$$

From Section 4.1.4 we have an estimate of v_i = 10 km/s – 20 km/s depending on the gas species and the measurement location. For simplicity's sake, a constant velocity of 14 km/s will be used for helium and 15 km/s will be used for hydrogen. Density

measurements are given in Tables 4.1 and 4.2. Given those inputs, along with a numerical model for magnetic field, β can be estimated at the centerline of each of the probe scan locations:

	z = 0.33 m	z = 0.43 m	z = 0.90 m	z = 1.57 m	z = 1.85 m
Hydrogen	β = 0.15	β = 0.16	β = 1.3	β = 7.5	β = 16
Helium	N/A	β = 0.64	β = 5.7	N/A	β = 57

Table 4.5: Estimate of centerline plasma β at the locations included in radial scans. N/A indicates that plasma density was not measured at this location.

The above table gives an approximate location at which the flow begins to experience magnetic detachment effects. The centerline β is greater than unity once the axial position z = 0.9 m is reached, suggesting that by this location in the experiment, the plume should begin to be detached from the influence of applied magnetic fields. Uncertainty in the flow velocity, and radial variations in density may move the initiation of $\beta > 1$ detachment upstream or downstream. Certainly by the time the plasma flow reaches z = 1.85 m, it is (theoretically) well beyond the influence of applied fields since β = 16 and β = 57 for hydrogen and helium flows, respectively.

Considering the full extent of the hydrogen flow velocity error bars: 15 km/s +/- 4 km/s, the plasma β on centerline will always reach unity before the ion gyroradius exceeds the $2w$ plasma radius. This is an important consideration because these are both potential, competing conditions for the plasma to become de-magnetized. In order to differentiate between the two conditions, the plasma flow must achieve $\beta > 1$ before $r_{ci} / r_p > 1$.

4.1.9 Cross-magnetic field diffusion regime

As was discussed in Section 2.4.3, the diffusion rate at low magnetic fields follows classical diffusion scaling. For greater magnetic field strength, cross-field diffusion is enhanced by convective motion. The enhanced diffusion regime is a bridge between classical diffusion and Bohm diffusion and according to Eq. 2.58 the onset of enhanced diffusion occurs at:

$$B \leq \left(\frac{n_e m_e}{\varepsilon_0} \right)^{1/2} \left(\frac{\varepsilon_0 T_e}{e^2} \right)^{1/3} \tag{4.17}$$

Figure 4.30 shows the diffusion regime encountered in the experiment, according to centerline plasma density and applied magnetic field. It is clear from this figure that the peak magnetic field in this experiment is almost two orders of magnitude below what is required to produce enhanced diffusion. Therefore, cross-magnetic field diffusion occurs according to classical diffusion in this experiment.

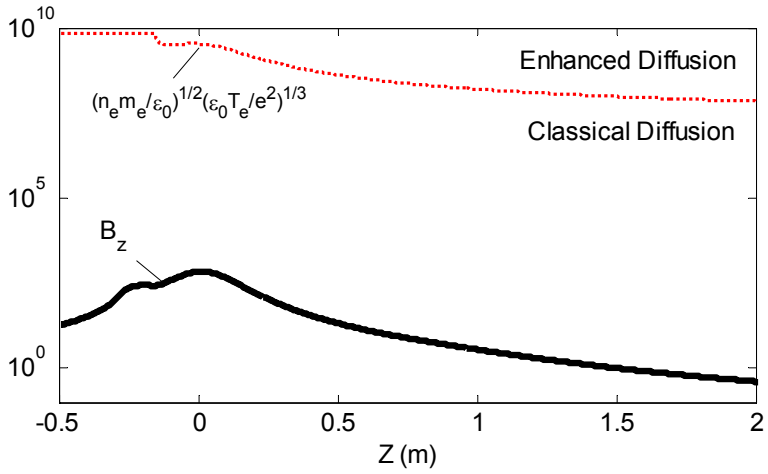

Figure 4.30: Cross-magnetic field diffusion regime for the plasma plume according to the limit condition in Eq. (4.17). Measurement according to centerline plasma density and applied magnetic field shows that the experiment meets the criterion for classical diffusion.

4.2 Reversed magnetic field experiments

An interesting study was conducted wherein the nozzle coil currents were reversed, providing a region of reversed magnetic field in the experiment. [Deline, 2006] The main choke magnet was held at +100 A, but the three nozzle coils wrapped around the spool piece were held at –40 A, -20 A and –20 A respectively. The reverse current configuration led to zero magnetic field strength on-axis after the magnet coils. (Figure 4.31) This resulted in lines of constant magnetic flux being discontinuous between the region of plasma production, and the downstream plasma diagnostics. (Figure 4.32) In the reverse field experiment, plasma would never reach the downstream measurement area if it were to completely follow lines of constant magnetic flux. If any plasma exhaust were to be detected in the downstream measurement area, this would suggest that stretching or breaking free from applied magnetic fields was occurring.

	I_gun	I_choke	I_noz #1	I_noz #2	I_noz #3
Config. A	5 A	100 A	10 A	3 A	3 A
Config. B	5 A	100 A	0 A	0 A	0 A
Config. C	5 A	100 A	-40 A	-20 A	-20 A
Config. D	5 A	100 A	+40 A	+20 A	+20 A

Table 4.6: Magnetic coil conditions for the reversed-field experiment

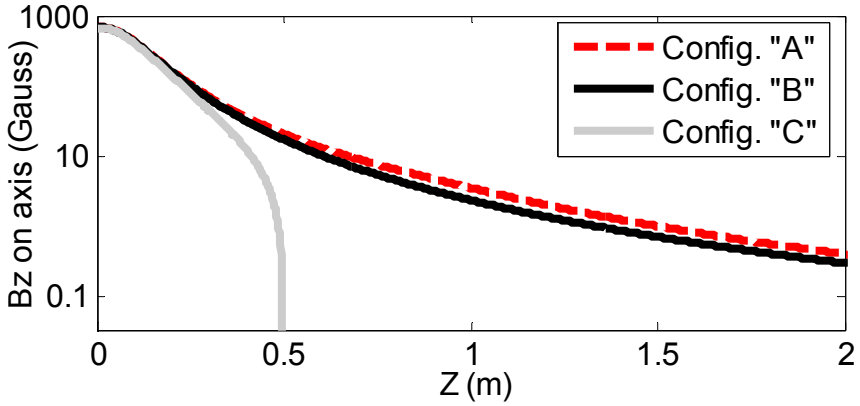

Figure 4.31 Axial magnetic field on the reverse coil experiment centerline. All configurations: 5A in the plasma source magnet and 100A in the choke magnet, with a peak field of 700 gauss. Magnet conditions are shown in Table 4.6.

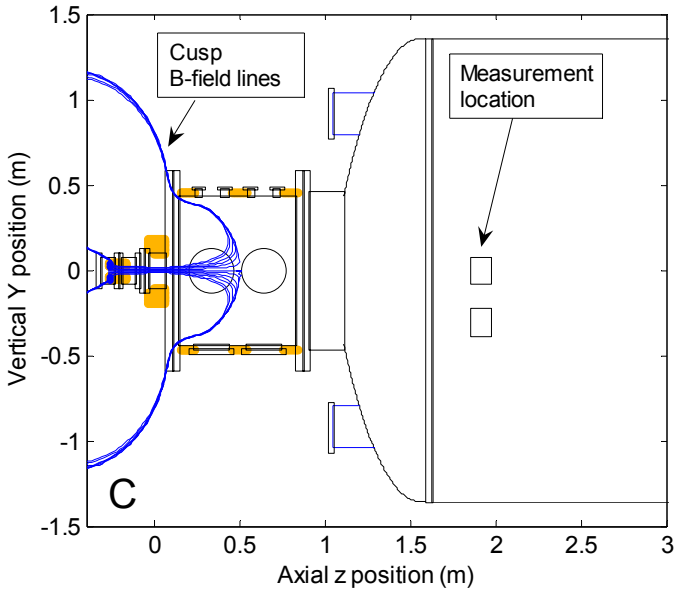

Figure 4.32: Lines of constant magnetic flux for magnet configuration 'C'. Note that no magnetic flux lines connect the upstream plasma source with the down-stream interferometer measurement region due to the reversed magnetic field.

Two identical plasma shots were produced using helium as a feed gas, with two different magnetic field configurations: Configuration 'B' using 0A in the three nozzle coils, and Configuration 'C' using reversed current in the three nozzle coils.

4.2.1 Interferometer density measurements

Plasma density measurements were taken by the z = 1.85 m microwave interferometer during both the standard (configuration 'B') and reverse (configuration 'C') shots. Both line integral density, and plume radius was recorded, as discussed in Section 4.1.1.2. It is also important to show that the plasma source was unchanged between the two shots- that the only change in the setup was with the nozzle magnetic field. The plasma source discharge voltage was 300V for both shots, and the discharge current for the two shots was also identical. This suggests that the initial conditions are identical for the two shots. (Figure 4.33)

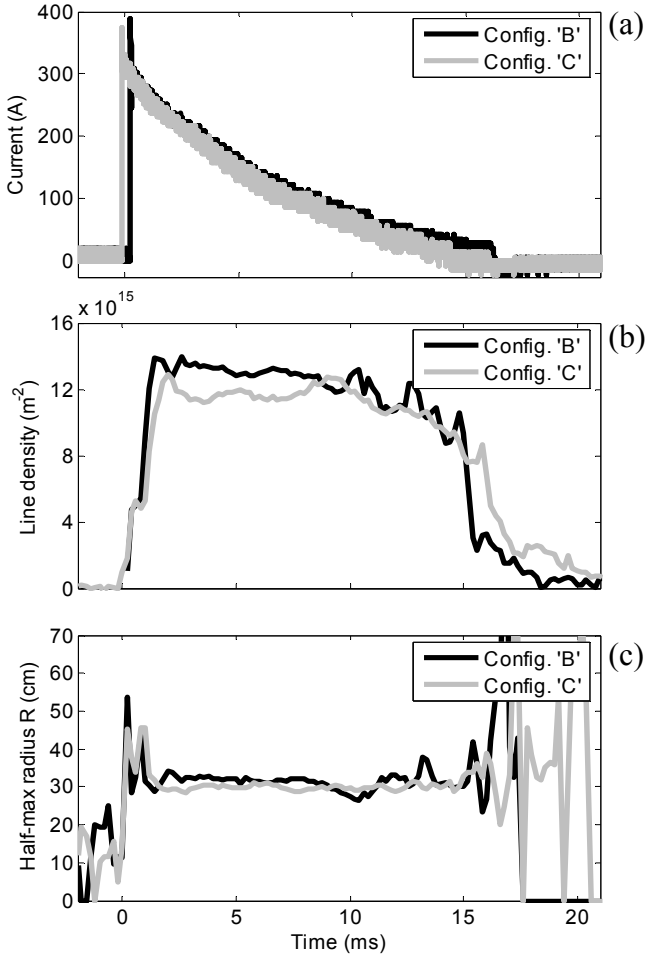

Figure 4.33: (a) Comparison of gun current between 5/4/06 shot 166 (nominal magnetic field) and shot 173 (reverse magnetic field) for 300V discharge voltage. Initial conditions for the two shots were very similar. (b) 15 GHz interferometer measurement at z = 1.85 m. Line integral density was the same within shot-shot variation for the two magnetic configurations. (c) Plume half-maximum radius at z = 1.85 m. The plume radius for both magnetic configurations was 30-35 cm.

The resulting downstream interferometer measurements show that despite the dramatic difference between the two magnetic configurations, the resulting plume measurements remain the same. Both show a peak line integral density of ~1.5×10^{16} m^{-2} with a plume radius of ~30-35 cm. The very small difference that can be perceived between the two conditions is due mostly to shot-to-shot variation, and certainly is not indicative of a

drastic change in the plume despite a large change in the applied magnetic field. (Figure 4.33) This evidence is a strong indicator that applied magnetic fields are not affecting the plasma exhaust's particle flux beyond a certain point in the magnetic nozzle.

4.2.2 Comparison with positive magnetic field adjustment

In the previous section, very little difference was measured by the downstream interferometer despite a very large change in the magnetic field. This might lead one to suspect that the magnetic nozzle has no influence on the downstream plume. However, this is not the case. There are three additional magnetic field profiles listed in Table 4.6 besides the cusp configuration: Config. A, B and D. The magnetic nozzle currents for these three configurations are: [10 A, 3 A, 3 A], [0 A, 0 A, 0 A], and [40 A, 20 A, 20 A] respectively. By investigating the plume's change for these three minor adjustments to the nozzle coil currents, the influence of the applied magnetic nozzle can be demonstrated.

The plasma source was operated under the same discharge conditions for these three nozzle configurations. Plume profile widths were determined at the axial position $z = 0.9$ m by the vertical Langmuir triple-probe array as discussed in Section 3.2.3. One single shot was taken for each magnetic field configuration, and each of the six Langmuir probe density responses was time averaged over the entire shot. This provides a plume density profile measurement for each shot.

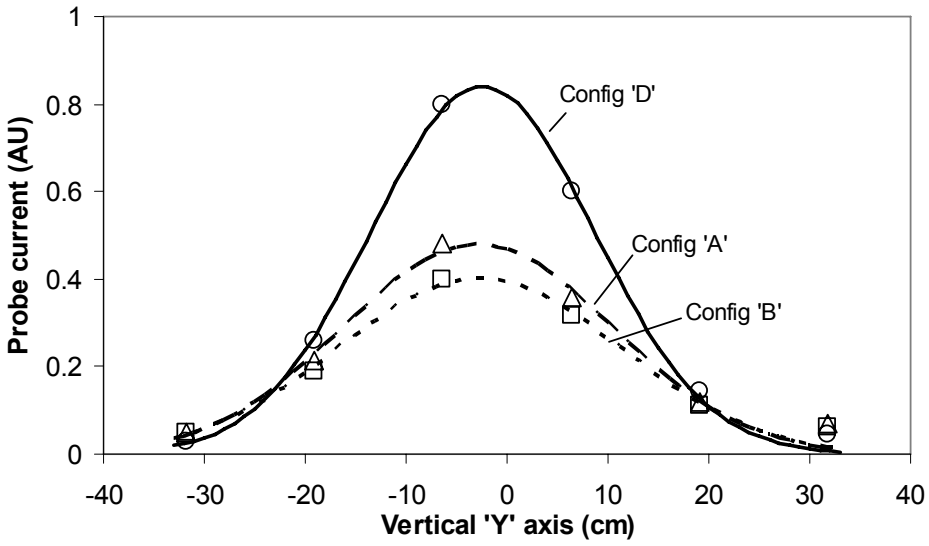

Figure 4.34: Plume radial profile for three magnetic nozzle configurations. Density is measured by vertical Langmuir probe array at z = 0.9 m and displayed as probe current (arb. units). Plume half-maximum radius R for the three configurations is: Config. A: 15.5 cm. Config. B: 16.3 cm. Config. D: 13 cm.

As shown in Figure 4.34, some variation does exist in the three magnetic profiles. In particular, the application of higher nozzle field creates a denser, narrower plume which is consistent with the magnetic nozzle affecting plume profiles. The result of applying the high nozzle field strength of configuration 'D' (40A, 20A and 20A in the last three nozzle coils) was to double the measured centerline density compared with the no-nozzle condition of configuration 'B'. The high-field configuration 'D' also resulted in a half-maximum radius of R = 13 cm which is a reduction from the configuration 'B' plume width of R = 16.3 cm.

As expected, the application of higher nozzle fields results in a narrower, denser plume. This can be seen as a verification of the nozzle's effect on the plume while the plume is still magnetically confined. This then brings up the question why a complete reversal of

current in magnetic nozzle coils (i.e. Configuration 'C') yielded no apparent difference in the downstream plume. One possible answer is that negative current in the nozzle coils reduced the magnetic field in the nozzle region, allowing magnetic detachment to occur farther upstream. The result of this earlier detachment was to impart the plume with a slightly narrower trajectory angle yielding no change in plume density and profile width at the downstream interferometer at z = 1.85 m, when compared with configuration 'B'. Another possible answer is that an additional cross-magnetic field transport phenomenon occurs in the presence of a strongly diverging magnetic field. For instance, high frequency electric fields have been discovered in prior experiments that involved plasma flowing perpendicular to an applied magnetic field. [Schmidt 1960], [Ishizuka 1982], [Brenning 2005]. In these previous studies the directed velocity of the plasma was hardly changed by the application of strong perpendicular magnetic fields. It is possible that a similar effect is arising in this experiment when strongly diverging magnetic flux lines are created as opposed to a small divergence angle magnetic nozzle. Further investigation of this additional cross-field transport effect is outside the scope of this work, but possible follow-on experiments are described in Section 6.2: Future work.

4.3 Charge exchange collision effects in the DDEX experiment

Ion-neutral collisions pose a source of error in the interpretation of this experiment because hypothetical deviations of the plasma from the magnetic field that would otherwise be attributed to magnetic detachment may in fact be caused by collisions. Experimental evidence of ion-neutral charge exchange collisions is therefore an important topic of discussion.

An example of the experimental effect of charge exchange collisions can be spotted in Figure 2.9 (b), which shows Mach probe data from an MPD thruster experiment. Insufficient pumping in this case led to a dramatic decrease in Mach number (ion velocity) at greater distances from the plasma source. Ion density (not shown) dramatically increases as well due to flux conservation. A similar effect should be sought in the present experiment.

In Section 3.1.3 the theoretical effect of ion-neutral collisions was discussed, and the measured neutral background pressure during a pulse was found to be between $4x10^{-5}$ Torr and $2x10^{-4}$ Torr. This yields an ion-neutral charge exchange mean free path in hydrogen of 2.2 m – 11 m, and about a factor of two less for helium. Due to the rising pressure in the vacuum chamber, collisional effects are likely to be more visible towards the end of a shot, and more apparent in experiments using helium rather than hydrogen.

Figure 4.28 therefore provides the best possibility for evidence of ion-neutral interaction. In comparing the upstream and downstream area integral density in helium, as described in Section 4.1.6, the downstream density appears to rise towards the end of a shot. This may indicate a slight deceleration due to charge exchange collisions. However, it is debatable whether Figure 4.28 or the hydrogen data in Figure 4.27 shows a substantial increase in density above what could be considered natural fluctuations. Compared with the large decrease in Mach number shown in Figure 2.9, the density change is rather small.

A second set of data to investigate is the axial scan of velocity shown in Figure 4.23. Although the error bars for this measurement are large, it does not give any indication of a substantial decrease in velocity by $z = 2$ m.

It can therefore be suggested that the pressure data can not conclusively rule out ion-neutral charge exchange collisions in the DDEX experiment. However the plume measurement data does not show conclusive evidence of a density rise or a velocity decrease commensurate with strong ion-neutral charge exchange collisions. It is therefore theoretically possible that ion-neutral collisions are occurring in this experiment, but the effect of charge exchange collisions was not seen in any experimental data. The experimental impact of ion-neutral momentum exchange collisions is considered in Section 5.1.5.3.

CHAPTER 5

SIMULATION AND ANALYSIS

5.0 Overview

The simulations considered in this chapter will help provide some answers to the questions posed in Chapter 1: Is magnetic detachment occurring in this experiment? Under what conditions will the magnetized plasma plume detach from its applied magnetic fields? And at what efficiency will this detachment occur? As we have already seen in the cusp magnetic field experiment of Section 4.2, conditions were found that demonstrate plasma transport across sharply diverging magnetic field lines. That was an example of magnetic detachment, because a magnetized plasma was observed to be unaffected by a large change in the applied magnetic field. The last two questions posed in Chapter 1 require a more detailed examination of experimental results in order to be answered.

Simulations were conducted based on the initial conditions found in the experiment. Two different computer codes are employed- one is a novel quasi-1D simulation developed for this dissertation, and the second is a previously published 2D code based on the ideal MHD equations. The two codes were able to duplicate a variety of the experimental measurements reported in Chapter 4, including plume profile widths and plasma density values. Velocity effects seen in the experiment are also compared with analytical

models, providing a better understanding of the magnetic nozzle's accelerating effects.

5.1 Quasi-1D Numerical simulations

Several models for plasma expansion were produced to accompany the above experimental data, evaluating the influence of high-β detachment. [Deline, 2007] These models were chosen to deal specifically with the measured plume diameters, given the assumption of constant velocity. The validity of this assumption as stated in Section 4.1.6 and 4.3 is good within ~20% for the beginning of a shot before the pressure rise has a chance to slow the flow down. The initial simulation couples a static 2D vacuum magnetic field map (shown in Figure 5.1) with a steady-state model in which the plume follows magnetic field lines exclusively. This is equivalent to the case of flowing plasma frozen onto vacuum field lines under steady state conditions.

Additionally, because the plume's radial density profile is approximately Gaussian at all locations, a quasi-1D assumption was used in which the plume's ½ maximum radius $R(z)$ is variable, but its density profile remains Gaussian. If the plasma plume is frozen onto magnetic field lines, the total captured magnetic flux $\pi R(z)^2 B_z(z)$ is conserved, and the plume width $R(z)$ is equal to:

$$R(z)/R_0 = \left(B_z(z)/B_{z,0}\right)^{-1/2} \tag{5.1}$$

where R_0 and $B_{z,0}$ are the plasma ½ maximum radius at $z = 0$ and magnetic field at z = 0, respectively. The radial expansion rate of the plume envelope dR/dz can be defined by a radial velocity v_r and a (constant) axial velocity v_z where:

$$\frac{dR(z)}{dz} = R_0 B_{z,0}^{1/2} \frac{d}{dz}\left(B_z(z)\right)^{-1/2} = \frac{dR}{dt}\left(\frac{dz}{dt}\right)^{-1} = \frac{v_r}{v_z} \tag{5.2}$$

5.1.1 Magnetic field model

The magnetic fields in the DDEX experiment were calculated over a 100 x 100 cell simulation space using an analytic expression for the off-axis magnetic field of an infinitely thin current loop. Each coil winding is considered a separate 1-D current loop, with the total magnetic field at each point in the simulation space equal to the sum of contributions from all the windings. The off-axis magnetic field from a thin cylindrical current loop of radius r_0 is [Jackson, 1975] [Jackson, 1999]:

$$B_z(r,z) = \frac{B_0}{\pi\sqrt{Q}}\left[E(k)\frac{1-\alpha^2-\beta^2}{Q-4\alpha} + K(k)\right] \tag{5.3}$$

$$B_r(r,z) = \frac{\gamma B_0}{\pi\sqrt{Q}}\left[E(k)\frac{1+\alpha^2+\beta^2}{Q-4\alpha} - K(k)\right] \tag{5.4}$$

Where B_0 is the centerline magnetic field in Tesla: $B_0 = \frac{I\mu_0}{2r_0}$, and $\alpha = r/r_0$, $\beta = z/r_0$, $\gamma = z/r$, $Q = \left[\left(1+\alpha\right)^2 + \beta^2\right]$, and $k = \sqrt{\frac{4\alpha}{Q}}$. The functions $K(k)$ and $E(k)$ are the complete elliptic integrals of the 1st and 2nd kind, respectively. A Matlab code determines the vacuum magnetic field map based on applied currents and coil geometries for the

various nozzle magnets. The resulting magnetic field map was successfully benchmarked against centerline magnetic field readings from a translation stage mounted three-axis Hall probe. [Chavers, 2006]

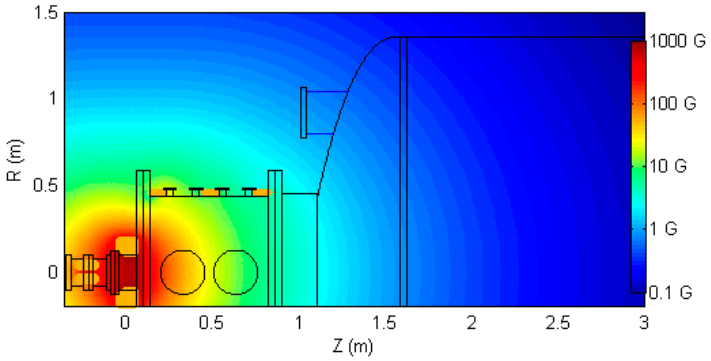

Figure 5.1: 2D Vacuum magnetic field model used for the numerical simulations. Hydrogen simulations used the coil conditions provided as Dataset #3 in Table 4.1, and helium simulations used the coil conditions in Dataset #4.

5.1.2 Experimental data inputs

Initial conditions were chosen for the plasma simulations based on the experimental setup. The electron temperature was set at T_e = 1.2 eV for hydrogen and T_e = 1.4 eV for helium according to measurements from Section 4.1.2. The simulation was quite insensitive to electron temperature, and minor adjustment of these values within T_e experimental uncertainty does not significantly affect the simulation. A constant axial velocity v_z was varied in the range of 16 km/s +/- 3 km/s for hydrogen and 14 km/s +/ - 2 km/s for helium. These values are within the error bars for the measurements discussed in Section 4.1.4, and are adjusted to show velocity's effect on the profile shape. The

initial density distribution inside the plasma source was based on the gun inner diameter of 1 cm. An initial plume radius equal to R_0 = 0.5 cm was chosen with a peak density of n_e = 8.75x10^{20} m^{-3}. These initial plasma conditions are within the reported parameters provided for the plasma source [Fiksel, 1996] and match the farthest upstream plasma density measurements made in the experiment, shown in Section 4.1.1.1. Helium simulations use the same initial column radius and a slightly higher initial density n_e = 1x10^{21} m^{-3}.

The experimentally determined plume densities and profile widths from Table 4.2 and Table 4.3 are used for comparison with the simulation results. This data is superimposed on top of the magnetic field map as shown in Figure 5.2 and Figure 5.3 for hydrogen and helium, respectively.

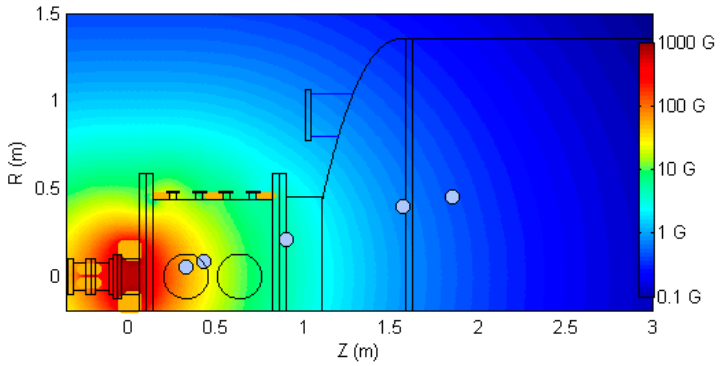

Figure 5.2: Experimentally determined density profiles for hydrogen from Table 4.2. White dots represent measured column half-maximum radius. The magnetic field is shown for the operating conditions of Dataset #3 in Table 4.1.

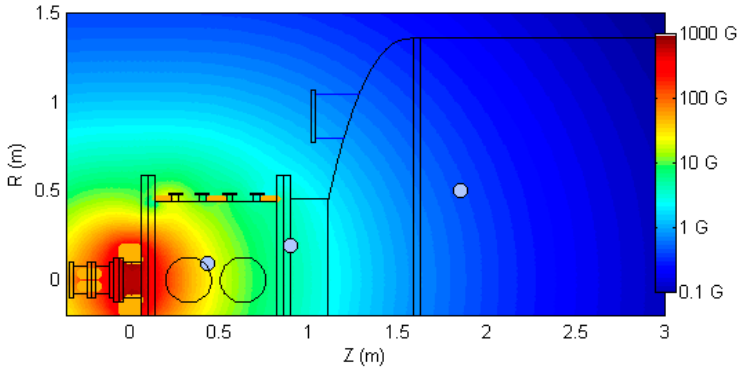

Figure 5.3: Experimentally determined density profiles for helium from Table 4.3. White dots represent measured column half-maximum radius. The magnetic field is shown for the operating conditions of Dataset #4 in Table 4.1.

5.1.3 Initial simulation #1: frozen-in condition

A MATLAB simulation based on Euler's method [Edwards, 1996] is used with axial step size dz = 6.7 mm and with initial conditions chosen according to Section 5.1.2. The axial step size was chosen small enough to not contribute to numerical inaccuracy. The profile width $R(z)$ is updated for each axial step based on Eq. (5.1) which assumes that plasma is frozen onto magnetic field lines. The centerline plasma density $n(z)$ is updated for each step by flux conservation:

$$\frac{d}{dz}\left(R(z)^2\, n(z)\, v_z\right) = 0 \tag{5.5}$$

The flow velocity is assumed constant, as discussed in Section 5.1. By following magnetic field lines out from the plasma source, the plume trajectory is plotted in Figure 5.4 by displaying $R(z)$ along with the experimentally determined profile widths:

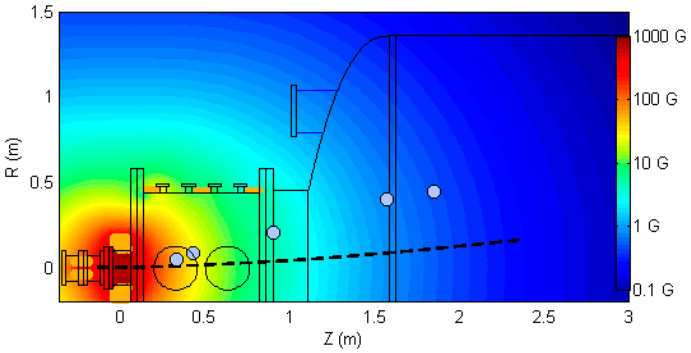

Figure 5.4: Initial frozen-in simulation for hydrogen showing experimental data points (white dots) and simulated plume trajectory (dashed).

It is clear from Figure 5.4 that the initial simulation does not match the experimental data very well. The experimental plume profiles were measured with high resolution, and uncertainties in plume width are on the order of 10%. Therefore, an appropriate simulation should come at least this close to matching the experimental data points. In the case of these frozen-in simulations, the plume width expands too slowly. This is also the case for the helium simulations, which are considered separately in Section 5.1.5.1.

5.1.4 Simulation #2: Classical cross-field diffusion

It was found that the radial expansion rate from the basic model in Section 5.1.3 is too slow to properly account for the measured plasma profiles. An improvement on this initial simulation includes the addition of an enhanced radial velocity term v_D into Eq. (5.2) to account for cross-magnetic field diffusion:

$$\frac{dR(z)}{dz} = \frac{v_r + v_D}{v_z} \tag{5.6}$$

Here, v_D is an approximate radial velocity due to diffusion, and is measured at the plume's half-maximum radius $R(z)$. For the purposes of this simple simulation, the magnetic nozzle is assumed to be paraxial, meaning radial magnetic field is ignored and v_D is assumed to be exclusively in the radial direction. The radial diffusion rate is included along with the plasma's perpendicular expansion due to magnetic field curvature.

As determined in Section 4.1.9, the cross-field diffusion rate is governed by classical diffusion. Using Fick's law, v_D can be defined from the classical diffusion coefficient [Chen 1984]:

$$\Gamma = nv_D = -D_e \nabla n_e \tag{5.7}$$

$$v_D = -D_e \frac{\nabla n_e}{n_e} \tag{5.8}$$

where the classical diffusion rate for electrons D_e was previously defined in Eq. (2.61) as:

$$D_e = \tfrac{10000}{8}\left(\tfrac{1}{2}\pi\right)^{1/2} \frac{{\omega_{pe}}^3}{{\omega_{ce}}^2} n^{-1} \left[1 + \left(\frac{2m_i}{m_i + m_e}\right)^{1/2}\right] \tag{5.9}$$

For this simulation, the magnetic field and electron density required to define ω_p and ω_{ce} were taken at the position $R(z)$ instead of on centerline. Using the Gaussian density profile from Eq. (4.1) to determine the density gradient, the diffusion velocity reduces to:

$$v_D = \frac{2\ln 2}{R(z)^2}\frac{10000}{8}\left(\tfrac{1}{2}\pi\right)^{1/2}\frac{\omega_{pe}{}^3}{\omega_{ce}{}^2}n^{-1}\left[1+\left(\frac{2m_i}{m_i+m_e}\right)^{1/2}\right] \tag{5.10}$$

If density and magnetic field values were taken from the centerline instead of at $R(z)$, the diffusion rate would be a factor of 2 faster due mainly to the increase in centerline plasma density. By using the density and magnetic field values at $R(z)$, the diffusion rate at the half-maximum radius is calculated, which is desired because the quasi-1D simulation defines the plume profile width by the half-maximum radius.

A simulation was performed using the enhanced perpendicular velocity drift in Eq. (5.10) included with the geometric expansion velocity v_r in Eq. (5.6). The same initial conditions and flux conservation assumptions that were used in Section 5.1.3 are used again. The resulting diffusion simulation for hydrogen is shown in Figure 5.5, with multiple diffusion rates shown, between 0.1 times v_D to the full v_D diffusion velocity.

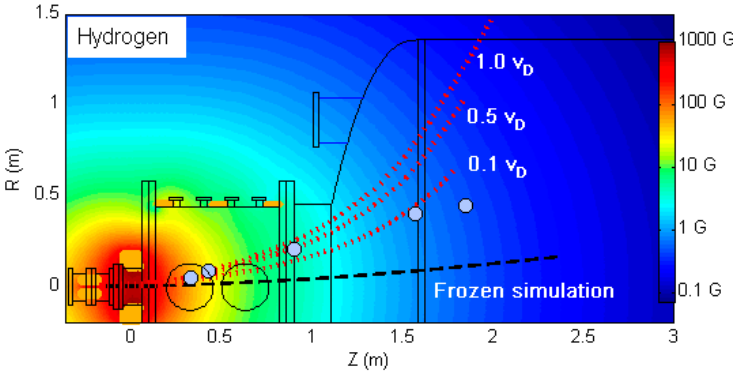

Figure 5.5: Numerical simulation for hydrogen comparing classical diffusion results (dots) for multiple diffusion rates. Radial diffusion velocity v_D was adjusted from 0.1 v_D to v_D. Also shown are frozen-in simulations (dash) and experimental data (white) from Figure 5.4.

The simulation results in Figure 5.5 show an improvement in fitting to the first three experimental data points. Particularly when compared with the frozen-in simulation, the cross-field diffusion simulation does a much better job of matching the experimental data. However, at an axial location much greater than z = 1 m the diffusion simulation diverges from the experimental conditions. If a lower diffusion rate is chosen, the simulated trajectories match the downstream density profiles better. However in reducing the diffusion rate, the upstream trajectories no longer fit. If the last two experimental data points are neglected, a cross-field diffusion velocity of 0.5 v_D best matches the initial three plume profiles. No diffusion rate could be chosen that would result in this particular simulation matching all five of the experimental data points.

While the use of Eq. (5.10) for radial velocity appears to satisfy certain experimental results within a factor of two, its use in diffusion simulations does present a theoretical problem. This is specifically because the radial velocity v_D is inversely proportional to radial position, instead of being constant with radial position. If a full 2D simulation were employed using the diffusion velocity in Eq. (5.10), the density profile would quickly cease to be a Gaussian as the center diffused faster than the outer edges. While this is not necessarily a problem for the quasi-1D simulations considered here, it suggests an incomplete physical picture that would have to be addressed for any future 2D simulations. The diffusion rate chosen for these simulations is to a certain extent chosen *a posteriori* in order to best fit the experimental data. This should not necessarily be considered a failing of the simulation, but a recognition that there is a factor of >2 uncertainty in the diffusion rate to account for errors in both the paraxial nozzle

assumption, the quasi-1D assumption, and the empirical nature of cross-magnetic field diffusion rates.

5.1.5 Simulation #3: Beta > 1 Detachment

Since no arbitrary diffusion rate could be chosen that would result in all of the data points being fit, and frozen flow assumptions resulted in far too narrow trajectories, a more sophisticated physical model is required to fix the simulation. The fact that the downstream data points do not fit at all may be due to a breaking of the magnetic confinement conditions, as discussed in Section 4.1.8 for high-β plasmas. Another term for this situation is magnetic detachment, which is predicted to occur when the plasma β increases above unity.

A third 1-D high-β trajectory model is produced using the same initial conditions as in Section 5.1.3, and the best-fit classical diffusion rate of v_D / 2. As will be seen, this model appears to fit all measured profile widths, both for helium and hydrogen data. In this model, β is an indication of plasma detachment which changes with z: $\beta(z) = m_i \mu_0 n(z) v_z^{\,2} / B^2(z)$. As was discussed in Section 4.1.8, the plasma β reaches unity by z = 0.9 m for both hydrogen and helium experiments. Upon reaching the $\beta > 1$ transition, the plasma plume is no longer affected by applied magnetic field, and the profile continues on a ballistic trajectory defined by:

$$\frac{d^2R(z)}{dz^2} = 0 \text{ for } \beta > 1 \tag{5.11}$$

From this point onward, the plume trajectory angle remains constant. The profile width still increases, and the centerline density still decreases according to Eq. (5.5). Since the simulation is quasi-1D, the entire plume is assumed to detach as a whole once the centerline plasma density achieves $\beta > 1$. In reality, this is not an accurate situation, since the plasma β is much lower towards the plume edges than in the plume center and hence the center should detach sooner. A full 2D simulation is required to simulate a more realistic detachment contour.

The third ($\beta > 1$) model was adjusted by assigning different axial velocities to the simulation's initial conditions. V_z remains constant with z despite the change in initial condition, and a comparison of the resulting trajectories can be seen in Figure 5.6 for the initial velocities v_z = 15 km/s, 17 km/s and 19 km/s. A change in axial velocity will affect the profile shape primarily by determining how early the plume detaches. Higher constant velocities result in quicker detachment, and thus narrower profiles. The higher constant velocity also reduces the relative effect of cross-magnetic field diffusion.

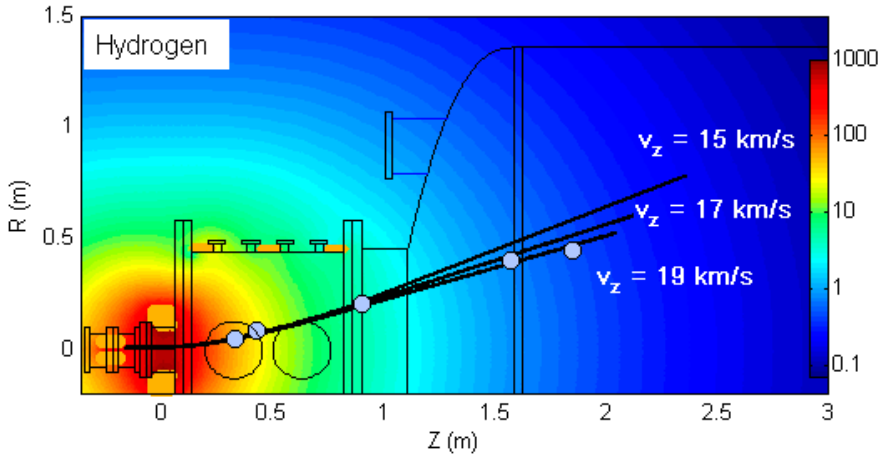

Figure 5.6: Comparison of high β detachment simulations with hydrogen for varying axial velocity. Velocity is constant with z. v_z = 19 km/s best fits experimental profiles (white circles).

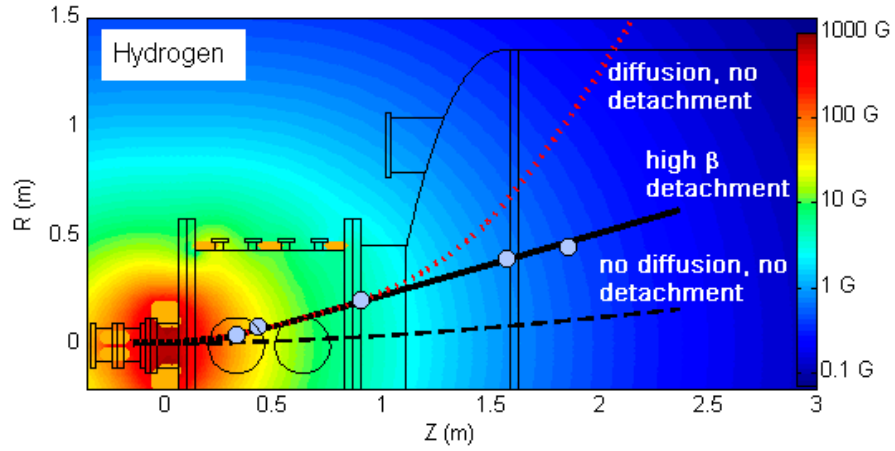

Figure 5.7: Plume trajectories for hydrogen. Black dashed line shows field line mapping only. Red dotted line shows field line mapping plus cross-field diffusion at v_D / 2 radial velocity. Black solid line shows field line mapping, plus cross-field diffusion, plus $\beta > 1$ detachment with an axial velocity equal to v_z = 19 km/s.

A comparison of the three simulation methods is shown in Figure 5.7 and shows the benefits of the high- β model. Simulation #1 which assumes the plume is frozen to magnetic field lines underestimates the plume width by a significant amount. The cross-field diffusion model (#2) will properly account for the upstream radial density profiles, but will not account for the downstream density profiles. Only the high-β detachment trajectory model (#3) was able to account for both the upstream and downstream column widths measured in the experiment. In particular, a flow velocity for hydrogen of v_z = 19 km/s best fit experimental profiles. This flow velocity is within measurement error bars.

A table of simulation results is included which compares measured and simulated density, velocity and profile width:

	Simulation values	Measured values
Velocity, z = 0.33 m	19 km/s	---
Velocity, z = 0.43 m	19 km/s	15 km/s
Velocity, z = 1.85 m	19 km/s	19 km/s
R(z) , z = 0.33 m	4.8 cm	5 cm
R(z) , z = 0.43 m	6.9 cm	8.5 cm
R(z) , z = 1.85 m	47 cm	45 cm
n_e, z = 0.33 m	9.6×10^{18}	1×10^{19}
n_e, z = 0.43 m	4.6×10^{18}	3.7×10^{18}
n_e, z = 1.85 m	9.9×10^{16}	1×10^{17}

Table 5.7: Hydrogen simulation results for high-β detachment simulation. Initial conditions are: R_0= 0.5 cm, v_0 = 19 km/s, $n_{e,0}$ = 8.75×10^{20} m^{-3}. Radial diffusion velocity is v_D / 2. Experiment values are taken from Section 4.1

While several assumptions were made in this 1D numerical simulation: constant velocity, vacuum magnetic fields, paraxial nozzle assumption and purely radial diffusion, the resulting simulations appear to match with hydrogen experimental data within error bars, but only when magnetic detachment is taken into account.

5.1.5.1 Helium simulations

Numerical simulations similar to those detailed above were also conducted for helium. As stated in Section 5.1.2, the initial conditions for helium were similar to those for hydrogen with identical plume width $R(z)$ = 0.5 cm and slightly higher density: n_e = $1x10^{21}$ m^{-3}. A constant flow velocity of v_i = 14 km/s +/- 2km/s and electron temperature T_e = 1.4 eV were used. Also, the radial diffusion velocity v_D was included, based on the classical diffusion Eq. (5.10). Figure 5.8 shows a comparison of radial velocity from 0.1 v_D to the full v_D diffusion velocity. Best agreement with the data was again found when a diffusion velocity equal to 0.5 v_D was used. A comparison of high-β detachment simulations with the other two helium simulations is shown in Figure 5.9.

As was the case with hydrogen simulations, the helium radial profiles could all be fit by the high-β detachment simulation. A table of simulation results is included which compares measured and simulated velocity, centerline density, and profile width.

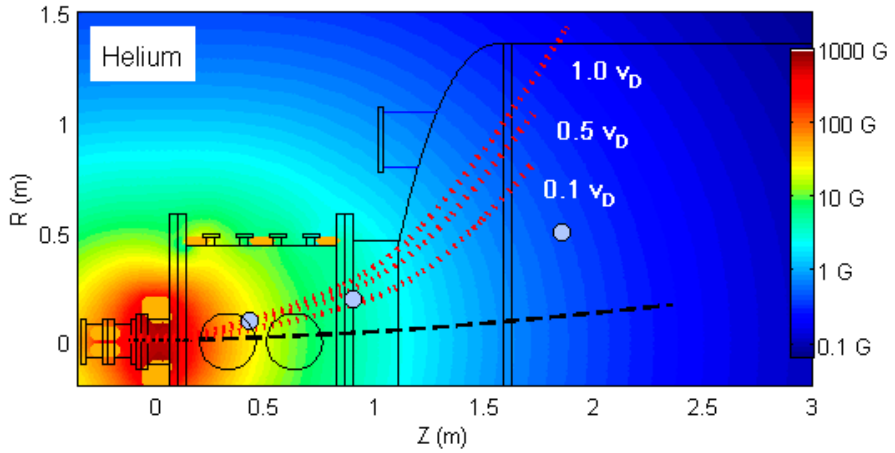

Figure 5.8: Numerical simulation for helium comparing classical diffusion results (red dots) for multiple diffusion rates. Radial diffusion velocity v_D was adjusted from 0.1 v_D to 1.0 v_D. Also shown are frozen-in simulations (black dashed) and experimental data (white) from Figure 5.3.

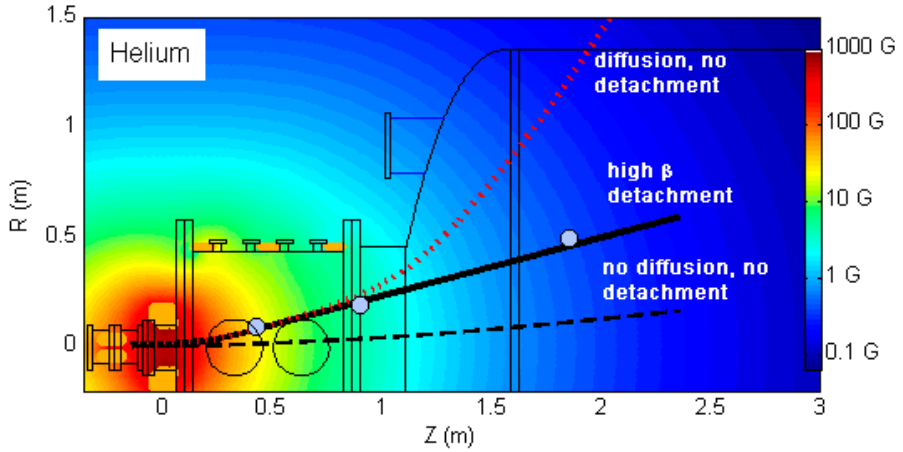

Figure 5.9: Trajectory simulations for helium. Black dashed line shows field line mapping only. Red dotted line shows field line mapping plus classical cross-field diffusion at v_D / 2 radial velocity. Black solid line shows field line mapping, plus cross-field diffusion, plus β > 1 detachment with an axial velocity equal to v_z = 14 km/s.

	Simulation values	Measured values
Velocity, z = 0.33 m	14 km/s	---
Velocity, z = 0.43 m	14 km/s	14 km/s
Velocity, z = 1.85 m	14 km/s	17 km/s
R(z) , z = 0.33 m	5.5 cm	---
R(z) , z = 0.43 m	8 cm	10 cm
R(z) , z = 1.85 m	46 cm	50 cm
n_e, z = 0.33 m	8.2×10^{18}	---
n_e, z = 0.43 m	4×10^{18}	3.5×10^{18}
n_e, z = 1.85 m	1.2×10^{17}	1×10^{17}

Table 5.8: Helium simulation results for high-β detachment simulation. Initial conditions are: R_0= 0.5 cm, v_0 = 14 km/s, $n_{e,0}$ = 1×10^{21} m^{-3}. Radial diffusion velocity is v_D / 2. Experiment values are taken from Section 4.1.

5.1.5.2 $\beta > 1$ detachment vs. $r_{ci} > r_p$ detachment

The above simulations indicate that magnetic detachment is occurring in the plasma flow. As stated in Section 4.1.7, there are two different theories regarding the onset of magnetic detachment: $\beta > 1$ and $r_{ci} > r_p$ and it may be difficult to discern between the two conditions in this experiment. Based on the experimental evidence, the specifics of exactly where and exactly how magnetic detachment is occurring are slightly ambiguous. For instance, uncertainty in flow velocity makes it difficult to pinpoint the exact axial location where plasma $\beta > 1$. Also the plasma radius r_p which is compared with ion cyclotron radius r_{ci} can be defined by the ½ maximum radius, or the $1/e$ radius, or the $2w$ radius with differences between the definitions or r_p ranging up to 70%. This suggests there is some ambiguity in determining where the condition for $r_{ci} < r_p$ magnetization is met, and where it is violated.

To investigate this effect further, the previously reported simulations were adjusted to achieve magnetic detachment, not when β >1, but when $r_{ci} > r_p$. Initial conditions and diffusion assumptions were chosen identical to those in Section 5.1.5 and 5.1.5.1. However, the detachment condition was changed such that when centerline $r_{ci} > R(z)$, the plume was assumed to detach, and the plume trajectory was kept constant.

The results of these alternate detachment simulations were not entirely conclusive. There was a significant shift in the centerline detachment position, with the hydrogen detachment point shifted back by 11 cm, and the helium detachment shifted back by 33 cm. However, the plume width was only increased by 12% and 14% respectively at z = 1.85 m. This is within the measurement uncertainty of plume width, and thus $r_{ci} > R(z)$ can not be excluded as a possible detachment mechanism. A different experiment would need to be devised to eliminate this possible detachment mechanism, even if $\beta > 1$ detachment is favored for reasons of theory.

5.1.5.3 $\beta > 1$ detachment vs. collisional dissipation

As stated in Section 4.3, plume measurements do not show measureable evidence of ion-neutral charge exchange collisions. However, pressure measurements can not rule out the possibility of some ion-neutral collisions in this experiment. It is therefore possible that ion-neutral momentum exchange collisions are responsible for some of the plume trajectories measured in this experiment. To address this issue, an investigation was made into what neutral pressure would be required to substantially affect measured plume trajectories. Figure 5.4 provides a good starting point for this analysis as it provides ideal

trajectories following the applied magnetic field line in absence of collisions or cross-field diffusion. In order to conduct this analysis, a quasi-1D simulation was conducted, assuming that ions follow magnetic field lines, but each instance of an ion-neutral momentum exchange collision would result in a radial displacement of the ion equal to the ion cyclotron radius. Momentum exchange collision cross-sections were taken from Table 3.1 using the total collision cross-section for helium. This helium collision cross-section is a worst-case estimate, since collision cross-sections for hydrogen are smaller.

Given these assumptions, the plume was simulated with initial conditions taken from plume profile widths at z = -0.16 m and z = 0.33 m. The required neutral pressure to allow collisional dissipation to account for the remaining plume widths was determined. In between the plasma gun aperture at z = -0.16 m and the upstream interferometer measurement point at z = 0.33 m, a neutral background pressure of 1×10^{-3} Torr is required to account for the plume width broadening. Between z = 0.33 m and z = 0.43 m, a neutral pressure of 4.5×10^{-4} Torr is required to account for the plume width at z = 0.43 m. It should be noted that both of these pressure values are several times greater than the peak chamber pressure of 2×10^{-4} Torr, measured inside the smaller (1 m diameter) spool piece at z = 0.5 m. Although a higher local pressure within the plume is possible, it is probably not much higher due to the very large (1 m) diameter chamber and the fact that molecular flow dominates at this pressure range.

In addition, the downstream measurement points are fit very poorly by assuming an increased plume width due to ion-neutral collisions. Indeed, by using initial conditions

equal to the measured plume width and density at z = 0.33 and following vacuum magnetic fields out to z = 1.85 m, the plume half-maximum diameter is too wide by 15 cm even without assuming any cross-field transport. Any additional assumption of ion-neutral collisions in this far region of the nozzle yields even greater divergence from the measured plume diameters.

In conclusion, to account for the plume widths measured at z = 0.33 m and z = 0.43 m, the required pressure acting through ion-neutral momentum exchange collisions is far greater than any measured pressures in the experiment. In addition, the far downstream plume width measured at z = 1.85 m cannot be accounted for at all, given any assumption of cross-magnetic field diffusion or ion-neutral momentum exchange collisions. Ion-neutral collisions can therefore not realistically explain any of the measured plume widths, and are expected to play a minimal role in the data and conclusions presented for this experiment.

5.1.6 Quasi 1D simulations of nozzle efficiency

The simulations in Section 5.1.5 can be employed to estimate the rocket thrust and nozzle efficiency, based on Eq. (2.68) and Eq. (2.69). These values were not backed up by experimental verification, but qualitative results can still be obtained from simulation, particularly for varying nozzle conditions. Assuming a Gaussian density profile from Eq. (4.1), a substitution can be made in Eq. (2.68) for thrust T:

$$T = 2\pi m_i n_{\max}(z) \int_{r=0}^{\infty} r\, v_z(r)^2\, 2^{\frac{-r^2}{R(z)^2}}\, dr \tag{5.12}$$

A further substitution must be made in Eq. (5.12) for the axial component of flow velocity $v_z(r)$. While the overall velocity v_0 is constant for this simulation, due to energy conservation the axial portion must be a function of r according to $\sqrt{v_z{}^2(r) + v_r{}^2(r)} = v_0$. This reflects the fact that a particle at a given z is going to have a higher directed velocity v_z on the centerline ($r = 0$) than a particle at the edge of the plume ($r = R$). The ratio v_r / v_z at the plume half-max radius R is defined by the trajectory angle θ by:

$$\theta = \tan^{-1}\left(\mathrm{d}R / \mathrm{d}z\right) \tag{5.13}$$

and:

$$v_z(r) = v_0 \cos(\theta) \tag{5.14}$$

The above definition of theta is determined by the plume angle at $r = R$. For all other radial positions other than the half-maximum radius, the derivative dr/dz is not tracked in the simulation. An alternate method for determining the ratio of v_r to v_z for these other radial positions requires a definition of trajectory angle that varies in r: $\theta(r)$ and is shown in Figure 5.10 and described here.

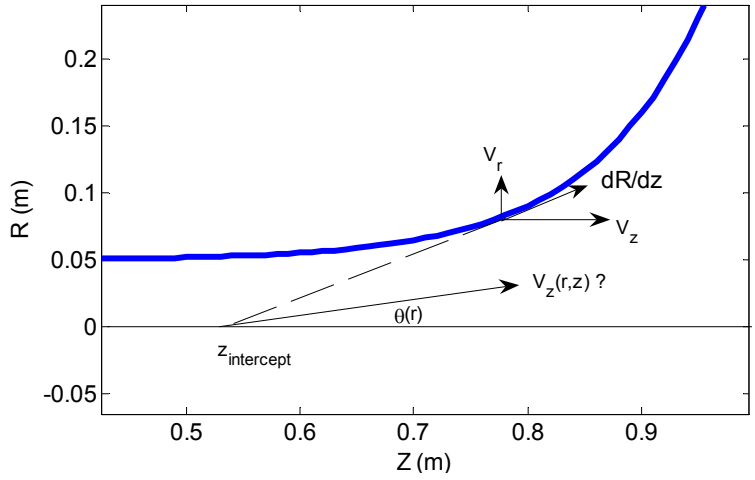

Figure 5.10: Determining $v_z(r)$ for a theoretical plume. Plume radius R is plotted against axial position z for a representative plume. The derivative dR/dz is found for a given axial position z_i. The z - intercept of the line tangent to $R(z)$ at point z_i is used to determine the trajectory angle $\theta(r)$, which is used in Eq. (5.14) to find $v_z(r)$.

With the value dR/dz in hand for a given axial position z_i, a z-intercept value $z_{intercept}$ can be found from the line tangent to the plume trajectory $R(z)$ at z_i. This intercept point on the z – axis is used as a plasma "point source" to find a trajectory angle for all r positions along the radial profile at z_i. The radially varying trajectory angle is found by trigonometry:

$$\theta(r) = \tan^{-1}\left(\frac{r}{z_i - z_{\text{intercept}}}\right) \tag{5.15}$$

which allows axial velocity v_z to be found by Eq. (5.14). It should be noted that $z_{intercept}$ has a different value for each axial position z_i along the plume due to the difference in dR/dz at that axial location. However, it is assumed to be the same for each position r along the profile. The two methods of determining θ in Eq. (5.13) and Eq. (5.15) yield the same result at the plume half-maximum point $r = R$.

A further simplification can be made for the inverse tangent in Eq. (5.15), which combined with Eq. (5.14) yields:

$$v_z(r,z) = v_0 \cos\left(\tan^{-1}\left(\frac{r}{z_i - z_{\text{intercept}}}\right)\right) \approx v_0 \frac{1}{\sqrt{1 + r^2/\left(z_i - z_{\text{intercept}}\right)^2}} \tag{5.16}$$

Substitution into (5.12) yields:

$$T(z) \approx 2\pi m_i n_{\max}(z) {v_0}^2 \int_{r=0}^{\infty} 2^{\frac{-r^2}{R(z)^2}} \frac{r}{1 + r^2/(z_i - z_{\text{intercept}})^2} \mathrm{d}r \tag{5.17}$$

which is solved numerically at each z position. For large z, this value asymptotically approaches the T_∞ thrust at detachment. To determine the T_0 initial thrust, the assumption is made that $v(r)$ is exclusively axial for the nozzle inlet initial conditions, and thus Eq. (5.17) at z_0 is:

$$T_0 = 2\pi m_0 n_0 {v_0}^2 {R_0}^2 / \ln 4 \tag{5.18}$$

Figure 5.11 shows a calculation of $\eta_{\text{noz}} = T(z)/T_0$ for the standard magnetic nozzle conditions used in Figure 5.6 for hydrogen. The asymptotic efficiency for this simulation was 91%, meaning that the total thrust at a distance far from the nozzle was 91% of the inlet thrust. The peak thrust from this simulation was $T_0 = 60$ mN.

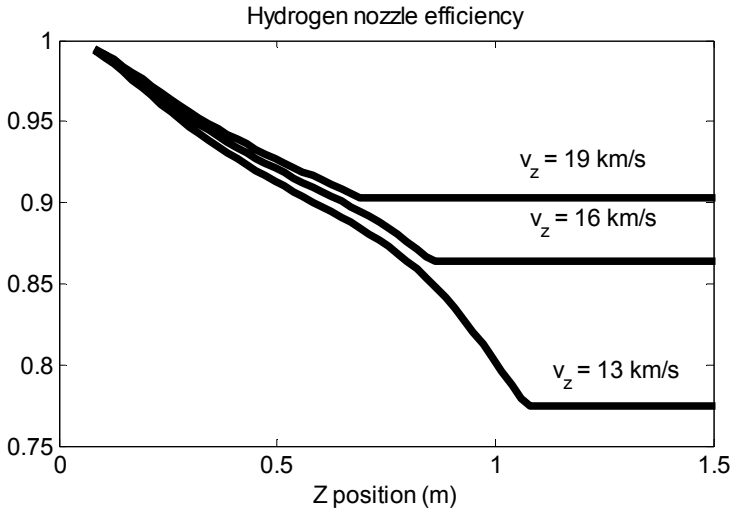

Figure 5.11: Nozzle efficiency η_{noz} for standard magnetic field simulations. Efficiency asymptotically approaches 91% for v_z = 19 km/s. A lower axial velocity decreases the nozzle efficiency. A lower limit to efficiency is reached at the point of detachment, which is somewhat of a 1-D numerical artifact.

Using this tool, a number of parameters can be changed to investigate their effect on efficiency. The first parameter adjusted was axial velocity. Not surprisingly, a decrease in axial velocity results in a decrease in nozzle efficiency. This is due to the wider profiles from increased radial diffusion, and due to the downstream shift of the $\beta > 1$ detachment point where the trajectory angle is greater. It should be noted in Figure 5.11 that the nozzle efficiency reaches an abrupt lower limit upon achieving the $\beta = 1$ condition on centerline. This is accurate as far as the assumptions of the 1-D model are concerned, and highlight the limitations of the 1-D assumptions. Subsequent simulations allowing for 2-D detachment contours are considered later (e.g. Figure 5.16), and do not show the same efficiency plateau.

The second parameter adjusted in this simulation was applied magnetic field. Magnetic field strength B was adjusted by changing the simulated current flowing in each of the

three nozzle coils wrapped around the chamber's spool piece. The efficiency improvement that results from a change in B depends less on the magnitude of B, and more on the gradient of B near the point of detachment. If a large axial gradient ∇B_z exists immediately prior to detachment, the trajectory angle becomes greater. A smaller magnetic field gradient results in a narrower trajectory. Using both positive and negative currents to custom tailor a shallow magnetic field gradient, the trajectories can be optimized to yield simulated nozzle efficiencies as high as 98%, as shown in Table 5.9.

Nozzle coil #1	Nozzle coil #2	Nozzle coil #3	η_{noz}
10A	3 A	3 A	0.91
40A	40 A	40 A	0.91
0A	0 A	0 A	0.87
0A	-20 A	35 A	0.98

Table 5.9: Nozzle efficiency for different simulated nozzle coil currents. Standard magnetic field conditions (1st entry) yielded 91% efficiency. Highest nozzle efficiency resulted from nozzle currents of 0 A, -20 A and 35 A.

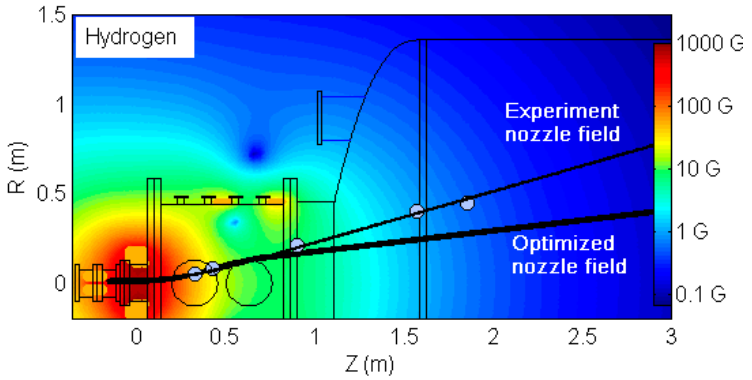

Figure 5.12: Magnetic field and plume trajectories optimized for nozzle efficiency. Applied nozzle currents of [0A, -20A, 35A] result in η_{noz} = 0.98.

Again, the efficiency improvements determined from simulation were not verified experimentally, and near 100% nozzle efficiency is probably not practically realizable. However these simulations highlight the importance of fully characterizing the rocket nozzle, and understanding the physical processes involved in magnetic detachment. Coupled with experimental verification, magnetic detachment simulations offer a valuable tool to future magnetic nozzle designers.

5.1.7 Limitations of the Quasi-1D simulation

Under standard magnetic field conditions, the quasi-1D simulations appear to predict plume profiles within measurement uncertainty. However certain operating conditions exist that could not be successfully modeled with this code. Section 4.0.1 dealt with the plasma source's response to increased magnetic field. These magnetic field conditions yielded much higher peak magnetic fields than the standard configuration: 2700 gauss vs. 700 gauss. In this preliminary experiment, the source magnetic field was decreased a factor of 6, leading to an increase in plume diameter by a factor of 1.5. When this condition is simulated using the above model however, the experimental results are not duplicated; simulated plume radii are too large by a factor of ~2. An adjustment of initial conditions within a range of experimental uncertainty was also unable to replicate the experimental results. This suggests a breakdown of the model under these much higher magnetic field conditions. The cause of this breakdown may be an indication of the need for a more comprehensive MHD simulation for the high n_e and B_z encountered in these conditions.

Also the cusp-magnetic field conditions given in Section 4.2 produced aberrant simulation results. The sharp reduction of magnetic field in the cusp field region resulted in high values of $\frac{d}{dz}B_z(z)$ that violate the quasi-1D, small divergence angle assumptions of the simulation. The resulting plume trajectories were strongly diverging for any initial conditions chosen, and do not approximate experimental results. Here too, significant factors not considered in the quasi-1D simulations are likely at play.

5.2 2D MHD simulations

A second code was developed by the University of Texas based on the ideal MHD equations. Details on the operation and underlying equations of this code can be found in [Breizman 2007] and are not discussed in detail here, as this code is mainly employed here to benchmark the quasi-1D code developed for this dissertation. The MHD model is an improvement over the previously discussed quasi-1D code in several regards. It is a two dimensional code allowing arbitrary radial density distribution, which allows for detachment contours rather than requiring the entire plume to detach at one axial position. As noted in Section 4.1.8, plasma β is not uniform across the plume radius due to the radial profile of density. The code also accounts for plasma diamagnetic currents, which will affect the total magnetic field within the plume. This provides for stretching of magnetic field lines as predicted by ideal MHD theory. However, also because the code uses ideal MHD theory, there is no provision for cross-magnetic field diffusion. Plasma density is effectively glued onto lines of constant magnetic flux, and cannot diffuse off of them. This may result in a more narrow density profile compared with the quasi-1D simulations if diffusion is important in this simulation regime.

5.2.1 MHD initial conditions

An MHD simulation was conducted approximating the conditions in the DDEX experiment. The initial conditions for this experiment were chosen to match the simulated plume conditions at z = 0.33 m at the upstream interferometer. These conditions are $n_{e,\max} = 1\text{x}10^{19}$ m^{-3}, R = 0.048 m, and v_z = 19 km/s. Additionally, a cold plasma (T_e = 0 eV) was assumed. This was done to disable ambipolar acceleration effects in the MHD code and to constrain v_z to a constant value. The initial conditions used in this MHD simulation begin at z = 0.33 m rather than at the plasma source at z = -0.15 m because without the capability to simulate cross-magnetic field diffusion, the resulting MHD trajectories are far too narrow. Even so, important details about the detachment process can still be modeled in this smaller scale simulation. Beginning with initial conditions at the upstream interferometer, downstream profiles are created and compared with both the quasi-1D simulation and experiment. An axisymmetric simulation area of width and length of 200x1000 units was utilized to provide adequate radial and axial resolution.

5.2.2 Plume profile comparison

The first comparison between the two simulations is made by comparing plume trajectories. Table 5.10 shows a summary of the density, velocity and profile width found at three axial positions from the MHD simulation. Not surprisingly, the MHD simulation compares favorably with both experiment and the 1D simulation, with density and profile widths coming within the error bars of experiment data, and coming within 10% of the quasi-1D simulations given in Section 5.1.5. The fact that the MHD

trajectory comes so close to quasi-1D simulations despite differences in the codes suggests that cross-magnetic field diffusion effects in this low- magnetic field downstream zone are negligible.

	MHD simulation	Quasi-1D Simulation	Measured values
Velocity, z = 0.33 m	**19 km/s**	19 km/s	---
Velocity, z = 0.43 m	**19 km/s**	19 km/s	15 km/s
Velocity, z = 1.85 m	**19 km/s**	19 km/s	19 km/s
R(z) , z = 0.33 m	**4.8 cm**	4.8 cm	5 cm
R(z) , z = 0.43 m	**7.9 cm**	6.9 cm	8.5 cm
R(z) , z = 1.85 m	**46 cm**	47 cm	45 cm
n_e, z = 0.33 m	**1×10^{19}**	9.6×10^{18}	1×10^{19}
n_e, z = 0.43 m	**4.1×10^{18}**	4.6×10^{18}	3.7×10^{18}
n_e, z = 1.85 m	**8.4×10^{16}**	9.9×10^{16}	1×10^{17}

Table 5.10: Comparison of MHD simulation results with quasi-1D and experiment results for plume radius and centerline density. Initial conditions at z = 0.33 m are set equal for MHD and quasi-1D simulations.

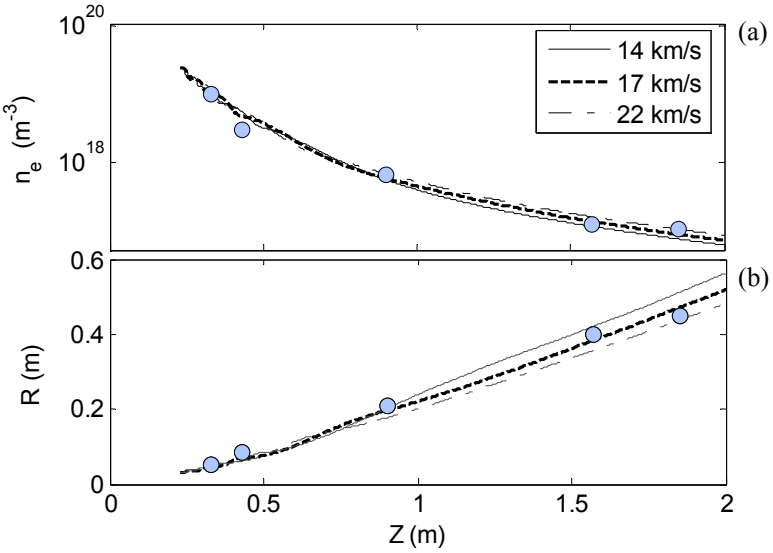

Figure 5.13: (a) MHD simulation results comparing plume centerline density (dashed line) with experimentally determined plume centerline density (circles). (b) MHD simulation results comparing plume ½-maximum radius (dashed line) with experimentally determined plume ½-maximum width (circles).

5.2.3 Vacuum vs. plasma magnetic fields

A major improvement in the MHD code vs. the quasi-1D code involves accounting for plasma currents, which influence applied magnetic fields. Azimuthal plasma current loops arise to oppose applied nozzle currents according to Lenz's law. The extent to which the applied field is reduced by the induced fields arising from diamagnetic currents depends on the kinetic energy available in the plasma flow. Results from the MHD simulation (Figure 5.14) show that the vacuum magnetic field can be reduced somewhat (up to 10-20%) on the plume centerline. The magnetic field reduction is less pronounced at the edges of the plume where the density is lower. There is also axial and radial variation in the magnetic field adjustment, which may just be numerical artifacts. Taking these issues into account, the diamagnetic current can be generalized to have the greatest effect at low magnetic field, shortly before detachment.

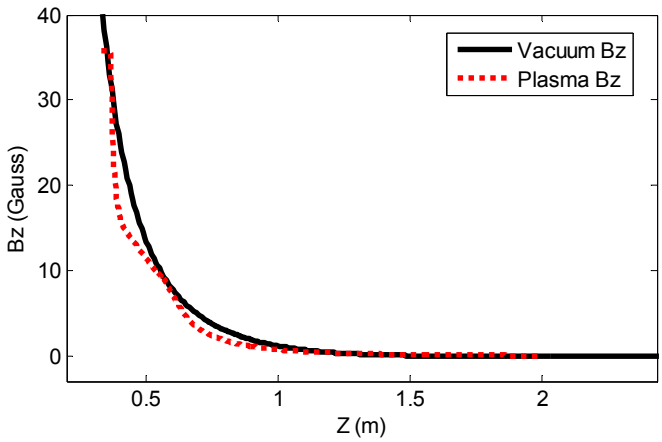

Figure 5.14: Comparison of plasma magnetic field with vacuum magnetic field for the MHD simulation, located on centerline. Some radial variation in plasma *B*-field is present, and not represented in this plot.

Despite the reduction in magnetic field, the plume profiles of the two simulations remain similar. What then would cause the two different simulations (1D and MHD) to lead to the same conclusions on profile shape? It is possible that the influence of cross-magnetic field diffusion in the 1D simulation performs a similar function to the diamagnetic current effects in the MHD simulation, resulting in slightly wider plume widths than would normally be expected. Another possibility is that the diamagnetic current provides negligible impact on the overall plume profile, and that the downstream plume width is determined mostly from initial conditions and the $\beta > 1$ position.

5.2.4 2D detachment contour

Another benefit of the 2D model is the ability to simulate 2D detachment contours. Since β is a function of n_e, v_z and B, the ratio of kinetic to magnetic energy density is much lower at the edges of the plasma column than on centerline, resulting in detachment occurring first at the plume's center. A 2-D plot of plasma β will show that rather than detaching at one axial position, the $\beta > 1$ detachment contour will extend out at an angle to the centerline. Figure 5.15 gives a 2-D contour plot of plasma β and shows the $\beta > 1$ contour stretching from $z = 0.4$ m on the plume centerline out past $z = 1.5$ at the plume edge. In fact, according to the MHD simulations, there is a tenuous outer portion of the plume that never reaches the $\beta = 1$ detachment condition, and is likely trapped on closed magnetic field lines barring other non-ideal factors. This can be seen by the fact that the trajectory angle at detachment increases with radial position to an angle approaching $\theta = 90^o$ at the plume edge.

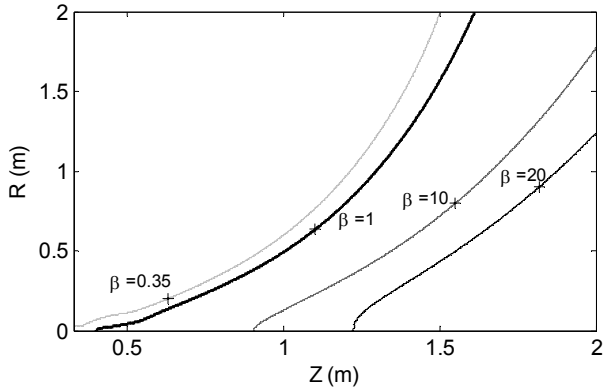

Figure 5.15: 2D Contour plots of plasma β showing lower β at the plume edge. If this were a 1D detachment contour, the $\beta = 1$ line would be vertical, and the plume trajectory angle would be constant with radius.

The effect of this 2D detachment contour and the trapped portion of the plume will unfortunately be to decrease the nozzle efficiency. Although the high-density core of the exhaust can detach and continue at a low trajectory angle, the tenuous outer plume detaches much later at a greater trajectory angle, if it detaches at all. This outer plume contributes less thrust to the overall total due to the higher cosine loss. The enhanced losses at the edges may also increase radial diffusion of the center plasma due to the increased density gradient.

5.2.5 2D simulation of nozzle efficiency

As stated above, the MHD simulations resulted in profile widths comparable to the quasi-1D simulations given similar upstream conditions. Although the ½ maximum profiles were similar, the 2D results show that a reduction in overall nozzle efficiency can be attributed to the tenuous outer portion of the plume which detaches at a much greater angle, if it detaches at all. According to MHD simulations, the overall nozzle efficiency is $\eta_{noz} = 85\%$ for the standard magnetic field configuration which represents a decrease of

5-6% compared to the quasi-1D simulations. The majority of this reduction arises from the ability to track a 2D detachment contour. The 2D simulation suggests that the core of the plume still detaches with high efficiency, while the plume edge detaches at lower efficiency representing a momentum flux decrease of ~6%. Figure 5.16 gives nozzle efficiency plots for the MHD simulations.

A second MHD simulation was run using the optimized magnetic field conditions theorized to increase efficiency in the quasi-1D simulation. The plasma initial conditions remained the same, while the magnet nozzle currents were adjusted to [0A, -20A 35A] rather than the standard coil currents: [10A, 3A, 3A]. Using the same analysis for efficiency as before, the nozzle momentum efficiency for the optimized MHD simulation was found to increase to 91%, a performance gain of 6%. As was the case with the quasi-1D simulation, carefully tailoring magnetic fields to reduce the magnetic field gradient in the area of $\beta > 1$ detachment yielded significantly improved efficiency.

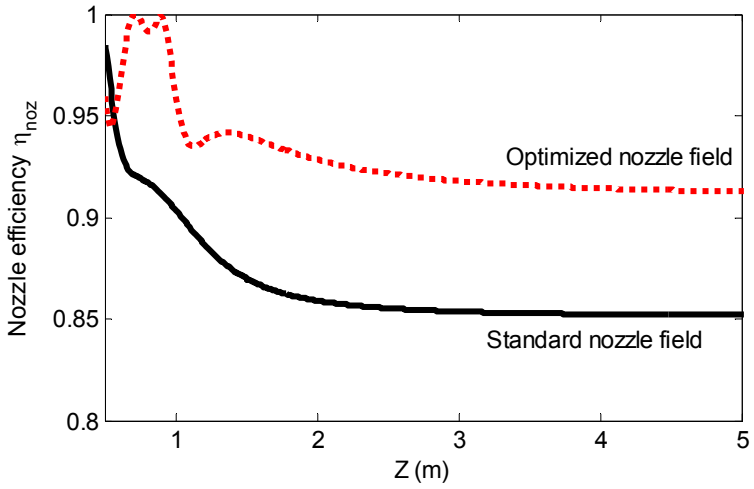

Figure 5.16: MHD simulations of nozzle efficiency η_{noz}. Standard nozzle field conditions show an efficiency of 85% while the optimized nozzle field yields η_{noz} = 91% and no nozzle coils yields η_{noz} = 83%. By comparison, quasi-1D simulations of the two conditions yielded nozzle efficiencies 4-7% greater.

Nozzle coil #1	Nozzle coil #2	Nozzle coil #3	**2D η_{noz}**	1D η_{noz}
10A	3 A	3 A	**0.85**	0.91
0A	0 A	0 A	**0.83**	0.87
0A	-20 A	35 A	**0.91**	0.98

Table 5.11: Comparison of simulated nozzle efficiency for quasi-1D simulation (from Table 5.9), and 2D MHD simulation. 2D simulations yield efficiency 4-7% lower than the equivalent 1D simulation due mostly to a 2-dimensional detachment contour that is less efficient.

Comparing the quasi-1D simulations with the MHD simulations serves to increase confidence in both models. This is particularly true because not only were experimental plume profiles successfully duplicated, but a theoretical nozzle efficiency increase found in one model was also found in the independent 2D simulation. The successful comparisons of the two codes in the mid-nozzle region and the far-nozzle region suggest that the effect of cross-magnetic field diffusion is small in this low B and n_e region. The slight difference between vacuum and plasma magnetic fields in the MHD code suggests that following vacuum magnetic fields in the quasi-1D code vs. plasma magnetic fields is an appropriate simplification. And the fact that plume half-maximum diameters were nearly identical for both simulations, while nozzle efficiency varied by 6-7% suggests that an inefficiency exists with the tenuous outer plume where detachment occurs later than in the high density core.

An important observation is that both simulations suggest that $\beta > 1$ magnetic detachment is occurring in the plume of the DDEX experiment.

5.3 Flow acceleration estimates

One assumption that has gone into both the 1D and 2D simulations that should be investigated in more depth is the assumption of constant velocity. As discussed in Sections 4.1.4, 4.1.5, and 4.1.6, some evidence exists for a slight increase in axial velocity from z = 0.33 m to z = 1.85 m. Flux conservation measurements with two simultaneous interferometers are consistent with a 15 +/- 10 % increase in flow velocity for hydrogen and 10 +/- 5% increase for helium. Ion density measurements based on Langmuir probe theory are best fit by the assumption that v_z increases by 20-25% between z = 0.43 m and z = 1.85 m. Also, an axial time of flight scan shows a similar increase for helium experiments.

A theoretical prediction of flow velocity increase can be based on Eq. (2.60), stating that conservation of magnetic moment leads to axial acceleration with magnetic field decrease:

$$v_{z1}^2 = v_{z0}^2 + v_{\perp 0}^2 \left(1 - B_1 / B_0\right) \tag{5.19}$$

This relationship is valid as long as the plume is magnetized. The above equation may provide a useful guide in predicting the change of axial velocity in this experiment. The initial conditions for hydrogen at z = 0.33 m are set equal to v_z = 14 km/s and $v_\perp$ equal to the thermal velocity $v_{th} = \sqrt{eT_e / M_i}$ at 1.2 eV: 10.7 km/s.

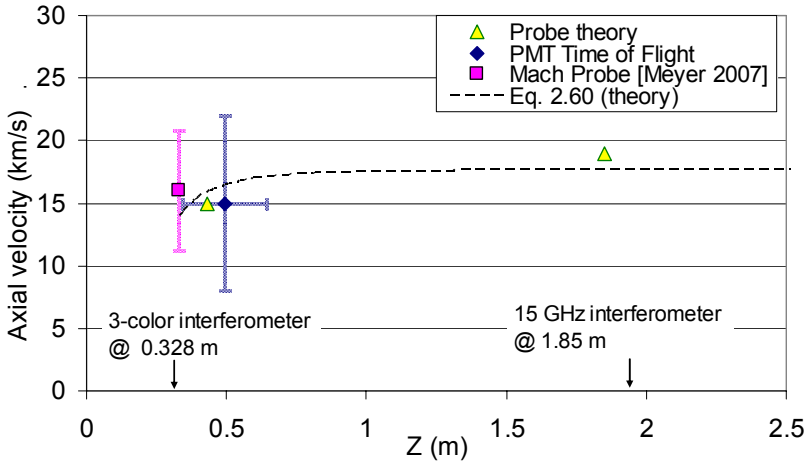

Figure 5.17: Comparison of theoretical velocity increase from Eq. (2.60) with measured velocity from Figure 4.24. Initial conditions at z = 0.33 m assumed are: v_z = 14 km/s and $v_\perp$ = 10.7 km/s. Predicted acceleration of 25% is consistent with experiment results.

According to Eq. (5.19), an acceleration of 25% is theorized between z = 0.33 m and z = 1.85 m. This falls within the error bars of velocity measurement, and conservation of flux measurements from Section 4.1.6. Due to the magnetic field drop-off, most of the acceleration occurs by z = 0.8 m before the $\beta > 1$ detachment point.

Likewise, helium simulations were produced with initial conditions taken at z = 0.43 m. v_z = 14 km/s while $v_\perp$ = the thermal velocity of helium at 1.4 eV: 5.8 km/s. An acceleration of 9% is predicted by Eq. (2.60) between z = 0.43 m and z = 1.85 m which is consistent with the conservation of flux measurements from Section 4.1.6 and is within error bars of experimental measurement.

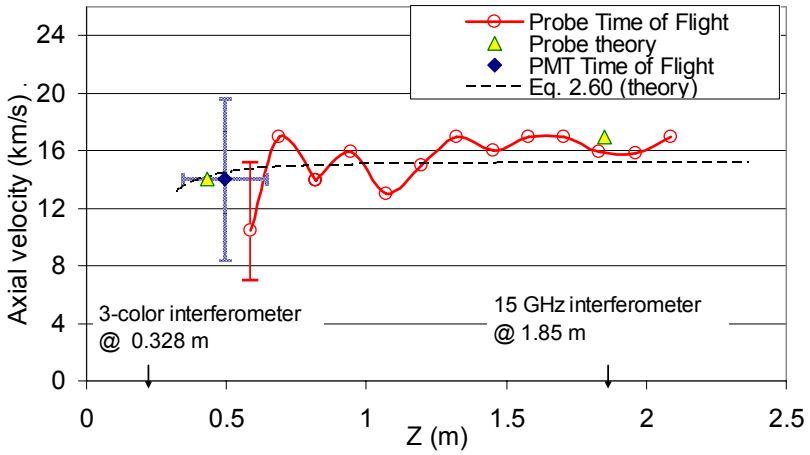

Figure 5.18: Comparison of theoretical velocity increase from Eq. (2.60) with measured velocity from Figure 4.23. Initial conditions at z = 0.43 m: v_z = 14 km/s and $v_\perp$ = 5.8 km/s. Predicted 9% acceleration is consistent with conservation of flux measurements from Section 4.1.6.

The results of these investigations suggest that some acceleration of the flow is consistent with both theory and experimental evidence. For simplicity's sake, numerical simulations in Sections 5.1 and 5.2 assumed a constant flow velocity. However, including the effect of flow acceleration in these simulations would produce only a small change in the final trajectory shape and nozzle efficiency. In fact, the nozzle efficiency would be improved by accounting for the conversion of perpendicular velocity to parallel directed motion.

CHAPTER 6

CONCLUSION

Several initial questions were posed in Chapter 1: Is magnetic detachment occurring in this experiment? Under what conditions will the magnetized plasma plume detach from its applied magnetic fields? And at what efficiency will this detachment occur? These questions were addressed to varying degrees through the course of this dissertation. In addition, results from analysis of the experiment setup and diagnostic devices were discussed, reducing the uncertainty of some of the experimental data.

In areas where the key questions posed in the introduction were not completely answered, suggestions are given for further avenues of research. In addition, as is the case with most successful experiments, new questions were raised that must be dealt with in turn.

6.1 Summary of findings

The DDEX experiment was one of the first to study a magnetized plasma exiting a magnetic nozzle and transitioning from low to high β ($\beta = m_i n_i \mu_0 v_i^2 / B^2$). Several experimental findings are presented, along with a summary of findings derived from matching numerical simulations.

6.1.1 Experiment results

A neutral background pressure analysis was conducted for the experiment's vacuum chamber, indicating that neutral collisions during the plasma pulse are less significant towards the beginning of a pulse, if at all. A long collisional mean free path during this time was the result of the experiment's large vacuum tank and fast pumping speed. The pressure analysis was backed up by conservation of flux measurements that showed little to no density spike at the downstream interferometer, which would have been evident in the event of significant ion-neutral collisions. This finding suggests collisional dissipation did not significantly influence measured plume trajectories, but may have resulted in slight deceleration towards the end of a pulse.

The effect that changing the magnetic field had on the plume width was investigated by adjusting the magnetic coil currents in the plasma source and in the magnetic nozzle. One conclusion of the test in Section 4.0.1 was that changing the coil current at the plasma source resulted in significant changes in the plume profile at an upstream location. However, in Section 4.2, similar changes in the nozzle coil currents even to the point of creating a reverse (cusp) magnetic field did not significantly affect plume profiles. This qualitatively suggests that the plasma in this experiment was confined by magnetic fields at the plasma source where β is low, but continues unimpeded by applied magnetic fields at a position where $\beta > 1$.

The subject of magnetic detachment was further investigated by comparing experimentally determined plume widths with simulated trajectories. Two independent

simulations predicted similar trajectories given the condition that high- β plasma is free from the influence of applied magnetic fields. This corresponds with the theory that magnetic detachment does occur for magnetized plasmas, and that its onset condition is $\beta > 1$. A slightly adjusted simulation that substituted the detachment condition $r_{ci} > R(z)$ for $\beta > 1$ also yielded similar plume trajectories, and so the exact mechanism for plasma detachment remains a bit uncertain, although $\beta > 1$ is the favored theoretical mechanism, and was a better fit to experimental results.

An estimate of ion flow velocity was also given based on direct experimental measurements, flux conservation estimates and conservation of magnetic moment theory. All three methods agree within error bars, and suggest a 10-30% axial acceleration, with hydrogen experiencing more acceleration than helium. While trajectory simulations assumed constant velocity for simplicity's sake, a variable velocity would not substantially affect the predicted density profiles. In fact the primary result of plume acceleration would be an improvement in estimated nozzle efficiency.

6.1.2 Simulation results

Other major findings resulting from simulations are as follows. Two independent numerical codes were employed – one assuming 1D profile shapes, and the second allowing for 2D profiles. The 1D code accounted for cross-field diffusion approximately equivalent to classical diffusion, and the 2D code solved the ideal MHD equations which do not account for cross-field transport. Despite the different architectures and assumptions, the two codes yielded nearly identical plume widths when starting with the

same magnetic field profile and plume initial conditions. This independent verification and benchmarking against experimental results helped to increase the confidence in both codes.

The two simulations also produced nozzle (thrust) efficiency estimates. Due to certain 1D assumptions, the 1D code results in a 4-7% over-estimate of nozzle efficiency in comparison with the 2D MHD code. In both cases, nozzle efficiency asymptotically approaches a constant value beyond the axial position where $\beta > 1$. When surveying a number of magnetic field configurations, the 2D code reports a nozzle efficiency of 83% for a simple magnetic dipole, or 91% for an optimized nozzle. Both efficiency estimates assume a constant ion flow velocity, which may not be the case; ion acceleration may improve the actual nozzle efficiency. These results, while unverified experimentally, help to highlight the importance of properly designing and characterizing the nozzle region of a potential thruster.

6.1.3 Diagnostic theory

Standard diagnostics theory was re-visited for the experimental conditions found herein. Specifically, Langmuir triple-probe theory was extended to make it compatible with a supersonic plasma plume. Prior theory was analyzed by computer simulations of current collected to a biased cylinder. For the experimental conditions considered in this work, an electron temperature calibration factor of 8-14% was deemed necessary, which fits within the measurement uncertainty of 15%-20%. General simulations were also considered including a number of flow velocities (M = 0-3.5) and probe dimensions (r_0 =

1-90). The results indicate that the T_e calibration factor is only weakly dependent on ion Mach number, and much more dependent on probe radius r_0. For probe radius to Debye length ratios of $r_0 > 70$, the T_e correction term is insensitive to both ion Mach number and probe bias. For a stationary plasma ($M = 0$) the simulations compared favorably with prior OML simulations at the small probe limit ($r_0 = 1$) and with ideal thin-sheath theory at the large probe limit ($r_0 = 90$).

A novel hybrid method of accurately determining density profiles was also developed based on RF interferometer and Langmuir probe measurements. This method was employed during the experiment, and yielded density measurement uncertainty of 9%-15%, which is on the order of the RF interferometer accuracy. A detailed error analysis was conducted for this method, in addition to a sensitivity analysis which determined the hybrid method to be relatively tolerant of errors in radial position and RF interferometer noise.

6.2 Future work

Some questions were not fully answered by this work and will require further investigations to be resolved. More experimental effort is necessary to fully understand nozzle efficiency and magnetic detachment in alternate magnetic field topologies. Also, the role of diffusion and other cross-magnetic field transport in this experiment remains unclear.

Computer simulations in Chapter 5 indicate that magnetic detachment is occurring when $\beta > 1$. Several details of the simulations remain unresolved however, including the influence of cross-magnetic field diffusion and diamagnetic currents. Although the 1D and MHD codes each only included one of the effects respectively, the resulting profile shapes were very similar, begging the question whether diffusion is an important effect at all, and if so, how should it properly be incorporated into a computer simulation. An additional uncertainty is the importance of ion cyclotron radius r_{ci} in detachment. Since the condition $r_{ci} > R(z)$ coincided fairly closely with the condition $\beta > 1$ in this experiment, it was difficult to exclude it as a magnetic detachment mechanism. Future experiments may be designed which make this distinction clear.

One of the questions posed in Chapter 1: "with what efficiency does the plume detach?" can only be partially answered. Experimental verification is required, entailing plasma density and flow velocity measurements at multiple radial positions, and at a distance sufficiently downstream to be considered detached. Density and profile shape were successfully determined in this experiment, but multiple radial velocity measurements were not made, particularly with low enough uncertainty to give accurate nozzle efficiency estimates. In addition, the downstream radial profile was only measured out to the half-maximum radius, which is not enough to accurately map the detached plume profile. A more accurate flow velocity measurement, when integrated with density over the entire radial profile, will provide the total momentum flux, and therefore the thrust and efficiency. Also, performing this operation during several different magnetic nozzle configurations, and comparing with simulated nozzle efficiencies will greatly improve

the confidence in the computer models, and their ability to predict nozzle efficiency improvements.

Another way in which this research can be applied in the future is to an actual proposed magnetized plasma thruster. The Ad Astra Rocket Company is in the process of evaluating a dual-stage plasma source utilizing a helicon antenna to create a high density plasma and an ion cyclotron resonance antenna to accelerate it. The thruster, termed VASIMR is part of the motivation for this research, and its development would benefit from these findings. A parametric study of VASIMR's nozzle efficiency using the techniques described in this dissertation would be useful for systems modeling and future design modifications.

Another avenue for further research includes better assessing the conditions seen during the cusp- coil experiment (Section 4.2), and the gun current experiment (Section 4.0.0). The 1D and 2D numerical simulations used to explain the majority of the experimental results of this dissertation appear to break down during these two special cases. The high magnetic fields and large magnetic field divergence under these conditions may require a more accurate diffusion simulation, or the invoking of new physics. In particular, the large magnetic curvature seen in the cusp magnetic field experiment has similarities to the experiments of Schmidt [Schmidt 1960], Ishizuka et al. [Ishizuka 1982] and Brenning et al. [Brenning 2005] . In these experiments, anomalous cross-magnetic field transport was identified and attributed to spontaneous high frequency electric field formation and E x B drift. Further diagnostics of the DDEX experiment with high frequency electrostatic

probes could determine if such processes are occurring during extreme cusp field conditions in this experiment.

In conclusion, much is still unknown about plasma detachment from magnetic fields. However, this dissertation has discussed methods and diagnostics that may be applied to the nozzle region of high powered magnetized plasma thrusters, and has identified possible physical effects occurring in this region. Further experiment and modeling is necessary to refine our knowledge of the nozzle region of thrusters, and will help improve the efficiency of the devices that may someday be carrying probes or humans far outside the earth-moon system.

APPENDICES

APPENDIX A

Error analysis for the Hybrid method

Error analysis for the hybrid measurement method was conducted based on standardized uncertainty. [Coleman, 1999] [Taylor, 1994] In the statistical analysis of a multivariable function, each individual element of uncertainty is weighted mathematically, to determine the function's overall level of uncertainty. Our function in question is n_i from Eq. (2.46):

$$n_i = V_i \alpha = V_i \left[\sum_{j=1}^{M} \frac{V_j}{N_j} \Delta x_j \right]^{-1} = f(V_j, N_j, \Delta x_j) \tag{A.1}$$

which is based on three independent measurements, each contributing to the overall error. Statistical analysis replaces each of the three variables $V_j, N_j, \Delta x_j$ with a normal distribution centered about the measured value, and with standard deviation $\sigma_{V_j}, \sigma_{N_j}, \sigma_{\Delta x}$. These sigma values represent the individual uncertainty in each of the three measurements. Likewise, σ_{n_i} represents the total overall error in the density measurement.

The position error $\sigma_{\Delta x}$ is assumed constant for all shots *i* and all time *t* and therefore has no subscript *j*. The position error is estimated to be half the incremental resolution of the translation stage x-axis, equal to 1.8º times the 0.25" / revolution screw pitch, with $\sigma_{\Delta x} / \Delta x = 0.125$ %.

The interferometer measurement error σ_{N_i} varies with shot number *i* and time *t*. For the upstream interferometer, σ_{N_i} is determined from the spread in densities among the three independent frequency channels of the instrument. For the downstream interferometer, σ_{N_i} is determined by Monte Carlo error analysis as detailed in Appendix B. Typical values of σ_{N_i} / N_i are 2-3% for the upstream interferometer and 4-5% for the downstream interferometer.

The probe voltage measurement error σ_{V_i} is set equal to the RMS value of steady state probe voltage prior to and directly following a plasma shot. This no-plasma condition gives a good estimate of random fluctuation in the probe voltage. While the probe data (taken at 50 kHz) is time averaged over ten samples for synchronization with the interferometer data (taken at at 40 kHz), σ_{V_i} is determined from un-averaged data to account for high speed fluctuations which may contribute to error. σ_{V_i} is then held constant with time for each plasma shot *i,* with $\sigma_{V_i} \sim$ 4-5 mV**.** σ_V / V is on the order of σ_N / N or greater for all of the data presented here.

We now derive the equation for σ_{n_i}, which neglecting correlations and considering bias and random errors together, is (from Taylor, 1994 eq. A-3):

$$\sigma_{n_i}^2 = \sum_{j=1}^{M} \left[\left(\frac{\partial n_i}{\partial V_j} \right)^2 \sigma_{V_j}^2 + \left(\frac{\partial n_i}{\partial N_j} \right)^2 \sigma_{N_j}^2 + \left(\frac{\partial n_i}{\partial \Delta x} \right)^2 \sigma_{\Delta x}^2 \right] \tag{A.2}$$

where

$$\frac{\partial n_i}{\partial V_j} = V_i \frac{\partial \alpha}{\partial V_j} + \alpha \delta_{ij} \tag{A.3}$$

$$\frac{\partial n_i}{\partial \Delta x} = \frac{-V_i \alpha}{\Delta x} \tag{A.4}$$

and

$$\frac{\partial n_i}{\partial N_j} = V_i \frac{\partial \alpha}{\partial N_j} \tag{A.5}$$

From Eq. (2.45): $\alpha = \left[\sum_{j=1}^{M} \frac{V_j}{N_j} \Delta x \right]^{-1}$, the partial derivatives of α are:

$$\frac{\partial \alpha}{\partial V_i} = -\left[\sum_{j=1}^{M} \frac{V_j}{N_j} \Delta x \right]^{-2} \frac{\Delta x}{N_i} = -\alpha^2 \frac{\Delta x}{N_i} \tag{A.6}$$

and

$$\frac{\partial \alpha}{\partial N_i} = \left[\sum_{j=1}^{M} \frac{V_j}{N_j} \Delta x \right]^{-2} \frac{V_i}{N_i^2} \Delta x = \alpha^2 \frac{V_i}{N_i^2} \Delta x \tag{A.7}$$

Therefore,

$$\sigma_{n_i}^2 = \sum_{j=1}^{M}\left[\left(V_i\frac{\partial\alpha}{\partial V_j}+\alpha_0\delta_{ij}\right)^2\sigma_{V_j}^2+\left(V_i\frac{\partial\alpha}{\partial N_j}\right)^2\sigma_{N_j}^2+\left(V_i\frac{\partial\alpha}{\partial\Delta x}\right)^2\sigma_{\Delta x}^2\right] \tag{A.8}$$

$$= M\frac{V_i^2\alpha^2}{\Delta x^2}\sigma_{\Delta x}^2+\sum_{j=1}^{M}\left[\left(-V_i\alpha^2\frac{\Delta x}{N_j}+\alpha\delta_{ij}\right)^2\sigma_{V_j}^2+\left(V_i\alpha^2\frac{V_j}{N_j^2}\Delta x\right)^2\sigma_{N_j}^2\right]$$

$$= M\frac{V_i^2\alpha^2}{\Delta x^2}\sigma_{\Delta x}^2+\sum_{j=1}^{M}\left\{\left(V_i\alpha^2\frac{\Delta x}{N_j}\right)^2\sigma_{V_j}^2+\left(V_i\alpha^2\frac{V_j}{N_j^2}\Delta x\right)^2\sigma_{N_j}^2+\delta_{ij}\left(\alpha^2-2V_i\alpha^3\frac{\Delta x}{N_j}\right)\sigma_{V_j}^2\right\}$$

$$= \alpha^2\left[M\left(\frac{V_i^2}{\Delta x^2}\right)\sigma_{\Delta x}^2+\left(1-2V_i\alpha\frac{\Delta x}{N_i}\right)\sigma_{V_i}^2\right]+\left(\alpha^2\Delta x V_i\right)^2\sum_{j=1}^{M}\left[\left(\frac{\sigma_{V_j}^2}{V_j^2}+\frac{\sigma_{N_j}^2}{N_j^2}\right)\left(\frac{V_j^2}{N_j^2}\right)\right]$$

Until we finally have:

$$\sigma_{n_i}^2 = \alpha^2V_i^2\left\{\left(1-2V_i\alpha\frac{\Delta x}{N_i}\right)\frac{\sigma_{V_i}^2}{V_i^2}+M\frac{\sigma_{\Delta x}^2}{\Delta x^2}+\alpha^2\Delta x^2\sum_{j=1}^{M}\left[\frac{V_j^2}{N_j^2}\left(\frac{\sigma_{V_j}^2}{V_j^2}+\frac{\sigma_{N_j}^2}{N_j^2}\right)\right]\right\} \tag{A.9}$$

This can be stated as a percentage of the total density measurement by dividing by $n_i^2=\alpha^2V_i^2$:

$$\frac{\sigma_{n_i}^2}{n_i^2} = \left(1-2V_i\alpha\frac{\Delta x}{N_i}\right)\frac{\sigma_{V_i}^2}{V_i^2}+M\frac{\sigma_{\Delta x}^2}{\Delta x^2}+\alpha^2\Delta x^2\sum_{j=1}^{M}\left[\frac{V_j^2}{N_j^2}\left(\frac{\sigma_{V_j}^2}{V_j^2}+\frac{\sigma_{N_j}^2}{N_j^2}\right)\right] \tag{A.10}$$

where $\sigma_{N_j}, \sigma_{V_j}, \sigma_{\Delta x}$ are the standard deviations for $N_j, V_j, \Delta x$ respectively. A 2-sigma (95%) error bar for the measured value n_i may be taken as $\pm 2\sigma_{n_i}$.

The sensitivity of the density error σ_{n_i} was investigated with respect to the measurement errors $\sigma_{N_j}, \sigma_{V_j}, \sigma_{\Delta x}$. Assuming, for simple illustrative purposes, a flat radial profile and fixed errors. Eq. (A.10) is re-stated:

$$\frac{\sigma_n^2}{n^2} = \frac{1}{M}\left[(M-1)\frac{\sigma_V^2}{V^2} + \frac{\sigma_{\Delta x}^2}{\Delta x^2} + \frac{\sigma_N^2}{N^2}\right] \tag{A.11}$$

This illustrates the relative weight of the probe voltage error σ_V. The point density error σ_n tends to scale directly with σ_V, but scales as $1/\sqrt{M}$ with σ_N and $\sigma_{\Delta x}$. Thus the hybrid approach is more tolerant of interferometer errors and translation stage position errors than of errors in the probe voltage measurement. This suggests that care should be taken to reduce the random noise in the Langmuir probe measurement path as this disproportionately affects the final measurement error.

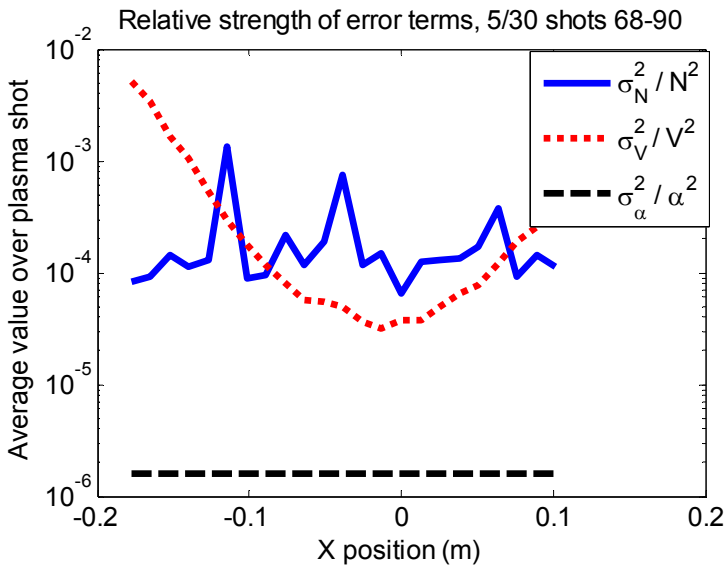

Figure A.1: Relative strength of error terms for a sample radial profile measurement. This shows the relative unimportance of the ΔX term in the error analysis and the relative importance of the probe voltage, particularly towards the edges of the plume.

For the upstream measurements, an additional term may be added to account for any errors introduced by the axial offset correction, $\sigma_{N_j}^2 \to \sigma_{N_j}^2 + \sigma_\gamma^2$. This error is difficult to quantify statistically but is assumed to no more than double the error in interferometer measurement.

APPENDIX B

Monte Carlo simulations of interferometer error and plume width error

When attempting to define the error bounds of a complicated multivariable function, it is sometimes easier to run a number (several thousand) of simulations with each of the input variables being changed by a small delta, chosen randomly from a normal distribution with width equal to the uncertainty of that input measurement. The output function will then change randomly due to the small changes of the input parameters. The output distribution's standard deviation gives a good measure of the overall uncertainty without having to determine it analytically. Monte Carlo simulation is a powerful statistical tool brought to bear on two particular problems – the first being an estimate of error in the 15 GHz interferometer measurement, and the second being an estimate of error in determining plasma column width measurements.

B.1 15 GHz interferometer error analysis

Two sources of error are assumed to contribute to the overall uncertainty in the interferometer measurement. The first is random fluctuations in the plasma measurement voltage, and the second is uncertainty in fitting the calibration constants to the calibration data. As shown in Figure 3.23 and Table 3.1 there is a 2-5% RMS error in fitting the

calibration data to the interferometer model. The calibration constant uncertainties represent systematic errors, "fossilized" from the calibration data. [Moffat, 1988] This discrepancy contributes to the overall uncertainty in the interferometer measurement. A method similar to [Dobson, 2004] was followed to determine the overall effect of this error.

A Gaussian distribution is used composed of V_i, $\bar{C}_i$ for the Monte Carlo simulation:

$$\bar{C}_i \equiv \bar{C}_0 \pm \sqrt{2} y_i \bar{\sigma}_C \tag{B.1}$$

$$V_i \equiv V(t) \pm \sqrt{2} y_i \sigma_V \tag{B.2}$$

where $V(t)$ is the microwave interferometer voltage measurement at time t, and $\bar{\sigma}_C, \sigma_V$ are the standard deviations of the calibration vector and interferometer random fluctuation respectively. σ_V is set equal to the standard deviation of the interferometer signal prior to plasma turn-on. y_i are derived from random numbers x_i such that $\mathrm{erf}[y_i] = x_i ; x_i = \{0..1\}$. For these simulations, i can be as high as 1000 to reach steady state. Each dimension k of the vector in Eq. (B.1) can be written separately:

$$C_{k,i} \equiv C_{0,k} \pm \sqrt{2} y_i \sigma_{C,k} \tag{B.3}$$

where $k = \{1..4\}$ for the four-element fit to Eq. (2.28) or $k = \{1..7\}$ for the seven-element fit to Eq. (2.30). $C_{0,k}$ then represents the best-fit calibration coefficients to the corresponding interferometer model. $C_{k,i}$ are elements of the Gaussian distribution $f(C_k)$ centered around $C_{0,k}$ with standard deviation $\sigma_{C,k}$. The derivation of $\sigma_{C,k}$ is as follows. The sum of squares residue *Res* from the calibration model is:

$$Res = \sum_{n=1}^{N} \left[V_n - \tilde{V}\left(x_n; C_{0,k}\right) \right]^2 \tag{B.4}$$

where V_n is the microwave interferometer signal voltage measured at calibration motor position x_n for $n = \{1..N\}$. A theoretical residue Res' was defined:

$$Res'(\bar{C}) = \sum_{n=1}^{N} \left[\tilde{V}(x_n; \bar{C}_0) - \tilde{V}(x_n; \bar{C}) \right] \cong \sum_{n=1}^{N} \sum_{k=1}^{K} \left[\frac{\partial \tilde{V}}{\partial C_k} \left(C_k - C_{0,k} \right) \right]^2 \tag{B.5}$$

and the $\sigma_{C,k}$ were determined from the conditions that (1) the mean value of Res' be equal to the measured residue from (B.4):

$$\overline{Res'(\bar{C})} \cong \sum_{k=1}^{K} \sigma_{C,k}^2 \sum_{n=1}^{N} \left(\frac{\partial \tilde{V}}{\partial C_k} \right)^2 = Res \tag{B.6}$$

and (2) the individual errors be proportional, statistically, to $\left(\partial \tilde{V} / \partial C_k \right)^{-1}$:

$$\sigma_{C,k}^2 \sum_{n=1}^{N}\left(\frac{\partial \tilde{V}}{\partial C_k}\right)^2 \cong \sum_{n=1}^{N}\left[\tilde{V}(x_n;C_0)-\tilde{V}(x_n;C_0+\hat{c}_k\sigma_{C,k})\right]^2 = \frac{Res}{K} \tag{B.7}$$

The quantity $\frac{\partial \tilde{V}(x_n;C_k)}{\partial C_k}$ is solved for each of the four elements in a modified version of Eq. (2.28):

$$\tilde{V}(x_n;C_k) = C_1\cos\left(C_2x_n + C_3\right) + C_4 \tag{B.8}$$

Resulting in the following:

$$\frac{\partial \tilde{V}(x_n)}{\partial C_1} = \cos\left(C_3 + C_2x_n\right) \tag{B.9}$$

$$\frac{\partial \tilde{V}(x_n)}{\partial C_2} = -C_1\sin\left(C_3 + C_2x_n\right)x_n \tag{B.10}$$

$$\frac{\partial \tilde{V}(x_n)}{\partial C_3} = -C_1\sin\left(C_3 + C_2x_n\right) \tag{B.11}$$

$$\frac{\partial \tilde{V}(x_n)}{\partial C_4} = 1 \tag{B.12}$$

The quantity $\sum_{n=1}^{N}\left(\frac{\partial \tilde{V}(x_n;C_k)}{\partial C_k}\right)^2$ is then solved numerically for the calibration data. A large number of data points $n = \{1000..12000\}$ is used which extends over a 2π cycle of

the interferometer signal. The standard deviations $\sigma_{C,k}$ are found from Eq. (B.7), with the fit residue *Res* determined from the sum of squares error that is reported from the curve fitting tool **cftool** in Matlab. Sample data for one channel of the 15 GHz interferometer is as follows:

Sum of Squares error:	*Res* = 0.285			
$\sum_{n=1}^{N}\left(\frac{\partial\tilde{V}}{\partial C_k}\right)^2$	C_1 = 5180	C_2 = 508	C_3 = 9.8	C_4 = 11000
σ_{Ck}:	σ_{C1} = 3.71 x10^{-3}	σ_{C2} = 1.2 x10^{-2}	σ_{C3} = 8.5 x10^{-2}	σ_{C4} = 2.6 x10^{-3}

Table B.1: Sample data for the I channel of MWI2 interferometer. Calibration 4/27/06 shot 64. *n* = {1000..12000}

Once the necessary $\sigma_{C,k}$ and σ_V are determined, the Monte Carlo simulation can be conducted using Eqs. (B.2), (B.3), (2.30) and (2.33). V_i and $C_{k,i}$ are chosen randomly from their respective Gaussian distributions and used in Eq. (2.33). The resulting phase is used in (2.25) to determine the line integral plasma density. Over several thousand random choices of V_i and $C_{k,i}$ an output distribution of N_e density is obtained, with mean $N_{e,0}$ and standard deviation σ_N. The uncertainty in the interferometer measurement is then stated as equal to $2\sigma_N$ which is a 95% confidence interval around the interferometer measurement.

B.2 Plume width error analysis

A similar technique to B.1 was pursued to determine the error in the measurement of plume column diameter *w*. At any point in time, the radial density profile *n*(*r*) can be fit to a theoretical Gaussian distribution:

$$\tilde{n}(r) = n_{\max} e^{\frac{-(r-r_0)^2}{2w_0^2}} \tag{B.13}$$

by minimizing the profile fitting residue *Res*:

$$Res = \sum_{m=1}^{M} \left[n(r_m) - \tilde{n}\left(r_m; r_0; w\right) \right]^2 \tag{B.14}$$

with *w* equal to the $1/\sqrt{e}$ radius. In order to determine the uncertainty for the plume width *w*, a Monte Carlo simulation replaces the measured density $n(r_m)$ with

$$n_i \equiv n(r_m) \pm \sqrt{2} y_i \sigma_n \tag{B.15}$$

where σ_n is the standard deviation of density uncertainty from Eq. (A.9) and y_i are derived from random numbers x_i such that $\text{erf}\left[y_i\right] = x_i ; x_i = \{0..1\}$. By propagating density uncertainties forward, the profile fit is calculated over several thousand random changes to n_i. The resulting Gaussian distribution of *w* is centered about the measured value w_0 with a standard deviation. The uncertainty in plume width is defined as $2\sigma_w$ which corresponds to a 95% confidence interval about the measured plume width.

B.3 Abel Inversion error analysis

An estimate of the experimental uncertainty from using the Abel inversion method can also be found using a method similar to that shown in B.1. The analytic function used to determine $\tilde{N}_e(y)$ is (from Eq. (2.38)):

$$\tilde{N}_e(y) = \left[C_2 \exp\left(\frac{-(y-C_3)^2}{C_1^2} \right) \right] \tag{B.16}$$

by minimizing the fit residue *Res*:

$$Res = \sum_{n=1}^{N} \left[N(y_n) - \tilde{N}(y_n; C_1; C_2; C_3) \right]^2 \tag{B.17}$$

Using Eq. (B.7) the quantity $\frac{\partial \tilde{V}(x_n; C_k)}{\partial C_k}$ is solved for each of the calibration coefficients in (B.16):

$$\frac{\partial \tilde{N}}{\partial C_1} = \frac{2C_2 \exp\left(-\frac{(y-C_3)^2}{C_1^2} \right)(y-C_3)^2}{C_1^3} \tag{B.18}$$

$$\frac{\partial \tilde{N}}{\partial C_2} = \exp\left(-\frac{(y-C_3)^2}{C_1^2} \right) \tag{B.19}$$

$$\frac{\partial \tilde{N}}{\partial C_3} = \frac{2C_2 \exp\left(-\frac{(y-C_3)^2}{C_1^2}\right)(C_3 - y)}{C_1^2} \tag{B.20}$$

The Matlab function cftool is used to determine the sum of squares error *Res* over the 45-point radial profile. A single time point t = 0.8 msec is chosen to simplify the error analysis. The sum of squares error at this time point is *Res* = 3.87x10^{32}. The quantity $\sum_{n=1}^{N}\left(\frac{\partial \tilde{V}(x_n;C_k)}{\partial C_k}\right)^2$ is then solved numerically, and Eq. (B.7) is again used to calculate the various σ_{Ck} error terms:

Sum of Squares error:	*Res* = 3.87x10^{32}		
C_k:	C_1 = 0.056 m	C_2 = 4.7x10^{16} m^{-2}	C_3 = 0.02 m
σ_{Ck}:	σ_{C1} = 3.5 x10^{-3}	σ_{C2} = 2.4 x10^{15}	σ_{C3} = 3.0 x10^{-3}

Table B.2: Abel inversion best-fit coefficients and their associated uncertainty interval. Data taken at t = 0.8 msec over a 45 point radial profile.

We can immediately determine the uncertainty term in the plume width from Eq. (2.39), since the plume width is purely a function of C_1. Given that the value of C_1 at t = 0.8 msec is C_1 = 0.056 m, the 2σ uncertainty is 0.007 m, or 12.5%.

The uncertainty in the amplitude in Eq. (2.39) is the RMS combination of σ_{C1} and σ_{C2}:

$$\sigma_{\text{ampl}} = \sqrt{\left(\frac{\sigma_{C2}}{C_2}\right)^2 + \left(\frac{\sigma_{C1}}{C_1}\right)^2} \tag{B.21}$$

This leads to a 2σ amplitude uncertainty of 16%.

APPENDIX C

VASIMR data and results

C.1 Overview

The VASIMR™ thruster (VAriable Specific Impulse Magnetoplasma Rocket) is a dual-stage plasma rocket employing helicon waves to create a plasma, and ion cyclotron resonance frequency waves (ICRF) to accelerate it. [Chang-Diaz 2000, Arefiev 2004] The thruster employs high magnetic fields (~1 T) and high power (> 60 kW peak) for the present configuration. The project was previously run by the NASA Advanced Space Propulsion Lab (ASPL), Houston TX. A congressional Space Act Agreement in June 2005 allowed the VASIMR™ technology to become privatized, and NASA ASPL was transformed into a private entity named Ad Astra Rocket Company. Prior to privatization, the experiment was operating in the VX-50 (50 kW total power) configuration. After 2006, the experiment underwent a power upgrade and was renamed VX-100. (100 kW total power) Certain details of this latter experiment's construction and performance remain restricted due to proprietary and State Department regulations.

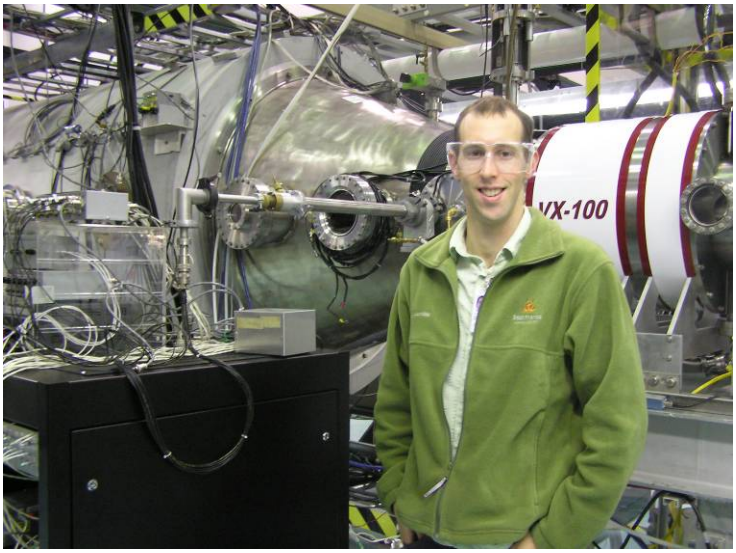

Figure C.1: The author in front of the VX-100 laboratory experiment. The left side of the picture shows the 4 m^3 vacuum dump tank connected to the conical expansion section. Electrical feedthroughs and viewports allow access to the plasma in this expansion section.

C.2 Experiment Setup

The VX-50 experiment consists of a linear arrangement of a gas injector, magnetic coils, helicon antenna, ICRF antenna, expansion cone and vacuum tank. The magnets used to produce the magnetized plasma were changed out for the VX-100 experiment, as were the antennas and other internal structures. The external pumping system and expansion chamber remain the same however, as do the plasma diagnostics. The general configuration of the VX-100 also remains the same as the VX-50 experiment. Where certain details of the VX-100 construction can not be included, a description of the VX-50 construction will be substituted.

C.2.1 Vacuum tank and magnetic field profile

A detailed model of the VX-50 experiment is shown in Fig. C.2. Four separate magnet coils produce the magnetic field configuration in the VX-50 experiment. When optimized for deuterium (as shown in Fig. C.2) the magnetic field peaks at 0.7 T with wide plateaus in the vicinity of the helicon antenna and the ICRF antenna. A similar profile is used in the VX-100 experiment, although upgraded water cooled magnets allow operation up to 2 Tesla which improves performance on heavier gasses (Neon and Argon).

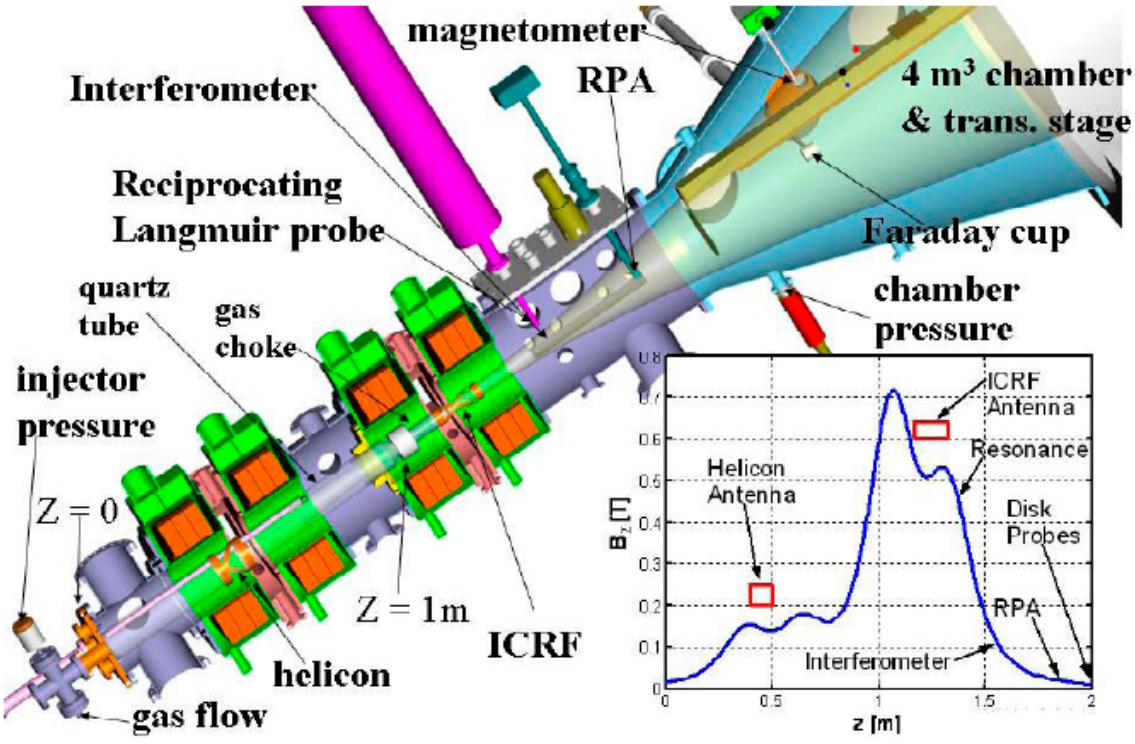

Figure C.2: VX-50 configuration and magnetic field profile. This profile is tailored for operation on deuterium.

The experiment is connected to a 4 m^3 vacuum tank which serves as a neutral gas dump. Neutral background pressure is high in this tank, peaking at $1x10^{-3}$-$1x10^{-4}$ Torr during a shot. The plasma is highly collisional in this region, making measurements of thrust and efficiency meaningless here. Measurements just downstream of the ICRF antenna do not suffer from the high collision rate, and upstream neutral pressures are lower. Therefore, diagnostics are placed as close to the last magnet as possible to mitigate the effect of ion-neutral collisions.

C.2.2 Experiment conditions

The experimental data considered here was collected over several shots on March 2, 2007. The VX-100 device was operating in helicon-only mode with 18 kW of RF power to the helicon. No power was coupled to the ICRF antenna during this experiment. A series of 40 shots was taken with 0.5 second duration resulting in repeatable plasma conditions. A neutral Argon flow rate of 1800 sccm provided neutral gas to the helicon source. This corresponds to a neutral atom flux of $8x10^{20}$ particles / s with an ionization fraction of 100%, as will be shown below.

C.2.3 Diagnostics

Multiple plasma diagnostics were used in the aft section of the VX-100 experiment. Diagnostics are located downstream of the last nozzle magnet (z = 1.48 m) before the ion plume becomes highly collisional. A two-axis translation stage provides axial and vertical scanning of the plume at this location. A suite of instruments is mounted on the boom of this translation stage, including a retarding potential analyzer (RPA), cylindrical

Langmuir probe and cylindrical flux probe. The RPA provides ion energy distribution, which is not considered here. The cylindrical Langmuir probe is a swept-bias probe providing ion saturation current, electron temperature and plasma potential. The cylindrical flux probe provides ion saturation current, and electron temperature, although the latter measurement is not analyzed here.

Two stationary diagnostics are also introduced in the downstream plasma plume. A 70 GHz microwave interferometer is stationed at z = 1.635 m with a horizontal field of view. A second feedthrough at z = 1.76 m allows the insertion of a 10-collector array of planar flux probes. These ten discs are 0.64 cm diameter collectors spaced 3 cm apart that collect ion current when biased to ion saturation. The probe array is inserted horizontally through a flexible Wilson seal that allows the shaft to be moved back and forth, permitting a horizontal scan across the entire plasma plume.

C.2.3.1 70 GHz interferometer

Two configurations of the 70 GHz interferometer were used during the VX-100 experiment. The initial utilization was of the old VX-50 interferometer consisting of external electrical components and waveguide, with the horn antennas mounted on the inside of the vacuum chamber. All data presented in this Appendix was taken with this configuration. A substantial undertaking commenced to redesign the 70-GHz interferometer to operate entirely inside the vacuum chamber. The configuration of this device is archived here. Identical oscillator components and similar mixer and splitter components were used in both interferometer setups. The horn antennas for the VX-50

setup had a separation of ~ 1 m which meets the far-field condition. Both configurations align the horn's E-plane with the thruster axis, resulting in the ordinary wave (o-wave) being launched in the plasma plume. A linear phase shifter was positioned in-line with the VX-50 interferometer's plasma leg allowing a phase calibration to be performed. No such calibration was included with the VX-100 upgrade.

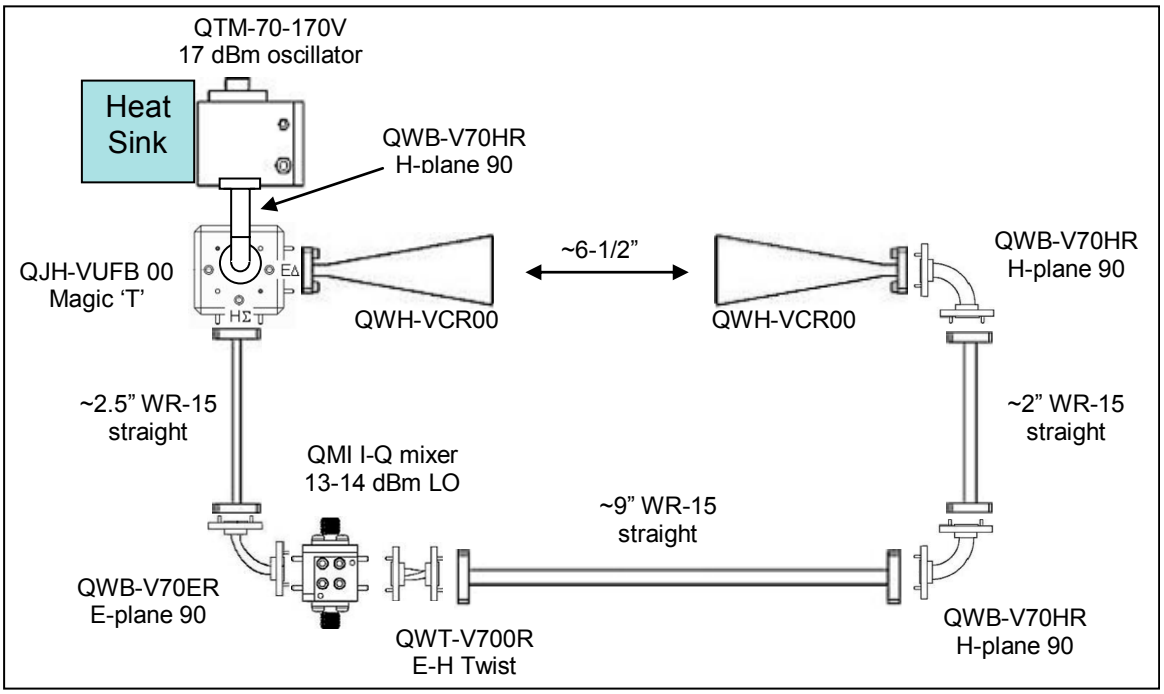

Figure C.3: 70 GHz interferometer schematic for VX-100 implementation inside vacuum chamber. Drawing shows configuration and Quinstar Inc. part numbers. The VX-50 experiment utilized a different setup with the waveguide routed around the outside of the vacuum chamber. Glass-mica feedthroughs allowed waveguide connections to the internally mounted horn antennas.

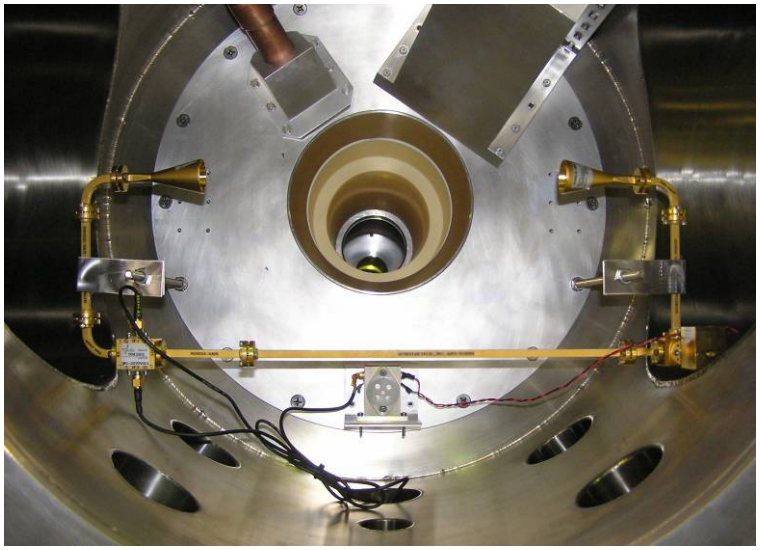

Figure C.4: 70 GHz interferometer mounted to the VX-100 experiment. Components were re-arranged from the schematic in Figure C.3, but the same parts were used.

At 70 GHz, the cutoff density for the ordinary wave is $6x10^{19}$ m^{-3}. Nonlinear effects manifest themselves at a density 50% below cutoff. Although the bulk plasma density in the VX-100 plume was below this level, sporadic density spikes were occasionally seen that resulted in the 70 GHz instrument cutting off. This was particularly seen at the higher power levels > 20 kW. To ensure a useable interferometer signal, the helicon power was maintained at 18 kW for these experiments.

C.2.3.2 Swept Langmuir Probe

Radial scans of plasma density and electron temperature were produced with a swept Langmuir probe. The probe is attached to the front of a retarding potential analyzer which is mounted to the two-axis translation stage. The cylindrical probe is composed of a thin tungsten wire with a collecting area of approximately $3x10^{-5}$ m^2. A $60V_{pp}$, 50 Hz

voltage sweep is sent to the Langmuir probe collecting current in the ion saturation zone, transition zone and electron saturation zone. RF compensation circuitry rejects high frequency components of the collected current for more accurate T_e and V_p measurements. [Paranjpe, 1990] [Sudit, 1993] [Flender, 1996]

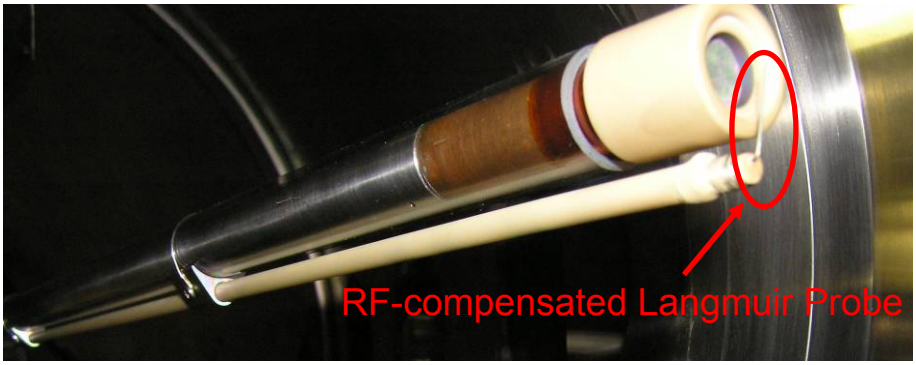

Figure C.5: Photograph of the RF compensated Langmuir probe at the end of a retarding potential analyzer. The entire instrument is mounted on a stainless steel boom attached to the 2-axis translation stage.

Rather than having a fixed bias as does a Langmuir triple-probe, the swept Langmuir probe undergoes the entire probe I-V sweep from ion saturation to electron saturation. The following analysis of Langmuir probe traces follows the approach given in [Choiniere, 2005] for non-flowing OML (thin probe) theory.

The plasma density $n_e \approx n_i$ is determined from the slope of the ion current squared to probe voltage: I_i^2 / V_0. This assumes that ion current follows the equation:

$$I_i = \sqrt{2}\frac{A_p e_c^{1.5}}{\pi\sqrt{m_i}} n_i \sqrt{\alpha T_i + U_{ev} + V_p - V_0} \qquad \text{(C.1)}$$

where U_{ev} is the ion flow energy in eV. For large V_0 the density n_i can be found by

$$n_i = \sqrt{-\frac{dI_i^2}{dV_0}} \frac{\pi\sqrt{m_i}}{\sqrt{2}A_p e_c^{1.5}} \tag{C.2}$$

Given this ion density, the electron current contribution can be extracted from the total Langmuir probe trace. By subtracting the ion current, the retardation regime of the electron characteristic can be analyzed to extract electron temperature. The next plot to be made is that of $\ln\left(I_e / I_{the}\right)$ where I_{the} is the electron thermal current:

$$I_{the} = A_p n_e e_c \sqrt{\frac{e_c T_e}{2\pi m_e}} \tag{C.3}$$

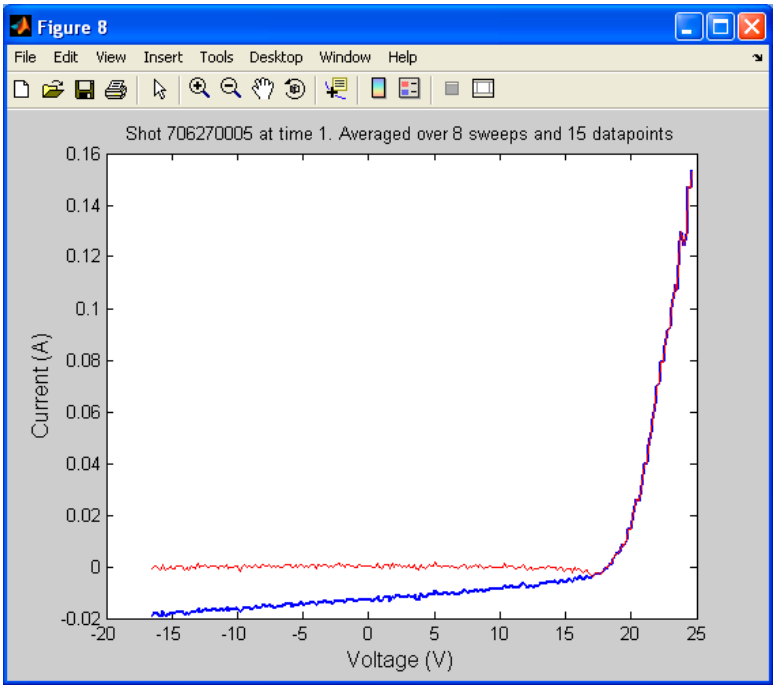

Figure C.6: Langmuir probe I-V trace. Blue line represents entire probe characteristic. Red line represents electron current only.

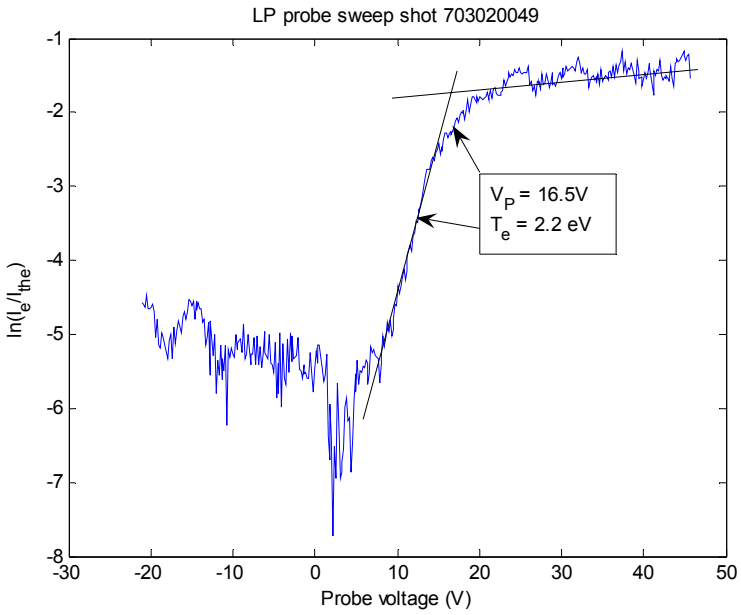

Figure C.7: Plot of ln(I_e / I_{the}) vs. probe voltage showing a linear fit in the electron retardation zone. Electron temperature is equal to the slope of the line in this fit.

Based on the exponential dependence of electron current to V_0 / T_e, the slope of the best fit line through this retardation zone ($V_f < V_0 < V_p$) is equal to the electron temperature.

C.2.3.3 Flux Probes

The two flux probes used in this experiment are of different construction, but of similar function. Both are biased to –40 V with respect to the experiment ground to collect ion saturation current. The electrodes of both flux probes are composed of exotic metal to limit the effect of secondary electron emission– Tungsten for the cylindrical flux probe

and Molybdenum[1] for the planar flux probe. [Barnett 1990] [Schächter 1998] Both have alumina ceramic as an insulating structure around the electrodes, and both utilize an isolation amplifier circuit to remove the –40 V common mode voltage from the small signal of the ion current. The measurement from these flux probes provides $\Gamma_i = n_i q v_i$ ion current density, which can be integrated over the plume area to produce total ion current.

The cylindrical flux probe (**Figure C.9**) was originally designed as a Langmuir triple probe. The electrodes are 4 mm diameter tungsten cylinders with 6 mm exposed above the alumina insulator. The junction between the conductor and insulator is recessed within the surrounding alumina tube to reduce the effect of the vacuum-conductor-insulator triple point. The two sets of three conductors are aligned linearly, and separated by 15 cm to act as a time of flight monitor. However, the shadowing of conductors by those positioned in front led to the re-tasking of the probe as a flux probe with only the foremost cylindrical electrode collecting ion current.

[1] Only one of the ten collectors is actually Molybdenum. The remainder are composed of stainless steel which also has a low secondary electron emission coefficient. The Molybdenum collector is compared with the others to see if secondary emission is a significant effect on a shot-shot basis.

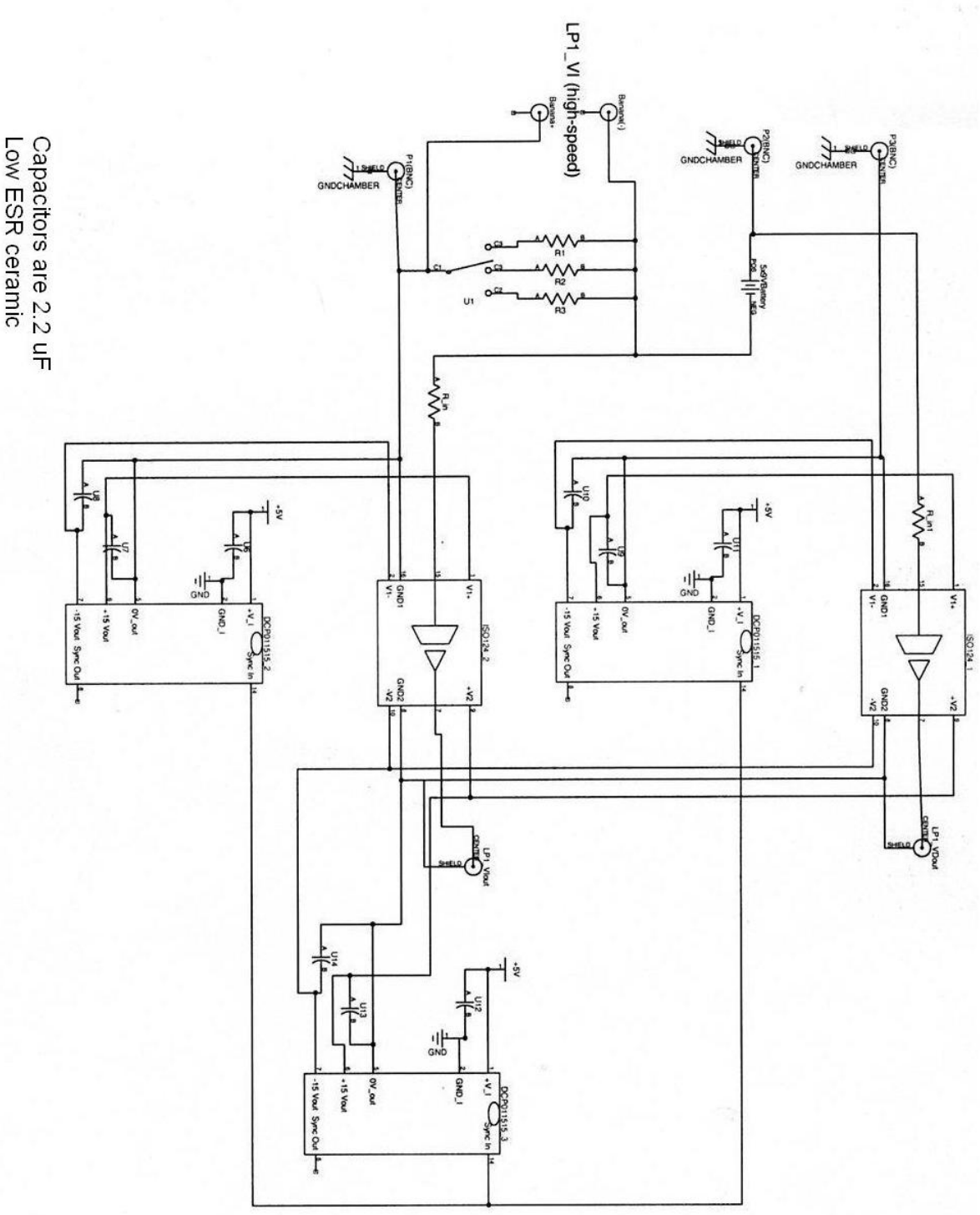

Figure C.8: Isolation amplifier schematic for Langmuir triple probe. A circuit based on this design was also used for swept Langmuir probe signal isolation, and for flux probe signal isolation. The main circuit components are ISO124 isolation amplifiers and DCP011515 dual switching power supplies.

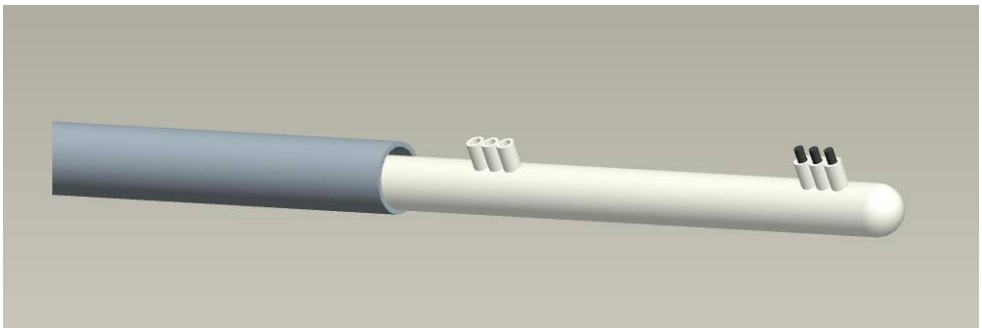

Figure C.9: Cylindrical flux probe, originally designed to be a Langmuir triple probe with time of flight capability. The electrodes are 4mm diameter Tungsten rods. When operating as a flux probe, only the rightmost electrode collects current.

The signal from the cylindrical flux probe was isolated from chamber ground using a unity-gain isolation amplifier circuit, shown in Figure C.8. This serves to remove the common mode voltage from the ion current signal and maintains isolation between instrument ground and chamber ground. The cylindrical flux probe is mounted to the end of a long stainless steel boom attached to the 2-axis translation stage. A similar boom holds the retarding potential analyzer and swept Langmuir probe at a vertical separation of 5 cm above the flux probe.

The ten-collector flux probe array (Figure C.10) collects a radial profile of ion current in the exhaust plume. The planar collectors are flat stainless steel discs of 6.4 mm diameter. The inter-electrode spacing is 3 cm and the alumina ceramic insulator supporting the discs has a small vacuum gap between the conductor and insulator, to minimize the insulator-vacuum-conductor triple point. The array can be extended all the way through the exhaust plume to collect a full horizontal profile.

Figure C.10: Flux probe array inserted in the exhaust plume. Multiple planar collectors are spaced along an alumina ceramic tube.

C.3 Experiment Results

Over the course of the multiple plasma shots, a vertical measurement scan was performed by the 2-axis translation stage scanning approximately in line with the 70 GHz interferometer at z = 1.635 m. A horizontal scan is subsequently performed by the 10-collector probe array at a position 12.5 cm downstream of the interferometer at z = 1.76 m. Due to the limitations on vertical travel in the vacuum chamber and the vertical offset of the two plume diagnostic booms, the swept Langmuir probe was only able to collect data for the top 65% of the plume, while the cylindrical flux probe was only able to collect data for the bottom 65% of the plume. The two instruments overlapped for 12 cm at the center of the plume. By scaling and summing the two scans, a total profile is produced.

The hybrid probe-interferometer method is employed to produce accurate radial density based on the 70 GHz data, the swept probe data, and the cylindrical flux probe data. (Figure C.11) The microwave interferometer measured a horizontal chord density while

the probe scan was conducted vertically, but this dichotomy was assumed to provide little additional error to the measurement due to the similarity in horizontal and vertical profile evidenced by the planar flux probe array measurements. A large asymmetry was found in the vertical density profile with the peak shifted up by +7 cm. A similar +7 cm shift to the right was found during the flux probe array's horizontal density scan.

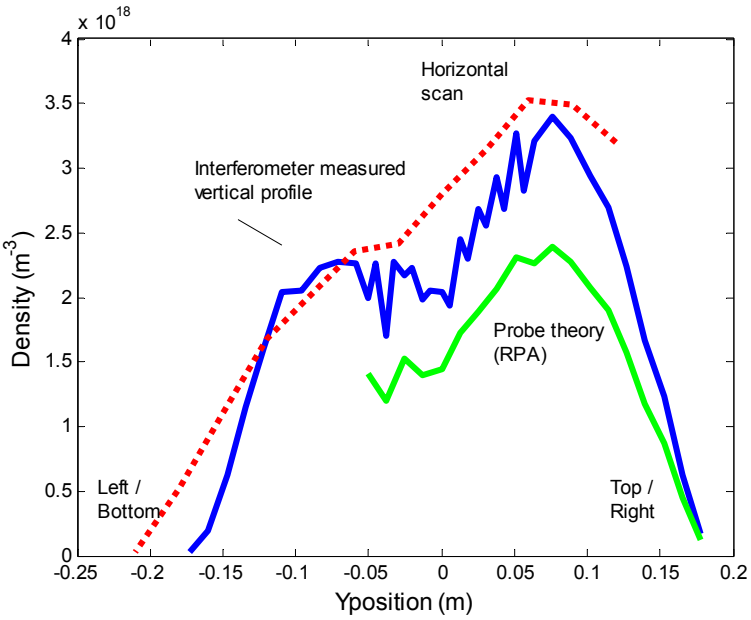

Figure C.11: Radial density profile measurement in the plume of the VX-100 experiment operating on Argon at 18 kW helicon power. Red dashed line: horizontal flux probe density with peak density adjustment based on 12.5 cm axial offset. Blue line: hybrid method based on 70 GHz interferometer and combined flux probe and swept Langmuir probe data. Light green line: density based on OML Langmuir probe theory.

The ten collector flux probe array measured ion current density at 12 separate positions during the multiple plasma shots. Although plasma density was not directly measured, an estimate of plasma density can be produced by combining an ion velocity with the measured ion flux. From prior measurements using the retarding potential analyzer, a typical ion energy of E_i = 15-16 eV was measured in the plume. This corresponds to a flow velocity of ~8.5 km/s with Argon. Since the horizontal scan was conducted at an axial position 12.5 cm behind the vertical scan, it was 24% wider and 50% less dense than the vertical scan. In Figure C.11, the horizontal density profile was adjusted to reflect this offset. The measured $R(z)$ by the two profile scans was different by 24%, so according to flux conservation the downstream peak density was increased by $(R_2 / R_1)^2$ = 53% to compare it directly with the vertical scan. The horizontal scan then compares quite favorably with the vertical scan, showing the same peak density offset and similar peak density.

The third density measurement included in Figure C.11 is the swept Langmuir probe density profile based on OML theory. As discussed above, calculation of the ion density in the neighborhood of the Langmuir probe is part of the electron temperature analysis. Since the swept Langmuir probe only covered 65% of the vertical scan, a partial density measurement results. In the region where the Langmuir probe and flux probe overlap, the qualitative agreement is good. The peak plasma density for the Langmuir probe theory is only 50-60% of the hybrid density result, which is similar to the findings in 4.1.4. This can therefore be considered a partial validation of the density profile produced by the hybrid probe measurement.

A 2D integral over the plume can be conducted, assuming axisymmetry and a velocity that is uniform over the profile. Of course, the plot in Figure C.11 shows that the plume was definitely not axisymmetric, so the validity of this operation is questionable. If the large density peak to the upper-right of the plume was a localized phenomenon, revolving the radial profile over π radians could result in a large over-estimate of the total ion flux. Also, assuming uniform velocity over the plume profile may introduce error to the total. Given these caveats, the 2D integral of flux is performed:

$$I_{tot} = \int_0^{\pi} \int_{-\infty}^{\infty} r\, nqv\, dr\, d\theta \tag{C.4}$$

where I_{tot} is the total ion current (flux) in the plume. Given the previous velocity measurement of v_i = 8.5 km/s, this results in a total ion flux of 1.4 x10^{21} ions / s or 225 Amps. Considering that the total neutral gas feed rate is 1800 sccm = 8x10^{20} particles / s the resulting ionization efficiency is 175%. This appears to be a physical impossibility, and could be an indication of several effects. The first possibility is the invalidity of the assumption of axisymmetry and constant velocity. This points to the need for a more accurate measurement of density and velocity over the entire plume, not just one or two radial scans. The second potential effect is neutral gas recycling. Prior to plasma turn-on, there is a large pre-pulse puff of neutral gas. This effectively fills the chamber with neutral argon prior to ignition, which could be contributing ions along with the 1800 sccm of propellant.

A second type of density scan was also performed on the VX-100: an axial density scan. By positioning the swept Langmuir probe on the chamber centerline and moving the translation stage backwards into the vacuum tank, an axial profile of density was collected over several shots. Starting just behind the microwave interferometer position at z = 1.68 m and moving back past z = 2 m, a density scan covering a factor of 3 decrease was produced. When plotted against a scaled measurement of magnetic field intensity in Figure C.12, the density begins diverging beyond z = 1.78 m. This may be an indication of a velocity decrease leading to the density not scaling with the magnetic field (as an ideal magnetized plasma should be doing). One possible cause of a velocity decrease is ion-neutral collisions which are expected to be an influence in the exhaust of this experiment. This departure of density from magnetic field scaling may be an indication of neutral particle effects in the VX-100 experiment.

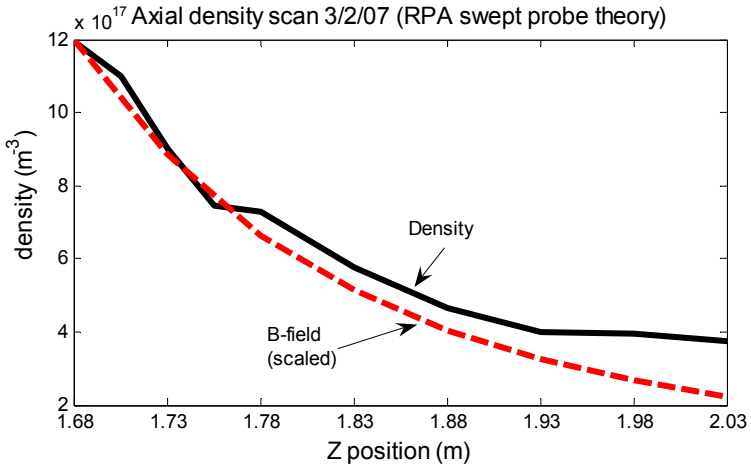

Figure C.12: Axial scan of density on the chamber centerline. Swept Langmuir probe provides density data based on OML analysis. Divergence of density from scaled magnetic field suggests possible neutral particle collisions.

C.4 Conclusion

Multiple radial and axial profiles of density were produced in the plume of the VX-100 thruster experiment. Correlation between instruments was good, despite differences in operation and construction. Both vertical and horizontal radial profiles detected non-axisymmetric density distributions with a peak density shifted 7 cm to the right and up. A 2D integral over the plume density and velocity produced a prediction of 175% ionization efficiency, which is attributed to errors in the axisymmetry assumption and possible netural gas recycling in the chamber. Despite these potential errors, very high neutral gas utilization is predicted in the VX-100 device (~100%). An axial survey of density showed density decreasing with axial position, but not proportional to the decrease in magnetic field. This raises the prospect of ion-neutral particle interaction leading to flow velocity reduction in this area of the experiment.

The limitations raised in this experiment have highlighted the importance of more accurate assessment of the ion flux in the exhaust of the VX-100 experiment. Fortunately, this undertaking has largely been started or completed in the form of improved plume diagnostics. Firstly, the cylindrical flux probe has been replaced by a planar flux probe with surrounding guard ring. This guard ring helps to minimize edge effects from a non-uniform plasma sheath surrounding non-guarded planar probes. A more accurate ion density measurement results. Secondly, the 70 GHz interferometer system has been improved by positioning it entirely inside the vacuum chamber, and placing it on a vertical translation stage allowing for radial profiles of density with Abel inversion. The third and potentially most significant improvement to the diagnostics

system is the inclusion of a pendulum flux probe which is swept across the entire plume area in a single shot. This addresses the problem of non-axisymmetric plume profiles by taking measurements at a number of positions in the plume per shot. When combined with ion energy distribution data from retarding potential analyzers, a radial scanning interferometer and a guard-ring flux probe, this greatly reduces the uncertainty inherent in plume measurements.

APPENDIX D

MATLAB code

A majority of the computer code utilized for data reduction and analysis in this experiment was written in MATLAB v7. A selection of code is archived here in the following order:

density_analysis_v4.m: An Interferometer data analysis program. Raw data files are selected for the downstream interferometer. A calibration of the interferometer is applied to the data, and spurious 2π phase shifts are removed. The data is scaled and compared with Langmuir probe data to determine the location of the spurious 2π phase shifts. The interferometer phase shift is converted to line integral density based on the interferometer wavelength. Results are saved in a comma separated file.

cfile_CAD_scan4_v4.m: One of many radial scan programs. Radial profiles are created via the hybrid method, reported earlier in this dissertation. Raw data saved by density_analysis_v4 is loaded for shots comprising a transverse scan. Both microwave interferometer data and Langmuir probe data for each shot is loaded, parsed and averaged. An implementation of the hybrid technique provides accurate radial density

profiles based on the radial Langmuir probe scan. Error bars are determined by Monte Carlo simulation.

magnetic_nozzle_sim_hydrogen.m: Quasi 1-D numerical simulation based on flux conservation, magnetic field mapping and high-Beta detachment. Initial conditions are provided based on experimental conditions. Plume trajectories are calculated and compared with experimentally measured column widths. Classical diffusion is included for cross-magnetic field transport.

For the most part, this code is included as a reference to the method employed – it is not reported here in complete form, and would not necessarily operate correctly without necessary data sources or subroutines. It is commented in a way which should make clear to anyone familiar with the MATLAB operating language what process was employed to collect and analyze data. However, don't expect to copy-paste this into Matlab and have it work as-is.

%density_analysis_v4.m

```
%Interferometer data analysis program - Used to analyze calibration shots and data taken on the DDEX %experiment with interferometer #2 and #3 (downstream interferometers.
%
%Enter in location of interferometer calibration file, then fit that file to  the analytical model used by Dobson, Jones, and Chavers.  the experiment data is then compared to the calibration and a plasma density is %determined.  Monte Carlo random analysis provides error bars given fossilized errors in the calibration %coefficient

%%%%%%%%%%%%%
%Load calibration file for both interferometers.
clear density2 density3 theta2 theta3
reply=input('Load new calibration? y/n [n]:','s');
if isempty(reply)
   reply = 'n';
end

if reply ~= 'n'
   clear all

   Datapath = uigetdir('D:\!Work\DDEX\Data\Run Date 04-27-2006\Plasma','Enter Data directory');
   [CI2  CQ2]  =  loadMWIcal(Datapath,2);          %Return  the  4  cal  coefficients  used  to  fit  to  a  sine  wave:  C1*sin(V(t)*C2+C3)+C4

   [CI3 CQ3] = loadMWIcal(Datapath,3);    %Return the 4 coefficients used to fit to a sine wave: C1*sin(V(t)*C2+C3)+C4

end

   if ~(CI2 | CQ2)
      disp('MWI2 cal not found'); MWI2flag=0;
   else
      MWI2flag=1;
   end
   if ~(CI3 | CQ3)
      disp('MWI3 cal not found'); MWI3flag=0;
   else
      MWI3flag=1;
   end

   if ~(CI2 | CI3 | CQ2 | CQ3)
      error('calibration file not found')
   end

%calculate the quadrature error Quadrature_offset
Quadrature_offset2 =min(abs(CQ2(3)-CI2(3)-[0,pi/2,-pi/2,3*pi/2,-3*pi/2]));

if MWI3flag
   Quadrature_offset3 =min(abs(CQ3(3)-CI3(3)-[0,pi/2,-pi/2,3*pi/2,-3*pi/2]));
end

%%%%%%%
%load the data file to analyze
if ~exist('Datapath')
   Datapath='D:\!Work\DDEX\Data\Run Date 04-27-2006\Plasma';
end
 Datapath = uigetdir(Datapath,'Enter Data directory'); [DataI2,DataQ2] = readMWIbin(Datapath,2);
    if ~(DataI2 | DataQ2)
      disp('MWI2 data not found'); MWI2flag=0;
   end
  [DataI3,DataQ3] = readMWIbin(Datapath,3);
      if ~(DataI3 | DataQ3)
      disp('MWI3 data not found');       MWI3flag=0;
   end
clear theta2 theta3

%%%%%%%%%%%
%isolate the data required.  look at 20ms before and 40ms after the peak phase.
[temp,maxindex]=max(abs(DataI2(:,2)));
[temp,stop]=min(abs(DataI2(:,1)-DataI2(maxindex,1)-0.020));
```

```
[temp,start]=min(abs(DataI2(:,1)-DataI2(maxindex,1)+0.040));
theta2(:,1) = DataI2(start:stop,1);
if MWI3flag  %If lower interferometer channel data exists
   theta3(:,1) = DataI3(start:stop,1);
end
%%%%%%%%%%
% Apply the simplified 4-calibration coefficient equation to find Theta phase:
theta2(:,2) = atan2(CI2(1).*(DataQ2(start:stop,2) - CQ2(4)) -tan(Quadrature_offset2).*(cos(Quadrature_offset2).* CQ2(1).*
(DataI2(start:stop,2) - CI2(4))) ...
   ,cos(Quadrature_offset2).* CQ2(1).* (DataI2(start:stop,2) - CI2(4)));

if MWI3flag
   theta3(:,2) = atan2(CI3(1).*(DataQ3(start:stop,2) - CQ3(4)) -tan(Quadrature_offset3).*(cos(Quadrature_offset3).*
CQ3(1).* (DataI3(start:stop,2) - CI3(4))) ...
   ,cos(Quadrature_offset3).* CQ3(1).* (DataI3(start:stop,2) - CI3(4)));
end

%%%%%%%
% determine the error bar in radians at this location.  MonteCarloError
% returns the sigma, so 2*sigma gives the approximate error bar.
clear Errortheta2 Errortheta3
for n = 1:length(theta2)
   Errortheta2(n,1) = 2*MonteCarloError(DataI2(start+n-1,2),DataQ2(start+n-1,2),CI2,CQ2,sigmaCI2,sigmaCQ2,sigmaV);
% Monte Carlo subroutine (not included in this Appendix)
   if MWI3flag
      Errortheta3(n,1) = 2*MonteCarloError(DataI3(start+n-1,2),DataQ3(start+n-
1,2),CI3,CQ3,sigmaCI3,sigmaCQ3,sigmaV);
   end
end

%%%%%%%%%%%%%%%%%%%%%
%Use unwrap code from MATLAB
[theta2(:,3),dp_corr2]=MWIunwrap(theta2(:,2)); % algorithm similar to MATLAB's unwrap  function
%Find initial phase
theta0_2 = mean(theta2(length(theta2)-100:length(theta2),3));
theta2(:,4)= theta2(:,3)-theta0_2;  %theta(:,4) is the normalized phase shift

%%%%%%%%%%%%%%%%%%%%%
%load the LP file–for correlating with interferometer data to find erratic 2pi shifts in interferometer data
clear LP1 LP2
[DataLP1,DataLP2] = readLPbin(Datapath);
if ~(DataLP1 | DataLP2)
      disp('LP data not found')
else

%chop the LP data
LP2(:,1) = DataLP2(start:stop,1); LP2(:,2) = DataLP2(start:stop,2);
LP2(:,3) = LP2(:,2) - mean(LP2(length(LP2)-100:length(LP2),2));
end

if MWI3flag   %Unwrap lower interferometer data and determine initial phase
   [theta3(:,3),dp_corr3]=MWIunwrap(theta3(:,2));

   %Find initial phase
   theta0_3 = mean(theta3(length(theta3)-100:length(theta3),3));
   theta3(:,4)= theta3(:,3)-theta0_3;

   %%%%%%%%%%%%%%%%%%%%%
   %MWIphaseAdjust - Adjust the phase of an input MWI reading by adjusting 2pi
   %phase missed at beginning of shot.  This code is not archived here.
   [theta2(:,4),dp2,theta3(:,4),dp3]=MWIphaseAdjust(theta2(:,4),theta3(:,4));
   dp_corr2 = dp_corr2+dp2;  %locations of 2pi adjustments that had to be made
   dp_corr3 = dp_corr3+dp3; %locations of 2pi adjustments that had to be made
end

%%%%%%%%%%%%
% Adjust MWI3 data based on LP2 data.  This does more 2pi fringe adjustment based on the langmuir %probe data.
%%%%%%%%%%%%
if CQ3(1)
   threshold = 4;  %value of LP data that should be used to match with interferometer
```

```
   [temp,LP2(:,3)]=correlateLPwithMWI(theta3(:,4),LP2(:,3),threshold);  %function not archived here
end

%%%%%%%%%%%%%%%%%%%
%  Adjust MWI2 data based on LP2 data.
%%%%%%%%%%%%%%%%%%%

threshold = 10;% value of LP data that should be used to match with interferometer
[theta2(:,4),temp]=correlateLPwithMWI(theta2(:,4),theta3(:,4),threshold); %function not archived here
[temp,LP2(:,3)]=correlateLPwithMWI(theta2(:,4),LP2(:,3),threshold); %function not archived here

%Convert phase shift [radians] to density

density2(:,1) = theta2(:,1);
if MWI3flag
   density3(:,1) = theta3(:,1);
end

Int_factor = 1;   %assuming square distribution across entire 1 meter distance
density2(:,2) = rad2dens(theta2(:,4),Int_factor); % Function to convert radians to density
density2Error = rad2dens(Errortheta2,Int_factor);

if MWI3flag
   density3(:,2) = rad2dens(theta3(:,4),Int_factor); density3Error = rad2dens(Errortheta3,Int_factor);
end

if DataLP2
   LP2(:,4) = rad2dens(LP2(:,3),Int_factor);
end

%%%%%%%%%%%%%%%%%%%%
 %chop and average the data, this average based on 50 kHz on DAQ6254
  Mave=10;  %Average over 10 data points
   Mm1ave=9;

    for j=1:floor(length(density2)/Mave)
      density2_ave(j,1)=mean(density2(j*Mave-Mm1ave:j*Mave,1));
      density2_ave(j,2)=mean(density2(j*Mave-Mm1ave:j*Mave,2));
      % positive error bars on density
      density2_ave(j,3)=mean(density2(j*Mave-Mm1ave:j*Mave,2)-density2Error(j*Mave-Mm1ave:j*Mave));
      % negative error bars on density
      density2_ave(j,4)=mean(density2(j*Mave-Mm1ave:j*Mave,2)+density2Error(j*Mave-Mm1ave:j*Mave));

      if MWI3flag
        density3_ave(j,1)=mean(density3(j*Mave-Mm1ave:j*Mave,1));
        density3_ave(j,2)=mean(density3(j*Mave-Mm1ave:j*Mave,2));
          %positive error bars on density
        density3_ave(j,3)=mean(density3(j*Mave-Mm1ave:j*Mave,2)-density3Error(j*Mave-Mm1ave:j*Mave));
          %negative error bars on density
        density3_ave(j,4)=mean(density3(j*Mave-Mm1ave:j*Mave,2)+density3Error(j*Mave-Mm1ave:j*Mave));
      end

      if DataLP2
         LP2_ave(j,1)=mean(LP2(j*Mave-Mm1ave:j*Mave,1));
         LP2_ave(j,2)=mean(LP2(j*Mave-Mm1ave:j*Mave,3));
         LP2_ave(j,3)=mean(LP2(j*Mave-Mm1ave:j*Mave,4));
      end
   end
   %find the Full Width Half Max based on 2 interferometer analysis
   if MWI3flag
      FWHM = 24*2.54*sqrt(-1*log(.5))./sqrt(-1.*log(density3_ave(:,2)./density2_ave(:,2)));
   end

%%%%%%%%%%%%%%%%%%%%
% plotting section - plot total theta error as a percentage
figure
plot(theta2(:,1),Errortheta2./theta2(:,4))
hold on
plot(theta2(:,1),theta2(:,4)./max(theta2(:,4)),'r')
hold off
```

```
temp=axis;
axis([0.446 0.458 0 1 ]) % for 6/1 data

%plot average density from microwave interferometer
figure
plot(density2_ave(:,1),density2_ave(:,2))
hold on

if MWI3flag
    plot(density3_ave(:,1),density3_ave(:,2),'r')
    plot(density3_ave(:,1),density3_ave(:,3),'r:')
    plot(density3_ave(:,1),density3_ave(:,4),'r:')
end
plot(density2_ave(:,1),density2_ave(:,3),':')
plot(density2_ave(:,1),density2_ave(:,4),':')

xlabel('Time(s)')
ylabel('Line integrated density over 1m path (m^-^2)')
set(gcf,'DefaulttextInterpreter','none')
title(['Plot of averaged density for ' Datapath(regexp(Datapath,'Run_'):length(Datapath)) '. Error bars shown.'])
if MWI3flag
    legend('MWI 2','MWI 3','ErrorBars')
    axis([density2(1690,1) density2(2445,1) min([density2(:,2);density3(:,2)]) max([density2(:,2);density3(:,2)])])
else
    legend('MWI 2','Langmuir probe')
end
hold off
%%%%%%%%%%%%%%%%%%%%%
%SAVE DATA TO FILE
%%%%%%%%%%%%%%%%%%%%%
if ~exist('Save_path')
    Save_path = uigetdir(Datapath,'Enter folder to save data');
else
    Save_path = uigetdir(Save_path,'Enter folder to save data');
end

%Make savefile directories
[s,mess,messid]=mkdir([Save_path,'\EMF']);
if mess
    disp(mess);
end

[s,mess,messid]=mkdir([Save_path,'\JPG']);
if mess
    disp(mess);
end

[s,mess,messid]=mkdir([Save_path,'\FIG']);
if mess
    disp(mess);
end

%suppress warnings due to legend having too few plots
warning off all;

savedata(1).filename=[char(Datapath(max(regexp(Datapath,'\'))+1:length(Datapath))) '_error'];
%save plots to file
saveas(gcf,[Save_path,'\EMF\',savedata(1).filename,'.emf']);
saveas(gcf,[Save_path,'\JPG\',savedata(1).filename,'.jpg']);
saveas(gcf,[Save_path,'\FIG\',savedata(1).filename,'.fig']);

%create save file variables
savedata(1).time2=density2(:,1);
savedata(1).dens2Error = density2Error;
if CQ3(1)
    savedata(1).time3=density3(:,1);
    savedata(1).dens3Error = density3Error;
end
%%%%%%%
%Use fprintf to save file
```

```
%print header
fid = fopen([Save_path '\' Datapath(regexp(Datapath,'Run_'):length(Datapath)) '_error.tab'],'wt');

if fid==-1
   disp(['The file could not be opened'])
   return
end

fprintf(fid,'Batch process run on %s\n',Datapath);
fprintf(fid,'Batch process run on %s\n',datestr(now));
fprintf(fid,'Cal coefficients\n');
fprintf(fid,'CI2:\tCQ2:\tCI3:\tCQ3:\n');
if CQ3(1)
   fprintf(fid,'%f\t%f\t%f\t%f\n',[CI2;CQ2;CI3;CQ3]);
else
   fprintf(fid,'%f\t%f\t%f\t%f\n',[CI2;CQ2;[0 0 0 0];[0 0 0 0]]);
end
fprintf(fid,'\n%s',savedata(1).filename);
if CQ3(1)
   fprintf(fid,'\n%s\t%s\t%s\t%s','MWI2_time','MWI2_error (m^-2)','MWI3_time','MWI3_error (m^-2)');
   fprintf(fid,'\n%f\t%f\t%f\t%f',[savedata(1).time2';savedata(1).dens2Error';savedata(1).time3';savedata(1).dens3Error']);
   else
   fprintf(fid,'\n%s\t%s','MWI2_time','MWI2_error (m^-2)');
   fprintf(fid,'\n%f\t%f',[savedata(1).time2';savedata(1).dens2Error']);
end
fclose(fid);

%%%%%
%Convert interferometer signal in radians to density
function [density] = rad2dens(theta,int_factor)
e_c = 1.6e-19;  %electric charge in coulomb
epsilon_0 = 8.85e-12;   %permittivity in  F/m
m_e = 9.1e-31;
f = 15e9;       % 15 GHz oscillator
c = 3e8;        %speed of light in vacuum
density = theta*2*epsilon_0*m_e*2*pi*f*c/e_c^2/int_factor;
```

```
%cfile_CAD_scan4_v4.m based in part on Jonathan Jones's (NASA MSFC) cfile_T.m customized to run on
%6/1/06 scans 16-29 with downstream interferometer.  RGB interferometer correlated for flux conservation
%calibration file in 5/31/06 scan 25.
%Code implements the hybrid probe analysis for a radial scan of langmuir
%probe along the downstream interferometer.

%Error bars are imported for interferometer data, and applied to the total scan based
%on RevSciInst error analysis

%modified 7/26/07 to include the most recent cal data, and to adjust the LP
%probe theory to account for matrix sheath expansion.
Plots = 1; %turn plots on or off

% file to read data from .tab file
 Datapath = 'E:\!Work\DDEX\Reduced data\6-1-06\shots 16-29 with LP z = 55\';
Datapath = uigetdir(Datapath,'Enter Data directory to run batch process on');
Savepath = uigetdir(Datapath,'Enter folder to save data');

D1=dir(Datapath);n=length(D1);ii=0;
Start_Shot=16;End_Shot=28;Num_Shots=End_Shot-Start_Shot+1;
jpos=[-18:3:18 ];%radial position of shots (in inches)
StartTime = 0.450; StopTime = 0.455; %desired start and stop of plot
for sh=Start_Shot:End_Shot;  % shot numbers to reduce
   if sh<10
      shot=strcat('000',num2str(sh));
   end
   if sh>9 & sh<100
      shot=strcat('00',num2str(sh));
   end
   if sh>99
      shot=strcat('0',num2str(sh));
   end
   for i=3:n  %read the density data into a data structure
      if length(D1(i).name)==12
         if strcmp(D1(i).name(5:8),shot)
            ii=ii+1;
            data(ii).name=D1(i).name;
            data(ii).shotnum=sh;
            path2=strcat(Datapath,'\',D1(i).name);
            try
               fid = fopen(path2,'r','l');
               if fid==-1
                  error(['Problems opening ' path2])
               end
               for i = 1:11
                  tline = fgetl(fid);
               end
               a= fscanf(fid, '%g %g %g %g %g %g', [6 inf]); a = a';  fclose(fid);
               data(ii).density2 = a(:,2);data(ii).density3 = a(:,4);
               data(ii).lp2_vi = a(:,6);data(ii).time = a(:,1);
            catch
               disp(['Could not open file '  path2]);
            end
         end
         %import errorbars into the structure
      elseif length(D1(i).name)==18
         if strcmp(D1(i).name(5:8),shot) && strcmp(D1(i).name(10:14),'error')
            path2=strcat(Datapath,'\',D1(i).name);
            try
               fid = fopen(path2,'r','l');
               if fid==-1
                  error(['Problems opening ' path2])
               end
               for i = 1:11
                  tline = fgetl(fid);
               end
               a= fscanf(fid, '%g %g %g %g', [4 inf]);a = a'; fclose(fid);
               data(ii).density2Error = a(:,2);data(ii).density3Error = a(:,4);
               data(ii).errorTime = a(:,1);
```

```
            catch
               disp(['Could not open file '  path2]);
            end
         end
      end
   end
end


%read the upstream RGB denstiy file
path3=('E:\!Work\DDEX\Data\RGB Interferometer 06-01-2006\');
path3 = [uigetdir(path3,'Enter directory with RGB data') '\'];
D1=dir(path3);n=length(D1);ii=0;
for sh=Start_Shot:End_Shot;  % shot numbers to reduce
   if sh<10
      shot=strcat('000',num2str(sh));
   end
   if sh>9 & sh<100
      shot=strcat('00',num2str(sh));
   end
   if sh>99
      shot=strcat('0',num2str(sh));
   end
   for i=3:n
      if length(D1(i).name)>28
         if strcmp(D1(i).name(6:9),shot)
            ii=ii+1;
            data(ii).name=D1(i).name;
            data(ii).shotnum=sh;
            path4=strcat(path3,D1(i).name);
            path5=strcat(path4, '\MWI1_RGB_D.bin');
            path6=strcat(path4, '\MWI1_DError.bin');
            data(ii).RGB_d=readbin(path5);  %read in RGB density and time.  Density in cm^-3
            data(ii).RGB_error=readbin(path6);  %read in RGB error and time.  Density in cm^-3
         end
      end
   end
end

LP2_VI_cal = 1/5.436; %opto-isolator calibration factor (divide by this to get true reading)
%Condition the data just loaded
for ii=1:Num_Shots
  %remove DC offset from langmuir probe data
   vi2_offset(ii)=mean(data(ii).lp2_vi(1:100));
   data(ii).lp2_vi=(data(ii).lp2_vi-vi2_offset(ii))/LP2_VI_cal;
  %sync up times of each shot by cutting data prior to LatestStart
   temp2=find(data(ii).lp2_vi > 0.02);
   RisingEdge(ii)=temp2(1);
   tempRGB = find(data(ii).RGB_d.dat > 1*10^11);
   RisingEdgeRGB(ii) = tempRGB(1);
  %determine RMS value for lp2 for subsequent error analysis
   temp=data(ii).lp2_vi(1:1000);
   data(ii).lp2_vi_sigma = norm(temp)/sqrt(length(temp));
end

%delay the start of data for shots that have an earlier rising edge

LatestStart=max(RisingEdge);
for ii = 1:Num_Shots
   CropIndex(ii) =LatestStart-RisingEdge(ii)+1;

data(ii).density2(CropIndex(ii):length(data(ii).density2))=data(ii).density2(1:length(CropIndex(ii):length(data(ii).density2)));

data(ii).density3(CropIndex(ii):length(data(ii).density3))=data(ii).density3(1:length(CropIndex(ii):length(data(ii).density3)));
   data(ii).lp2_vi(CropIndex(ii):length(data(ii).lp2_vi))=data(ii).lp2_vi(1:length(CropIndex(ii):length(data(ii).lp2_vi)));
   data(ii).time(CropIndex(ii):length(data(ii).time))=data(ii).time(1:length(CropIndex(ii):length(data(ii).time)));

data(ii).density2Error(CropIndex(ii):length(data(ii).density2Error))=data(ii).density2Error(1:length(CropIndex(ii):length(data
(ii).density2Error)));
```

```
data(ii).density3Error(CropIndex(ii):length(data(ii).density3Error))=data(ii).density3Error(1:length(CropIndex(ii):length(data
(ii).density3Error)));
end
%%%%%%%%%%%%%%%%%%%%
%chop and average the data, this average based on 50 kHz on DAQ6254 and
%40 kHz on RGB data
for ii = 1:Num_Shots
    Mave=10;  %number of shots to average LP and downstream interferometer
    Mm1ave=Mave-1;
    Mave2=8;  %number of shots to average upstream interferometer over
    Mm1ave2=Mave2-1;
    %average LP and downstream MWI data based on 50 kHz data rate
    for j=1:floor(length(data(ii).density2)/Mave)
        data(ii).lp2_vi_ave(j)=mean(data(ii).lp2_vi(j*Mave-Mm1ave:j*Mave));
        data(ii).density2_ave(j)=mean(data(ii).density2(j*Mave-Mm1ave:j*Mave));
        data(ii).density3_ave(j)=mean(data(ii).density3(j*Mave-Mm1ave:j*Mave));
        data(ii).time_ave(j)=mean(data(ii).time(j*Mave-Mm1ave:j*Mave));
        data(ii).density2Error_ave(j)=mean(data(ii).density2Error(j*Mave-Mm1ave:j*Mave));
        data(ii).density3Error_ave(j)=mean(data(ii).density3Error(j*Mave-Mm1ave:j*Mave));
    end

    %average RGB data based on 40 kHz data rate.
    for j=1:floor(length(data(ii).RGB_d.dat)/Mave2)
        data(ii).RGB_d.ave(j)=mean(data(ii).RGB_d.dat(j*Mave2-Mm1ave2:j*Mave2));
        data(ii).RGB_error.ave(j)=mean(data(ii).RGB_error.dat(j*Mave2-Mm1ave2:j*Mave2));
        data(ii).RGB_d.aveT(j)=mean(data(ii).RGB_d.t(j*Mave2-Mm1ave2:j*Mave2));
    end
 %sync up times of each MWI shot by comparing to RisingEdge.
    temp2=find(data(ii).lp2_vi_ave > 0.02);
    RisingEdge(ii)=temp2(1);
 %sync up times of each RGB shot by comparing to RisingEdgeRGB
    tempRGB = find(data(ii).RGB_d.ave > 1*10^11);
    RisingEdgeRGB(ii) = tempRGB(1);
    data(ii).RGB_d.ave=data(ii).RGB_d.ave(RisingEdgeRGB(ii)-
RisingEdge(ii)+1:length(data(ii).lp2_vi_ave)+RisingEdgeRGB(ii)-RisingEdge(ii));
    data(ii).RGB_error.ave=data(ii).RGB_error.ave(RisingEdgeRGB(ii)-
RisingEdge(ii)+1:length(data(ii).lp2_vi_ave)+RisingEdgeRGB(ii)-RisingEdge(ii));
    data(ii).RGB_d.aveT=data(ii).RGB_d.aveT(RisingEdgeRGB(ii)-
RisingEdge(ii)+1:length(data(ii).lp2_vi_ave)+RisingEdgeRGB(ii)-RisingEdge(ii));
 %determine sigma (LP2 error) for averaged LP2 data
    temp=data(ii).lp2_vi_ave(1:100);
    data(ii).lp2_vi_sigma_ave = norm(temp)/sqrt(length(temp));
end

%Sort the shots into a position in ascending order
clear sortData
[jsort,Isort]=sort(jpos);

for i=1:Num_Shots
    data(Isort(i)).pos = jsort(i);
    sortData(i)=data(Isort(i));
end
%%%%%%%%%%%%%%%%%%%%%%%%%%%%%%%%%%%%%%%%%%%%%%%%%%%%%%%%%%%%%%%%%%%%%%%%%%%
%%%%%%%%%%%%
%Determine the hybrid probe beta based on interferometer and probe data
clear beta beta2 n2
for i=1:length(data(ii).time_ave)
    beta(i)=0;
    beta2(i)=0;
    for ii=1:Num_Shots-1
        if jsort(ii+1)>jsort(ii)
            beta2(i)=beta2(i)+abs((sortData(ii).lp2_vi_ave(i)/(sortData(ii).density2_ave(i))))*abs(jsort(ii+1)-jsort(ii))*.0254);   %be
sure path is right
        end
    end

beta2(i)=beta2(i)+abs((sortData(Num_Shots).lp2_vi_ave(i)/(sortData(Num_Shots).density2_ave(i))))*abs(jsort(Num_Shots)
-jsort(Num_Shots-1))*.0254);  %be sure path is right
```

```
    for jj=1:Num_Shots
        sortData(jj).n2(i)=sortData(jj).lp2_vi_ave(i)/beta2(i);
        n2(jj,i)=sortData(jj).lp2_vi_ave(i)/beta2(i);


    % LP scan only covers +/- 46 cm of the plume.  for a 91cm FWHM this is
    % only 78.8% of the total plume density.
    Scan_percentage = 0.788;
         sortData(jj).n2(i)=sortData(jj).lp2_vi_ave(i)/beta2(i)*Scan_percentage;
        n2(jj,i)=sortData(jj).lp2_vi_ave(i)/beta2(i)*Scan_percentage;
        sortData(jj).beta2(i) = beta2(i)/Scan_percentage;
   end
end

% fit data to probe theory.  Adjusted for optoisolator calibration coeff.
e_c = 1.602e-19;    %electron charge (C)
q_i = 1*e_c;    %ionic charge (C)
m_i = 1.67e-27*1;   %Hydrogen mass (kg)
S_frontal = 0.9*5*1e-6; %probe frontal area (m^2)
S_p = S_frontal*pi; % LP2 probe total area
r_p =0.9/2*1e-3;     %probe radius (m)
R_sense  = 100;     %sensing resistor (ohms)
T_e = 1.2;           %Electron temp (eV)
T_i = 1.2;         %ion temp (eV)
Ma = 1.95;  %Ion mach number
%v_i = sqrt(e_c*T_i/m_i)*Ma;
v_i = 19e3;         %ion velocity (m/s)
V_p = 40;           %probe voltage (V)

%%%%%%
s = v_i*sqrt(m_i/2/e_c/T_i); % scaled velocity for combined probe theory
I_thermal = S_p*q_i*sqrt(e_c*T_i/(2*pi*m_i)); %Random probe current collection / n_i

clear velocity fitfactor
for jj = 1:Num_Shots
%velocity based on flux probe data: I_flux = n*q*v*S_p
    plasmaIndex=find(sortData(jj).n2>0.001*max(sortData(jj).n2));
    b = sortData(jj).lp2_vi_ave(plasmaIndex);
    A = sortData(jj).n2(plasmaIndex)*q_i*S_frontal*R_sense;
    [velocity(jj),temp] = lsqr(A',b',1e-5,500);
    %ion density based on combined thin-sheath theory, s = v_i*sqrt(m_i/2/e_c/T_i)
    % I_thermal = S_p*n_i*q*sqrt(e_c*T_i/(2*pi*m_i))
    % For s>1:  I = I_thermal * a/r*2/sqrt(pi)*s*(1+1/(4*s^2))
    % For s<1: I = I_thermal * a/r * (1+s^2/2)
    %
    % where a/r is the sheath radius / probe radius.  Use matrix sheath
    % a = r_p+debye*(2*V_p/T_e)^1/2;  %
     debye = sqrt(8.85e-12/1.6e-19*T_e./sortData(jj).n2);
     a = r_p+debye*(2*V_p/T_e)^1/2;  %Matrix sheath
     if s>1
        sortData(jj).LPprobetheory_ave=sortData(jj).lp2_vi_ave/R_sense/I_thermal./(a)*r_p/(2/sqrt(pi)*s*(1+1/(4*s^2)));
%combined probe theory large s
    else
        sortData(jj).LPprobetheory_ave=sortData(jj).lp2_vi_ave/R_sense/I_thermal./(a)*r_p/(1+s^2/2);    %combined    probe
theory small s
    end
    [fitfactor(jj),temp] = lsqr(sortData(jj).n2(plasmaIndex)',sortData(jj).LPprobetheory_ave(plasmaIndex)',1e-6,300);

    %ion density based on standard probe theory: I = 0.61*q_i*n_0*
    % *sqrt(e_c*T_i/m_i)*S_p
    %9_6_07 use matrix sheath expansion to determine probe collection area.
    % S_p = pi*2a * 5mm

    S_p = pi*2*a*5e-3;
    sortData(jj).LPstandardprobetheory=sortData(jj).lp2_vi_ave/R_sense/q_i./S_p/0.61/sqrt(e_c    *T_e/m_i);       %standard
probe theory
end

%Fit the profile at each position in time to a Gaussian.  FWHM compares
%MWI_2 with MWI_3.  FWHM2 uses a fit to the langmuir probe scan
```

```
clear FWHM FWHM2 fjj RMSError;jj=1;
for i = StartIndex:StopIndex  % time location of the plasma shot
   fjj(jj,:) = g_fit_new2(jsort',n2(:,i),[10,1e16,0]);  %use new gaussian fit program CAD
   FWHM2(jj)=abs(fjj(jj))*.0254*2*(log(2))^0.5;
    % determine RMS error from fit (as a percentage of magnitude)
   RMSError(jj) = norm(n2(:,i)'-fjj(jj,2)*exp(-((jsort-fjj(jj,3)).^2)/fjj(jj,1)^2))/norm(n2(:,i))/sqrt(length(n2(:,i)));
   jj=jj+1;
end
%take average FWHM over all shots
FWHM=0;
for ii = 1:Num_Shots
   FWHM                                                =FWHM+                                                24*.0254*sqrt(-1*log(.5))./sqrt(-
1.*log(data(ii).density3_ave(StartIndex:StopIndex)./data(ii).density2_ave(StartIndex:StopIndex)));
end
FWHM = FWHM ./ Num_Shots;

%%%%%%%%%%%%%%%%%%
% Error analysis
% Errorbar equation:  sigma_n^2 = Beta^2*V_i^2*[M*(sigma_alpha^2/alpha^2)+
% (1 - 2V_i*Beta*alpha/N_i)*sigma_v_i^2/V_i^2] + (Beta^2 * alpha*V_i)^2*
% SUM(jj:1:M) [ (sigma_V_jj^2/V_jj^2 + sigma_N_jj^2/N_jj^2)*(V_jj^2 / N_jj^2)]

 alpha = 2*0.0254; sigma_alpha = 1.59e-5;M = Num_Shots;
% sigma_V_i(jj) = data(jj).lp2_vi_sigma_ave;  %This assumes sigma_ave is used
for i = 1:length(sortData(1).time_ave); %StartIndex:StopIndex   % % look at error
   SumError(i) = 0;
%       Error equation for alpha_i = non-constant.  use sigma_vi not sigma_vi_ave
   for jj = 1:M
      %%% lp2_vi_sigma_ave averaged
SumError(i)=SumError(i)+ (sigma_alpha^2/alpha^2+data(jj).lp2_vi_sigma_ave^2/data(jj).lp2_vi_ave(i)^2 + ...
         (data(jj).density2Error_ave(i)/2)^2/data(jj).density2_ave(i)^2)*(data(jj).lp2_vi(i)^2 *alpha^2 / ...
         data(jj).density2_ave(i)^2);
   end
   for jj = 1:M
      %%% lp2_vi_sigma_ave averaged
   n2Error(jj,i)=2*sqrt( beta2(i)^-2*data(jj).lp2_vi_ave(i)^2*(( ...
         (1-2/beta2(i)*alpha*data(jj).lp2_vi_ave(i)/data(jj).density2_ave(i))*data(jj).lp2_vi_sigma_ave^2 / ...
         data(jj).lp2_vi_ave(i)^2) + beta2(i)^-2  * SumError(i)));
   end
end
sigmaAlpha2_alpha2 = sigma_alpha^2 / alpha^2;
for jj =1:M
    %%% lp2_vi_sigma_ave averaged
    sigmaV2_V2(jj) =  mean(sortData(jj).lp2_vi_sigma_ave.^2 ./ (sortData(jj).lp2_vi_ave(StartIndex+6:StartIndex+13)).^2);
    sigmaN2_N2(jj) =  mean((sortData(jj).density2Error_ave(StartIndex+6:StartIndex+13)/2).^2./ ...
       sortData(jj).density2_ave(StartIndex+6:StartIndex+13).^2);
end

%%%%%%%%%%%%%%%%%%
%%determine errorbars on FWHM2.  takes 3-4 hours to run.  not all functions
%%are archived here.
% clear n2dist FWHM2_alt FWHM2_error
% jj=6;
% for i = StartIndex+5:StartIndex+15  % time location of the plasma shot
%    temp = size(n2Error);
%    clear sigmaMonteCarlo
%    for N = 1:1000
%       n2dist = n2(:,i) + randn(temp(1),1).*n2Error(:,i);
%       sigmaMonteCarlo(N,:) = g_fit_new2(jsort',n2dist,[10,1e16,0]);  %use new gaussian fit program CAD
%       sigmaMonteCarlo(N,1)=abs(sigmaMonteCarlo(N,1))*.0254*2*(log(2))^0.5; % adjust to FWHM
%    end
%    [FWHM2_alt(jj),FWHM2_error(jj)] = normfit(sigmaMonteCarlo(find(sigmaMonteCarlo(:,1)<2)));
%    FWHM2_error(jj)
%    jj=jj+1;
% end

%% Determine conservation of flux based on RGB vs. MWI interferometer data
RGB_FWHM = 0.093;   %9.3cm full width half max
RGB_sigma = RGB_FWHM*0.5*(2*log(2))^-.5;    %Sigma width for Gaussian distribution
RGB_2D_IF = 2*pi*RGB_sigma^2; %2D integral of Gaussian with peak = 1
```

```
RGB_1D_IF = sqrt(RGB_2D_IF); %1D integral of Gaussian with peak = 1

Ka_FWHM = 0.90;  %90cm full width half max
Ka_sigma = Ka_FWHM*0.5*(2*log(2))^-.5;%Sigma width for Gaussian distribution
Ka_2D_IF = 2*pi*Ka_sigma^2; %2D integral of Gaussian with peak = 1
Ka_1D_IF = sqrt(Ka_2D_IF);  %1D integral of Gaussian with peak = 1

for ii = 1: Num_Shots
   if ii == 2
      figure
   else
      figure(1)
   end
   semilogy((data(ii).time_ave-0.451)*1000,abs(data(ii).density2_ave)./Ka_1D_IF.*Ka_2D_IF,'k','LineWidth',2);hold on
   semilogy((data(ii).time_ave-
0.451)*1000,0.5*(data(ii).RGB_d.ave+[data(ii).RGB_d.ave(2:300),1]).*1e5./RGB_1D_IF.*RGB_2D_IF,'b','LineWidth',2);hol
d off
   xlabel('Time (ms)','FontSize',12);ylabel('Density integrated over profile m^{-1}','FontSize',12)
   ArealFraction(1:299,ii)                =                abs(data(ii).density2_ave(1:299))./Ka_1D_IF.*Ka_2D_IF                ./
(.5*(data(ii).RGB_d.ave(2:300)+data(ii).RGB_d.ave(1:299)).*1e5./RGB_1D_IF.*RGB_2D_IF);
   ArealFraction(300,ii)=1;
end
figure(Num_Shots+1)
plot(data(1).time_ave,mean(ArealFraction'),'LineWidth',2)
xlabel('Time (s)','FontSize',12);ylabel('n_{1.85} / n_{0.33}  density ratio ','FontSize',12)

figure(Num_Shots+2)
plot((data(1).time_ave-0.451)*1000,mean(ArealFraction'),'LineWidth',5)
xlabel('Time (ms)','FontSize',18);ylabel('n_{1.85} / n_{0.33}  ','FontSize',18)

figure(Num_Shots+3)
errorbar((data(1).time_ave(200:215)-
0.451)*1000,mean(ArealFraction(200:215,:)'),std(ArealFraction(200:215,:)'),'k','LineWidth',2)
xlabel('Time (ms)','FontSize',12);%ylabel('n_{1.85} / n_{0.33}  ','FontSize',18)

%%%%  Gaussian fitting function - fits a shifted gaussian function to x-y data
function [estimates, model] = g_fit_new2(xdata, ydata,start_point)
model = @gaussfun;
if ~exist('start_point')
   start_point= [10,1e12];
end
start_point(3) = 0;
estimates = fminsearch(model, start_point, optimset('MaxIter',5000,'MaxFunEvals',5000,'Display','off'));
   function [sse, FittedCurve] = gaussfun(params)
      A = params(2);sigma = params(1);x_off = params(3);
      FittedCurve = A.* exp(-((xdata-x_off) ./ sigma).^2);
      ErrorVector = FittedCurve - ydata;
      sse = sum(ErrorVector .^ 2);
   end
end
```

```
%magnetic_nozzle_sim_hydrogen.m: simulation of 5/30/06 hydrogen scan.
%Quasi 1D magnetic field  simulation using Hydrogen, classical diffusion,
% constant velocity and 1.2eV Te.

%spatial grid subdivisions
divisions_in_z = 2000; divisions_in_r = 10;
%84 current sources and 10,000 points takes about 8 seconds to calculate on a 2.7 ghz Pentium IV

%earth magnetic field
%In huntsville, field runs north to south, at a 45 (actually 64 deg) degree angle with respect to the ground
%DDEX is oriented north to south, so that Bz_earth is positive with respect to model
earth = 1;  %switch to turn earth's field off and on
B_earth = 0.52/10000;Bz_earth = -cos(64)/2*B_earth;Br_earth = -sin(64)/2*B_earth;

zmax = 1.5;% axial limit of simulation
number_of_stages=7;     %number of nozzle magnets
turns_in_r = [10 15 10  2  1  1  4];  turns_in_z = [30 20 13  15  21  15  9];  % coil windings for each magnet
%radius to center of innermost coil         z position of center of leftmost coil
stage(1).rmin=1*.0254;                      stage(1).zmin=-1.14;%.475-3*.0254
stage(1).block_height = 1*.0254;                stage(1).block_width =  4*.0254;

stage(2).rmin=.75*.0254;                     stage(2).zmin=-.5;
stage(2).block_height = 1*.0254;                stage(2).block_width = 1*.0254;

stage(3).rmin = 5.*.0254;                   stage(3).zmin = -.91;  %N2 coil
stage(3).block_height = 2.5*.0254;              stage(3).block_width = 4*.0254;

stage(4).rmin = 18.*.0254;                   stage(4).zmin = -.72;     %Magnet 4
stage(4).block_height = .0808*.0254*2;           stage(4).block_width = 3.5*.0254;

stage(5).rmin = 18.*.0254;                   stage(5).zmin = -.42;
stage(5).block_height = .0808*.0254;            stage(5).block_width = 3.5*.0254;

stage(6).rmin = 18.*.0254;                   stage(6).zmin = -.12;
stage(6).block_height = .0808*.0254;            stage(6).block_width = 3.5*.0254;

stage(7).rmin = 4*.0254;                    stage(7).zmin = -.88; %additional coil for choke field
stage(7).block_height = 1*.0254;                stage(7).block_width = 3*.0254;
% ----------------------------------define currents-------------------------------------
ampsperturn = [5 0 100 10 3 3 100] ;  %nominal currents
%ampsperturn = [5 0 100 0 -20 35 100] ;  %optimized efficiency
%=============================================================================================

for ii = 1:number_of_stages
   stage(ii).coil_current = ampsperturn(ii);
end
for ii = 1:number_of_stages
   stage(ii).block_subdivisions_r = turns_in_r(ii);
   stage(ii).block_subdivisions_z = turns_in_z(ii);
   stage(ii).stage_current = turns_in_r(ii)*turns_in_z(ii)*ampsperturn(ii);
end


%----Calculate the current sources for the magnetic nozzle
current_source_count = 0;
for ii = 1:number_of_stages
   %determine the type of stage to determine the method for determining the current source parameters r, z, and I
   number_of_sources = stage(ii).block_subdivisions_r*stage(ii).block_subdivisions_z;
   current_per_source = stage(ii).stage_current/number_of_sources;

   dr = stage(ii).block_height/stage(ii).block_subdivisions_r;
   dz = stage(ii).block_width /stage(ii).block_subdivisions_z;
   for rr = 1:stage(ii).block_subdivisions_r
      for zz = 1:stage(ii).block_subdivisions_z
         current_source_count = current_source_count + 1;
         coil_current(current_source_count) = current_per_source;
         coil_z(current_source_count) = dz*(zz-1) + dz/2 + stage(ii).zmin;
         coil_r(current_source_count) = dr*(rr-1) + dr/2 + stage(ii).rmin;
      end
```

```
   end
end

%eliminate coils that have no current (have been turned off)
   no_current_indices = find(coil_current==0);
   if(isempty(no_current_indices))
   else
      number_of_coils_off = length(no_current_indices);
      current_source_count = current_source_count - number_of_coils_off;
      if(current_source_count==0)
         'no current, thus no field for this run'
         break
      else
         [dummy,ii] = sort(abs(coil_current));
         coil_current = coil_current(ii);
         coil_r      =      coil_r(ii);
         coil_z      =      coil_z(ii);
         coil_current = coil_current(number_of_coils_off + 1:current_source_count + number_of_coils_off);
         coil_r      =      coil_r(number_of_coils_off + 1:current_source_count + number_of_coils_off);
         coil_z      =      coil_z(number_of_coils_off + 1:current_source_count + number_of_coils_off);
      end
   end
%==================================================definition of grid
%---determine boundaries based on coil specifications

r0 = 0;r1 = min(coil_r(:));
z0 = min(coil_z(:));z1 = max(coil_z(:));
dz = z1-z0;dr = r1-r0;
if(dz==0), dz = dr; end
z0 = z0-dz/2;z1 = max(z1+dz/2,zmax);dz = z1-z0;
dz = dz/(divisions_in_z);dr = dr/(divisions_in_r);
rv = [r0:dr:r1]';r = rv*ones(1,divisions_in_z+1);
zv = [z0:dz:z1];z = ones(divisions_in_r+1,1)*zv;
%====================end definition of grid
%alocate memory for Br, Bz, r, z
Br = zeros(divisions_in_r+1,divisions_in_z+1);
Bz = zeros(divisions_in_r+1,divisions_in_z+1);
%add the earth's field
if(earth);    Br = Br+Br_earth;    Bz = Bz+Bz_earth;  end

%=======================================loop over geometry to calculate magnetic induction field
%[Br,Bz] = Bcalc(Br,Bz,r,z,coil_r,coil_z,coil_current)
for rr = 1:divisions_in_r+1
   for zz = 1:divisions_in_z+1
      [Br(rr,zz), Bz(rr,zz)] = Bcalc(Br(rr,zz),Bz(rr,zz),r(rr,zz),z(rr,zz),coil_r,coil_z,coil_current);
   end
end
%==========================plot data
figure(1), plot(coil_z+.862, coil_r,'.','color',[1 .7 .1]), set(gca,'ylim',[-r1 r1]), hold on; r1;
figure(1), plot(coil_z+.862,-coil_r,'.','color',[1 .7 .1]), axis equal
xlabel('Z (m)'), ylabel('R (m)')
drawchamber2(.862,0,1)% draw the chamber with metric units and a 0.862 m offset
%------------ Draw surface plot of magnetic field
clear r2 z2 Br2 Bz2
divisions_in_Br = 100;divisions_in_Bz = 100;
rbounds = [-0.5,1.5];zbounds = [-.4,3];
for rr = 1:divisions_in_Br+1
   r2(rr) = rr*(rbounds(2)-rbounds(1))/divisions_in_Br+rbounds(1);
end
for zz = 1:divisions_in_Bz+1
   z2(zz) = zz*(zbounds(2)-zbounds(1))/divisions_in_Bz+zbounds(1);
end
for rr = 1:divisions_in_Br+1
   for zz = 1:divisions_in_Bz+1
      [Br2(rr,zz), Bz2(rr,zz)] = Bcalc(0,0,r2(rr),z2(zz)-.862,coil_r,coil_z,coil_current);
   end
end
figure(1);hold on
pcolor(z2(:),r2(:),log10(1e4*sqrt(Bz2.^2+Br2.^2)))
shading interp;hold off;
```

```
colorbar('YLim',[-1 3], 'YTick',[-1 0 1 2 3],'YTickLabel',{'0.1 G','1 G','10 G','100 G','1000 G'})

%================================
%Begin quasi-1D nozzle simulation
%================================
T_e = 1.2;  % Electron temperature for hydrogen simulation
e_c = 1.602e-19;
m_i = 1.67e-27 * 1;  % Ion mass for hydrogen
m_e = 9.1e-31;
gamma = 1;  %Ratio of specific heats
Cs = sqrt(gamma*e_c*T_e/m_i); %ion sound speed
n_0 = 8.75e20;% initial density peak at z = -0.16m
FWHM_0 = 0.01;% initial full width half max at z = -0.16m
v_0 = 19e3;% initial velocity at z = -0.16m
fudgefactor = 0.5; %classical diffusion multiplicative adjustment.  =1 for
n_lamda_D2 =.548*T_e;    %n*(lambda_D)^2 determine the regime of diffusion (bohm vs. classical)

%set initial conditions at z =  -0.16m (plasma gun aperture)
[temp,index0] = min(abs(z(1,:)+0.862+0.16)); v(1,1:index0)=v_0; ne(1,1:index0)=n_0;
B0 = Bz(1,index0 );FWHM(1,1:index0)=FWHM_0;r_larmor(1,1:index0) = sqrt(T_e)/B0/1e4;
Thrust_0=2*pi*m_i*v_0^2*n_0*getthrust((index0)*dz,FWHM_0/2);Thrust(1,1:index0)=Thrust_0;

Beta(1,1:index0)=(v(1,1:index0).*sqrt(4*pi*1e-7*ne(1,1:index0)*m_i)./Bz(1,1:index0)).^2;
BetaIndex = 0;

for i = index0:divisions_in_z
   % calculate larmor radius, plasma frequency and cyclotron frequency for classical diffusion estimation
   r_larmor(1,i)=sqrt(T_e)/Bz(1,i)/1e4;
   omega_p(1,i)=56.4*sqrt(ne(1,i));   %plasma electron frequency
   omega_p(2,i)=omega_p(1,i).*sqrt(0.5); %omega_p at FWHM
   omega_p(3,i)=omega_p(1,i).*sqrt(0.05); %omega_p at 2W
   omega_c(1,i)=1.76e11*Bz(1,i);

   Thrust(1,i)=2*pi*m_i*v_0^2*ne(1,i)*getthrust((i-index0)*dz,FWHM(1,i)/2);
   %look for beta >1
   if (Beta(1,i) > 1 && z(1,i)>-.862) || BetaIndex
      if ~BetaIndex
         BetaIndex = i;
         %continue linear FWHM and 1/R^2 ne
         dFWHM = FWHM(i)-FWHM(i-1);
      end

      FWHM(1,i+1) = FWHM(1,i)+dFWHM;
      %determine n_e from flux conservation
      ne(1,i+1) = ne(1,i)*v(1,i-1)*FWHM(1,i)^2/v(1,i)/FWHM(1,i+1)^2;
      %velocity is constant
      v(1,i+1) = v(1,i);
   else
      %determine v_perp using FWHM/2
      [Brtemp,Bztemp] = Bcalc(0,0,FWHM(1,i)/2,z(1,i),coil_r,coil_z,coil_current);
      omega_c(2,i)=1.76e11*Bztemp;
      %use Okuda et al diffusion rates
      if omega_p(2,i)/omega_c(2,i)>(n_lamda_D2)^(1/3)
         %use classical diffusion

v_perp(1,i)=fudgefactor*10000/8*2*log(2)*4/FWHM(1,i)^2*sqrt(pi/2)*omega_p(2,i)^3/omega_c(2,i)^2/(0.5*ne(1,i))*(1+(2*m
_i/(m_i+m_e))^.5);
      elseif omega_p(2,i)/omega_c(2,i)<(n_lamda_D2)^(1/4)
         %use Bohm diffusion
         v_perp(1,i) = 0.345*T_e/Bztemp/FWHM(1,i)^2;  %real Bohm scaling
      else
         %use intermediate diffusion
         v_perp(1,i)=1/16*sqrt(T_e*e_c/(2*pi*ne(1,i)*(m_i+m_e)))*fudgefactor;
      end

      %limit v_perp to Cs.  Perpendicular diffusion limited to thermal rate
      if v_perp(1,i)>Cs
         v_perp(1,i)=Cs;
      end
      %determine FWHM from B-field scaling
```

```
      FWHM(1,i+1)=FWHM(1,i)*sqrt(Bz(1,i)/Bz(1,i+1));
      %include cross-field diffusion
      FWHM(1,i+1) = FWHM(1,i+1) + 2*v_perp(1,i)/v(1,i)*dz;  %factor of 2 because the column is expanding upwards and
downwards
      %determine n_e from flux conservation
      ne(1,i+1) = ne(1,i)*v(1,i-1)*FWHM(1,i)^2/v(1,i)/FWHM(1,i+1)^2;
      %constant velocity
      v(1,i+1)=v(1,i);
   end
end
%plot FWHM on figure 1
figure(1);hold on;plot(z(1,index0:divisions_in_z)+.862,FWHM(1,index0:divisions_in_z)./2,'k','LineWidth',3)
%% Include data points on figure 1
figure(1);hold on;plot([0.33 .43 0.9 1.57 1.85],[0.1 .17 .42 .8 .9]./2,'ko','Markersize',8,'Markerfacecolor',[.7 .78 1])
hold off



function [Br, Bz]= Bcalc(Br,Bz,r,z,coil_radius,coil_z,coil_current)
%Magnetic field calculation at a given r,z location.  Code written by Greg Chavers - MSFC
%magnetic permeability of free space
mu0 = 4*pi*1e-7;
B0 = coil_current.*mu0./2.0./coil_radius;
alpha   = abs(r./coil_radius);
dz      = z - coil_z;
beta    = dz./coil_radius;
Q       = ((1+alpha).^2 + beta.^2);
M       = 4.0.*alpha./Q;
gamma   = dz./(r+eps);
[K,E]   = ellipke(M);
Bz = sum(B0./pi       ./sqrt(Q).*(E.*((1-alpha.^2-beta.^2)./(Q-4.*alpha))+K));
Br = sum(B0./pi.*gamma./sqrt(Q).*(E.*((1+alpha.^2+beta.^2)./(Q-4.*alpha))-K));

function [thrust_out]=getthrust(z,R)
%function to complete numerical integration of T(z) by performing the
%integral Int[r/(1+r/z)^2 *2^-(r^2/R^2),r,0,4R]
thrust_fun = @(r)(r./(1+(r./z).^2) .*2.^-(r.^2/R^2));
thrust_out = quad(thrust_fun,0,4*R);


%draw the vacuum chamber spool.  Code written by Greg Chavers - MSFC
function drawchamber2(x0,y0,useSIunits)
if(useSIunits),
   %first, put x0, y0 into inches and convert later
   x0 = x0/.0254; % set x0 at spool piece chamber interface
   y0 = y0/.0254;
   conversion = .0254;
else
   conversion = 1.0;
   x0=x0-1.437/.0254; % set x0 at spool piece chamber interface
end
%left and right large flange on spool
rectangle('position',cf46(x0-31.5,y0)*conversion)
rectangle('position',cf46(x0-30,y0)*conversion)
rectangle('position',cf46(x0-1.5,y0)*conversion)
%'barrel' of spool
spool_radius = 17.25;
rectangle('position',[(x0-28.5) -spool_radius 27 34.5]*conversion)
%adjacent conflat to mount spool to 'nipple' on chamber
rectangle('position',cf46(x0,y0)*conversion)
 %chamber nipple
nipple_length = 8.1;
rectangle('position',[(x0+1.5) -18 nipple_length 36]*conversion)

%plot the vacuum chamber, using a curve fit for the door, y = -x^n
chamber_radius = 53.5;door_length = 27.74;door_slope = 9/2;
n=(door_length*door_slope/chamber_radius);
xend=(chamber_radius/door_length)^(1/(n-1));
x = [0:.01:xend];  y=-x.^n;p = length(y):-1:1;   y=y(p);  %reverse order on y
%scale x and y and adjust position to fit door size
x =  x0 + 1.5 + nipple_length + x/(-y(1))*(chamber_radius-spool_radius);
```

```
y = -y/y(1)*(chamber_radius-spool_radius);y = y + abs(y(1)) + spool_radius;
x = x*conversion;  y = y*conversion;
plot(x,y,'k','linewidth',1)
plot(x,-y,'k','linewidth',1)
rectangle('position',[x(end) -y(end) 1.5*conversion 2*y(end)])

%draw the ports on the chamber door, connecting to the closest points on the curve describing the chamber
y1 = 31.25*conversion;y4 = 41.13*conversion;dx = 6.28*conversion;
[dummy,iy1]=min(abs(y-y1));[dummy,iy4]=min(abs(y-y4));
x1 = x(iy1); y1 = y(iy1);x4 = x(iy4); y4 = y(iy4);x2 = x1-dx;  y2 = y1;x3 = x2;     y3 = y4;
lh1 = line([x1 x2],[y1 y2]); set(lh1,'linewidth',1);lh2 = line([x2 x3],[y2 y3]); set(lh2,'linewidth',1)
lh3 = line([x3 x4],[y3 y4]); set(lh3,'linewidth',1);lh4 = line([x1 x2],[-y1 -y2]); set(lh4,'linewidth',1)
lh5 = line([x2 x3],[-y2 -y3]); set(lh5,'linewidth',1);lh6 = line([x3 x4],[-y3 -y4]); set(lh6,'linewidth',1)
%draw the conflat on the ports
rectangle('position',[(x2/conversion-1) (y1/conversion+9.88/2-11.64/2) 1 11.64]*conversion)
rectangle('position',[(x2/conversion-1) -(y1/conversion+9.88/2+11.64/2) 1 11.64]*conversion)
%draw the vacuum chamber, last flange, and door
chamber_length = 15*12;
rectangle('position',[(x(end)+1.5*conversion) -y(end) chamber_length*conversion 2*y(end)])
rectangle('position',[(x(end)+(1.5+chamber_length)*conversion) -y(end) 1.5*conversion 2*y(end)])
x = x+x(end)-x(1)+(3+chamber_length)*conversion;
plot(x,y(p),'k','linewidth',1);plot(x,-y(p),'k','linewidth',1);plot([x(end),x(end)],[y(1),-y(1)],'k','linewidth',1)
%10" conflat ports, viewing
rectangle('Curvature', [1 1],'position',[(x0 -26)  -5  10 10]*conversion)
rectangle('Curvature', [1 1],'position',[(x0 -14) -5  10 10]*conversion)
%10" conflat ports, at bottom
drawcf10(x0 - 21, y0,conversion);drawcf10(x0 - 9,y0,conversion)
%3" conflat ports, on top
drawcf03(x0-24, y0,conversion);drawcf03(x0-18,y0,conversion)
drawcf03(x0-12,y0,conversion);drawcf03(x0-6,y0,conversion)
%nipple, flange stacks, collar, quarts tube, antennae on spool
radius = 4;width = 4;r_flange1 = 9.85/2;r_flange2 = 9.85/2;r_flange3 = 4;
radius2 = 3;width2 = 3;r_flange4 = 2;w_flange = 1;r_collar = 1;
w_collar = 1.25;x1_antennae = x0-19.5;r_antennae = r_collar;
w_antennae = 3.25;r_tube = 1.75/2;w_tube = 27.75;x1_tube = x0-w_tube-4*w_flange-width;
rectangle('position',[(x0-31.5-width) (y0-radius) width 2*radius]*conversion)
rectangle('position',[(x0-31.5-width-1*w_flange) (y0-r_flange1) w_flange 2*r_flange1]*conversion)
rectangle('position',[(x0-31.5-width-2*w_flange) (y0-r_flange2) w_flange 2*r_flange2]*conversion)
rectangle('position',[(x0-31.5-width-3*w_flange) (y0-r_flange3) w_flange 2*r_flange3]*conversion)
rectangle('position',[(x0-31.5-width-3*w_flange-width2) (y0-radius2) width2 2*radius2]*conversion)
rectangle('position',[(x0-31.5-width-4*w_flange-width2) (y0-r_flange3) w_flange 2*r_flange3]*conversion)
rectangle('position',[(x0-31.5-width-5*w_flange-width2) (y0-r_flange3) w_flange 2*r_flange3]*conversion)
rectangle('position',[(x0-31.5-width-5*w_flange-2*width2) (y0-radius2) width2 2*radius2]*conversion)
rectangle('position',[(x0-31.5-width-6*w_flange-2*width2) (y0-r_flange3) w_flange 2*r_flange3]*conversion)

function x = cf46(x0,y0)
%return coordinates for large flanges on spool in inches
%the vector x refers to x, y, width, and height of rectangle,
%where x and y are the lower left corner of rectangle
x(1) = 0   + x0;x(2) = -23 + y0;x(3) = 1.5;x(4) = 46;

function drawcf10(x0,y0,conversion)
%draws 10" conflats on spool
x = -5  + x0;y = -19.25 + y0;w = 10;h = 1;
rectangle('position',[x     y     w h]*conversion)
rectangle('position',[(x+1) (y+1) 8 h]*conversion)

function drawcf03(x0,y0,conversion)
%draws 3" conflats on spool top
x = -1.5  + x0;y = 18.75  + y0;w = 3;h = 0.5;
rectangle('position',[x        y  w    h]*conversion)
rectangle('position',[(x0-0.75) 17.25 1.5  1.5]*conversion)
```

BIBLIOGRAPHY

BIBLIOGRAPHY

Anderson, J.D. *Modern Compressible Flow*, McGraw Hill, NewYork, 1990

Ando, A. Inutake, M. Hatanaka, M. Hattori, K. Tobari, H. and Yagai, T. "Alfvén wave excitation and single-pass ion cyclotron heating in a fast-flowing plasma", Physics of Plasmas **13** 057103, 2006

Arefiev, A.V. and Breizman, B.N. "Theoretical components of the VASIMR plasma propulsion concept", Physics of Plasmas **11** (5) pp. 2942-2949, 2004

Arefiev, A.V. and Breizman, B.N. "Magnetohydrodynamic Scenario of Plasma Detachment in a Magnetic Nozzle" Physics of Plasmas, Vol. 12, No. 4, 2005

Balanis, C.A., *Antenna Theory – Analysis and Design,* John Wiley & Sons, Inc., 1997

Barnett, C.F. (ed.) ORNL "Redbook", *Atomic Data for Fusion. Volume 1: Collisions of H, H_2, He, and Li Atoms and Ions with Atoms and Molecules* ORNL-6086 (1990)

Bartmess, J. and Georgiadis, R. "Empirical methods for determination of ionization gauge relative sensitivities for different gases", Vacuum **33** (3) pp. 149-153, 1983

Breizman, B. Tushentsov, M. and Arefiev, A. "Magnetic Nozzle and Plasma Detachment Scenario", paper IEPC-2007-180, 30th International Electric Propulsion Conference, Florence, Italy, September 17-20, 2007

Brenning, N. Hurtig, T. and Raadu, M.A. "Conditions for plasmoid penetration across abrupt magnetic barriers", Physics of Plasmas, Vol. 12, No. 1, 2005

Bufton, S. "Exit plane plasma measurements of a low-power hydrazine arcjet", PhD Thesis University of Illinois, Urbana-Champaign 1996

Cassabry, J. "Theoretical performance of an MHD nozzle using super-Alfvenic detachment", paper AIAA-2006-5160, 42nd AIAA Joint Propulsion Conference, Sacramento, CA, July 9-12 2006

Chang, J. Kamitsuma, M. and Chen, S. "Theory of Instantaneous triple-probe method for direct-display of plasma parameters in a low density flowing collisionless plasma", Planet. Space Sci. **25** p. 973 (1977)

Chang-Diaz, F.R. "The VASIMR Rocket" Scientific American. Vol 283, No. 90, 2000

Charles, C. and Boswell, R. "Current-free double-layer formation in a high-density helicon discharge", Applied Physics Letters **82** (9) pp. 1356-1358 2003

Charles, C. et al., "Helicon Double Layer Thrusters", AIAA 2006-4838, 42nd AIAA Joint Propulsion Conference, Sacramento, CA, 2006

Chavers, G. et al., "Status of magnetic nozzle and plasma detachment experiment", AIAA Space Technology and Applications International Forum, February 2006

Chen, F.F. *Introduction to plasma physics and controlled fusion*, Plenum Press, New York, 1986

Chen, S.L. and Sekiguchi, T., "Instantaneous Direct-Display System of Plasma Parameters by Means of Triple Probe," Journal of Applied Physics*,* **36,** 8, pp. 2363-2375, 1965

Choi, Y. et al., "Determination of Plasma Flow Velocity by Mach Probe and Triple Probe with Correction by Laser-Induced Fluorescence in Unmagnetized Plasmas", Japanese Journal of Applied Physics **45** 7, 2006

Choiniere, E. Bilen, S. Gilchrist, B. Fuhrhop, K. and Gallimore, A. "Experimental investigation of electron collection to solid and slotted tape probes in a high-speed flowing plasma", IEEE Transactions on Plasma Science **33** p. 1310, 2005

Choinière, E. "Theory and experimental evaluation of a consistent steady-state kinetic model for 2-D conductive structures in ionospheric plasmas with application to bare electrodynamic tethers in space," Ph.D. dissertation, Univ. Michigan, Ann Arbor, MI, Sep. 2004.

Choiniére, E. and Gilchrist, B. "Self-Consistent 2-D Kinetic Simulations of High-Voltage Plasma Sheaths Surrounding Ion-Attracting Conductive Cylinders in Flowing Plasmas", Transactions on Plasma Science **35**, 1, 2007

Choinière, E. Private communication. The KiPS-2D code was designed, debugged and operated by Eric Choinière. The author provided Eric the conditions for individual simulations including probe radius, bias condition and flow velocity. Simulation results including ion and electron current was returned by Eric to the author for subsequent reduction and analysis. 2008

Chubb, D.L. "Fully ionized quasi-one-dimensional magnetic nozzle flow" AIAA Journal **10**, (2), 1972

Cohen, S.A. Seifert, N.S. Stange, S. Boivin, R.F. Scime, E.E. and Levinton, F.M. "Ion acceleration in plasmas emerging from a helicon-heated magnetic-mirror device", Physics of Plasmas **10**, (6) pp. 2593-2598, 2003

Coleman, H.W. and Steele, W.G. Jr., *Experimentation and Uncertainty Analysis for Engineers*, Wiley, New York, 1999

Davis, C. "Experimental Validation of Single Pass Ion Cyclotron Resonance Absorption in a High Speed Flowing Plasma Applied to the Variable Specific Impulse Magnetoplasma Rocket (VASIMR)", PhD. Dissertation, University of Michigan, 2006

Dawson, J.M. Okuda, H. and Carlile, R.N. "Numerical Simulation of Plasma Diffusion across a Magnetic field in Two Dimensions", Physical Review Letters, **27** 8, 1971

Deline, C. Chavers, G. Gilchrist, B. "Physics of Plasma Detachment in a Magnetic Nozzle", paper AIAA-2006-4653, 42nd AIAA Joint Propulsion Conference, Sacramento, CA July 9-12 2006

Deline, C. Gilchrist, B. Bengtson, R. Jones, J. Chavers, G. Dobson, C. "Simulation and measurement of high-Beta plasma in a magnetic nozzle", paper AIAA 2007-5259, 43rd AIAA Joint Propulsion Conference, Cincinnati, OH, July 8-11, 2007

Deline, C. Gilchrist, B. Chavers, G. Jones, J. Dobson, C. Schuettpelz, B. Bengtson, R. and Breizman, B. "Plasma expansion in a paraxial magnetic nozzle", 33rd IEEE International Conference on Plasma Science, Traverse City, MI June 4-8, 2006

Deline, C. Gilchrist, B. Squire, J. Chavers, G. Jones, J. Dobson, C. and Bengtson, R. "Measurement of Magnetic Detachment Effects in a Magnetic Nozzle", 30th International Electric Propulsion Conference, Florence, Italy, September 17-20, 2007

Deline, C. Gilchrist, B. Dobson, C. Jones, J. and Chavers, G. "High accuracy plasma density measurement using hybrid Langmuir probe and microwave interferometer method", Review of Scientific Instruments **78**, page 113504, 2007

Dobson, C. Jones, J. and Chavers, D.G. "Instrument reflections and scene amplitude modulation in a polychromatic microwave quadrature interferometer" Review of Scientific Instruments **75** (3) 2004

Dobson, C. Private communication, Time of flight data provided courtesy of C. Dobson, MSFC 2007

Edwards, C.H. and Penney, D.E. *Differential Equations: Computing and Modeling*, Prentice Hall, New Jersey, 1996

Fiksel, G. Almagri, A.F. Craig, D. Lida, M. Prager, S.C. and Sarff, J.S. "High current plasma electron emitter" Plasma sources science and technology **5** pp. 78-83, 1996

Flender, U. Nguyen, B. Thi, M. Wiesemann, K. Khromov, N. and Kolokolov, N. "RF harmonic suppression in Langmuir probe measurements in RF discharges", Plasma Sources Science & Technology, **5** p. 61 1996

Fruchtman, A. "Electric field in a double layer and the imparted momentum", Physical Review Letters **96** (6) article 065002 2006

Gerwin, R.A. Marklin, G.J. Sgro, A.G. and Glasser, A.H. "Characterization of Plasma Flow Through Magnetic Nozzles" Report AL-TR-89-092, Astronautics Laboratory (AFSC), Edwards AFB, CA, 1989

Gesto, F.N. Blackwell, B.D. Charles, C. and Boswell, R.W. "Ion detachment in the helicon double-layer thruster exhaust beam" Journal of Propulsion and Power, Vol. 22, No. 1, 2006

Gilbody, G. and Hasted, H. "Anomalies in adiabatic interpretation of charge-transfer collisions", Proceedings of the Royal Society of London A **238** (1214) pp. 334-343, 1957

Gilchrist, B. Ohler, S. and Gallimore, A. "Flexible microwave system to measure the electron number density and quantify the communications impact of electric thruster plasma plumes", Review of Scientific Instruments **68** (2) 1997

Glover, T. "Measurement of plasma parameters in the exhaust of a magnetoplasma rocket by gridded energy analyzer and emissive Langmuir probe", PhD Dissertation, Rice University, 2002

Gottardi, N. "Evaluation of electron density profiles in plasmas from integrated measurements", Journal of Applied Physics **50**, 4, 1979

Granville-Phillips co., "Series 370 Stabil-Ion vacuum measurement system installation, operation and maintenance instructions", Granville-Phillips Instruction Manual catalog # 370119-04, 1999

Griffin, M.D. House of Representatives Committee on Science Hearing on the Future of Human Space Flight, 16 Oct, 2003

Ha, J.H. Nam, Y.U. Cheon, M.S. and Hwang, Y.S. "An improved Abel inversion method modified for tangential interferometry in tokamak" Review of Scientific Instruments **75**, 10, 2004

Heald, M.A., Wharton, C.B., *Plasma Diagnostics with Microwaves*, R.E.Krieger, New York 1978

Hoegy, W.R., and L.E. Wharton, "Current to moving spherical and cylindrical electrostatic probes", Journal of Applied Physics, vol. **44**, no. 12, p. 5365, 1973

Hooper, E.B. "Plasma Detachment from a Magnetic Nozzle", Journal of Propulsion and Power 9 (5) 1993

Hopman, H.J., Alberda, H., Attema, I., Zeijlemaker, H., Verhoeven, J., "Measuring the secondary electron emission characteristic of insulators," Journal of Electron Spectroscopy and Related Phenomena 131-132 pp. 51-60, 2003

Huba, J.D., *NRL plasma formulary*, Office of Naval Research, Washington DC, 2006

Humble, R.W. Henry, G.N. and Larson, W.J. *Space Propulsion Analysis and Design*, McGraw-Hill, 1995

Hurtig, T., Brenning, N., Raadu, M.A. "The penetration of plasma clouds across magnetic boundaries: the role of high frequency oscillations", Physics of Plasmas vol. **11** no. 7, 2004

Hutchinson, I.H., *Principles of Plasma Diagnostics*, University Press, Cambridge, 2002

Ilin, A.V., Chang Diaz, F.R., Squire, J.P., Tarditi, A.G., Breizman, B.N., and Carter, M.D., "Simulations of Plasma Detachment in VASIMR," 40th AIAA Aerospace Science Meeting, Paper 2002-0346, Jan. 2002

Inutake, M. Ando, A. Hattori, K. Tobari, H. and Yagai, T. "Characteristics of a supersonic plasma flow in a magnetic nozzle", Journal of Plasma Fusion Research **78** (12) pp 1352-1360, 2002

Ishizuka, H. and Robertson, S. "Propagation of an intense charge-neutralized ion beam transverse to a magnetic field", Physics of Fluids **25**, 2353 1982

Jackson, J.D. *Classical Electrodynamics*, 2nd edition, Wiley, New York, 1975

Jackson, R.H. "Off-Axis Expansion Solution of Laplace's Equation: Application to Accurate and Rapid Calculation of Coil Magnetic Fields", IEEE Transactions on Electron Devices, **46,** pp. 1050-1062, 1999

Jeffreys, H. and Jeffreys, B., *Methods of Mathematical Physics*, University Press, Cambridge, 1946

Kamitsuma, M. Chen, S.L. and Chang, J.S. "The theory of the instantaneous triple-probe method for direct-display of plasma parameters in low-density collisionless plasmas", J. Phys. D: Appl. Phys., **10**, pp.1065-1077 (1977)

Kammash, T. "A fusion propulsion system for rapid interplanetary travel", Acta Astronautica **47** (2-9) pp. 97-102 2000

Karavasilis, K. Moskal'ov, S. Sagdeev, R. Usikov, D. and Chang-Diaz, F. "Trajectory simulations for plasma propelled spacecraft", AIAA-2001-919 Aerospace Sciences Meeting and Exhibit, 39th, Reno, NV, Jan. 8-11, 2001

Kinderdijk, H. and Van Eck, J. "Comparison of electron densities measured with Langmuir probes and with two different microwave devices", Physica **59** p. 257-284 (1972)

Kong, J.A., *Electromagnetic Wave Theory*, EMW publishing, Cambridge, MA 2000

Kraft, D.J. et al., "Analysis of multifrequency interferometry in a cylindrical plasma", Review of Scientific Instruments **77**, 10E910, 2006

Laframboise, J.G. "Theory of Spherical and Cylindrical Langmuir Probes in a Collisionless, Maxwellian Plasma at Rest" PhD Dissertation, University of Toronto, 1966

Langmuir, I. and Mott-Smith, H.M., "The Theory of Collectors in Gaseous Discharges," Physical Review, **28** pp. 727-763, 1926

Lieberman, M. and Lichtenberg, A. *Principles of plasma discharges and materials processing*, Wiley & Sons, New York, 1994

Lieberman, M.A. and Charles, C. "Theory for formation of a low-pressure, current-free double layer", Physical Review Letters, **97** (4) 2006

Longmier, B. Baalrud, S. and Hershkowitz, N. "Nonambipolar electron source", Review of Scientific Instruments, **77** 113504, 2006

Martinez-Sanchez, M. and Pollard, J.E. "Spacecraft electric propulsion – an overview", Journal of Propulsion and Power, **14**, 5 pp. 688-699, 1998

McDaniel, E. *Atomic Collisions: heavy particle projectiles*, Wiley & Sons, NY 1993

McLatchy, C.S. Boucher, C. Poirier, D.A. and Gunn, J. "Gundestrup: A Langmuir/Mach probe array for measuring flows in the scrape-off layer of Tdev", Review of Scientific Instruments **63**, p. 3923, 1992

McMahon, J. Xu, G. and Laframboise, J. "The effect of ion drift on the sheath, presheath, and ion-current collection for cylinders in a collisionless plasma" Physics of Plasmas vol. **12** page 062109, 2005

Meige, A. Boswell, R.W. Charles, C. and Turner, M. "One-dimensional particle-in-cell simulation of a current-free double layer in an expanding plasma", Physics of Plasmas vol. **12** no. 5 article 052317, 2005

Meyer, J. "Experimental Study of Plasma Separation from a Magnetic Field", Master's Dissertation, University of Texas, Austin, 2007

Mikellides, I.G. Mikellides, P.G. Turchi, P.J. and York, T.M. "Design of a Fusion Propulsion System – Part 2: Numerical Simulation of Magnetic-Nozzle Flows", Journal of Propulsion and Power **18** (1) 2002

Miller, J.S. et al., "Xenon charge exchange cross sections for electrostatic thruster models", Journal of Applied Physics **91** (3) 2002

MKS Instruments customer support, private communication 10/24/07

Moffat, R.J. "Describing the Uncertainties in Experimental Results", Experimental Thermal and Fluid Science **1**, 1 pp. 3-17, 1988

Mott-Smith, H.M. and Langmuir, I. “The Theory of Collectors in Gaseous Discharges”, Physical Review, **28**, 4, pp. 727-763, 1926

Ogram, G. Chang, J. and Hobson, R. “The triple-probe method applied to the direct display of plasma parameters in a supersonic flowing continuum plasma”, Journal of Applied Physics **50,** p. 726, 1979

Ohler, S. “Space electric propulsion plasma characterization using microwave and ion acoustic wave propagation”, PhD. Dissertation, University of Michigan, 1996

Okuda, H. and Dawson, J.M. “Theory and numerical simulation on plasma diffusion across a magnetic field”, Physics of Fluids, **16,** 3, 1973

Oleson, R. "Electric Propulsion Technology Development for the Jupiter Icy Moon Orbiter", 40th AIAA Joint Propulsion Conference, Ft. Lauderdale, FL AIAA-2004-3449, 2004

Oliver, A.D. and Phillips, B. “Integrated lens with dielectric horn antenna” Electronics Letters 29 (13) 1993

Overzet, L.J., Hopkins, M.B., “Comparison of electron-density measurements made using a Langmuir probe and microwave interferometer in the Gaseous Electronics Conference reference reactor”, Journal of Applied Physics **74**, 7, pp 4323-4330, 1993

Paranjpe, A. McVittie, J. and Self, S. “A tuned Langmuir probe for measurements in rf glow discharges”, Journal of Applied Physics. **67** p. 6718, 1990

Parker, E.N. “Dynamics of the interplanetary gas and magnetic fields”, Astrophysical Journal, Vol. 128, No. 3, 1958

Racca, G. D “Capability of solar electric propulsion for planetary missions”, Planetary and Space Science **49** pp. 1437-1444, 2001

Raizer, J.P. *Gas Discharge Physics*, Springer, Berlin, 1991

Randolph, T. Kim, V. Kaufman, H. Kozubsky, K. Zuhrin, V. and Day, M. “Facility Effects on Stationary Plasma Thruster Testing,” IEPC-93-93 23rd International Electric Propulsion Conference, Seattle, WA, Sept 13-16, 1993

Rayman, M.D. Varghese, P. Lehman, D.H. and Livesay, L.L. “Results From The Deep Space 1 Technology Validation Mission”, Acta Astronautica **47**, 2000

Sankaran, K. Cassady, L. Kodys, A. and Choueiri, E. “A survey of propulsion options for cargo and piloted missions to Mars”, Annals, N.Y. Academy of Science, **1017** pp. 450-467, 2004

Schächter, L. Dobrescu, S. Badescu-Singureanu, A. and Baltateanu, N. "High secondary electron emission for an enhanced electron density in electron cyclotron resonance plasma", Review of Scientific Instruments **69** p. 706, 1998

Schmidt, G. "Plasma motion across magnetic fields", Physics of Fluids **3** (6) pp. 961-965 1960

Schuettpelz, B. Li, Z. and Cassabry, J. "Plasma Diagnostics Supporting Magnetic Nozzle Plasma Detachment Demonstration Experiment," paper AIAA-2006-515942nd AIAA Joint Propulsion Conference, Sacramento, CA, July 9-12, 2006

Sercel, J.C. "A Simple Model of Plasma Acceleration in a Magnetic Nozzle", 21st International Electric Porpulsion Conference, 1990

Smith, L.M. and Keefer, D. R. "Abel inversion using transform techniques", Journal of Quantitative Spectroscopy and Radiative Transfer **39** 5, 1988

Spores, R.A. Pobst, J.A. Schilling, J.H. and Erwin, D. A. "Performance effects of interaction between a low-power arcjet and its power processing unit", paper AIAA 92-3238, 28th Joint Propulsion Conference, Nashville, TN, 1992

Squire, J. Chang-Diaz, F.R. Carter, M. Cassady, L. Chancery, W. Glover, T. Jacobson, V. McCaskill, G. Bengtson, R. Bering, E. and Deline, C. "High Power VASIMR Experiments using Deuterium, Neon and Argon", paper IEPC-2007-181 30th International Electric Propulsion Conference, Florence, Italy, September 17-20, 2007

Squire, J.P. et al., "Progress in experimental research of the VASIMR engine", Fusion Science and Technology vol. **43** no. 1T pp. 111-117, 2003

Stix, T.H., *Waves in Plasmas*, Springer-Verlag, New York, 1992

Sudit, I. and Chen, F. "RF compensated probes for high-density discharges", Plasma Sources Science & Technology, **3** p. 162, 1994

Tallents, G., "Interferometry and refraction measurements in plasmas of elliptical cross-section", Journal of Physics D: Applied Physics, **17** pp. 721-732, 1984

Taylor, B.N and Kuyatt, C.E. "Guidelines for Evaluating and Expressing the Uncertainty of NIST Measurement Results", NIST Technical note 1297, National Institute of Standards and Technology, 1994

Tikhonov, V. Semenikhin, S. Brophy, J. and Polk, J. "Performance of 130 kW MPD Thruster with an External Magnetic Field and Li as Propellant", International Electric Propulsion Conference., paper 97-117, 1997

Tilley, D. Gallimore, A. Kelly, A. and Jahn, R. "The adverse effect of perpendicular ion drift flow on cylindrical triple probe electron temperature measurements" Review of Scientific Instruments **65,** p. 678, 1994

Tipler, P. and Llewellyn, R. *Modern Physics,* W.H. Freeman & Co., NY, 2000

Toki, K. Shinohara, S. Tanikawa, T. and Shamrai, K.P. "Small helicon plasma source for electric propulsion", Thin Solid Films **506-507** pp. 597-600, 2006

Vest, C., "Interferometry of strongly refracting axisymmetric phase objects", Applied Optics, **14** pp1601-1606, 1975

Walker, E.L. and Seikel, G.R. "Axisymmetric expansion of a plasma in a magnetic nozzle including thermal conduction," NASA Report TND-6154, 1971

Wertz, J.R. *Space Mission Analysis and Design, 3rd Edition,* Microcosm Press, 1999

Wessel, F. and Robertson, S. "Polarization of an intense space-charge-neutral ion beam incident upon a magnetic field", Physics of Fluids **24** (4), 1981

Wessel, F. Rostoker, N. Fisher, A. Rahman, H.U. and Song, J.H. "Propagation of neutralized plasma beams", Physics of Fluids B **2** (6), 1990

White, R.J. and Averner, M. "Humans in Space", Nature **409** 1115-1118, 2001

Whittaker, G.T. and Watson, G.W. *A Course of Modern Analysis*, Cambridge University Press, Cambridge, UK, 1902

Williams, C. "Application of Recommended Design Practices for conceptual nuclear fusion space propulsion systems", AIAA 2004-3534, 40th AIAA Joint Propulsion Conference, Ft. Lauderdale, FL, 2004

Woo, H. Chung, K. Choi, Y. Lee, M. Zimmerman,D. and McWilliams, R. "Effect of Supersonic Ion Beams on the Triple Probe Measurement", Contributions to Plasma Physics **46**, p. 451, 2006

Xu, G. "The interaction of a moving spacecraft with the ionosphere: Current collection and wake structure" PhD. Dissertation, York University, 1992